Advanced scattering techniques for the investigation of radiation-induced damage in nuclear materials

by

Ela Young

A thesis submitted to the University of Birmingham

for the degree of

DOCTOR OF PHILOSOPHY

School of Metallurgy and Materials

College of Engineering and Physical Sciences

University of Birmingham

September 2021

UNIVERSITY OF
BIRMINGHAM

University of Birmingham Research Archive
e-theses repository

This unpublished thesis/dissertation is under a Creative Commons Attribution-NonCommercial-NoDerivatives 4.0 International (CC BY-NC-ND 4.0) licence.

You are free to:

Share — copy and redistribute the material in any medium or format

The licensor cannot revoke these freedoms as long as you follow the license terms.

Under the following terms:

Attribution — You must give appropriate credit, provide a link to the license, and indicate if changes were made. You may do so in any reasonable manner, but not in any way that suggests the licensor endorses you or your use.

NonCommercial — You may not use the material for commercial purposes.

NoDerivatives — If you remix, transform, or build upon the material, you may not distribute the modified material.

No additional restrictions — You may not apply legal terms or technological measures that legally restrict others from doing anything the license permits.

Notices:

You do not have to comply with the license for elements of the material in the public domain or where your use is permitted by an applicable exception or limitation.

No warranties are given. The license may not give you all of the permissions necessary for your intended use. For example, other rights such as publicity, privacy, or moral rights may limit how you use the material.

Unless otherwise stated, any material in this thesis/dissertation that is cited to a third-party source is not included in the terms of this licence. Please refer to the original source(s) for licencing conditions of any quotes, images or other material cited to a third party.

Abstract

Harsh fission and fusion reactor environments lead to radiation damage in nuclear materials in the form of nanoscale precipitation events. Such microstructural changes can ultimately compromise macroscopic material properties. Understanding the evolution of nuclear material properties over their operational lifetime is crucial for the provision of safe, reliable nuclear power generation.

This thesis aims to demonstrate how advanced scattering techniques can contribute to the understanding of nanoscale transitions in nuclear materials systems. It focuses on materials of interest in the current nuclear landscape where knowledge gaps and contradictions exist on the structural and compositional properties of both thermal ageing induced and irradiation induced precipitates. Specifically, it presents novel applications of small angle scattering (SAS) techniques to the study of both thermal ageing induced and irradiation induced precipitation damage to showcase the versatility of SAS for characterising the differences between the two mechanisms of precipitation damage. The systems of interest are life-limiting nuclear materials such as low alloy reactor pressure vessel (RPV) steels and tungsten as a fusion plasma-facing material. These material systems were chosen as they are critical for the future of nuclear power generation (advanced light water fission reactors and commercial fusion reactors) where there is an industry requirement to increase the understanding of how thermal ageing induced and irradiation induced precipitation damage can lead to adverse material property evolution.

A high Ni RPV weld thermally aged for 100 000 hours at 330 °C was studied using SAS to complement previous findings from other investigative techniques. Magnetic precipitates with mean radius 2.01 ± 0.06 nm were observed using small angle neutron scattering. The first use of anomalous small angle x-ray scattering on this RPV material system allowed for the explicit consideration of the role of iron and vacancies on thermal ageing induced precipitation which is often omitted in literature.

A series of model Fe-Cu-Mn-Ni RPV alloys were thermally aged to elucidate the role of alloying elements on precipitate nucleation and growth. SAS was used to extract precipitate properties and also for a novel in-situ ageing study on the kinetics of precipitation. The structure and likely composition of thermal ageing induced precipitates was confirmed. It was found that Mn suppresses precipitate growth in the presence of Cu and Ni during thermal ageing. A comparison between the mechanisms of thermal ageing and irradiation induced precipitation was made.

A novel proton irradiation configuration was used to investigate transmutation reactions and precipitation damage in pure tungsten. Displacement damage up to 0.414 dpa was reached, with small fractions of rhenium, osmium and tantalum transmuted during irradiation. Due to the limited transmutation, the matrix damage was identified, using SANS, as a network of spherical nanoscale voids that increase in size and volume fraction with increasing damage in irradiated tungsten.

Material hardening and embrittlement due to the presence of nanoscale precipitates has been quantified for each material system using microindentation and nanoindentation hardness techniques.

ACKNOWLEDGEMENTS

The first acknowledgement goes to my mentor and original supervisor, Dr Mark Laver, who taught me the master craft of neutron and x-ray scattering. Thank you for encouraging me, inspiring me, challenging me, and guiding me through the world of advanced scattering. I would never have found my passion for these techniques without your support. I am especially grateful for all the food and beer, the beamtime grafts, and the opportunities to travel to new places and collaborate with brilliant scientists.

To Dr Biao Cai, my current supervisor, who supported me through a pivotal point in this work and has continued to support me endlessly. Thank you for giving me insight, advice, and direction at the time I needed it most.

To my co-supervisors, Professor Paul Bowen, Dr Yu-Lung Chiu and Dr Daniel Reed. I am eternally thankful for all the mentoring and practical support you have provided me throughout the peaks and troughs of my (eight!) years at the University of Birmingham.

To my research colleagues Camilla, Stavros and Rob. I can't thank you enough for your friendship over the years. Thank you for your efforts and company during experiments and for always bringing laughter when everything seems to be going wrong. The scattering dream team! In extension to this, a special thanks goes out to everyone in the 1B20 office who shared the postgraduate Met&Mat experience.

Additional acknowledgement is needed for all of the instrument scientists and local contacts across the world. Thank you for the practical support and experimental guidance over a plethora of scattering beamtimes.

To Annie and Sarah. Without you, this PhD would not have been practically possible. Thank you for letting me be part of the furniture.

To my friends and family. Thank you for always being interested in my work. A special thanks to mum for never putting boundaries on my dreams and always encouraging me to do what I love, and to my siblings for always being at the end of the phone.

Finally, to Jonny. Thank you for encouraging me down this path of science and for always supporting my goals. You inspire me every day and without you I would not have made it to the end. I will be forever grateful for the years of intellectual discussions and unequivocal emotional support. Thank you for being a rock in times of uncertainty and for sharing the lowest lows and the highest highs of this work, and ultimately, thank you for always believing in me and teaching me to never give up.

Life need not be easy, provided only it is not empty

- Lise Meitner

CONTENTS

CHAPTER 1

INTRODUCTION

1.1 Motivation

1.1.1 Background

Over the last 70 years, the energy demand has increased drastically due to an increasing population and high levels of consumption attributed to the digital age, as shown in Figure 1.1. This global demand is predicted to continually increase over the next 30 years [1].

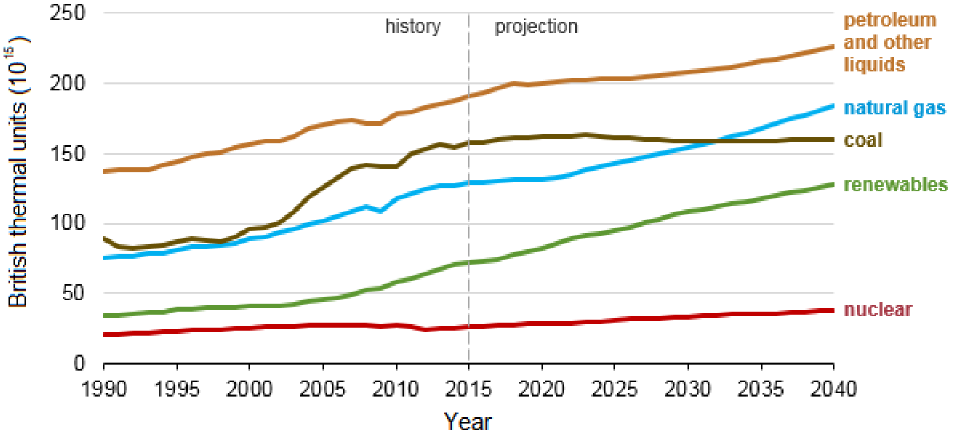

Figure 1.1: Graph showing global energy consumption as a function of time separated out per energy source [2].

Now more than ever, as we observe both an increase in demand and a reduction in finite resources for energy production, there is a requirement to provide a reliable, sustainable baseline method of producing energy. The net zero target on carbon emissions has been set to 2050 by the UK Government's Climate Change Act [3]. Whilst such a target can only be met with a collaborative effort from renewable energy sources, such as wind, solar, and hydrogen technologies, the continued operation and development of nuclear reactors will play a crucial role in contributing to carbon-free electricity generation.

For 50 years, nuclear reactors have contributed to a significant portion of the civil power generation industries on an international scale. Historically in the UK, net nuclear power generation has come from the operation of fission reactors. The current operational fleet of generation III reactors are all owned and operated by EDF Energy, with 11 reactors (10 advanced gas-cooled reactors (AGRs) and 1 pressurised water reactor (PWR)) split over 6 sites [4].

In combination these reactors have produced a total of approximately 2000 TWh of electricity over their lifetime, with a contribution to the UK energy generation of 17.3 % in 2019, as shown in Figure 1.2.

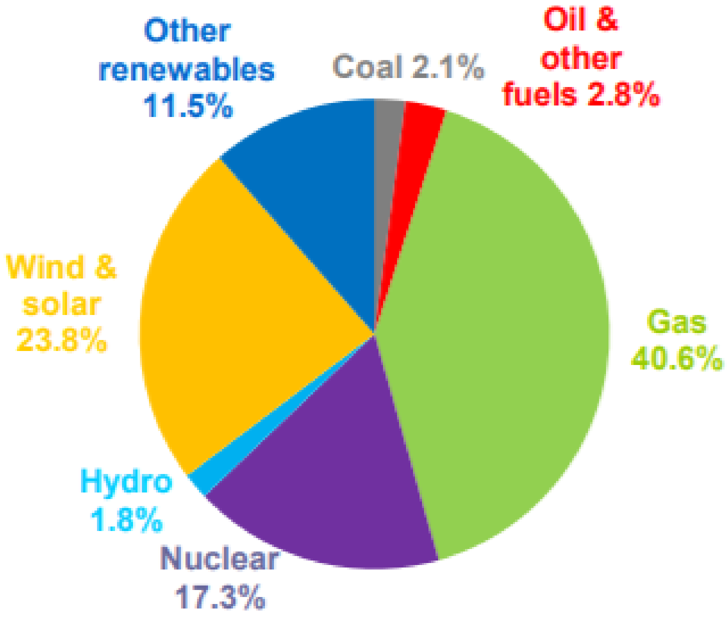

Figure 1.2: Pie chart showing energy production in the UK by source in 2019 [5].

The earliest stations in the fleet began operation in 1976, and most reactors had an initial operating period outlined as 40 years. Through EDF's lifetime management strategy, the operational life of the UK reactor fleet has been significantly extended. The lifetime management strategy is reliant on the formation of safety cases for all aspects of the plant that provide evidence of safe continued operation in line with the nuclear safety principles outlined by the UK regulator (Office for Nuclear Regulation, ONR). Such evidence includes detailed modelling and damage assessments, inspection, and monitoring of components.

These reactors are coming towards the end of their lives within the next 10 to 15 years, meaning there needs to be planned construction and operation of new reactors to fill the power generation gap. It is noted that EDF has proposed an additional 20 year life extension for the Sizewell B PWR [4]. In addition, there are several proposed future sites of generation III+ reactors in the UK by a joint venture between EDF and China Generation Nuclear (CGN) using the French European Pressurised Reactor (EPR) design:

- Hinckley point C (under construction)
- Bradwell B (proposed)
- Sizewell C (proposed)

For the two operational PWRs at Sizewell B and the proposed future EPRs, the study of life-limiting light water reactor (LWR) materials is crucial. Such life-limiting materials include structural ferritic low alloy steels that must be qualified for continued safe operation. Low alloy steels must also be considered in the design of generation IV advanced reactor systems, such as molten salt reactors and fast reactors. The development of advanced nuclear steels that are resistant to radiation damage is critical for the lifetime performance of future fission reactors, to which this work contributes.

In addition to fission reactor advances, endeavours to commercialise nuclear fusion for power generation have been ongoing over the last 60 years to keep up with ageing fission reactors and increased demand for safer nuclear energy. Plasma physics experiments from the 1970s, such as the Joint European Torus (JET) project, have demonstrated successful power output from nuclear fusion. However, there is yet to be a fusion device that can output more power than the heat required to generate the plasma [6]. With the EU Roadmap to fusion [7] outlined by the EUROfusion and Fusion for Energy programmes, upcoming international projects such as ITER and DEMO showcase the continued growth of the fusion research and development field. Nuclear fusion has a unique set of advantages over traditional fission, including the use of abundant fuel (hydrogen and its isotopes), the absence of nuclear accident or proliferation risks from the use of fissile uranium or plutonium fuel, and less long-lived waste products. Despite this, the development of commercial fusion reactors is accompanied by a large set of known challenges (e.g. transmutation effects and degradation of superconducting magnets) and unknown challenges associated with long term power generation that have not yet been realised due to the current maturity of fusion devices. Whilst the regulatory process has not yet been outlined for commercial fusion reactors in the UK, and whilst the operational safety considerations are different, it is likely it will follow a similar evidence-based safety case approach as for fission reactors. As such, this work aims to test the current understanding of irradiation-induced damage and fill knowledge gaps on the mechanisms of nanoscale precipitation and the associated evolution of hardness in critical nuclear fusion materials.

1.1.2 Material challenges

1.1.2.1 Fission

A key challenge for the safe operation of LWRs is the integrity of the reactor pressure vessel (RPV). The RPV itself is considered a life-limiting component due to its safety function and size, as it is uneconomical to replace. It acts as the primary containment for the reactor core, as shown in Figure 1.3, and must be able to withstand high pressure at a range of temperatures.

RPVs are typically ferritic low alloy steel systems made up of plates and forgings that are welded together. Austenitic stainless steel is used to line the inner RPV surface due to its superior corrosion resistance. The austenitic stainless steel cladding is welded to the ferritic RPV whih can result in the build up of residual stresses during operation due to the difference in the thermal expansion coefficients [8]. These residual stresses can lead to crack initiation and propagation in combination with thermal and mechanical stresses during operation of LWRs, and so the cladding interaction must be considered during the qualification of RPV materials.

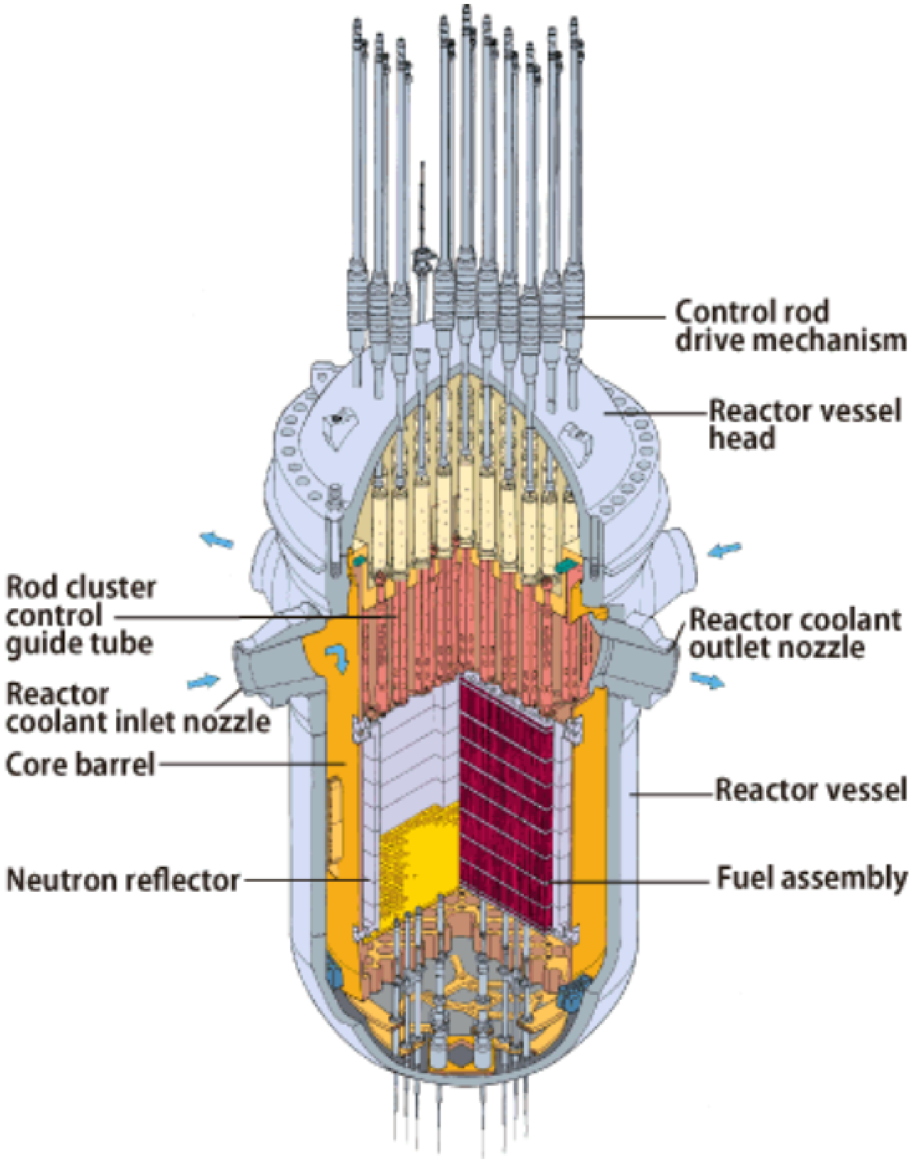

Figure 1.3: Schematic diagram of the RPV of a pressurised light water reactor [9].

Under exposure to elevated temperatures (around 300 °C) and harsh radiation fields (primarily neutron and gamma) over their lifetime in a reactor, RPV steel alloys undergo significant microstructural changes, including matrix damage and solute precipitation on the nanoscale. These thermal ageing and irradiation damage processes ultimately lead to macroscopic changes in properties such as strength and hardness. Hence, an understanding of the evolution of mechanical properties of the RPV over its lifetime (from construction through to decommissioning) must be demonstrated. In combination with design codes, regulatory standards, and detailed material qualification, tolerances on the property evolution through life, i.e. the amount of damage that an RPV can sustain whilst still performing its primary containment safety function, must be outlined in the relevant safety cases. This is important for current and future life extension principles for LWRs, but also for the design of advanced reactor systems that may also utilise low alloy steels as structural materials [10].

It has been shown through multiple irradiation and thermal ageing damage studies on RPV steels that embrittlement can occur which leads to an increase in the ductile-to-brittle transition temperature (DBTT) and a decrease in fracture toughness [11, 12, 13, 14]. During normal operation, the RPV temperature is above the DBTT and so the low alloy steels remain ductile. However, an increase in DBTT can mean that if the reactor core is cooled rapidly during shutdown or accident scenrarios, the RPV temperature could decrease below the DBTT. Such an effect can compromise the structural integrity of the RPV if the temperatures, and hence stresses, in the RPV change rapidly. Understanding the evolution of mechanical properties is crucial in normal operation where resistance to pressurised thermal shock is critical [15], but also under severe accident scenarios, such as loss of coolant accidents and Fukushima-type core loadings.

This field of research has been ongoing for many decades, however there are still knowledge gaps on microstructural evolution and solute precipitation in service that exist due to the complexity of the loading conditions and damage mechanisms in low alloy steels. For example, the solubility of certain alloying elements such as Cu, Mn and Ni in an Fe matrix have been disputed [16, 17, 18, 19], in addition to the effect of certain alloying elements on both the irradiation and thermal ageing induced precipitation process [20, 21]. Recently, the composition of induced precipitates in RPV steels have been studied with a particular focus on the Fe and vacancy contents, with several studies reporting contrasting findings [22, 23, 24]. As a result, a combination of investigative techniques is required during damage studies to validate the observations of precipitate structure and composition. It is also apparent that during such studies, the mechanisms of irradiation *and* thermal ageing induced precipitation should be considered since both are pertinent to reactor materials. A detailed literature review is presented in later chapters.

1.1.2.2 Fusion

A key challenge in fusion research is the qualification of materials under extreme temperature and irradiation flux loadings, which are typically more onerous than in current generation fission reactors. This is particularly important for plasma facing components (PFCs) such as the first wall material and divertor that are subject to:

- High energy neutron interactions (> 14 MeV)
- High temperatures (> 500 °C [12])
- High heat fluxes (> 10 MW/cm^2 at the divertor [25])

The evolution of plasma facing material (PFM) properties during operation are at the forefront of current fusion materials research. Such candidate materials include tungsten and beryllium due to their excellent physical and thermal properties that are retained at high temperatures. The divertor function is to act as an exhaust for the plasma by removing impurities. The divertor system is located at the base of the tokamak where it must be able to withstand extreme heat fluxes and temperatures. For the ITER design, the divertor is comprised of 54 cassettes, each with a plasma facing tungsten monoblock with its own dedicated cooling system [26]. A CAD diagram of a single cassette is shown in Figure 1.4.

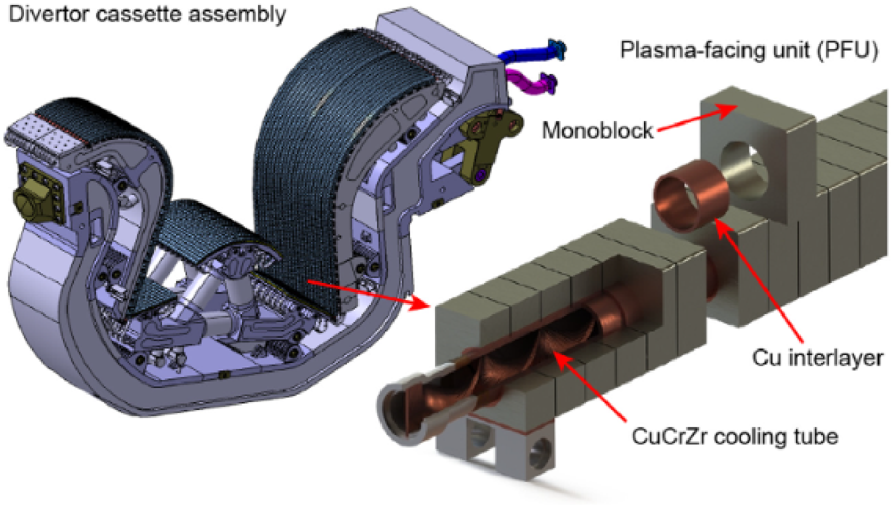

Figure 1.4: CAD diagram of a single divertor cassette for the ITER divertor [26].

The damage mechanisms at play in PFMs are similar to those observed in RPV steels due to the presence of high neutron fluxes and temperatures, where induced nanoscale precipitation can increase hardness and reduce fracture toughness. The divertor itself must be able to retain its structural integrity and thermal properties over its lifetime in a fusion reactor.

A key phenomenon in PFMs that must be understood and quantified by research studies is the transmutation of the original material due to high energy neutron interactions. This is more pertinent for fusion materials where the neutron energy spectrum is significantly shifted to higher energies dependent on the fuel. For deuterium-tritium fuel, the fusion reaction emits neutrons with 14.1 MeV.

Transmutation, in addition to matrix damage caused by incident radiation, can lead to precipitation of unfavourable alloying elements. In tungsten, the transmutation of rhenium and osmium can form brittle precipitate phases during its lifetime as a divertor material that can lead to compromises in mechanical and physical properties [27, 28]. The current scientific research focusses on transmission electron microscopy (TEM) based studies of such precipitates. TEM only characterises small sample volumes, so it can be complimented with alternative investigative techniques such as small-angle scattering (SAS) to obtain statistically averaged bulk precipitate properties as a method of validation.

1.2 Aims and objectives

Harsh fission and fusion environments lead to irradiation induced and enhanced damage and thermal ageing where knowledge gaps on nanoscale material transitions, such as solute precipitation, exist. Induced solute precipitation events can compromise macroscopic material properties. The structural integrity of such nuclear materials that exhibit precipitation damage is of increasing importance, especially as many current nuclear installations are at a fundamental point where their suitability for continued operations is being considered and where new reactor designs are under development.

The primary aim of this work is to demonstrate how advanced scattering techniques can provide vital insight into the research and design of nuclear materials, and be used as a validation tool for other damage characterisation techniques. SAS uses subatomic particles, such as neutrons and x-rays, to probe materials at atomic scales to obtain information such as shape, size, size distribution, and composition of scattering objects. This work will showcase how a variety of SAS techniques can be combined to provide a comprehensive understanding of nanoscale solute precipitation. This will provide knowledge on precipitation events in RPV steels and tungsten, as introduced in Section 1.1, that have a critical impact on the evolution nuclear material properties.

The advanced scattering techniques, including variations of small-angle neutron scattering (SANS) and small-angle x-ray scattering (SAXS), have been used to study thermally aged and irradiation induced precipitation damage in three different systems that span across various nuclear material lifecycle stages, ranging from in service and candidate RPV steels, to high purity candidate PFMs. The decision to investigate a range of materials across the reactor lifecycle is especially important in the current nuclear climate whereby the life extension of operational fission reactors, the design of advanced fission reactors and large-scale fusion reactors are being considered. The SAS investigations chosen to quantify precipitation events in each material system are as follows:

1. SANS and anomalous small-angle x-ray scattering (ASAXS) for the study the magnetism of precipitation in an *in-service* type high Ni RPV weld steel to **add value to data gained from other investigative techniques**;
2. Using novel SANS and ASAXS experimental setups as a demonstration of the **study of nanoscale precipitation kinetics** in *current* model low alloy RPV steels; and
3. SANS as an investigative technique for studying precipitation damage in high purity tungsten as a *future* PFM **induced using novel irradiation methods**.

The key scattering techniques employed include SANS, SAXS, ASAXS with novel experimental setups to map precipitate and void shape, size distributions, and stoichiometry. The combinations of such techniques for forming robust conclusions on precipitate damage in nuclear materials is explored in this work. It will be shown how the unique set of advantages and disadvantages of other techniques used to study precipitation damage, such as atom probe tomography (APT) or positron annihilation spectroscopy (PAS), mean that one must ensure enough overlap in the assumptions and validity of analysis methods to give confidence in obtained results.

1.3 Outline

The structure of the remainder of this thesis is as follows:

- Chapter 2: An introduction to advanced scattering theory is presented. It introduces concept of thermal ageing and irradiation damage in nuclear materials, and how one can investigate precipitation damage specifically using SAS. A general understanding of the neutron and x-ray interactions with matter is presented, alongside derivations of key scattering equations and quantities needed for the study of nuclear material systems. It also provides discussions on experimental parameters and how one can extract useful information from SAS data to form a quantitative map of induced precipitate properties in the three material systems of choice.

- Chapter 3: An overview of the common methodologies employed for the study of all three materials systems of interest is provided. This includes key details such as sample preparation, metallurgical characterisation techniques, and the approach to detailed analysis of SAS data.

- Chapter 4: A presentation of how SAS can add value to data gained from other investigative techniques in a material where precipitation has been observed. This aims to validate previous investigations on a novel high Ni RPV weld, which has been thermally aged for 11 years. It presents SANS and ASAXS data which can extract structural precipitate information, shed light on the role of magnetism in precipitates, provide an assessment of the Fe and vacancy content of the induced precipitates. The results are critically assessed against other RPV steel compositions studied in literature and significantly shorter accelerated thermal ageing investigations.

- Chapter 5: A presentation of how SAS can be used to demonstrate material transitions in-situ and test the understanding of current RPV materials. It utilises a series of model low alloy RPV steels, where the key elements of interest (Cu, Mn and Ni) and their role on irradiation and thermal ageing induced precipitation are investigated. A thermal ageing SAXS and SANS study has been carried out to elucidate the role of these elements on precipitate structure, composition, and magnetism. A novel in-situ ageing SANS experiment is also presented to investigate the kinetics of precipitation and how this can translate to predicting long term properties of in-service RPV alloys.

- Chapter 6: A presentation of a SANS study to investigate transmutation and solute and void precipitation in high purity tungsten. Here, a novel method of proton irradiation is developed to encourage the transmutation of tungsten and the formation of irradiation induced precipitates and voids at varying damage levels. The effect of this proton irradiation on displacement damage, transmutation reactions, induced activity, precipitate type (solute or voids) and properties, and material property evolution is investigated in a SANS study on this high purity system. The results are used to evaluate the expected damage induced over its lifetime as a PFM and to inform the tolerance on such property changes to ensure it continues to meet its operational requirements.

- Chapter 7: A summary of the conclusions on the use of SAS to study radiation and thermal ageing induced precipitation damage in nuclear materials is provided. This presents the overall findings for each material system in the context of how the information can be used in the field of research and for SAS investigations in other nuclear systems.
- Chapter 8: A presentation of potential future work. This summarises the areas of interest identified through this work that are outside of the scope of this thesis, but that would nonetheless be exciting to provide answers for.

CHAPTER 2

ADVANCED SCATTERING FOR THE STUDY OF RADIATION DAMAGE

2.1 Introduction

A primary aim of this work is to show how advanced scattering techniques can be an invaluable tool for the study of nanoscale microstructural evolution in nuclear materials caused by thermal ageing and irradiation. This chapter introduces on the mechanisms of radiation induced damage that can lead to precipitation events. It will also introduce the choice of the material systems studied in this work with regards to current knowledge gaps and points of interest.

This chapter focusses the advanced scattering techniques of interest and the motivation for using such techniques to quantify radiation induced precipitation damage. It presents fundamental neutron and x-ray scattering theory that will enable the reader to understand the experimental methodologies and interpret the results presented in later chapters in this work.

2.2 Radiation-induced damage

As introduced in Chapter 1, understanding the mechanisms of radiation damage and induced nanoscale microstructural changes can form a link between radiation exposure and material properties. The key challenges facing fission and fusion reactors are linked to safe and reliable nuclear materials. The mechanisms of irradiation induced displacement damage and thermal ageing precipitation are discussed in this section.

With the current civil nuclear reactor fleet in the UK approaching the end of power generation in the next 15 years, there are several proposed generation III+ PWRs under consideration to fill the gap. The RPV of a PWR acts as structural containment to the primary circuit and is a barrier to radioactive material release. RPVs are typically made of low alloy ferritic steels and are not designed to be replaceable components, and so their structural integrity over the reactor lifecycle must be maintained with consideration of the high temperatures and neutron fluxes experienced. This is a key research area where the current understanding must be challenged and developed.

The qualification of candidate fusion materials remains a particular challenge for the commercialisation of fusion devices, as outlined by the EU roadmap [7]. This is strongly coupled to the future regulatory requirements for such installations. Of particular interest is the radiation induced property changes in PFMs such as tungsten. In a similar way to fission materials, there is a need to contribute to the literature by understanding the nature of radiation induced damage mechanisms and their subsequent effects on the microstructure and mechanical properties.

2.2.1 Microstructural effects of irradiation

There are there two main types of irradiation damage: displacement damage and transmutation. The former is considered to be the driving force for precipitation events in response to bombardment with high energy radiation. The latter is an important secondary phenomenon when considering the fraction of solute atoms present in the material matrix that is available for the precipitation process. The fundamental mechanisms of displacement damage are discussed to provide a basic understanding.

The primary knock-on atom (PKA) is the first atom that recoils when incident with a high-energy radiation particle, for example a neutron. These PKAs can then collide and produce higher order knock-on atoms, displacing the original atoms in the material and until they deposit their energy; the result is a collision cascade whereby the damage is concentrated in a small volume [11]. This collision cascade ultimately induces point defects in the lattice in the form of interstitial and vacancy pairs, often referred to as Frenkel pair defects. In crystalline systems, such defects can migrate through the lattice and cluster into matrix damage. It should be noted that over 95% of interstitial and vacancy defects caused by the PKA recombine.

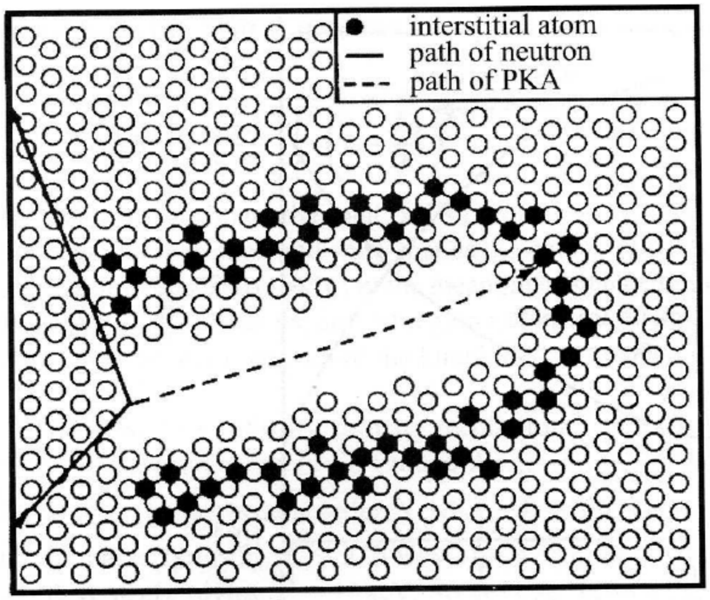

Figure 2.1: Schematic diagram of the damage spike [11].

The resultant damage can be quantified by the displacements per atom (dpa) – that is, the average number of displacements an atom experiences due to the incident radiation. The damage rate, R, as a function of energy of incident radiation (displacement rate per unit volume), can be described by

$$R = N \int_{E_{min}}^{E_{max}} \phi_D(E)\sigma_D(E)dE \tag{2.1}$$

where N is the atomic number density of the material, $E_{\mathrm{min/max}}$ are the minimum and maximum energy or the incident particle respectively, ϕ(E) is the incident particle flux as a function of energy, and σ_D(E) is the displacement damage cross section as a function of energy, described by

$$\sigma_D = \int_{T_{min}}^{T_{max}} \sigma(E,T)v(T)dT \tag{2.2}$$

where $T_{\mathrm{min/max}}$ are the minimum and maximum energy transferred to the incident primary recoil atom in the collision respectively, σ(E,T) is the cross section for the PKA-lattice atom interaction, and v(T) is the number of atomic displacements caused by the collision with the PKA. In the Kinchin and Pease displacement damage model [29], a hard-sphere interaction model is used for such collisions to obtain v(T).

It is assumed that below a threshold energy, E_D, an atomic displacement does not occur. This displacement energy is used to define trends of v(T) in the Kinchin and Pease model as

$$v(T) = \frac{2}{T}\left[\int_{0}^{E_D} v(E)dE \; + \int_{E_D}^{2E_D} v(E)dE \; + \int_{2E_D}^{T} v(E)dE\right] \tag{2.3}$$

where the first integral is equal to zero, the second is equal to 1, and the third is a monotonically increasing function with T as $\frac{T}{2E_D}$ up to T = E_C. Above E_C, the number of displaced atoms remains constant at $\frac{E_C}{2E_D}$. This is shown schematically in Figure 2.2. The reader is referred to [11] for more detail on displacement damage interactions in irradiated materials.

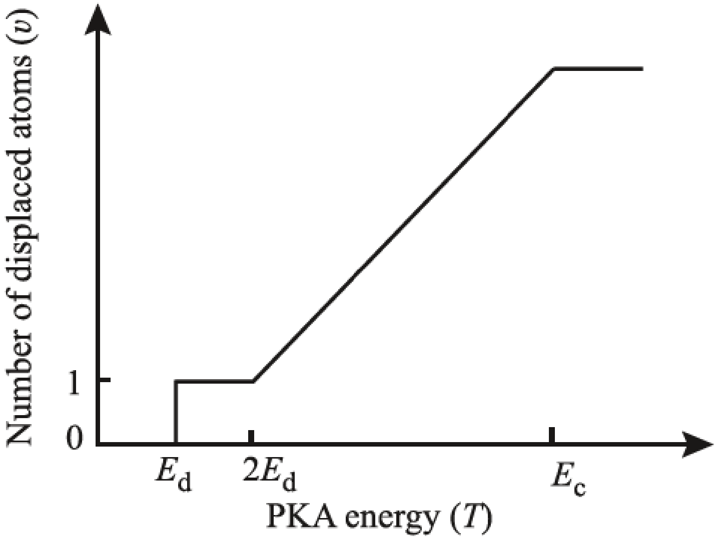

Figure 2.2: Evolution of the Kinchin and Pease model for atomic displacements as a function of PKA energy [11].

Additional lattice effects can contribute to the total number of recoil atoms produced by a PKA, which challenge the set of assumptions on which the original Kinchin and Pease model was based. As such, there have been several modifications to the Kinchin and Pease model, which account for energy loss by electron excitations, realistic energy transfer cross sections, consideration of the displacement threshold energy in the overall energy balance of the system, and the crystallinity of systems allowing for focussing and channeling of point defects [11]. The Norgett Robinson Torrens (NRT) model [30] is the recognised international standard model since it includes such modifications. It describes the total number of interstitial-vacancy pairs produced by a PKA as

$$\upsilon_{NRT} = \begin{bmatrix} 0 & \text{when} & T_D < E_D \\ 1 & \text{when} & E_D < T_D < \frac{0.8 T_D E_{PKA}}{2E_D} \\ \frac{0.8 T_D E_{PKA}}{2E_D} & \text{when} & \frac{0.8 T_D E_{PKA}}{2E_D} < T_D < \infty \end{bmatrix} \tag{2.4}$$

where $\mathrm{T_D}$ is the fraction of the kinetic energy of the PKA, $\mathrm{E_{PKA}}$, dissipated during elastic collisions, and $\mathrm{E_D}$ is the threshold displacement energy. $\mathrm{T_D}$ explicitly accounts for energy losses during the cascade to electron excitation.

The mobility of point defects in the lattice, such as vacancies and self/solute interstitials, left over after the original damage cascade can lead to three main microstructural changes that can result in embrittlement [11, 31, 32, 33]

- Matrix damage - clusters of vacancies and interstitials that can precipitate to form fine scale secondary defects such as dislocation loops and voids.
- Segregation - segregation of small elements such as P, Cr and Si to grain boundaries.
- Precipitation - clustering of interstitial solute atoms that impede dislocation movement.

The defects induced in the microstructure, after accounting for recombination, often result in evolution of material properties which may affect performance in reactor environments where safety and integrity are critical. For example, the decrease in toughness via hardening mechanisms, such as matrix damage and solute precipitation, is a direct consequence of an increased number density of obstacles that can reduce dislocation mobility in the matrix. This can compromise the structural integrity of such materials and thus presents itself as a costly and inherently unsafe problem in materials subject to high levels of damage. Hence, quantifying the ability of nuclear materials to maintain their properties in response to microstructural evolution during operation is a crucial area of research. This is of particular importance for PFMs in fusion reactors where mechanical properties, such as toughness, are required to be maintained at high temperatures to maximise performance.

Plasma facing components in fusion reactors typically have the most onerous neutron flux and temperature exposures. The tungsten divertor at ITER is predicted to experience damage levels up to 0.6 dpa over its operational lifetime [34], and so an understanding of precipitation events induced by this level of displacement damage is crucial. In addition, the effect of transmutation due to high energy neutron exposure on the type and fraction of solute atoms present in the matrix is vital for understanding the evolution of mechanical properties. The majority of research on radiation induced damage in candidate PFMs, such as tungsten, has been confined to quantification using laboratory based microscopy techniques [35, 36]. In tungsten, at high damage levels transmuted elements such as Re and Os have been found to form brittle precipitate phases [28, 37, 38], and voids have been observed at low damage levels, however there are limitations to the documented findings on the size distribution of such precipitates and voids, leaving gaps that can be filled by advanced scattering studies of radiation damage.

The evolution of mechanical properties due to radiation damage is also key for RPV steels where a high fracture toughness and low DBTT is required to provide resilience over long operating lifetime periods and in accident scenarios. In RPV steels, radiation induced precipitation is dominated by the presence of Cu, Mn, Ni and Si interstitials within the predominantly Fe matrix. Historically, high Cu RPV steels have been found to favour the formation of copper rich precipitates due to neutron exposure [39]. At sufficiently high damage levels, Mn, Ni and Si have been observed in such copper rich precipitates [40, 41]. Modern RPV alloys have favoured low bulk Cu contents to minimise such effects of Cu on radiation induced precipitation, however the property evolution has been found to still depend on the presence of Mn and Ni. The role of Mn and Ni on precipitation is particularly important for low Cu in-service RPVs and remains under review in the literature [19, 42].

2.2.2 Microstructural effects of thermal ageing

Whilst the mechanisms of inducing microstructural damage are different to irradiation, thermal ageing can lead to matrix precipitation events that affect properties in an analogous way to those induced by interactions with a PKA.

In the absence of irradiation, the increased diffusivity of alloying elements at elevated reactor temperatures coupled with the solid solution solubility in the matrix can lead to clustering and subsequent precipitation of solute atoms [43, 44]. Solute precipitation is closely coupled with the presence of vacancies in a material, where vacancies directly facilitate the random diffusion of solute atoms in the matrix. When similar solute atoms come into contact, they form a cluster which acts as a nucleation point for precipitation, whereby further matrix solute atoms preferentially join cluster due to the reduction in interfacial energy. This leads to precipitate growth on the nanoscale, which can directly impede dislocation motion. The temperatures and timescales at which such thermal ageing induced precipitation events occur are highly dependent on the solubility of alloying elements in the material matrix [43]. Hence, thermal ageing induced precipitation events in nuclear material systems are an important damage mechanism that must be considered over a reactor lifetime, due to high temperature exposure and onerous operation periods.

This is a particularly pertinent phenomenon in RPV steels, where the increased mobility of solute atoms that have limited solubility in Fe, such as Cu, Mn, and Ni, play a key role in thermal ageing induced precipitation [17, 18, 20, 45]. At elevated temperatures, these elements often redistribute themselves and cluster together to form precipitates in the matrix, because it is favourable for them to minimise their energy. This process is highly nuanced and depends on the relative quantities of each element, ageing time, and temperature as to how much precipitation is thermodynamically stabilised.

The synergistic role of Cu, Mn and Ni on precipitate nucleation and growth is still under dispute [46, 47, 48]. Thermal ageing studies in low alloy RPV steels have shown that vacancies in the matrix play a key part in the precipitation process [23, 49]. Previous studies that have considered the coupled vacancy and Fe content of thermal ageing precipitates report contrasting findings [13, 22, 50], and so the interplay between Fe, vacancies, Cu, Mn and Ni during thermal ageing is still a key area of interest in the literature. The study of thermal ageing can also provide insight into the role of temperature in the irradiation induced precipitation process due to the enhanced diffusion of solute atoms [20, 21, 48, 51, 52].

The majority of thermal ageing induced precipitation studies in RPV steels are carried out at elevated temperatures to reduce the ageing time required [19, 53]. In this work, a high Ni RPV weld alloy has been selected as part of the advanced scattering investigation due to its novel thermal ageing history. It has been thermally aged under represenatitive in-service LWR conditions: 100 000 hours (≈11 years) at 330 °C. This long-thermally aged weld has been previously studied using APT [54] which provides an exciting opportunity to validate and challenge the structural and compositional precipitate information obtained.

The specific roles of alloying elements in the precipitation nucleation and growth process in RPV steels can be investigated using model compositions. This allows for isolation of elements of interest such as Cu, Mn and Ni, and has been successfully completed in radiation induced damage studies previously [50, 55, 56, 57]. The same approach can be applied to thermal ageing studies that aim to elucidate the interaction between alloying elements and their combined effects on structural and compositional precipitate properties.

2.2.3 Quantifying radiation-induced precipitation damage

There are several methods of quantifying radiation induced precipitation damage that have been used in literature studies over the last 40 years to contribute to understanding and provide validation, including small-angle scattering, atom probe tomography (APT), transmission electron microscopy (TEM), positron annihilation spectroscopy (PAS), and hardness testing.

When reviewing the existing understanding of radiation induced precipitation from literature, it is important to note that each investigative technique has its own unique set of advantages and disadvantages, as discussed in later paragraphs. The maximum impact comes from utilising a range of techniques to corroborate results. In this work, multiple advanced scattering techniques have been used in combination to quantify both thermal ageing and irradiation induced precipitation damage. This has been coupled with metallurgical and property characterisation techniques, such as microscopy and hardness testing, to understand the macroscopic effect of nanoscale evolution on material properties.

This work aims to demonstrate the value of using advanced scattering techniques in the study of such systems, to validate and add insight to questions raised by other radiation damage quantification techniques. The key materials systems of interest have been identified as low alloy RPV steels and high purity tungsten, where advanced scattering techniques can contribute to key knowledge gaps in the understanding of nanoscale property evolution and validate results obtained from other investigative techniques. For example, radiation induced precipitate studies in tungsten use TEM as a primary investigative tool [35, 58, 59], presenting a unique opportunity for a novel study of precipitation damage in tungsten using SANS. In addition, a large number of previous studies on the roles of Cu, Mn and Ni on thermal ageing induced precipitation in RPV steels use APT [21, 47, 54, 60, 61]. The long mean free neutron path presents a unique opportunity to perform in-situ ageing studies on model RPV alloys to elucidate the mechanisms of precipitate nucleation and growth and contributions from the key alloying elements. The magnetic nature of neutrons can be used to provide additional compositional information, in combination with anomalous x-ray dispersions.

Advanced scattering techniques such as SAS can provide the shape, size distribution, and volume fraction of scattering objects. For simple nuclear material systems, such as high purity tungsten as a candidate PFM, bulk precipitate structural and compositional information can be extracted using SAS. In complex alloy systems where there are multiple elements that contribute to the scattering contrast, SAS cannot determine precise precipitate compositions [62]. However, the magnetic nature of neutrons means that experimental SANS setups can be tailored to allow the extraction of the magnetic to nuclear scattering ratio (the so-called A ratio) which can provide insight to the key alloying element fractions within precipitates [50] and the magnetic nature of precipitates [22, 63, 64]. This is key for contributing to knowledge gaps on the role of alloying elements on precipitation in RPV low alloy steels. Anomalous dispersions of scattering profiles near to elemental absorption edges can be utilised through ASAXS to provide explicit compositional information in combination with SANS, however the resolution is highly dependent on the fractions of atoms present in the initial samples. This phenomenon is discussed in detail in Section 2.5.1.2.

It is noted that a considerable barrier to the study of irradiation damage using small-angle scattering is faced when considering the feasibility of experiments. Since the majority of neutron or x-ray sources are located abroad there is an instant limit on the amount of damage that can be induced in samples where transport to international facilities is required. The damage induced must be large enough that one can quantify radiation induced changes in the microstructure, but small enough that one does not induce certain transmutation reactions with long-lived harmful daughter products that may exceed transportation limits [65]. This work couples precipitate information obtained from advanced scattering techniques with hardness testing to quantify precipitation induced hardening and embrittlement effects.

Meanwhile, APT can deliver precipitate composition and has been used widely in nuclear material damage studies [21, 66, 67, 68, 69, 70]. However, it does not provide accurate volume fraction information and has a tendency to underestimate the number densities of small precipitates [71]. In addition, APT is a destructive technique.

Electron microscopy techniques alone provide limited information on composition of precipitates at the nanoscale resolution required, and they are not bulk investigative techniques. However, TEM is a useful tool for studying matrix damage, such as dislocation loops and voids, since it allows observation of the real space microstructure [39, 45, 72].

As a result, the current state of science can often include inconsistencies of observations of precipitate properties when a single technique is used. This highlights the need for a combination of techniques to be used to compliment and validate findings. Chapter 4 is an example of such a collaboration, where small-angle scattering has been completed on a long thermally aged RPV weld steel that has previously been studied using APT.

It is however noted that other forms of damage, such as dislocation loops, segregation, and irradiation induced creep, also contribute to hardening and embrittlement. Such studies play an equally important role in understanding the operational nature of nuclear materials and are vital for the development of novel systems that can withstand fission and fusion reactor developments in the future.

2.3 Probing condensed matter with subatomic particles

Subatomic particles, such as neutrons and x-rays, have been historically used to probe condensed matter systems due to their fundamental properties.

Thermal neutron wavelengths are of the same order of magnitude as interatomic spacings (1-10Å) [73], and owing to their mass and neutral charge, they are deeply penetrating which allows for the measurement of bulk properties. Moreover, their irregular cross section dependence makes them useful for studying samples containing light elements, as highlighted in Figure 2.3. X-rays can also be used to study bulk condensed matter systems, however their scattering probability is a direct function of atomic number due to the nature of their interaction with matter. In addition, x-ray scattering can be used to resolve compositional information on systems by capitalising on the anomalous dispersion phenomenon. This is discussed in more detail in Section 2.5.1.2.

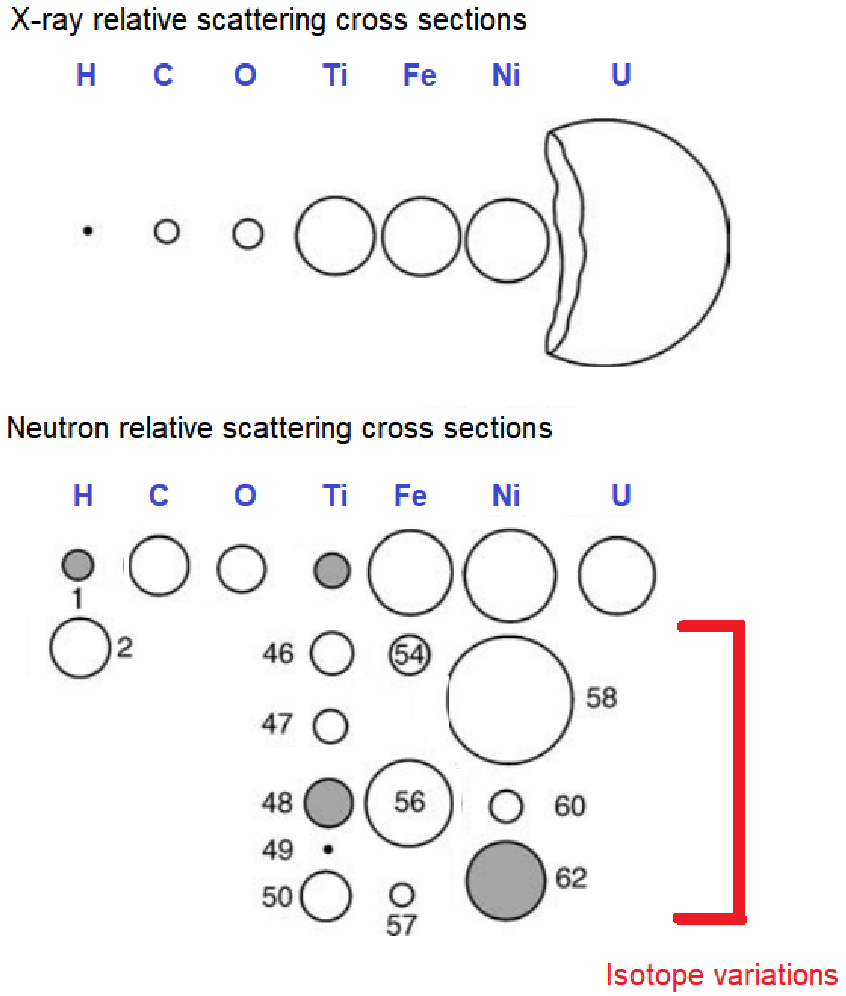

Figure 2.3: Schematic diagram representing relative neutron and x-ray scattering cross sections for elements. Adapted from [74].

When a neutron or x-ray photon is scattered by matter, its transfer of momentum can be described by [73]

$$\frac{h\mathbf{q}}{2\pi} = \frac{h(\mathbf{k} - \mathbf{k}')}{2\pi} \tag{2.5}$$

where k and k' are the wavenumbers of the initial and scattered particle respectively, given by k = $\frac{2\pi}{\lambda}$ where λ is the particle wavelength. The quantity **q** is known as the scattering vector, and is equal to **k** - **k**'; this relationship can be seen schematically in Figure 2.4. Scattering events between incident radiation and atoms can be split into two categories - elastic, where there is no energy transfer, and inelastic where there is energy transfer (also referred to diffraction or spectroscopy in this context).

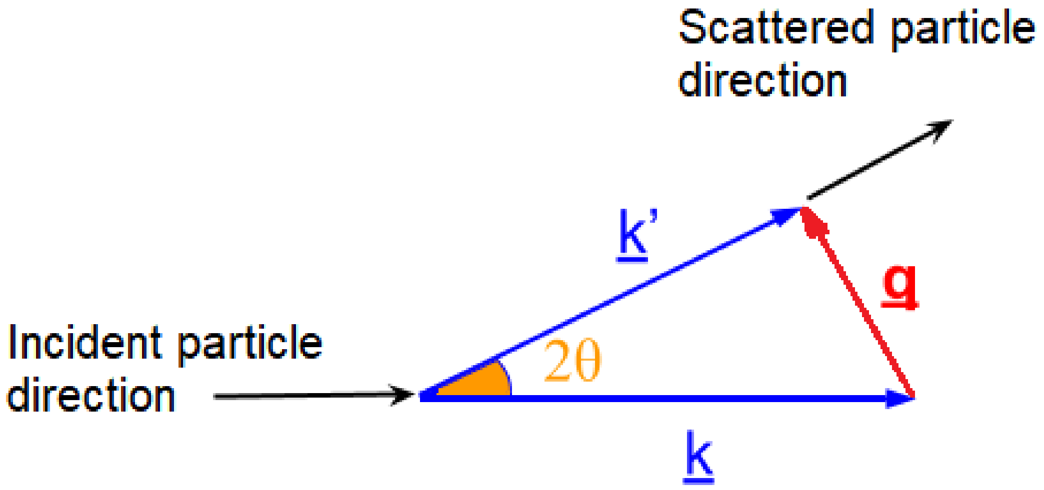

Figure 2.4: Schematic diagram showing the scattering triangle, where 2θ is the scattering angle.

The scattering interactions with matter can be utilised to probe condensed matter systems, with each particle having its own unique set of advantages and disadvantages. Often, multiple advanced scattering techniques are used as complementary probes of materials systems. Some examples of complementary scattering techniques used to probe physical systems include: small-angle scattering to extract size and shape information, single crystal or powder diffraction to extract crystal structure and composition, and triple axis spectroscopy for lattice dynamics and excitations.

In this work, small-angle neutron scattering and anomalous small-angle x-ray scattering have been used in combination to investigate radiation induced precipitation events. Small-angle scattering is a diffraction technique, and hence only elastic scattering theory is considered in this chapter from this point forward.

2.4 Neutron scattering

This section provides an introduction to elastic neutron scattering and the basic theory required to understand how important information can be extracted from material systems. For more detail on SANS theory, the keen reader is referred to [75, 76, 77].

2.4.1 Neutron-nucleus scattering interactions

When a neutron approaches an atomic nucleus, the interaction is dependent on the strong nuclear force, which is repulsive at very short distances (<1 fm), resulting in scattering. Due to the relatively long neutron wavelength compared to the nucleus radius, neutron-nucleus scattering is isotropic. As a result, each nucleus effectively acts as a point scatterer in the material [73]. The first step in understanding this interaction is the solution to the Schrodinger equation for a single elastic neutron-nucleus scattering event with a simple square well potential [78].

$$\left[-\frac{\hbar^2}{2m}\nabla^2 \ + \ V(r)\right]\Psi(r) = E_s\Psi(r) \tag{2.6}$$

The wavefunction of the incident neutron beam, $\Psi_i(\mathbf{r})$, is a plane wave solution

$$\Psi_i(r) = \exp(i\mathbf{k}\cdot\mathbf{r}) \tag{2.7}$$

where $\mathbf{r}$ is the displacement of the neutron from the nucleus and $\mathbf{k}$ is the incident wavenumber.

The wavefunction of the scattered neutrons, Ψ_s(r), can be described by a spherical wave solution

$$\Psi_s(r) = \frac{\exp(ik'r)}{r} \tag{2.8}$$

where k' is the scattered neutron wavenumber. As such, the solution of the Schrodinger equation for the scattering event can be described by the first Born approximation

$$\Psi(\mathbf{r}) = exp(i\mathbf{k}\cdot\mathbf{r}) + \frac{\exp ik'r}{r}f(\theta) \tag{2.9}$$

where f(θ) is the scattering amplitude described by

$$f(\theta) = \frac{m}{2\pi\hbar^2}\int \exp(-i\mathbf{q}\cdot\mathbf{r}')V(\mathbf{r}')dr' \tag{2.10}$$

where $\mathbf{q}$ is the scattering vector as introduced in equation 2.5 and V(r') is the interaction potential. The scattering amplitude is a Fourier transform of the interaction potential, showing that neutron scattering occurs in reciprocal space (i.e. a Fourier transform of real space).

The first Born approximation ultimately describes the transformation of the initial plane wave neutron into a scattered spherical waveform, which is shown schematically in Figure 2.5.

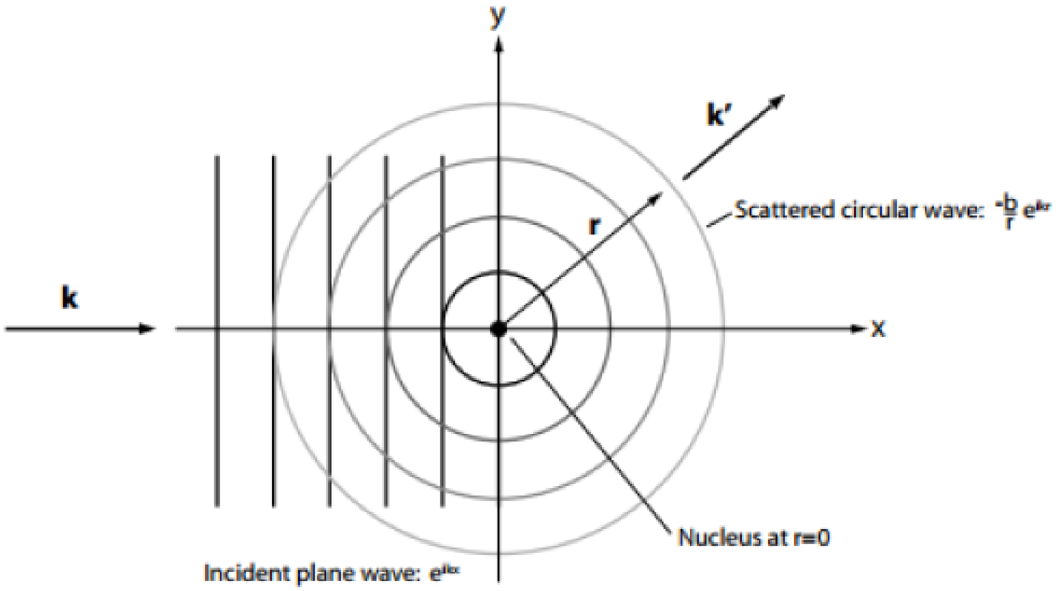

Figure 2.5: Schematic diagram of a neutron scattering from a nucleus [75].

The scattering amplitude of the scattered neutron defines the strength of a particular neutron-nucleus interaction. This is formally defined as the scattering length, b [78].

As such, the scattered wave function can now be defined as

$$\Psi_s(r) = \frac{-b}{r} \exp(ik'r) \tag{2.11}$$

where the minus sign indicates a repulsive interaction potential. For neutron-nucleus interactions in a 3D system, the scattered wavefunction is summed over all nuclei giving

$$\Psi_{s,3D} = -\sum_i \frac{b}{r} \exp(ikr) \exp(i\mathbf{q} \cdot \mathbf{r}) \tag{2.12}$$

The scattering length can be either nuclear or magnetic, whereby the neutron interacts with the nucleus in a classical collision overcoming the strong nuclear force, or with the magnetic moment arising from by unpaired electrons in certain atoms. The differences in scattering lengths based on each interaction type are presented in more detail in Section 2.4.2.

The overall neutron interactions in a sample are described in the form of a differential cross section, $\frac{d\sigma}{d\Omega}$, which is essentially the probability of neutrons scattering into a solid angle dΩ in the θ, ϕ direction as shown schematically in Figure 2.6. Hence, the total neutron scattering cross section, σ_s, is described by

$$\sigma_s = \int \frac{d\sigma}{d\Omega} d\Omega \tag{2.13}$$

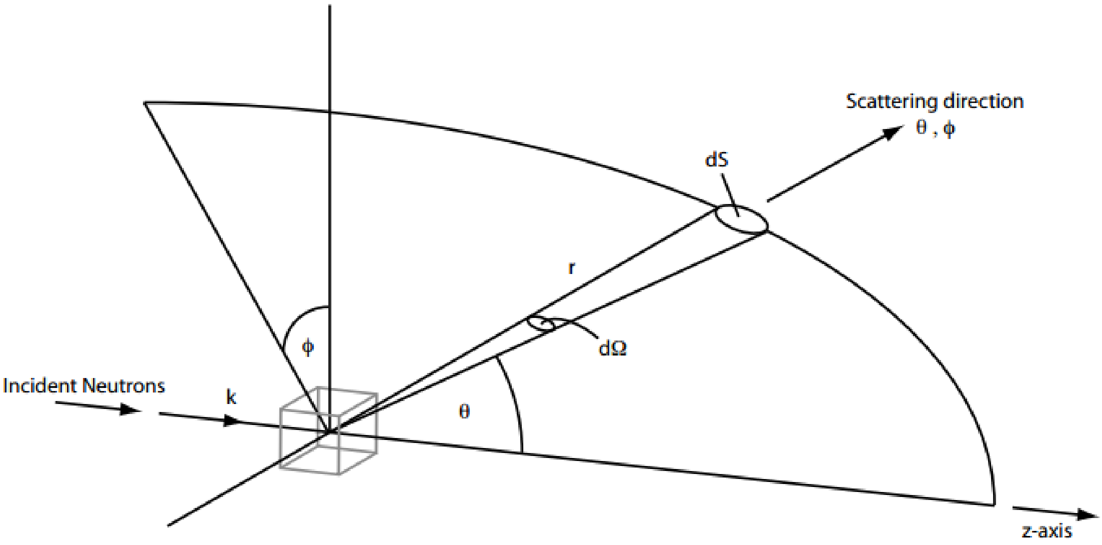

Figure 2.6: Schematic diagram of neutrons scattering through a sample into a solid angle dΩ in the θ, ϕ direction [75].

This differential microscopic neutron scattering cross section is the ratio of the scattered to the incident neutron flux. Combining this with the first Born approximation from equation 2.9, the differential cross section can be described by Fermi's Golden Rule

$$\frac{d\sigma_s}{d\Omega} = \frac{k'}{k} \left| \frac{m}{2\pi\hbar^2} \int \exp(-i\mathbf{q} \cdot \mathbf{r}') V(\mathbf{r}') dr' \right|^2 \tag{2.14}$$

The useful information extracted from the differential microscopic scattering cross section is primarily due to coherent scattering from a particular scattering object, as described by the equation above. However, multiple scattering objects with a variety of scattering lengths exist in a sample due to a distribution of elements and isotopes. Thus, there is also an incoherent scattering contribution to the total scattering cross section. The total scattering cross section is simply a sum of the coherent and incoherent components [31, 74]

$$\sigma_{total} = \sigma_{coh} + \sigma_{incoh} \tag{2.15}$$

where both components are related to the mean and variance of scattering length by

$$\sigma_{coh} = 4\pi < b >^2 \tag{2.16}$$

$$\sigma_{incoh} = 4\pi(< b^2 > - < b >^2) \tag{2.17}$$

The total scattering cross section is therefore a function of scattering length, given by

$$\sigma_{total} = 4\pi < b^2 > \tag{2.18}$$

The differential cross section can be written as a function of scattering vector, by summing over all scattering objects, N [74, 75]

$$\frac{d\sigma}{d\Omega} = \frac{1}{N}\left|\sum_i^N b_i \exp(i\mathbf{q}\cdot\mathbf{r})\right|^2 \tag{2.19}$$

The sum of the bound scattering lengths over all atoms in a sample can be replaced by an integral of the scattering length density, ρ, over the sample volume V

$$\sum_i b_i = \int_V \rho(r)dr \tag{2.20}$$

It is noted that as there are nuclear and magnetic scattering lengths, there are also nuclear and magnetic scattering length densities.

The nuclear or magnetic scattering length density, $\rho_{N/M}$, for a single phase system can be described by

$$\rho_{N/M} = \frac{1}{V}\sum_i^J b_{coh,i,N/M} = \sum_i^J N_i b_{coh,i,N/M} \tag{2.21}$$

where V is the total scattering volume [Å^3], N$_i$ is the atomic number density of element i [atoms/Å^{-3}], and $b_{coh,i,N/M}$ is the nuclear or magnetic bound coherent scattering length for element i. The number density of a specific element within a sample is calculated by

$$N = \frac{N_A d}{M} X \tag{2.22}$$

where X is the elemental fraction, N_A is Avogadro's constant [6.0223 x 10^{23} mol^{-1}], d_i is the macroscopic density [gÅ^{-3}] and M is the molar mass [gmol^{-1}].

In a two phase system, the difference between the scattering length densities of each phase is called the contrast. The nuclear/magnetic contrast, $\Delta\rho_{N/M}$, for J elements in a multiphase sample (precipitates in matrix) is given by

$$\Delta\rho_{N/M} = \left(\sum_{i}^{J} b_{i,N/M} N_{i,p}\right) - \left(\sum_{i}^{J} b_{i,N/M} N_{i,m}\right) \tag{2.23}$$

where $N_i, p/m$ and $b_i, N/M$ denote the number density and neutron scattering length of alloying element i respectively, where subscripts N and M denote nuclear and magnetic contributions, and subscripts p and m denote precipitate and matrix.

2.4.2 Scattering length calculations

As mentioned in Section 2.4.1 , the nuclear and magnetic scattering length densities, ρ, describe the strength of the nuclear and magnetic neutron interactions with elements in the sample. Hence, they are a direct function of the composition of said sample.

The strength of the neutron-nucleus interaction is described by the nuclear bound coherent scattering length for said nucleus i, $b_{N,i}$. These values are tabulated for all elemental isotopes in [79].

The strength of the dipole-dipole interaction between the magnetic moment of a neutron and an unpaired atomic electron can be described by the amplitude of the magnetic scattering [78, 80]

$$b_H = \frac{\gamma_n e^2}{2 m_e c^2} \tag{2.24}$$

where γ_n is the gyromagnetic ratio of the neutron [1.913], e is the charge of an electron [6.022 x 10^{-19} J], m_e is the mass of an electron [9.11 x 10^{-31} kg], and c is the speed of light [2.997 x 10^{-8} ms^{-1}]. For the neutron-electron interaction in a specific element i, the magnetic scattering length is described by

$$b_{M,i} = m_i b_H \tag{2.25}$$

where m_i is the atomic magnetic moment of element i in Bohr magnetons [μ_B] and b_H is the magnetic scattering amplitude of a neutron [2.7 x 10^{-5} Åμ_B^{-1}] [81, 82].

The magnetic moment per atom of element i must be calculated next. This is dependent on the crystal structure of the element since this determines the number of atoms per unit cell. The magnetic moment per atom is given by

$$m_i = \frac{M_{sat,i}}{D_i} \tag{2.26}$$

where M_{sat} is the saturation magnetisation [Am^{-1}] and D is the number of atoms in the unit cell per unit cell volume [atomsÅ^{-3}]. It must be noted that the magnetic interaction is only relevant to atoms with an uneven number of unpaired atomic electrons, hence in the case of RPV steels one is only concerned with Fe and Ni.

The weld steels investigated in Chapter 4 are ferritic and hence contain BCC Fe with a lattice parameter of 2.86 Å. The number of atoms in a BCC unit cell is 2, and so $D_{Fe} = \frac{2}{2.86^3} = 8.549 \text{ x } 10^{-2}$ atomsÅ^{-3}. For FCC Ni with a lattice parameter of 3.52 Å, $D_{Ni} = \frac{4}{3.52^3} = 9.17 \text{ x } 10^{-2}$ atomsÅ^{-3}.

The saturation magnetisation of Fe and Ni can be calculated using

$$M_{sat,i} = m_i \mu_B D_i \tag{2.27}$$

however it is clear that the theoretical m_i is needed (documented in [83]). It is noted that the documented theoretical values are valid for 0 K only, so it is more is more accurate to use experimental data [84] - $M_{sat,Fe} = 17.45 \text{ x } 10^5$ Am^{-1} and $M_{sat,Ni} = 5.21 \text{ x } 10^5$ Am^{-1}.

Hence, $m_{Fe} = \frac{17.45 \text{ x } 10^5}{8.549 \text{ x } 10^{-2}} = 2.209\ \mu_B$, and $m_{Ni} = \frac{5.21 \text{ x } 10^5}{9.17 \text{ x } 10^{-2}} = 0.613\ \mu_B$.

Table 2.1: Table of nuclear [79] and calculated magnetic neutron scattering lengths. Values in brackets denote errors.

Element	Nuclear scattering length [fm]	Magnetic scattering length [fm]
Fe	9.45	5.96 (0.02)
Ni	10.30	1.65 (0.01)
Cu	7.72	0
Mn	-3.73	0
Si	4.15	0
Vacancy	0	0

The nuclear and magnetic scattering lengths will be invaluable when considering the composition of precipitates obtained from SANS data in subsequent chapters. Specifically, they allow for assumptions to be made in the empirical modelling and can provide direct compositional information through evaluation of the ratio between nuclear and magnetic scattering intensities.

2.5 X-ray scattering

2.5.1 Atomic scattering interactions

2.5.1.1 Photon-electron

X-rays interact with matter through the electron clouds surrounding atoms. Unlike the solution to the Schrodinger equation for neutrons, scattering events between x-ray photons and atomic electrons is anisotropic since the x-ray wavelength is on the same scale as the electron cloud. Hence, the x-ray scattering amplitude has an angular (q) dependence. The difference between anisotropic x-ray scattering amplitude and isotropic neutron scattering amplitude for potassium is shown in Figure 2.7.

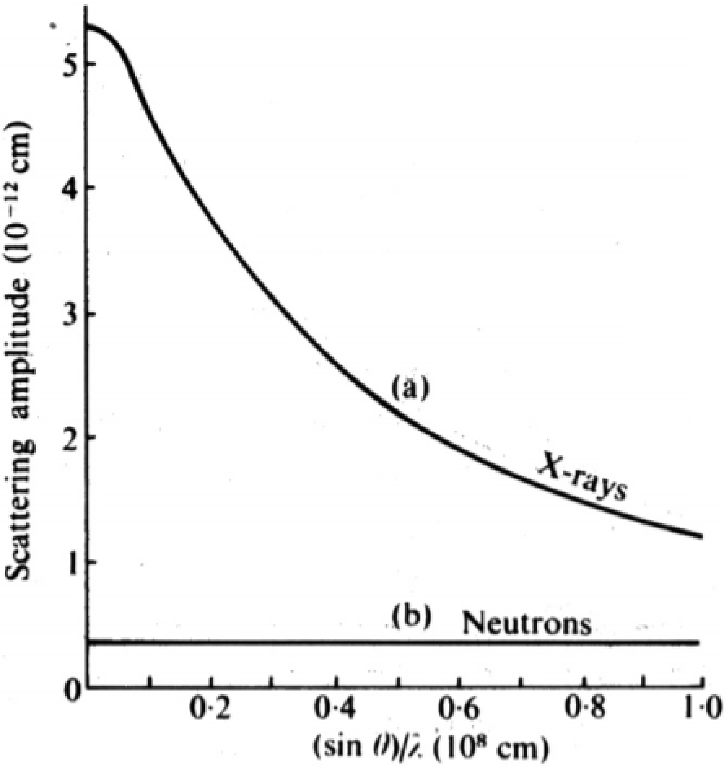

Figure 2.7: Graph showing the angular q-dependence of the scattering amplitude of potassium for neutrons and x-rays [85].

The scattering amplitude is a function of the Thomson scattering length of an electron, r_e, and the atomic form factor, f_0, by

$$f(\theta) = f_0 r_e \tag{2.28}$$

where

$$r_e = \frac{e^2}{4\pi\epsilon_0 m_e c^2} = 2.82 \times 10^{-15} m \tag{2.29}$$

The scattered wavefunction is proportional to the scattering amplitude. In a similar way as for neutrons, the atomic form factor can be integrated over the total scattering volume, V, to include all photon-electron scattering contributions

$$f_0 = \int_V \eta(r) \exp(i\mathbf{q} \cdot \mathbf{r}) dr \tag{2.30}$$

where η(r) is electron density that describes the strength of the interaction as the volume integral of the bound coherent x-ray scattering length, analogous to the scattering length density for neutrons. Hence, the scattered wavefunction can be described as

$$\Psi_{s,3D}(r) = r_e \int_V \eta(r) \exp(i\mathbf{q} \cdot \mathbf{r}) dr \tag{2.31}$$

The principles of small-angle scattering *e.g.* Bragg diffraction are valid in both SANS and SAXS, however there are some differences that are born of the fundamental properties of the interaction particles. In the case of SAXS, since x-ray photons are chargeless and massless particles, they do not have an intrinsic magnetic moment and instead of interacting with the nucleus, they interact with the electrons in atomic orbitals. This means that the magnitude of scattered intensity increases monotonically with atomic number, and the scattering contrast is a result of differences in electron density, $\Delta\eta$ (analogous to $\Delta\rho$ in SANS) described by

$$\Delta\eta = \left(\sum_i^J b_i N_{i,p}\right) - \left(\sum_i^J b_i N_{i,m}\right) \tag{2.32}$$

where $N_i, p/m$ and b_i denote the number density and x-ray scattering length of alloying element i respectively, where subscripts p and m denote precipitate and matrix.

2.5.1.2 Anomalous dispersions

Anomalous SAXS allows one to extract compositional information through measuring scattering intensity at a variety of incident x-ray energies. At x-ray energies equal to the elemental absorption edges of interest, an anomalous correction must be made to account for anomalous dispersions.

The scattered intensity is a function of the x-ray atomic scattering factor, f(Z), which is in itself proportional to the atomic number of the scattering nuclei. This is analogous to the neutron scattering form factor. The complex atomic scattering factor for x-rays is described by

$$f(E) = f_0 + f'(E) + if''(E) \tag{2.33}$$

where f_0 is the scattering factor far from an absorption edge (equivalent to the atomic number Z), and f' and f" are the anomalous dispersion corrections. These anomalous corrections have been comprehensively derived and by Cromer and Liberman [86].

The scattering contrast in x-ray scattering is from the interaction with the electrons. The difference of electron densities between the precipitates and matrix, $\Delta\eta$ as described in equation 2.32, is proportional to the square modulus of f(E) and is given by

$$\Delta\eta(E)^2 \propto f(E) * f(E) = f_0^2 + 2f_0 f'(E) + f''(E)^2 \tag{2.34}$$

By scanning the incident x-ray energy through each absorption edge of interest (system dependent), one can extract the contrast as a function of energy through each absorption edge and fit the data with the expression

$$\Delta\eta(E) = d_p \left(\frac{\sum_i X_i f_i(E)}{\sum_i X_i M_i} \right) - d_m \left(\frac{\sum_j X_j f_j(E)}{\sum_j X_j M_j} \right) \tag{2.35}$$

where $d_{p/m}$ is density of precipitates / matrix, X is fraction of element i/j (at%), and M is molar mass of element i/j (i for precipitate, j for matrix). This isolates the contribution from the resonant atoms at their respective absorption edges to find the exact stoichiometry of the precipitates [87, 88].

2.5.2 Scattering length calculations

The bound coherent x-ray scattering length, b_i, is given by

$$b_i = Z_i r_e \tag{2.36}$$

where Z is the atomic number of element i, and r_e is the classical electron radius, *i.e.* the scattering length of a single electron, = 2.85 x 10^{-5} Å.

Using this, the scattering lengths of all elements of interest in the RPV steels used in this work can be calculated, and are presented for reference in Table 2.2.

Table 2.2: Table of bound coherent x-ray scattering lengths for the alloying elements of interest.

Element	X-ray scattering length [fm]
Fe	74.10
Ni	79.80
Cu	82.65
Mn	71.25
Si	39.90

The calculated x-ray matrix SLDs for the long thermally aged RPV weld used in Chapter 4 and all model RPV alloys used in Chapter 5 are shown in Table 2.3.

Table 2.3: Table of matrix x-ray scattering length densities for all model RPV alloys and weld samples.

Sample	Matrix x-ray scattering length density [Å^{-2}]
1.1	6.2932 x 10^{-5}
1.2	6.2971 x 10^{-5}
1.3	6.3007 x 10^{-5}
2.1	6.3191 x 10^{-5}
2.2	6.3212 x 10^{-5}
3	6.3113 x 10^{-5}
4	6.3030 x 10^{-5}
5.1	6.2839 x 10^{-5}
5.2	6.3190 x 10^{-5}
6.1	6.3144 x 10^{-5}
6.2	6.3164 x 10^{-5}
7.1	6.3168 x 10^{-5}
7.2	6.3236 x 10^{-5}
8	6.3125 x 10^{-5}
Weld A	6.2471 x 10^{-5}

2.6 Small-angle scattering

2.6.1 Distances and angles

Small-angle scattering involves the scattering of an incident particle from a sample through small angles, with the resultant scattered particles detected by a 2D detector. The scattering vector defined in equation 2.5 defines the momentum transfer of the interaction. The elastic scattering vector can hence be described by the schematic in Figure 2.8, where $|\mathbf{k'}| = |\mathbf{k}|$.

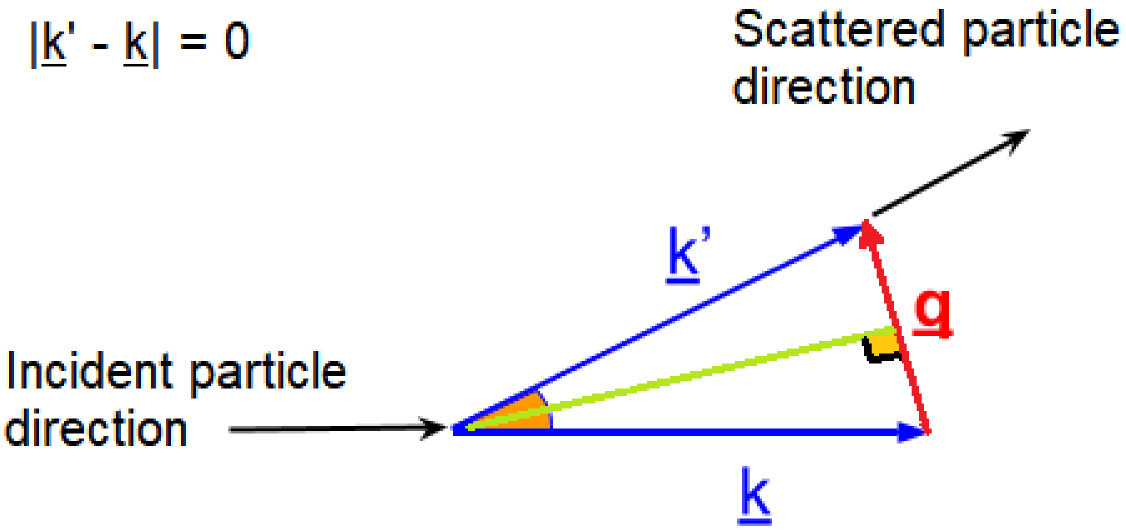

Figure 2.8: Schematic diagram showing the elastic scattering triangle.

Using simple trigonometry from the scattering triangle and the wavenumber definition, the scattering vector can be described by

$$\mathbf{q} = 2k\sin\theta = \frac{4\pi}{\lambda}\sin\theta \tag{2.37}$$

where 2θ is the scattering angle.

During small-angle scattering, when the incident particles interact with the sample, they are diffracted. This diffraction follows Bragg's law

$$\lambda = 2d\sin\theta \tag{2.38}$$

where λ is the particle wavelength, d is the distance in real space, and 2θ is the scattering angle. Therefore, the scattering vector can be described in terms of real space distance as

$$q = \frac{2\pi}{d} \tag{2.39}$$

For SANS, typical wavelengths of neutrons required are in the thermal region of 1 to 20 Å, and typical probing length scales are 10 to 1000 Å, depending on the instrument configuration. To probe condensed matter systems, the neutron wavelength must be of a similar size to the structures being studied, and so the scattering angle must be very small, typically $< 1°$.

2.6.2 Macroscopic differential scattering cross section

Due to the wave nature of neutrons/x-rays, both phase and amplitude of the scattered particles can be obtained to provide information on the scattering system. During small-angle scattering, information cannot be simply obtained by an inverse Fourier transform of the scattered intensity, and so phase information is lost. Spectroscopic inelastic scattering methods allow for extraction of phase information.

For small-angle scattering, the coherent scattering contains information on the system, whilst incoherent scattering is background noise that does not provide useful information to the overall measured signal.

The macroscopic differential scattering cross section is the typical unit of intensity extracted from small-angle scattering experimental data. It is a normalisation of the microscopic differential scattering cross section by sample volume, giving

$$\frac{d\Sigma}{d\Omega} = \frac{N}{V}\frac{d\sigma}{d\Omega} \tag{2.40}$$

where N is the number density of scatterers and V is the total scattering volume. Combining this with equation2.19, one obtains the so-called Rayleigh-Gans equation for absolute scattering intensity

$$\frac{d\Sigma}{d\Omega} = \frac{1}{V}\left|\int_V \rho(\mathbf{r})\exp(i\mathbf{q}\cdot\mathbf{r})\right|^2 \tag{2.41}$$

The macroscopic differential scattering cross section can be used to extract structural information on the scatterers. By considering the neutron interactions with nuclei in the sample, it can be described by

$$\frac{d\Sigma(q)}{d\Omega} = V_p N|\Delta\rho|^2 F(q)S(q) \tag{2.42}$$

where V_p is the volume fraction of scatterers, N is the number density of scatterers, $\Delta\rho$ is the difference in scattering length densities, ρ, of the scatterers and the matrix $(\rho_p - \rho_m)$ also known as the scattering contrast, F(q) is the form factor, and S(q) is the structure factor.

The form factor is a function that describes the structural information of the scatterers. One can obtain this through empirical model fitting of common shapes and distributions with known form factors. Alternatively, analytical methods such as the maximum entropy method [89, 90] or Monte Carlo modelling [91, 92] can be used, which does not impose certain assumptions onto the data. The implementation of such methods is discussed in Section 3.4.2. All of these analysis techniques have been carried out using the McSAS software [93], and the NIST NCNR analysis [94] and Irena [95] macros in Igor Pro to show a comprehensive comparison between the analysis techniques.

The structure factor describes the interaction between scatterers, and is a useful measure in correlated systems. In the case of precipitates in a metal matrix, the samples can be treated as monodisperse, dilute scattering systems; the precipitates are non-interacting, and hence the structure factor is negligible [77].

One can extract compositional information from the scattering objects in the A ratio [50, 56] for magnetic scattering systems, which is a direct function of the macroscopic differential scattering cross section

$$A_{ratio} = \frac{I_N + I_M}{I_N} = \frac{I_M}{I_N} + 1 \tag{2.43}$$

where $\mathrm{I_N}$ and $\mathrm{I_M}$ are the absolute intensities of the nuclear and magnetic scattering contributions respectively. More detail on the use of the A ratio quantity in SANS analysis is described in Section 3.4.2.3

The macroscopic incoherent scattering cross section, Σ_{incoh}, is related to the microscopic incoherent scattering cross section, σ_{incoh}, by

$$\Sigma_{incoh}\ [cm^{-1}] = \frac{\sigma_{incoh}\ [cm^2]}{V_m\ [cm^3]} \tag{2.44}$$

where V_m is the molecular volume (inverse of the atomic number density).

Recalling that the overall measured scattering intensity is the differential scattering cross section, the measured incoherent background intensity can be found by dividing the macroscopic incoherent scattering cross section by the solid angle, $\Omega = 4\pi$. This is a useful tool for considering the contributions of elements to the incoherent background scattering.

2.6.3 Instrument configuration

2.6.3.1 SANS

A schematic diagram of a typical SANS instrument can be seen below in Figure 2.9.

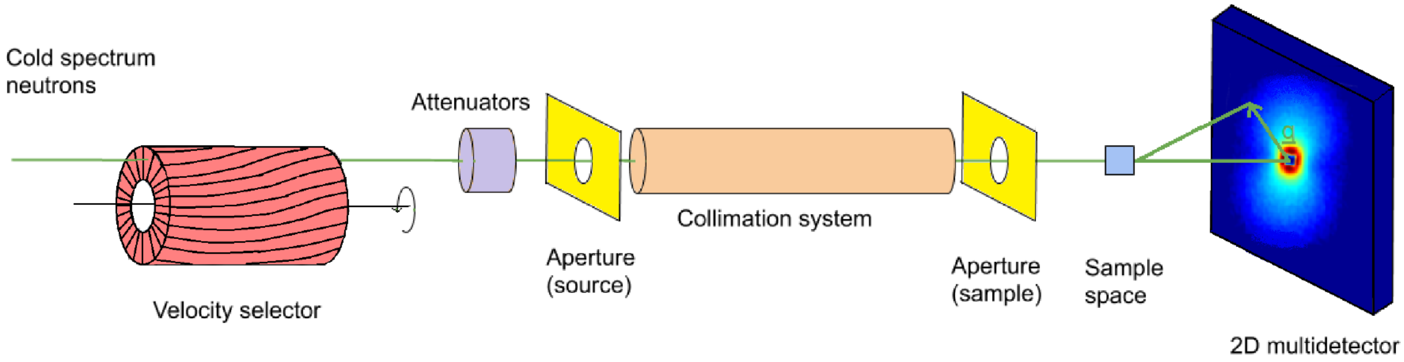

Figure 2.9: Schematic diagram showing the main components of a SANS instrument.

The cold spectrum neutrons generated by the neutron source are transported through evacuated neutron guides that use total internal reflection to minimise losses down the length of the instrument.

The neutron beam is then monochromated by a mechanical velocity selector, which can be adjusted to give the necessary neutron wavelength for the experiment (typical range is 4.5 Å to 40 Å). The resultant beam has a typical wavelength and angular spread of 10% and 0.1° respectively.

The collimation system is a series of neutron guides and apertures of certain sizes that focus the neutron beam on the sample, with a distance that can be varied to balance resolution and intensity as set values in the range of 1 to 20 m on SANS1 at the FRMII [96] and 1.4 to 17.6 m on D22 at the ILL [97].

The apertures, attenuators and beam stops are directly upstream of the sample space. These are used to change the size and/or shape of the beam illuminated on the sample, and also to protect the detector from damaging exposure to high flux neutrons. The neutrons from the source travel through an evacuated system to prevent scattering and absorption upstream of the sample.

In the sample space, sample environment equipment can be used to provide a variety of experimental conditions, for example, a vacuum furnace, a cryostat for low temperature requirements, or a standard electromagnet due to the large neutron mean free path.

Finally, a large 2D moveable He-3 tube multidetector produces a reciprocal space image once incident with scattered neutrons from the sample. The combination of collimation distance and sample-detector distance is what determines the achievable q-range (hence the detectable real space length scales within the sample).

2.6.3.2 SAXS

The physics of SAXS is very similar to SANS, and for comparison a typical SAXS beamline is shown in Figure 2.10. The beamline used in these works was the SAXS/WAXS beamline at the Australian Synchrotron, Melbourne [98].

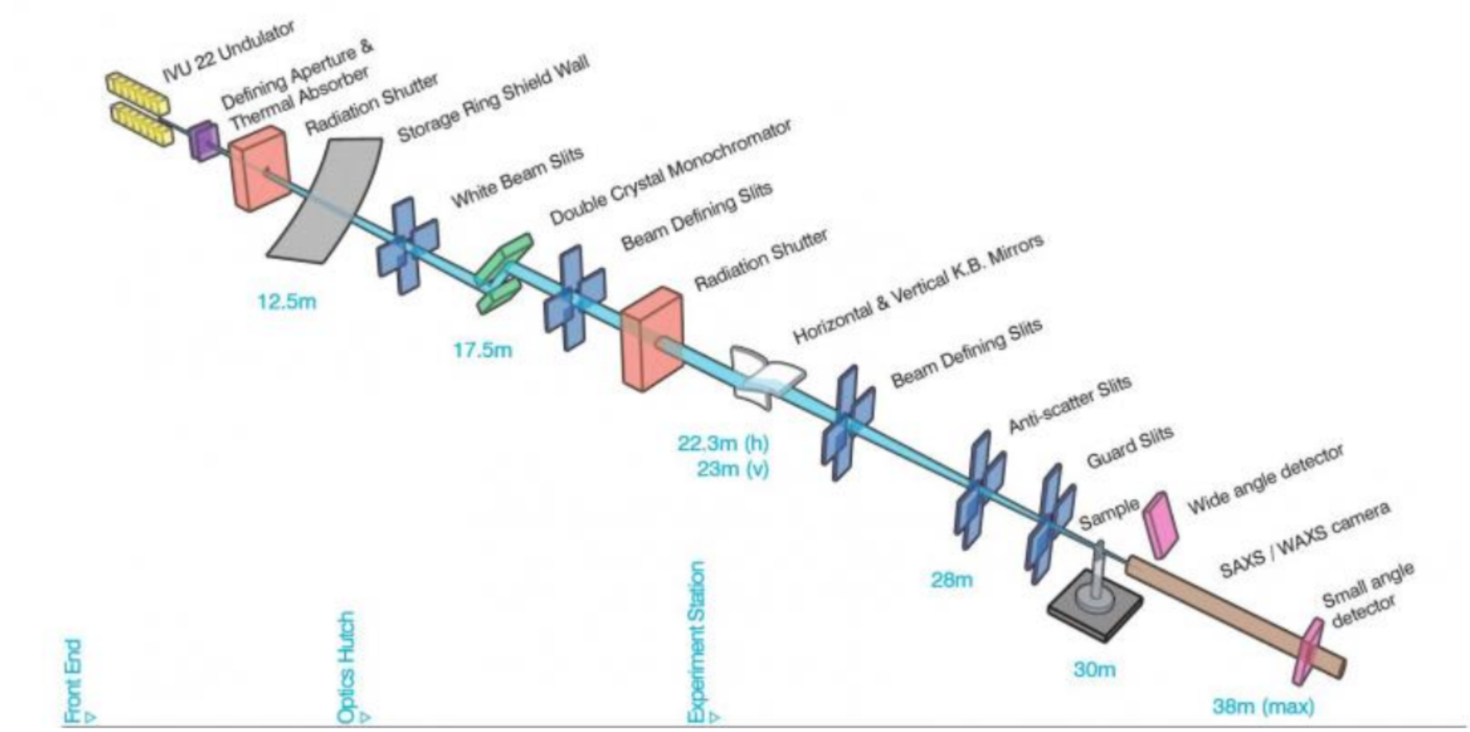

Figure 2.10: Schematic of the layout of the SAXS/WAXS beamline at the Australian Synchrotron [99].

A white beam of photons of all energies is produced by the synchrotron. A double crystal Si(311) monochromator selects photons of a specific energy from the white beam, through Bragg reflections and certain levels of harmonics. The single-energy beam is then focussed using a series of apertures, slits and mirrors down to a size of 250 x 25 μm. The entire system is under vacuum.

A series of attenuators can be used to attenuate the incident beam flux to prevent saturation of the detector. The detector used was a 1 m^2 Pilatus 13 2M detector (1280 x 1790 pixels of size 172 x 172

μm). A beamstop was also used to prevent damage by the direct beam with a diode detector installed so the direct beam intensity and sample transmission and thickness can be measured. The detector itself was located within an 8 m evacuated tank with movable sample-detector distance - this allows for a variety of q-ranges to be reached without having to insert tubes of a specific length.

2.6.4 Extracting information

The employment of small-angle scattering to study irradiation induced microstructures in nuclear materials can provide fruitful results. Specifically, it allows for extraction of information such as the shape, size, distribution, volume fraction, and composition of precipitates.

To be able to obtain such useful information from the 2D reciprocal space scattering raw data, multiple corrections are required. To be able to make the necessary corrections, several additional measurements must be taken for each experimental configuration alongside the sample measurements. These measurements allow for the subtraction of background, corrections for absorption, and the calibration of the measured scattering profiles.

The methods of reducing the raw data and the required measurements for both SANS and SAXS are discussed in detail in Section 3.4.1.

The data reduction process transforms the measured scattering intensity into the differential macroscopic scattering cross section as a function of scattering vector on an absolute scale. These I(q) profiles must then be analysed to extract information on the sample system through consideration of the various contributions of scattered particles to the coherent macroscopic differential cross section. An example of such an I(q) profile is shown in Figure 2.11.

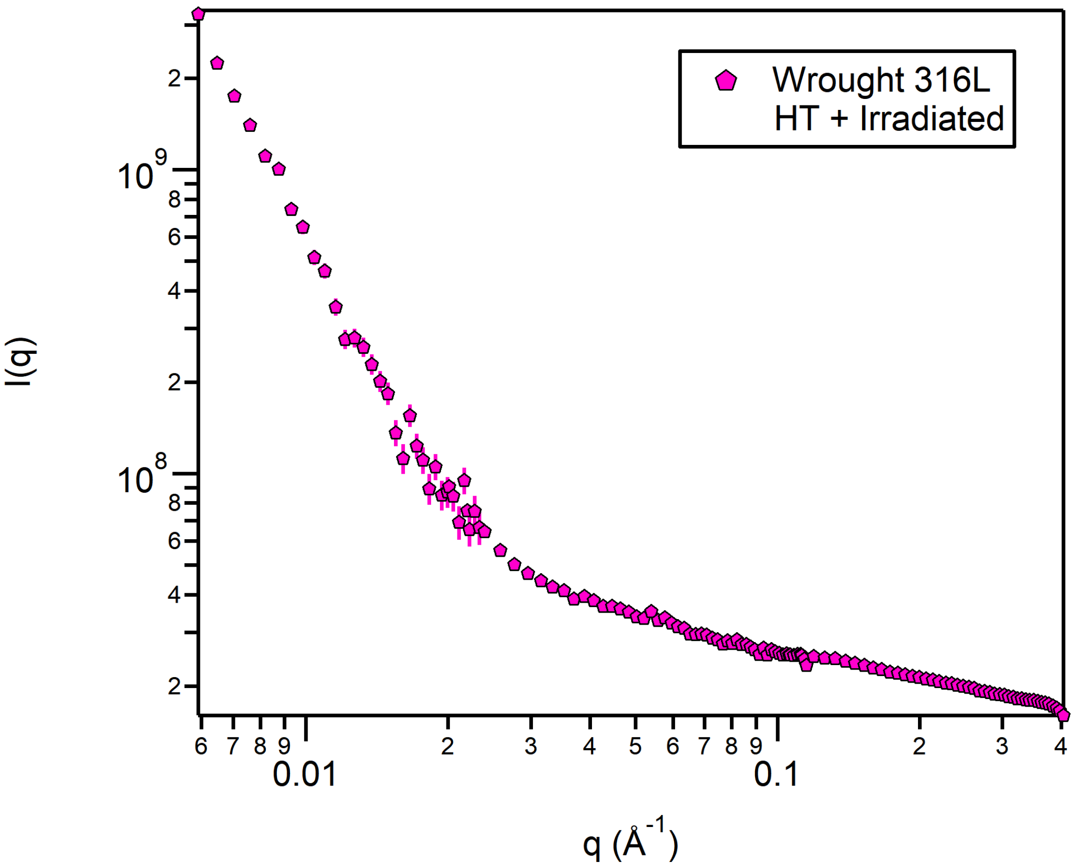

Figure 2.11: I(q) total (nuclear + magnetic) scattering for irradiated wrought 316L austenitic heat treated at 1160 °C for 4 hours and proton irradiated at 290 °C to 0.04 dpa.

The main method of data analysis to extract form factors of scatterers is by empirical curve fitting. However, imposing empirical models onto experimental I(q) scattering data is a partially subjective process. One may select an initial model based on what they want to find and make some arbitrary assumption about data, which may skew their consideration of alternative models to extract the form factor. This can also be reiterated by the fact that a low chi-squared value doesn't necessarily mean that the model is the best fit of the data. Empirical fitting is a widely used technique in small-angle scattering studies [13, 41, 100], but it is perhaps more robust to consider additional methods of extracting information from scattering profiles. These alternatives include Monte Carlo fitting and the maximum entropy method. All three model-dependent techniques are utilised in this work for comparison purposes; as such, the basis of each method is discussed in Section 3.4.2.

CHAPTER 3

COMMON EXPERIMENTAL METHODS

3.1 Introduction

This chapter presents an overview of the common experimental techniques employed throughout this work.

It begins by introducing the sample preparation processes for the metallurgical and advanced scattering characterisation techniques. Then, it gives an overview of the common metallurgical characterisation techniques employed. Finally, a detailed, step-by-step approach to the complex task of small-angle scattering data analysis is presented, explicitly covering the necessary corrections and data reduction process. A variety of data analysis methods are discussed, highlighting their strengths and potential limitations for studying nanoscale precipitation damage events.

3.2 Sample preparation

3.2.1 Microindentation hardness testing and EDX

To study polycrystalline materials using microindentation hardness testing and energy dispersive x-ray spectroscopy (EDX), the samples must have a uniform thickness and a high quality polished surface finish. This is particularly important for microindentation hardness testing, where a physical indentation is made on the surface of the sample, and the geometry of the indent is used to calculate the material hardness. Any surface abrasions or scratches can negatively affect the accuracy of the indentation results, particularly at low indentation loads since the indentation geometry is resolved by an optical microscope.

The ideal sample is mounted to prevent movement under applied load during microindentation hardness testing and using a conductive material for EDX analysis. The samples have been mounted in conductive Bakelite using a hot mounting press, and then subsequently polished using standard metallurgical procedures as follows.

Firstly, the samples are manually ground using 240, 400, 800 and 1200 grit wet'n'dry SiC discs with a water lubricant. The surface should be continually examined between stages using an optical microscope to ensure that all surface scratches are uniform across the sample and are of similar sizes and depths.

To achieve the desired surface finish, the samples are finely ground and polished. This work used a semi-manual technique on a Struers LabroPol machine at 200 rpm with a water lubricant and an MD-Dur polishing disc. The best finish is obtained when a constant downwards pressure is applied and the sample moved in small circles in an opposite direction to the polisher, avoiding the centre of the pad where removed material and dirt builds up due to the centripetal forces. A diamond suspension is used during the fine grinding and polishing stages of sizes 9 μm, 6 μm, 3 μm and 1 μm respectively. Finally, the low alloy steel samples were finished with colloidal silica to achieve a mirrored surface.

It should be noted that between each grinding and polishing step, the samples were cleaned in ethanol in an ultrasonic bath to minimise the contamination of different size abrasive particles from previous stages, which may introduce detrimental surface damage.

3.2.2 SEM and optical microscopy

To achieve contrast from electron and optical microscopy techniques, the surface of the sample must be etched. The etchant chemically attacks grain boundaries, and other defects, due to their low Gibbs free energy, revealing the underlying microstructure. Special care must be taken during the etching process since the solutions are often irritants and/or corrosive. The etching is carried out in a dedicated fume cupboard using appropriate personal protective equipment (face shield, thick rubber gloves and apron).

In order to successfully etch a sample, the procedure outlined in Section 3.2.1 is followed to achieve a high quality polished surface. Then, a suitable etchant is carefully selected depending on the sample of interest, since too strong an etchant can over-etch the sample and remove all of the underlying structures, and too weak an etchant can under-etch the sample and not provide enough contrast to allow the microstructure to be visible during microscopy.

The low alloy steel samples in this work were etched using a 2% Nital solution (2% nitric acid, 98% methanol). The polished samples were submerged in a small beaker of etchant using metal tongs until the surface began to appear dull (between 5 and 10 seconds depending on the specific alloy composition). The samples were then thoroughly cleaned in methanol to remove any excess etchant from the surface. This stage is crucial in ensuring the samples do not become over-etched. Finally, the samples were rinsed in water and dried thoroughly to avoid surface oxidation and corrosion between preparation and measurement.

3.2.3 SANS

Neutrons have the added ability to be able to study bulk (larger) samples due to their neutral charge and hence long attenuation length. However, the low alloy steel samples fabricated during this work are too thick to use directly in a SANS experiment.

To maximise the transmission of neutrons, 1 mm thick slices were taken of each sample using a SiC cutting wheel with feed speed 0.01 mm/s. The thickness was measured using a micrometre of resolution 0.001 mm, since a precise thickness measurement is needed to extract the absolute scattering intensities of the samples.

The method of cutting a precise thickness of sample is flawed when using a cutting wheel as angles can be easily introduced if the sample is not sufficiently clamped in place. For example, the low alloy steel samples were originally 8 mm diameter spheres, so many of the slices were wedge-like and required a robust multi-point method of measuring the sample thickness.

3.2.4 SAXS

Due to strongly correlated electron-photon interactions in solid matter, the absorption length of x-rays in the soft energy region used in SAXS ($<$ 10 keV to minimise sample damage) is very short ($<$ 100 μm). Since SAXS is carried out in transmission, one must consider the optimal thickness for a reasonable signal intensity. X-ray transmission, T, through a sample follows the Lambert-Beer law

$$T = e^{-\mu t} \tag{3.1}$$

where μ is the attenuation coefficient [m^{-1}] and t is material thickness [m]. The transmission is a function of material density, absorption cross section, and x-ray energy. One ideally needs a transmission of around 30%, meaning typical samples should be below 10 μm thickness. This could be achieved by manual polishing, but one runs the risk of the entire sample surface area becoming too small to study. The limiting factor is not just x-ray beam size, but also sample mounting capabilities and inducing surface stresses in the sample.

An alternative approach of twin-jet polishing was utilised since the optimal thickness is also below 10 μm. This technique creates a physical hole in the centre of the samples, and close to this hole the sample thickness is a few hundred nanometres, giving a transmission of approximately 90%. A schematic diagram of the process can be seen below in Figure 3.1. It is noted that the ASAXS technique is used to resolve precipitate composition, where TEM alone cannot resolve such compositions and has the added complication of the magnetic interactions between Fe-based samples and the electrons.

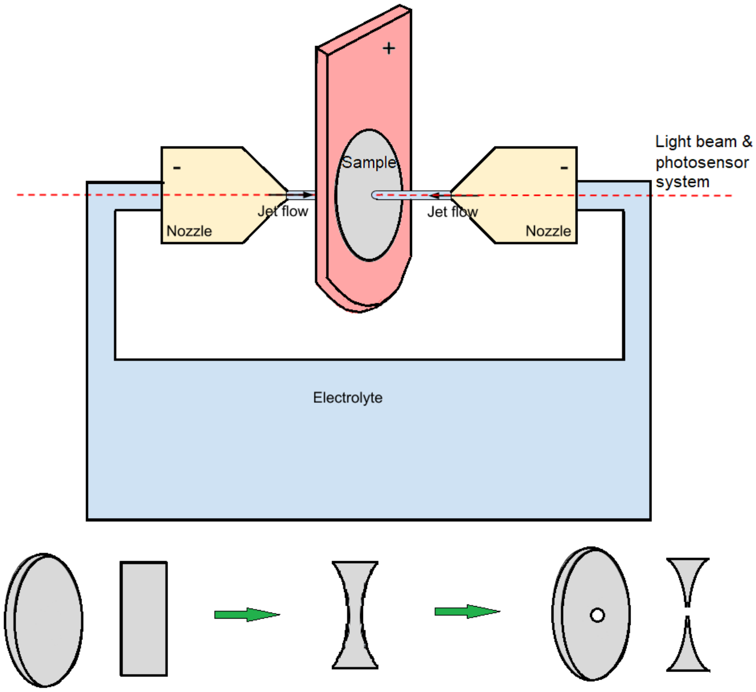

Figure 3.1: Schematic diagram showing the twin-jet polishing technique using a Struers Lapropol polisher.

Firstly, samples were cut into ≈1 mm slices using a SiC cutting wheel with a feed speed of 0.1 mms^{-1} to avoid inducing surface stresses. Then samples were hand ground using SiC wet'n'dry paper (120P and 240P grit) to a thickness of 100 μm. Secondly, the samples were stamped into 3 mm discs using a steel hole punch, ready for electrochemical thinning using the twin-jet polishing technique. Several discs were stamped of each sample to allow for averaging of results.

Next, one must establish a suitable electrochemical, operating voltage, and temperature. This was completed by reviewing several literature sources on similar low alloy steels, most of which varied in condition slightly. After several trials, the most consistent/optimal parameters where found to be a 95% methanol 5% perchloric acid mix operating at T = -20 °C and V = 20 V, with a photosensitivity of 5.

Thee following process was then completed in a fume hood:

1. Put in electrochemical and liquid nitrogen into Struers Lapropol container and leave to cool
2. Insert disc into Struers Labropol disc holder
3. Set voltage and photosensitivity

4. Jets automatically turn off when a hole is detected in the centre of the disc, dependent on the photosensitivity value selected
5. Rinse in ethanol and dry
6. Check for oxidation

The outcome is a twin-jet polished area with a diameter of approximately 2 mm, giving more than enough surface area for studying with SAXS.

Since the final samples are so thin, and being primarily iron, they are susceptible to fast oxidation which can severely degrade the samples. This degradation can be in the form of oxides which can confuse small-angle scattering signals, and also dirt and surface deposits, which will dominate in thin samples due to the surface area to volume ratio since small-angle scattering is concerned with bulk, average behaviour. To mitigate this, the samples were stored in a vacuum chamber and transported to experiments in argon backfilled sample tubes sealed with Parafilm™.

3.3 Metallurgical and mechanical property characterisation

3.3.1 Microindentation hardness testing

Microindentation hardness testing is used in this work to quantify the effect of thermal ageing induced damage on material properties in low alloy RPV steels. Microstructural changes induced by such damage can lead to hardening and embrittlement. The increase in hardness attributed to precipitation damage is measured using microindentation hardness testing at room temperature. It is noted that the shift in DBTT can only be measured using Charpy impact testing, which is a destructive technique and is not available for the size of samples used in this work.

The microindentation hardness testing technique works by applying a constant load through a diamond indenter tip with a known geometry. A set of indents is taken in the sample, with enough distance between them so that the plastic flow of the sample does not impact subsequent adjacent indents, and with enough indents to ensure adequate statistics.

Each indent is observed through an in-situ optical microscope so as to determine the contact area of the indent. The dimensions of the contact area are directly related to the hardness of the sample if the indenter load is known. A Vickers indent geometry is shown schematically in Figure 3.2. It is worth noting that there are a variety of indenter tip shapes available for microindentation hardness testing, but the Vickers geometry was used for this work.

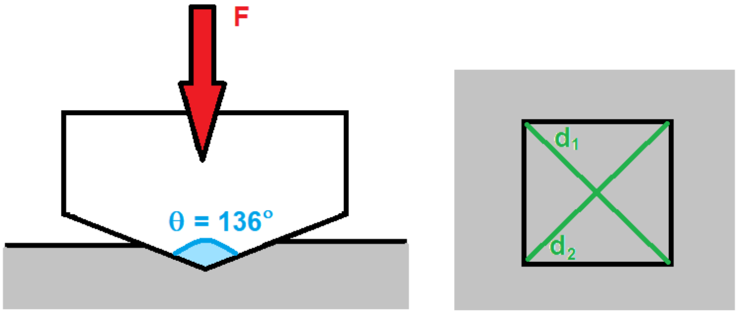

Figure 3.2: Schematic diagram of microindentation technique for Vickers indenter geometry.

The Vickers hardness, Hv, can be calculated as the force per area of the indent. Using the indenter geometry, this can be written as

$$Hv = \frac{2F \sin\frac{136}{2}}{d^2} = 1.854\frac{F}{d^2} \tag{3.2}$$

where F is the indenter load [kgf], d is the arithmetic mean of two diagonals d_1 and d_2 [mm], and 136° is the angle of the Vickers microhardness pyramid indenter.

To prepare the samples for microindentation hardness testing, a standard polishing procedure was carried out, as described in Section 3.2.1. The mounted samples were then used in a DuraScan G5 microindenter machine with a Vickers pyramid indenter tip and a translatable sample table. For all samples in this work, a low load of 0.1 kgf was used.

3.3.2 Nanoindentation hardness testing

Nanoindentation hardness testing has been used in this work to quantify the effect of irradiation induced damage on material properties in tungsten, as presented in Chapter 6. Nanoindentation hardness testing has been used to quantify mechanical properties in the thin tungsten samples where microindentation hardness testing is not feasible. Specifically, continuous stiffness measurements have been used to extract the evolution of elastic modulus and hardness as a function of displacement damage in the irradiated tungsten samples.

Due to the radioactivity of the tungsten samples, nanoindentation was completed at the Materials Research Facility (MRF) at Culham Centre for Fusion Energy (CCFE) where they have remote handling facilities for active samples. The instrument used was a G200 Agilent Technologies nanoindenter.

During continuous stiffness measurements, a continuously increasing load is applied to a sample through an indenter tip [101]. The load as a function of depth into the sample is measured - an example load curve for unirradiated tungsten is show in Figure 3.3.

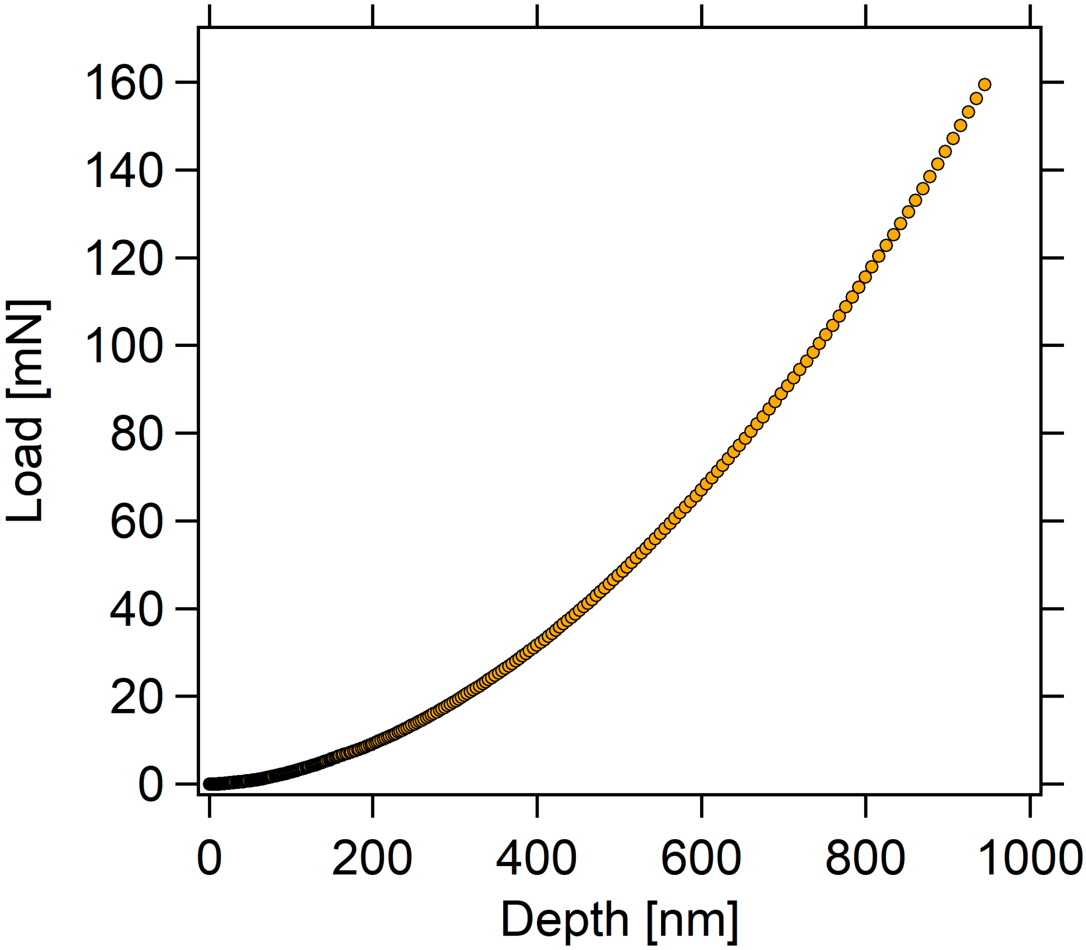

Figure 3.3: Indenter load-depth curve in unirradiated tungsten.

The gradient of the load-depth curve, $\frac{dP}{dh}$, is equivalent to the contact stiffness. This allows the reduced elastic modulus, E*, to be obtained through the following equation

$$E^* = \frac{1}{2}\frac{dP}{dh}\frac{\sqrt{\pi}}{\sqrt{A}} \tag{3.3}$$

where A is the projected contact area of the indenter. The reduced elastic modulus is the modulus of the whole indenter-sample system, and is related to the indenter, i, and sample, s, properties through

$$\frac{1}{E^*} = \frac{1-\nu_s^2}{E_s} + \frac{1-\nu_i^2}{E_i} \tag{3.4}$$

where $\nu_{i/s}$ and $E_{i/s}$ are the respective indenter and sample Poisson's ratios and elastic moduli. This analytical model developed by Oliver and Pharr [102, 103] is well-established and widely accepted in literature.

The indenter tip used during the nanoindentation hardness testing was a Berkovich tip. The geometry of the Berkovich indenter is shown schematically in Figure 3.4.

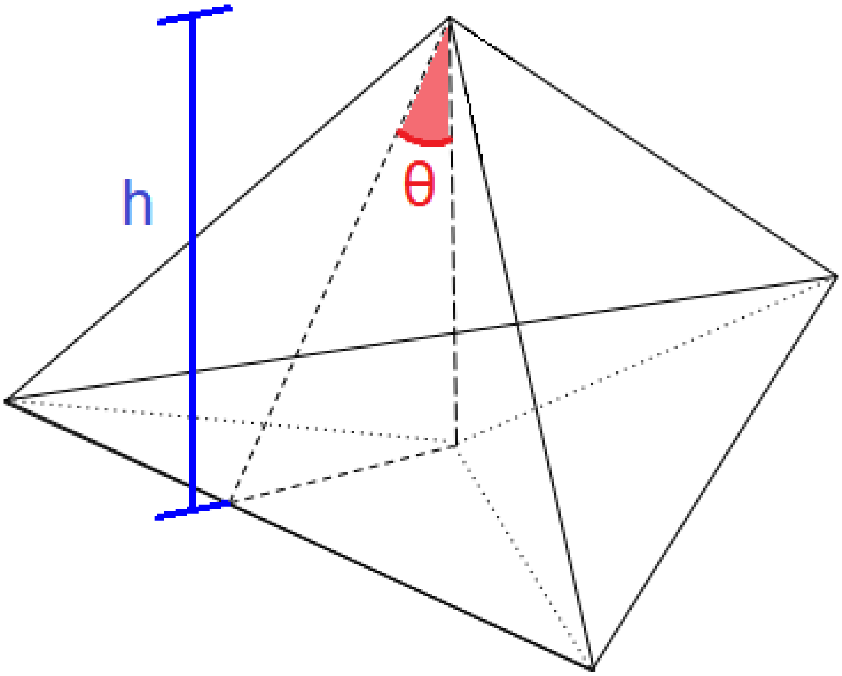

Figure 3.4: Schematic geometry of a Berkovich indenter tip showing semi-angle, θ, and tip height, h.

Using the known geometry of the indenter, the contact area during indentation can be calculated. This is important in nanoindentation where the indents are not reliably resolvable using an optical microscope as in microindentation.

Projected contact area of a Berkovich indenter tip, A, can be described as [104]

$$A = 3\sqrt{3}h^2 \tan\theta \tag{3.5}$$

where h is the depth of indentation and θ is the semi-angle of the indenter tip ($\theta = 65.27°$ for a Berkovich indenter). Hence, the projected contact area is

$$A = 24.56h^2 \tag{3.6}$$

Using equation 3.3 and equation 3.6, the reduced modulus of the indenter-sample system for a Berkovich indenter can be described by

$$E^* = \frac{1}{2h}\frac{dP}{dh}\frac{\sqrt{\pi}}{\sqrt{24.56}} \tag{3.7}$$

Combining this with equation 3.4 and the Poisson's ratio of the sample means that the elastic modulus of the material of interest can be obtained. The Poisson's ratio used in the calculations for pure tungsten was 0.28 [105]. There is a geometry correction factor required when using the derived analytical equations above, since they are adapted from conical indenter shapes. The correction factor that must be applied to E* calculated from equation 3.7 for a Berkovich indenter tip is 0.967 [104].

The material hardness, H, can be calculated using the projected contact area through the following relationship

$$H = \frac{P}{A} \tag{3.8}$$

where P is the mean contact pressure at maximum load.

3.3.3 SEM and EDX

SEM was used to characterise the microstructure of the samples of interest in this work. EDX was used to quantify the final matrix compositions of the model RPV alloys fabricated and investigated in Chapter 5. EDX was used purely to aid SAS analysis for the matrix scattering length densities as the resolution is too low to obtain accurate precipitate compositions. The instrument used for both SEM and EDX was a JEOL JSM-6060LV SEM.

The samples were prepared for SEM following the method described in 3.2.2. For iron based samples, the accelerating voltage used was 20 kV. The vacuum chamber is initially vented to mount sample within the holder, and then re-evacuated. Corrections for lens astigmatisms were applied and focussing was completed for differing levels of magnification to obtain a range of microstructural images for each sample.

The microscope was used in backscattered electron mode for EDX measurements. The samples were prepared for EDX following the method outlined in 3.2.1. It is noted that EDX was completed before SEM to avoid the contribution of a post-etching oxide film to the compositional profiles of any steel samples. Eight EDX spectra were taken at systematic points within each sample and then averaged to provide compositional information.

3.3.4 Optical microscopy

Optical microscopy was used as a complimentary technique to SEM to observe microstructural features within the RPV steels studied in Chapters 4 and 5.

The samples were prepared using the method described in Section 3.2.2. The instrument used for optical microscopy was a Zeiss Axioskop 2 plus microscope. The microscope was controlled using the AxioVision software.

The sample was mounted and aligned using the mechanical sample table. The eyepiece lens was manually focussed first, and then the brightness and contrast were adjusted to allow for clear images for a range of magnifications for each sample.

Image stitching was used, in combination with a focus correction, to ensure each part of the sample was fully in focus. The micrographs were exported with appropriate scale bars. It is noted that the electron backscattered diffraction technique (an accessory to SEM) can be used to obtain grain size, however in this work the line intersection technique from the optical micrographs using ImageJ [106] was utilised.

3.4 Small-angle scattering analysis

3.4.1 Data reduction

3.4.1.1 Neutron corrections

In order to make conclusions about induced damage in the samples, the absolute scattering intensity must be obtained by applying a specific set of corrections to the raw scattering data.

The differential scattering cross section, $\frac{d\Sigma(q)}{d\Omega}$, derived in Section 2.4.1, is related to the measured scattering intensity, $\mathrm{I_S}$, by

$$I_S = I_0 A t \Omega T_S T_E \epsilon \frac{d\Sigma(q)}{d\Omega} + BG \tag{3.9}$$

where $\mathrm{I_0}$ is incident beam intensity, A is sample area, t is sample thickness, Ω is the solid angle into which the neutrons are scattered, $\mathrm{T_{S/E}}$ is sample and empty cell transmission, ϵ is detector efficiency, and BG is a source of background counts not from sample scattering.

The transmission of a sample or empty cell is the ratio between the flux transmitted to the incident flux ($\frac{I_S}{I_E}$ and $\frac{I_E}{I_0}$ respectively) [76]. It corrects for the reduction of neutron flux through either the sample or sample holder due to absorption interactions or multiple scattering events where the neutron momentum is reduced to zero. To compute these transmissions, a measurement of the incident beam through the empty holding cell and a measurement of the incident beam with no sample stick present is required for each collimation distance. To minimise the effects of multiple scattering events, the sample transmission is ideally kept above 70%.

The raw scattering measurements must be calibrated in order to normalise the scattering intensity as a function of scattering vector. The use of a standard sample in which the predominant scattering is incoherent is a widely accepted technique to give intensity on an absolute scale [107]. Since hydrogen has a high incoherent neutron scattering cross section and scatters isotropically, H_2O is commonly used for this [77].

Finally, one should consider which scattered neutrons that are contributing to the signal actually provide information about the sample. Neutrons incident on the detector are from three main sources:

1. Neutrons scattered by the sample
2. Neutrons that pass through the sample but are scattered by something other than the sample
3. Background neutrons *i.e.* neutrons that reach the detector without passing through the sample and electronic noise in the detector itself.

It is essential that the background counts that contribute to the BG term in equation 3.9 are accounted for when analysing scattering profiles to yield true results. Thus, the above contributions must be separated by carrying out the following measurements [76, 108]:

- Scattering from the sample itself, $\mathrm{I_S}$, which contains contributions from all sources listed above
- Scattering from the empty sample holding cell, $\mathrm{I_E}$, which contains contributions from sources 2 and 3 listed above
- Scattering measured with a strong neutron absorber (*e.g.* Cd) placed between the beam and the sample, $\mathrm{I_{Cd}}$, which contains the background contribution 3 listed above.

Hence, the absolute scattering intensity can be found through applying the following corrections to the raw data

$$\frac{d\Sigma(q)}{d\Omega} = \frac{1}{I_0 \Omega \epsilon A t}\left[\frac{1}{T_S T_E}(I_S - I_{Cd}) - \frac{1}{T_E}(I_E - I_{Cd})\right] \tag{3.10}$$

All data corrections were applied to the raw 2D sample scattering ASCII data files using the GRASP software package [109].

In order to convert from 2D data into 1D data the absolute scattered intensity must be radially averaged to produce an absolute intensity versus scattering vector, I(q), profile. The radial averaging is completed in GRASP using a range of sectors. The sectors chosen for radially averaging are dependent on the nature of the neutron scattering interactions, i.e. nuclear or magnetic. Nuclear scattering is isotropic and so 360° sectors can be used to increase the statistics. For systems that require separation of the nuclear and magnetic scattering, as in the RPV steel alloys in Chapters 4 and 5, segment sectors are chosen to allow for extraction of relevant scattering contributions. In this case, one should select an appropriate sector size that maximises the signal to noise ratio to ensure good statistics. An example of radial averaging sectors for an RPV steel is shown in Figure 3.5.

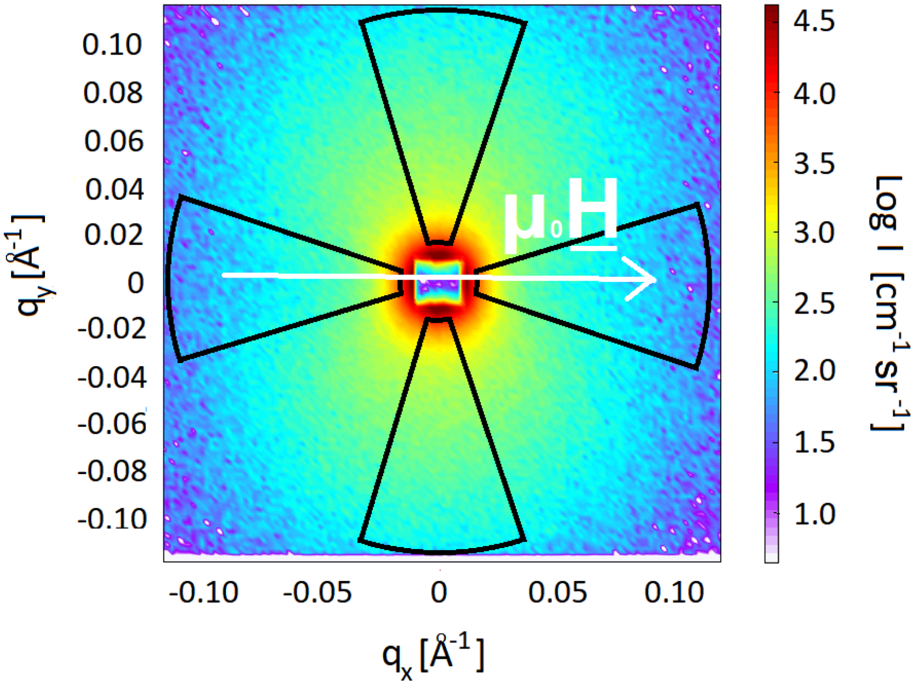

Figure 3.5: GRASP 2D detector image of RPV steel showing sectors for radial averaging (black) with applied field direction in the horizontal plane. Vertical sectors = nuclear + magnetic scattering. Horizontal sectors = nuclear scattering.

It is worth noting that in SANS experiments, the real space distances being probed can range from angstroms to hundreds of nanometres. This correlates to reciprocal space q-ranges that can only be achieved by overlapping measurements from multiple instrument configurations.

Recapping that the q-range is a function of collimation distance, wavelength, and sample-to-detector distance, varying combinations are used to achieve the desired q-range, balancing the instrumental resolution and the beam flux to obtain data in realistic timescales. Particular care must be taken to ensure sufficient overlap between each q-range configuration, since the noise increases at high q values where incoherent background scattering dominates the signal.

The reduced and overlapped I(q) scattering profiles can then be used in subsequent data analysis using standard plots or detailed model fitting.

3.4.1.2 X-ray corrections

Equations 3.9 and 3.10 in Section 3.4.1.1 that describe the differential macroscopic scattering cross section contain common parameters to those required for SAXS. Hence, similar data corrections must be made to the measured scattering intensity, $\mathrm{I_S}$, in order to extract absolute I(q) scattering profiles

$$\frac{d\Sigma(q)}{d\Omega} = \frac{CF}{I_0 mt}\left(\frac{I_S - DF}{T_S} - \frac{I_E - DF}{T_E}\right) \tag{3.11}$$

where CF is calibration factor for absolute scaling (from glassy carbon measurements), $\mathrm{I_0}$ is the incident beam flux, m is the measurement time, t is sample thickness, DF is the detector dark field correction, $\mathrm{T_{S/E}}$ is the sample and empty cell transmission respectively, and $\mathrm{I_E}$ is the measured background (empty cell) intensity.

The sample transmission is equal to $\frac{B_S}{B_E}$, where $\mathrm{B_S}$ and $\mathrm{B_E}$ are the beamstop diode detector counts with the sample and empty cell respectively. The incident beam flux is measured by the beamstop diode detector during empty measurement and so is equivalent to $\mathrm{B_E}$.

The sample thickness is related to transmission through Lambert-Beer law in equation 3.1.

The glassy carbon calibration factor was found by scaling the measured glassy carbon scattering profiles, $\mathrm{I_{GC}}$, to the published absolute scattering intensity for glassy carbon, $\frac{d\Sigma}{d\Omega}$,(Standard Reference Material 3600 [110]), accounting for its thickness, $\mathrm{t_{GC}}$, and its transmission, $\mathrm{T_{GC}}$, through

$$CF = \frac{\frac{d\Sigma}{d\Omega} t_{GC} T_{GC}}{I_{GC}} \tag{3.12}$$

The thickness of the glassy carbon sample used was 1 mm, and its transmission was found using $\frac{B_{S,GC}}{B_E}$.

The q-calibration was applied using a silver behenate scattering sample with a known lattice parameter of 5.8 nm.

Considering the aforementioned corrections, the required measurements for SAXS data reduction and analysis are:

- Sample transmission
- Empty cell transmission
- Incident beam intensity (empty beamstop measurement)
- Sample scattering

- Empty cell scattering
- Dark field contribution
- Glassy carbon standard sample scattering
- Silver behenate standard sample scattering

For ASAXS where a variety of incident x-ray energies are used, the above measurements are required for each energy used and an energy calibration of the monochromator is also required.

Once the necessary corrections are applied, masks are setup on the 2D detector images to prevent integration over areas with no intensity. Masks were applied to dead pixels, the beamstop arm, and to the gaps between detector modules. An example detector image with corrections and masks applied is shown in Figure 3.6.

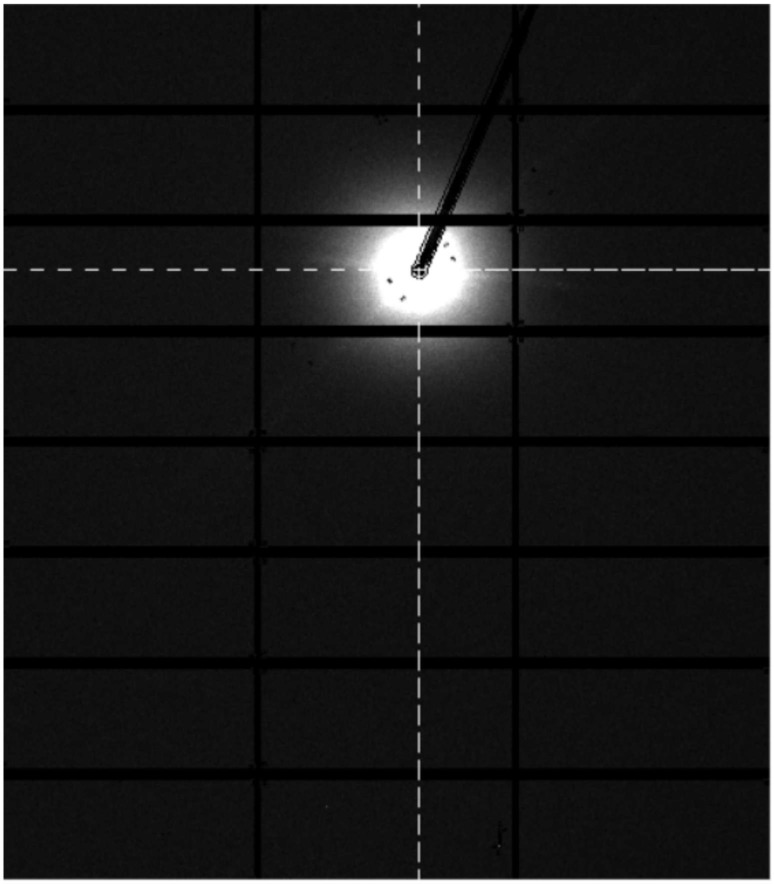

Figure 3.6: Corrected 2D detector image of an RPV weld at E = 6.809 keV. Masked areas are shown in black.

Finally, as for SANS, the 2D masked data is radially averaged to obtain absolute I(q) profiles for all energies with sufficient signal-to-noise ratios.

3.4.2 Data analysis

3.4.2.1 Model-independent analysis

Regardless of the material system under investigation, there are several qualitative model-independent analyses that can be carried out on reduced small-angle scattering data.

The Porod scattering approximation is a power law dependence of absolute scattering intensity [75] that is valid in high-q, described by

$$I(q) = Aq^{-m} + BG_{incoh} \tag{3.13}$$

where A is the scaling coefficient, m is the exponent, and $\mathrm{BG}_{\mathrm{incoh}}$ is the incoherent background scattering. The exponent m details the nature of such interfaces.

The Porod plot of log(I) vs log(q) indicates scattering from interfaces within the sample at relatively small length scales in comparison to the size of scatterers. Q-dependent exponents are shown schematically in Figure 3.7 for different scattering interfaces. In the Porod plot, the gradient is equal to the exponent m through

$$\log[I(q) - BG_{incoh}] = \log(A) - m\log(q) \tag{3.14}$$

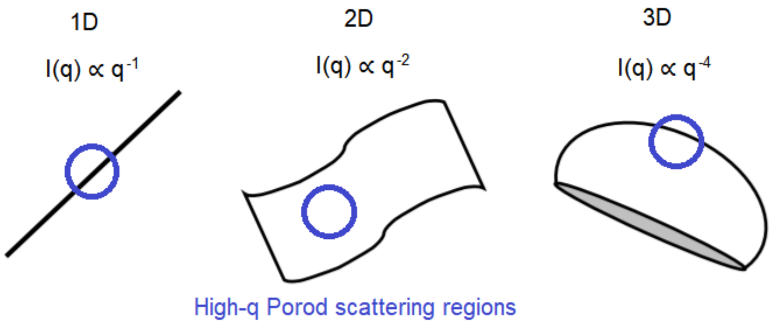

Figure 3.7: Schematic diagram showing the high-q Porod scattering regions and q-dependent exponents for 3 types of scattering object. Adapted from [77].

In this work, all samples investigated using SAS are polycrystalline metal systems, where the scattering interfaces are 3D and can be attributed to microstructural features such as grain boundaries with a corresponding Porod exponent of 4.

The Guinier plot of ln(I) vs q^2 is valid in at low-q values in the range $qR_q < \sqrt{3}$. As such, it requires a careful q range. It can detail information on the largest scatterers in the system, in the form of the Guinier radius, R_g.

The gradient of a Guinier plot, m, is related to the Guinier radius by

$$m = R_g^2 3 \tag{3.15}$$

Hence, linear least-squares fitting can be used to extract the radius of gyration of a system of scatterers.

The error on the extracted R_g can be derived using standard error propagation

$$\sigma(R_g) = \frac{\partial R_g}{\partial m}\sigma(m) \qquad = \frac{\sigma(m)}{2}\sqrt{\frac{3}{m}} \tag{3.16}$$

In a system of spherical scatterers, R_g is related to the scatterer radius, R, by

$$R_g = \frac{5}{3}R^2 \tag{3.17}$$

It is noted that whilst these plots can provide an insight into the general properties of the scattering system, more detailed data analysis is often required to fully quantify the system properties.

3.4.2.2 Empirical model fitting

In order to obtain a more detailed understanding of small-angle scattering data, empirical modelling can be employed. Empirical models can be fit to I(q) scattering profiles to obtain the form factor, volume fraction, contrast contributions, and structure factor to the differential scattering cross section (derived in detail in Section 2.4.1). Such fitted parameters detail the shape, size distribution, composition, number density, and interaction of the scatterers within a material system.

In this work, initial guesses of models to fit stem from expected form factors for irradiation and thermal ageing precipitation damage noted in literature. Common precipitate shapes include polydisperse spheres, core shells, and ellipsoids [14, 22, 24, 111, 112, 113].

A combination of the aforementioned models are used to investigate the goodness of fit and choose the best-estimate form factor, considering the physical implications of the fitting parameters, the associated errors, and the chi-squared measures.

For spherical scatterers with a log-normal size distribution, if the scaling factor of the distribution is set to equal the volume fraction of precipitates, ϕ, the outputted value is the absolute differential macroscopic cross section, $\frac{d\Sigma}{d\Omega}$, in units of cm^{-1}sr^{-1}

$$\frac{d\Sigma}{d\Omega} = I(q) = \left(\frac{4\pi}{3}\right)^2 N_p \Delta\rho^2 \int_0^\infty f(R) R^6 F(qR)^2 dR \tag{3.18}$$

where the number density of precipitates $\mathrm{N_p}$ is equal to $\frac{\phi}{<V_p>}$, where $<\mathrm{V_p}>$ is the average volume of a precipitate; $\Delta\rho$ is the scattering contrast from the difference between the scattering length densities of the solvent, ρ_{matrix}, and solute, ρ_{precip}. $\mathrm{F(qR)^2}$ is the form factor for a spherical scattering object given by [77]

$$F(qR)^2 = \left[\frac{3(\sin qR - qR\cos qR)}{(qR)^3}\right]^2 \tag{3.19}$$

where R is the mean radius of the precipitates, and f(R) is the normalised log-normal distribution of precipitates as a function of radius, given by

$$f(R) = \frac{1}{\sigma R\sqrt{2\pi}} \exp\left[-\frac{1}{2\sigma^2}(\ln(R) - \mu)^2\right] \tag{3.20}$$

where σ is the polydispersity of the size distribution, and $\mu = \ln(\mathrm{R_{med}})$ where $\mathrm{R_{med}}$ is the median radius. The mean radius of the log-normal distribution of spherical scatterers can hence be described by

$$R = \exp\left(\mu + \frac{\sigma^2}{2}\right) \tag{3.21}$$

It should be noted that volume fraction and contrast are multiplicative in the model and thus are not independent of one another. This means two of the three parameters should be held constant during fitting. Choosing which quantity to hold depends on what type of information is deemed most important to extract. Volume fractions are readily available and are convincing from APT data, however the non-magnetic assumption of precipitates is a questionable one. It is often assumed by many researchers as it makes the analysis easier, however it is a conflicting subject and so naturally it shall become a prime focus of this analysis. Hence, the volume fraction is simply treated as a scale factor during model fitting, only indicating relative amounts rather than absolute. This allows for the explicit calculation of true nuclear and magnetic scattering length densities of precipitates which can allude to compositional information. This can be investigated primarily through fitting to give an idea of the magnitudes and in more detail through the ratio of the nuclear and magnetic scattering intensities (the A ratio).

It is worth noting that other analysis methods can be used to provide confidence in the fitted models. The maximum entropy [89, 90] and Monte Carlo [92] analytical techniques which do not impose certain *a priori* assumptions on the contrast or volume fraction of the scatterers, or direct comparison to SAXS data, are examples of such alternatives. Such methods should be used to support empirical modelling to form robust conclusions from small-angle scattering data.

A common approach to empirical model fitting includes initial fitting of two models simultaneously, for both the scatterers and matrix, if the matrix system is understood. In the 3D polycrystalline metal samples used in this work, there will likely be a Porod scattering contribution at high-q ($I(q) \propto q^{-4}$, also available from the model-independent Porod plot). The coefficients of the Porod model obtained through fitting can then be used to subtract grain boundary scattering and leave precipitate-only scattering. This removes a level of complexity in the modelling process. In addition, multiple scattering datasets can be fitted through a global fitting process to allow for linking of specific physical parameters.

Another common technique considers subtraction of the scattering profile from a virgin sample of the same composition. This will remove the incoherent background, and show I(q) profiles with contributions solely from thermal-ageing/irradiation induced damage.

3.4.2.3 A ratio

As mentioned in Section 2.6.2 one can extract compositional information from the scattering objects from the A ratio that is a function of the absolute intensities of the nuclear and magnetic scattering contributions (equation 2.43).

The importance of limiting the number of variables when fitting, *e.g.* calculating the nuclear and scattering length densities of the matrix and setting to constant values in the fitting becomes apparent here when trying to simplify the calculation. Since the volume fraction was held as a relative scale factor and the nuclear and magnetic form factors are one in the same, the A ratio reduces to

$$A_{ratio} = \frac{\Delta\rho_M^2}{\Delta\rho_N^2} + 1 \tag{3.22}$$

Hence, the A ratio is a function of the scattering length density and relative fractions of elements in precipitate and matrix, which can elucidate precipitate compositions in a known bulk matrix. This is because the intensity in the A ratio equation is directly related to the differences in scattering contrasts from each element.

As shown in equation 3.22, the A ratio is a function of the nuclear and magnetic contrast in the sample, $\Delta\rho$, where $\Delta\rho$ is simply the difference between the scattering length density of the precipitate and matrix (derived previously in Section 2.4.1).

Recapping, the nuclear and magnetic scattering length densities summed over i elements is given by

$$\rho_i = \sum_i N_i b_i \tag{3.23}$$

where N_i and b_i are the number density [Å^{-3}] and nuclear ($b_{N,i}$) or magnetic ($b_{M,i}$) scattering lengths [Å] of element i.

Remembering that contrast, $\Delta\rho$, is $\rho_p - \rho_m$, and that number density $N_i = \frac{x_i}{V}$, the nuclear and magnetic contrasts can be written as

$$\Delta\rho_N = \frac{1}{V}[(x^p_{Fe}b_{N,Fe} + x^p_{Cu}b_{N,Cu} + x^p_{Mn}b_{N,Mn} + x^p_{Ni}b_{N,Ni} + x^p_{Si}b_{N,Si} + x^p_{vac}b_{N,vac}) - \tag{3.24}$$

$$(x^m_{Fe}b_{N,Fe} + x^m_{Cu}b_{N,Cu} + x^m_{Mn}b_{N,Mn} + x^m_{Ni}b_{N,Ni} + x^m_{Si}b_{N,Si})]$$

$$\Delta\rho_M = \frac{1}{V}[(x^p_{Fe}b_{M,Fe} + x^p_{Ni}b_{M,Ni} + x^p_{vac}b_{M,vac}) - (x^m_{Fe}b_{M,Fe} + x^m_{Ni}b_{M,Ni})] \tag{3.25}$$

where V is the sample volume [Å^3], x is the elemental fraction [arb.], b is the scattering length [Å], and superscripts p and m represent precipitate and matrix respectively.

3.4.2.4 Maximum entropy

The maximum entropy method (MEM) for small-angle scattering data analysis was first developed by Potton et al. [89] to extract the particle size distribution, p(R), from a system of non-interacting spherical scatterers. The motivation for its development is to provide a solution to the linear inverse problem presented by small-angle scattering data, whereby p(R) is a continuous function yet there are a finite number of absolute scattering intensities obtained over a specific experimental q range.

The developed method has overcome several challenges associated with solving the linear inverse problem of extracting the particle size distribution from measured scattering intensity: the MEM calculates a size distribution that is inherently positive and provides a unique function which is most compatible with the discrete data set [90].

The foundation of the technique is based on the fact that the most compatible unique solution to a discrete probability distribution is a solution which maximises the entropy of the system [114, 115]. The entropy, S, can be described by

$$S = -\sum_{i=1}^{N} p_i \log p_i \tag{3.26}$$

where p$_{i\rightarrow N}$ is the set of particle size frequency values to be found, which are related to the form factor of the scatterers through the differential macroscopic cross section derived in Section 2.4.1. The discrete p(R) solution is constrained through the comparison between the experimental and simulated absolute intensities where the chi-squared value cannot exceed the number of data points [89].

The MEM was tested by Potton et al. for several simulated input size distributions. An example for a simulated unimodal Gaussian size distribution for spherical SAS data between 0.0183 Å^{-1} to 0.1825 Å^{-1} with 1% errors applied is shown in Figure 3.8. The calculated probability distribution is in strong agreement with the input data, showing a high degree of accuracy of the MEM. This highlights the benefits of MEM as a validation tool for the empirical model fitting method of SAS data analysis.

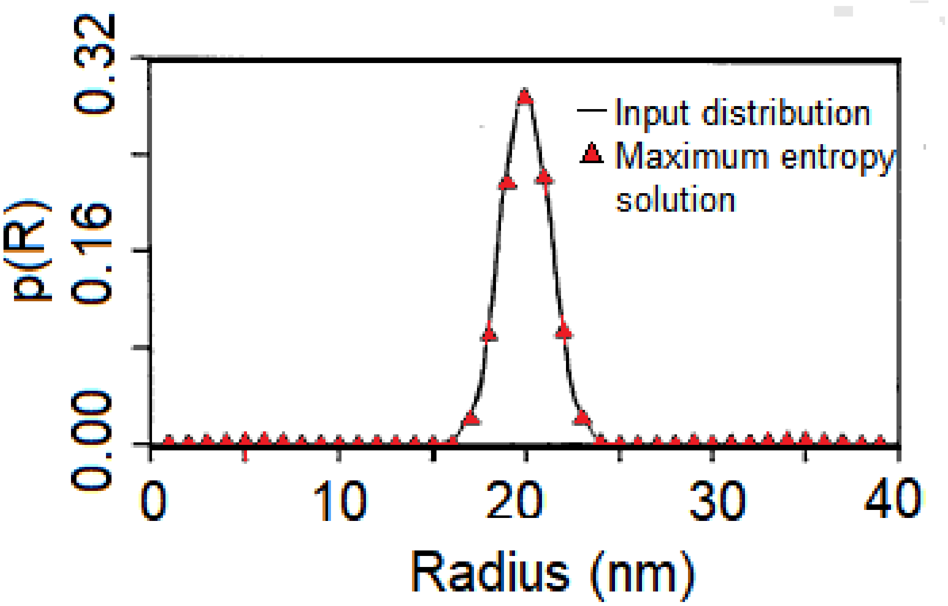

Figure 3.8: Proof of concept of the maximim entropy method for extracting a discrete particle size distribution (red) from a continuous input distribution (black). Adapted from [89].

3.4.2.5 Monte Carlo

A Monte Carlo method for analysing small-angle scattering data has been developed by [91]. This technique can extract a particle size distribution as a function of radius, p(R), from a system of non-interacting spherical scatterers with a discretised absolute scattering intensity.

This methodology has been developed further by [92], which has built the Monte Carlo algorithm into the McSAS data analysis software [93]. Within McSAS, an initial guess of the differential macroscopic cross section is made from the contribution of scattering from spheres with randomly selected radius R between the real space size limits over a defined number of iterations, $\mathrm{n_i}$. The calculated scattering intensity for such a system can be described by

$$I(q) = N_p \sum_{i=R_{min}}^{i=R_{max}} p(R) R_i^6 F(qR_i)^2 \Delta R \tag{3.27}$$

where $\mathrm{N_p}$ is number density of scatterers and F(qR) is the spherical form factor, and $\mathrm{R_{min/max}}$ are described by the reciprocal space data range as $\mathrm{R_{min}} > \frac{\pi}{q_{max}}$ and $\mathrm{R_{max}} < \frac{\pi}{q_{min}}$, and ΔR is the discrete bin width of the size distribution based on $\mathrm{R_{min}}$ and $\mathrm{R_{max}}$.

From each iteration, a particle size within the range $\mathrm{R_{min}}$ to $\mathrm{R_{max}}$ is selected at random and its contribution to the calculated scattering intensity is recorded. The output size distribution is determined by comparison of this calculated contribution to the experimental scattering intensity for each iteration. The radius change between each iteration is either accepted or rejected dependent on whether it minimises the reduced chi-sqaured value, χ_r^2, described by [100]

$$\chi_r^2 = \frac{1}{N-M}\sum_i \left[\frac{I_C(q_i) - I_E(q_i)}{\sigma(q_i)}\right]^2 \tag{3.28}$$

where $\mathrm{I_{C/E}(q)}$ is the calculated and experimental absolute scattering intensities respectively, $\sigma(\mathrm{q_i})$ is the estimated error on each data point, N is the number of data points used in the fit, and M is the degrees of freedom of the calculated intensity. This criteria allows for computation of the mean and standard deviation of the frequency for each radii bin. The propagated error on each bin is described by

$$\sigma(q_i) = \left[\frac{1}{N_{q_i} - 1}\sum_{p=1}^{N_{q_i}} (I_p - I_{q_i})^2\right]^{\frac{1}{2}} \tag{3.29}$$

where N_{q_i} is the total number of experimental data points in each bin, $\mathrm{I_p}$ is the intensity of the data point in the bin, and I_{q_i} is the mean intensity in the bin.

Once the reduced chi-squared has reduced below 1, the Monte Carlo fit has converged and the process is complete.

Figure 3.9 shows the accuracy of the Monte Carlo approach to a set of simulated SiC SAXS data. As for the MEM, this shows how the Monte Carlo method can be a useful validation tool for the empirical model fitting method of SAS data analysis.

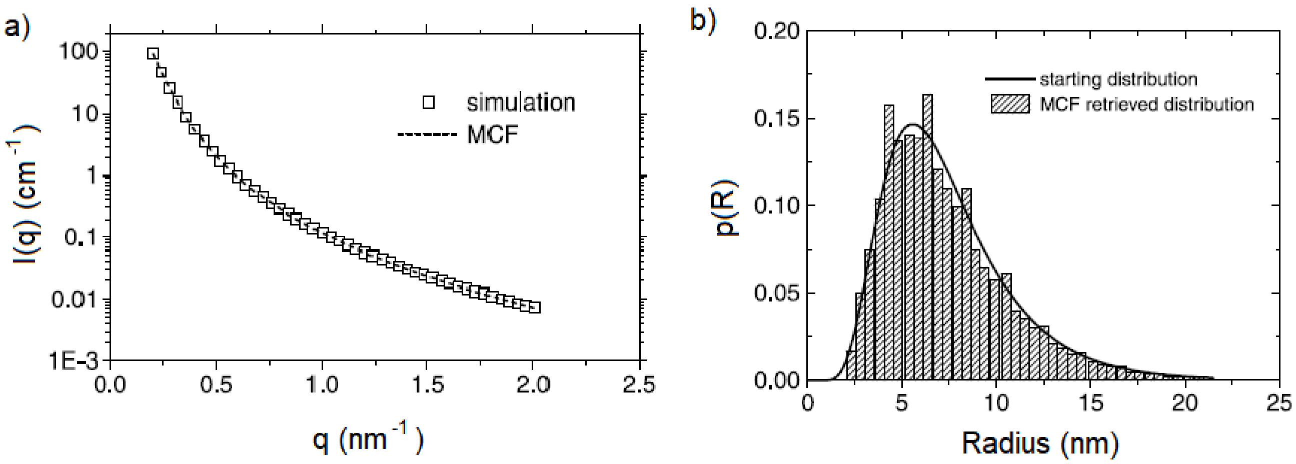

Figure 3.9: Proof of concept of Monte Carlo technique for fitting SiC simulated SAXS data with a log normal distribution of width 3.5 nm and median radius of 7.5 nm from [91]. a) Monte Carlo fit compared to simulated scattering profile. b) Resultant particle size distribution.

CHAPTER 4

THERMAL AGEING INDUCED PRECIPITATION IN HIGH NI REACTOR PRESSURE VESSEL STEEL WELDS

4.1 Introduction

The principal aim of this research is to investigate the mechanisms and microstructural effects of precipitation damage using advanced scattering techniques. This chapter focuses on the concept of precipitation damage in RPV steels. Its overall aim is to showcase how small-angle scattering can be used to quantify thermal ageing induced damage and link the results to the effects on physical properties, and to contribute to findings from other investigative techniques such as atom probe tomography (APT).

The RPV of a nuclear fission reactor is the primary containment of the active core and is considered to be the only component of the reactor that is uneconomically viable to replace, often labelling it as the life-limiting factor [12]. A typical RPV is made up of castings, forgings and welds of low alloy ferritic steels (e.g. SA508, SA5033B), since the RPV has specific mechanical requirements of high strength but also ductility. It must also have a high fracture toughness and be resistant to thermal shock, in order to withstand extreme scenarios such as a loss-of-coolant accident. Understanding the behaviour of the RPV in a reactor environment is crucial for supporting safety cases to allow for life extension of current power plants to additional operating periods of up to 60 years, and also for the development of safe reactor materials for advanced reactor systems. Moreover, one of the biggest issues facing the next generation of nuclear reactors in the UK is the large financial overheads and the economic impact of such large investments. The most reliable way to reduce the impact of such barriers is to reduce the risk of financing by proving the reactor will last for, and exceed, the planned period of operation.

Over the development of first to now fourth generation fission reactors, studies of RPV steels have been at the forefront of nuclear materials research, with a vast majority focusing on the characterisation of irradiation and thermal ageing induced damage [50, 69]. Radiation damage is a multifaceted phenomenon, depending on many factors such as temperature, damage profile, and material composition. The harsh neutron environment that the RPV is exposed to over its lifetime can induce a significant amount of damage in the steels, often in the form of irradiation and thermal ageing induced precipitation and segregation [11, 116, 117]. At the temperature conditions in a light water reactor (LWR), ≈ 300 °C, this matrix damage can lead to embrittlement of the RPV [70, 118, 119, 120]. The works in this chapter focus on precipitation damage in LWR low alloy RPV steels, since these are the most commonly implemented generation III reactor types across the world. Such considerations are also valid for the material challenges faced in generation III+ reactors, most of which are advanced concepts that build on LWR designs. The techniques presented here can also be applied to radiation damage studies that pave the way more more complex and harsh reactor types such as high-temperature gas reactors, molten salt reactors, and fast neutron reactors.

This chapter studies precipitation in a thermally aged RPV weld material, with composition shown in Table 4.1. This particular sample has been chosen due to its novel thermal history which is analogous to exposure temperature and time in a typical LWR: aged for 100 000 hours (approximately 10 years) at 330 °C . The sample itself was obtained from Rolls-Royce and has previously been a part of an APT study [54]. It is classed as a high Ni, high Cu weld, allowing one to study the morphology of thermal aged induced precipitates, the role of Cu and Ni in precipitation, and the contested topic of the Fe/vacancy content of said precipitates. This chapter introduces studies of precipitation in RPV steels and the adverse effects on macroscopic mechanical properties. It discusses the reliability of APT as a method of characterising precipitation in reactor steels and the integral contribution that small-angle scattering has made to understanding the properties of ageing induced precipitates and thus microstructural evolution as a function of time in service. It is shown that whilst small-angle neutron scattering (SANS) is a valuable tool, for a complete and comprehensive understanding of precipitation in RPV steel systems it should be complemented by alternative techniques such APT, anomalous small-angle x-ray scattering (ASAXS), or transmission electron microscopy (TEM). A summary of literature using these separate methods can also be found to highlight the usefulness of each and the importance of combining efforts to obtain reliable results.

The results from optical microscopy, microindentation hardness testing, SANS and ASAXS are presented, obtaining novel information on thermal ageing induced precipitate shape, size, and composition through multiple experimental methods and analysis techniques. The importance of this is highlighted when forming robust conclusions on properties such as precipitate shape, size distribution, number density/ volume fraction, and compositional variance. A particular focus has been made on the magnetic treatment of precipitates and the consideration of overlooked fractions of Fe and vacancies in the precipitates. The implications of these with respect to the lifetime of such materials under reactor conditions will be considered, and the crucial relationship between thermal ageing and precipitation at reactor temperatures is explored in depth.

4.2 Thermal ageing induced precipitation in RPV steels: a review

4.2.1 Low alloy RPV steels

The irradiation conditions in LWRs have been mimicked in a number of damage studies in low alloy RPV steels, where the precipitation of dislocation loops and other secondary defects leads to radiation induced and enhanced clustering of certain alloying elements present in the solid-solution steel matrix [13, 50, 69]. The temperature exposure in a LWR environment coupled with the limited solubility of alloying elements such as Cu, Mn and Ni in the Fe matrix can lead to thermal ageing induced precipitation alongside irradiation induced and enhanced precipitation. These mechanisms are tightly bound and nuanced, meaning the role of ageing must not be overlooked.

Thermal ageing and irradiation induced precipitation leads to hardening and embrittlement of the steels due impedance of dislocation motion. This increases the probability of crack initiation and propagation in the material [121], which can ultimately compromise the integrity of the RPV coupled with an increased risk of structural failure under accident scenarios in service. The embrittlement can be attributed by a change in the ductile to brittle transition temperature (DBTT), a decrease in the fracture toughness, and an increase in the hardness of the steel.

4.2.1.1 Precipitation in high Cu RPV steels

The large neutron fluxes experienced over their lifetimes (up to 10^{20} n/cm^2), and exposure to temperatures > 300 °C, can induce a significant amount of damage in RPV steels due to the long range of neutrons and increased diffusion of alloying elements. This damage is often in the form of radiation induced precipitation and segregation at temperatures around 300 °C, but at higher temperatures one must consider additional effects of bubbling, void formation, and creep behaviour.

It has been found that the presence of Cu as an impurity from the weld filler material in earlier RPV steel alloys has a tendency to form nanoscale Cu-rich precipitates due to irradiation and thermal ageing which significantly embrittle the material [13, 122]. This embrittlement can be quantified by an increase in the DBTT and a reduction in fracture toughness, as shown in Figure 4.1.

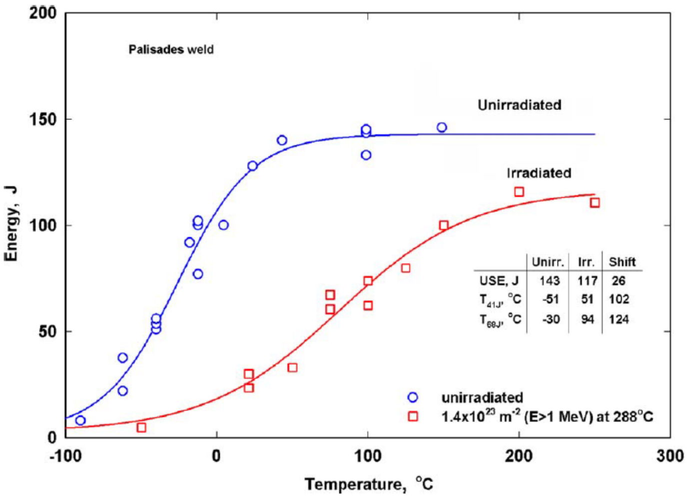

Figure 4.1: Graph of impact energy versus temperature for a high Ni high Cu RPV weld, indicating the DBTT shift and decrease in fracture toughness upon neutron irradiation with 1.4 x 10^{23} m^{-2} (E > 1 MeV) at 288 °C [66].

The presence of proton irradiation induced precipitates in high Cu RPV alloys at low irradiation damage levels, at a variety of irradiation temperatures, has been confirmed using SANS [31, 123, 124]. Through analysis of scattered intensity versus scattering vector, q, plots, spherical precipitates with a log-normal shape distribution and an average radius of 5 nm for a high Cu RPV steel irradiated to 13 mdpa at 400°C (see Figure 4.2) were identified. It is clear from the SANS and from hardness testing that precipitates are Cu-rich and increase in size with increasing irradiation temperature.

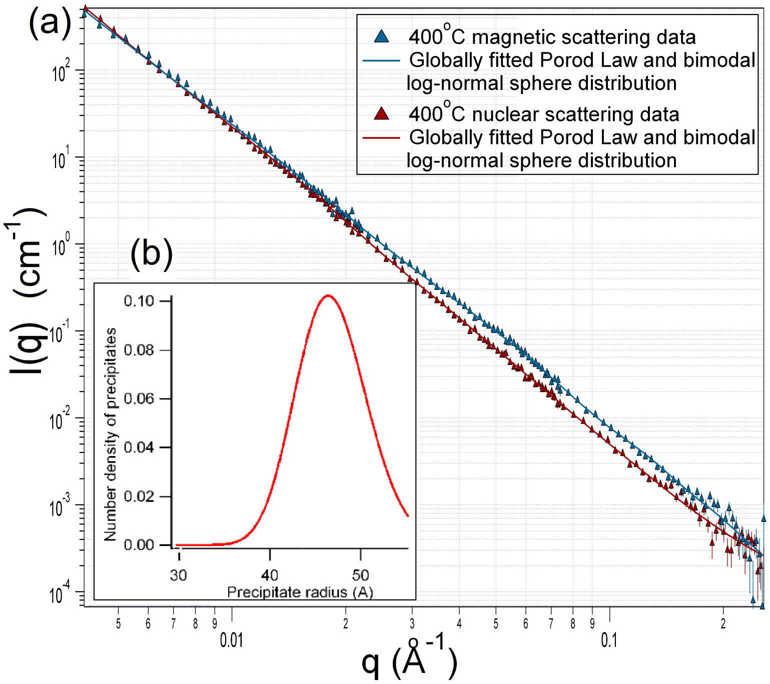

Figure 4.2: (a) I(q) for high Cu RPV steel irradiated at 400 °C with induced damage of 13mdpa, with fitted Porod and bimodal log-normal sphere models. The Porod dependence comes from the microstructure and carbides at much larger scales in these steel samples. (b) Graph of precipitate radius distribution [31].

It has been documented that for low alloy RPV steels containing > 0.1 wt% Cu (denoted as high Cu steels), even a small dose of radiation [124] or exposure to temperatures of 500 °C for as little as 10 minutes [125] will induce the formation of Cu-rich precipitates in size range 1-5 nm. This is a direct result of the low solubility of Cu in Fe, where it has a strong affinity to precipitate out of the matrix [126].

As a result of these findings, these high Cu steels have been exchanged with more favourable low Cu alloys (< 0.1 wt% Cu). However, where Cu-rich precipitates are no longer a concern, Mn, Ni and Si have an increased significance in precipitation in low Cu thermally aged alloys; now, the nature of the formation of MnNiSi-enriched precipitates and the role of Cu are a crucial research area for the development of structurally reliable pressure vessel materials [60, 67].

4.2.1.2 Precipitation in high Ni RPV steels

High Ni RPV materials are linked to life extension issues in the current generation of fission reactors. Of particular interest is the late-blooming G-phase ($Mn_6Ni_{16}Si_7$) [127], on which there have been multiple studies. First discovered in thermally aged Ni superalloys, the research was extended to general stainless and ferritic RPV steels when the reduction in Cu in such materials led to the discovery of irradiation induced MnNiSi-rich precipitates [128, 129]. The nature of such G-phase precipitates has been studied in depth [66, 130], but the status quo in the context of RPV steels remains unclear. There have been multiple APT and TEM studies in both thermally aged and irradiated samples where the findings on precipitate size, composition and formation mechanism either contradict one another or find only pre-G-phase type structures. For example, APT studies have found MnNiSi precipitation in high Ni RPV steels [21, 60], but the observed compositions differ between these studies and also between whether the material was thermally aged and neutron irradiated.

The G-phase seems to be present after long times at elevated temperatures, often referred to as a late-blooming phase, and it has been postulated to exist on shorter time scales under irradiation because of the role radiation damage has in the redistribution of solute elements within the lattice [116]. Since this irradiation induced precipitation occurs at similar temperatures to that of thermal ageing studies, it may just be that the irradiation is accelerating the precipitation process. An elucidation of the mechanisms of such formation is needed to better understand the role of temperature and fluence on RPV materials.

SANS is a robust way of measuring nanoscale precipitation in bulk materials, owing to the large penetration depth of the neutron. Due to neutron-nuclei interactions, SANS can provide details on the shape, size distribution, number density and volume fraction of scattering objects [73], as discussed in depth in Section 2.4.1. The magnetic dipole interaction of the neutron and scattering atom can also be exploited to find specific compositional information relating to the magnetism of the scatterers [75], however it is important to note that in the context of precipitation in RPV steels it cannot determine precise precipitate composition since there are multiple alloying elements to consider [62]. This highlights the importance of using other techniques to support and quantify SANS results, since in the study of nanoscale precipitation damage there is not one well-rounded technique that can be used alone. SAXS can be used to compliment SANS studies and validate observed precipitate properties. Other x-ray properties, such as anomalous dispersion effects of elements in the vicinity of their absorption edges, can be used to detail stoichiometry of scatterers in a system through the ASAXS technique [131]. By scanning the x-ray energy through the absorption edge, one can extract the resonant scattering contribution of the scatterers, detailing exact compositional information. This can be invaluable in the investigation of radiation induced precipitation where there are multiple elements to consider, and so it can be directly coupled with structural and magnetic precipitate information gained from SANS. In addition to ASAXS, APT can deliver precipitate composition, however it does not provide accurate volume fraction information and has a tendency to underestimate the number densities of small precipitates due to the uncertainty in the boundary assumed between precipitate and matrix [71]. It can also often overestimate the quantity of Fe in precipitates due to the same uncertainty [132], and does not consider the vacancy fraction in such precipitates, which is known to play an important role. Moreover, electron microscopy alone cannot provide information on composition of precipitates; combining electron microscopy with EDX does not give a high enough resolution for nanoscale precipitate compositions. TEM can also be highly influenced by the magnetism in these ferritic steels. The electrons interact with unpaired electrons of Fe in steel samples which can lead to deflection of the electron beam and hence difficulty in obtaining images. In addition, since the electron beam trajectory is controlled by electromagnets, one may experience difficulty inserting small samples due to interactions with electromagnets (i.e. physical movement). Microscopy only studies localised regions in a material and so does not give a complete picture alone. As a result, there are discrepancies between techniques and there is often limited collaboration between groups studying radiation damage.

4.3 Materials and methods

4.3.1 Sample details

Understanding the microstructural evolution of RPV alloys under typical LWR operating conditions is crucial in predicting material integrity over time in-service. The thermal history of RPV alloys plays an important role in nanoscale precipitation that can lead to hardening and embrittlement.

A high Ni high Cu RPV weld alloy aged for 100 000 hours at 330 °C has been selected for this study, with composition listed in Table 4.1. This will allow for investigation of the effects of Cu and Ni on thermal ageing induced precipitation under long term ageing conditions. APT has been previously carried out with this specific sample and other similar compositions at shorter ageing times [54], but it has not yet been investigated with small-angle scattering or quantitative methods. This makes it a prime choice for an advanced scattering damage study, directly allowing for an investigation of how the ageing time affects precipitation in such alloys and how this transfers into macroscopic material changes via embrittlement.

Table 4.1: Composition of main elements in RPV weld material in at%. There are trace amounts of Al, V, Sn, As and Sb also present.

Cu	**Ni**	**Mn**	**Si**	**C**	**Mo**	**S**	**P**	**Cr**	**Fe**
0.44	1.66	1.38	0.75	0.190	0.024	0.016	0.018	0.054	95.22

It is important to study long scale ageing times in RPV steels for multiple reasons. Primarily, it provides a realistic glimpse into exposure in a LWR since it mimics lifetime ageing. This is reiterated by the fact that there are limited studies in literature for ageing times on this length scale (most studies are carried out at much shorter ageing times on the order of 10^2 hours). Moreover, it allows us to investigate the role of Cu and Ni on *thermal aged* induced precipitation in high Ni high Cu RPV welds, a damage mechanism in high Cu RPV steels which has been somewhat overlooked, with the majority of studies focussing on irradiation damage.

The thermal history of the sample after weld formation is as follows [54]:

1. Annealing at 920 ± 20 °C for 6 hours and water quenching (post-weld)
2. Tempering at 600 ± 15 °C for 42 hours
3. Stress relief at 650 ± 15 °C for 6 hours
4. Ageing at 330 °C for 100 000 hours and water quenching.

It is important to address the fact that the ageing temperature is around 40 °C higher than typical RPV exposure in a LWR (290 °C). This is a pragmatic temperature difference that allows for a more reasonable ageing time, whilst ensuring the mechanisms of precipitation do not differ significantly [54].

It should also be noted that after each heat treatment a slow cooling rate of 50 °C hour^{-1} was achieved and the sample was sealed in quartz under argon to minimise oxidation during ageing.

The unaged version of this RPV weld will also be investigated to provide a direct comparison for the effects of thermal ageing on precipitation. For the rest of this chapter, the aged and unaged welds will be referred to as weld A and weld B respectively.

4.3.2 SANS

SANS has been used specifically to investigate the effects of thermal ageing induced precipitation in weld A and weld B. The samples were selected for an advanced scattering study due to their novel thermal history, as detailed in Table 4.2. This will allow for an in-depth investigation into the evolution of precipitation through ageing of a material, focusing on the quantification of precipitate structure, magnetic properties, and compositional information. It is noted that the dimensions of both samples differ slightly due to slicing using a SiC cutting wheel.

Table 4.2: Properties of weld A and weld B.

Sample	Thickness [mm]	Thermal history
Weld A	Wedge sample; 2.118 to 2.692	Thermally aged at 330 °C for 100 000 hours
Weld B	0.514	Unaged

4.3.2.1 Experimental measurements

The main SANS measurements were taken using the SANS-1 instrument at the FRM-II neutron source in Garching [96].

The total scattering vector range used was $0.006 < q < 0.404$ Å^{-1} ($104.72 > d > 1.52$ nm) obtained by using sample-detector and collimation distances shown in Table 4.3. The neutron wavelength used was $\lambda = 4.5$ Å with wavelength resolution $\frac{\Delta\lambda}{\lambda} = 10\%$. The sample aperture used was 6 mm diameter. The detector used was a moveable 1.00 x 1.02 m^2 He-3 multidetector made from an array of 128 tubes with a resoultion of 8 mm [96].

To gather scattering profiles from a large q-range, three different sample-detector distances were used throughout the experiment, as detailed in Table 4.3, to obtain three separate q-ranges; these will be overlapped during data reduction using the process detailed in Section 3.4.1.1.

It is important to note that care was taken when selecting the collimation distances and neutron apertures, since each is a compromise between the resolution and the flux at the sample.

Table 4.3: Selected conditions for forming three well-overlapped q-ranges on SANS1 at FRMII.

Property [unit]	Low q	Medium q	High q
q range [$Å^{-1}$]	0.006 to 0.035	0.020 to 0.115	0.071 to 0.404
Wavelength [Å]	4.501	4.501	4.501
Sample-detector distance [m]	20	6	1.65
Collimation distance [m]	20	6	2

In order to investigate the possibility of a core shell precipitate structure (with shell thickness < 1 nm), as alluded to by various literature studies [54], SANS data was also taken on the D22 instrument at the ILL [97] to access higher q values made possible by the ability to horizontally offset the detector. The neutron wavelength used was $\lambda = 5.0$ Å with wavelength resolution $\frac{\Delta\lambda}{\lambda} = 10\%$. The sample aperture used was 6 mm diameter. The detector used was a 102.4 x 98.0 cm^2 He-3 multidetector with pixel size 0.8 x 0.8 cm, consisting of 128 vertical detector tubes spaced by 8 mm [97]. The experimental configuration used to achieve an extra high q range is shown in Table 4.4.

Table 4.4: Selected conditions for reaching extra high q range on D22 at ILL.

Property [unit]	Extra high q
q range [$Å^{-1}$]	0.1 to 0.6404
Sample-detector distance [m]	1.8
Collimation distance [m]	2
Detector offset in x [mm]	300

The specific experimental setup used is shown schematically in Figure 4.3. The role of the Helmholtz coils is to provide an homogeneous magnetic field to the sample in the plane perpendicular to the neutron beam. This field was 0.5 T to saturate and align the magnetic domains in the sample along the field direction, meaning any scattering along the direction of the applied field is purely nuclear. This technique allows for full separation of the nuclear and magnetic scattering contributions, which can be useful when considering the composition of the scatterers in the system. This was completed for both weld A and weld B.

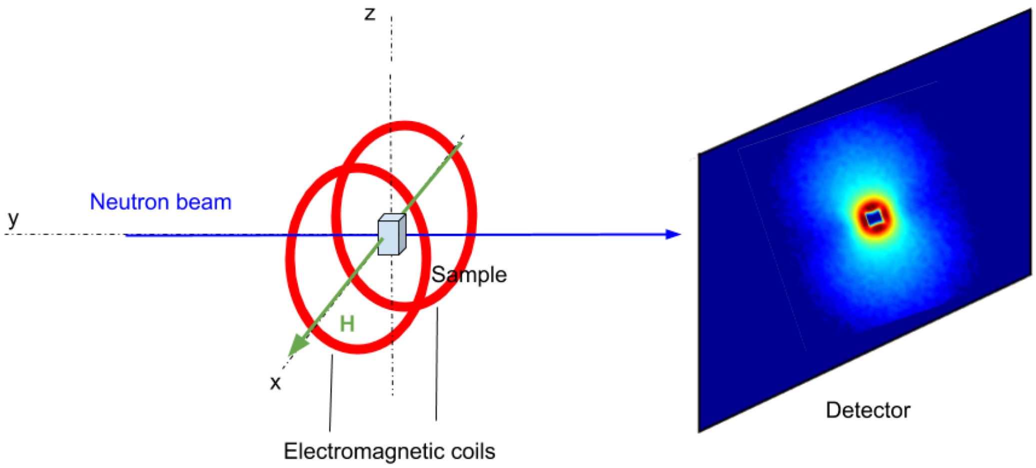

Figure 4.3: Schematic of the experimental SANS setup showing direction of applied field (green arrow) with respect to the neutron beam (blue arrow).

Each weld sample was mounted between two 17 mm aluminium rings in the sample space, and the final SANS measurements taken were:

- Scattering through a H_2O cell to calibrate the detector
- Scattering through cadmium to correct for electronic background
- Scattering through each empty aluminium ring in zero field for transmission calculations
- Scattering through each sample at each q-range

4.3.2.2 Data reduction and analysis

GRASP [109] was used reduce the data, by applying the necessary corrections detailed in Section 3.4.1.1 to put the data on an absolute scale.

In order to convert from 2D data into 1D data the absolute scattered intensity must be radially averaged to produce a one dimensional intensity versus scattering vector, I(q), profile. To complete this radial averaging, one should select an appropriate sector size that balances signal to noise ratio and good statistics. The sectors used for radial averaging had an azimuthal angle $\theta = 35°$ to obtain the best signal-to-noise ratio [133]. In this particular setup, as shown in Figure 4.3, the scattering along the applied field direction (horizontal) is purely nuclear. To extract magnetic scattering, one must subtract the pure nuclear scattering from the combined nuclear and magnetic scattering (vertical). These sectors have been imposed onto the 2D raw detector image in Figure 4.4.

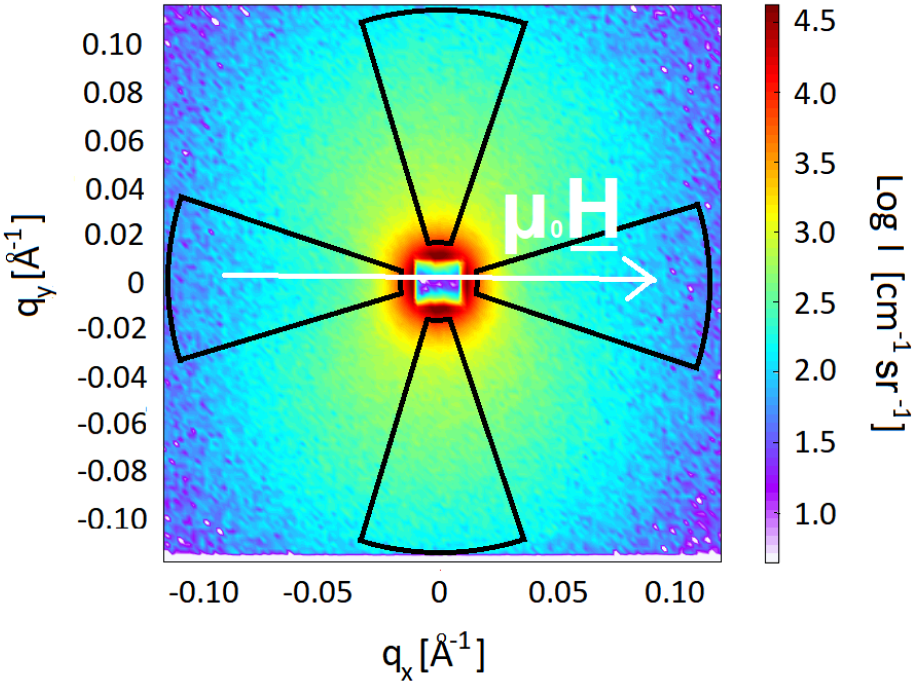

Figure 4.4: 2D medium q detector image in weld A showing nuclear and magnetic scattering, superimposed with applied field direction (white arrow) and sectors used for radial averaging (black). Vertical sectors = nuclear + magnetic scattering. Horizontal sectors = nuclear scattering. Sector angle $\theta = 35°$ to maximise signal to noise ratio.

To highlight the specific effect of the magnetic field on the scattering from the sample, one can radially average over the whole detector with respect to the azimuthal angle. The $I(\theta)$ profile is shown in Figure 4.5. Magnetic neutron scattering is known to give a $\cos^2\theta$ scattering contribution [134], which is clearly indicated by the fit of $I = I_0 + A\cos^2(\theta + \phi)$ where I_0 is a constant offset, A is a scaling coefficient, and ϕ is the phase.

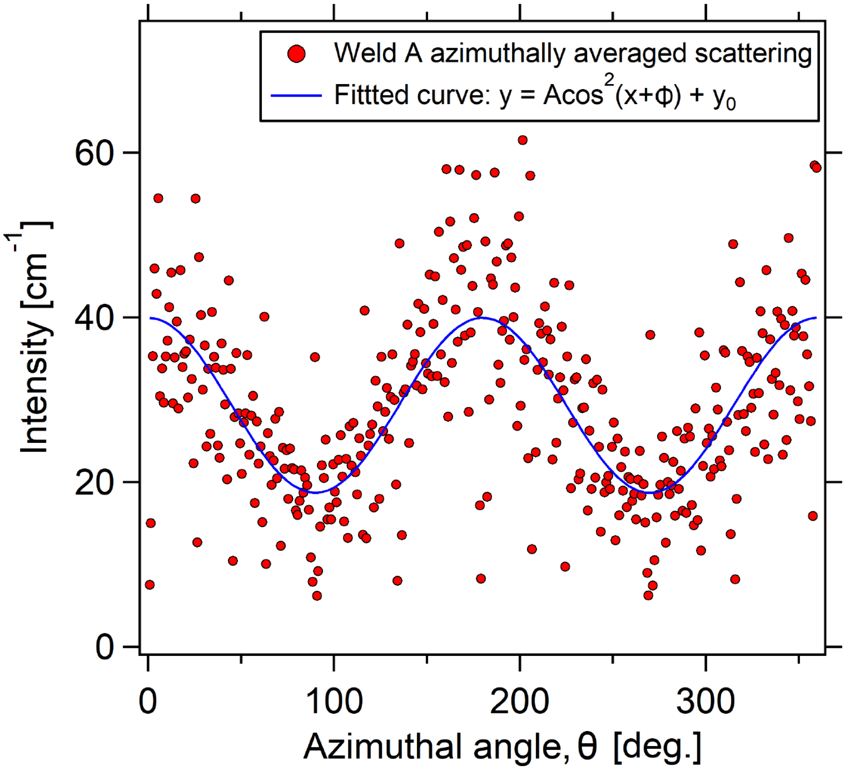

Figure 4.5: Graph of radially integrated intensity vs azimuthal angle (red circles) with fitted $\cos^2\theta$ dependence (blue line) in weld A to highlight presence of magnetic scattering.

Next, each q-range was overlapped using the process outlined in Section 3.4.1.1, and the horizontal I(q) profile was subtracted from the vertical I(q) profile, leaving the magnetic scattering. These stages were completed using the NIST NCNR macros [94] in Igor Pro. The resultant nuclear and magnetic I(q) profiles can be seen in Figure 4.6.

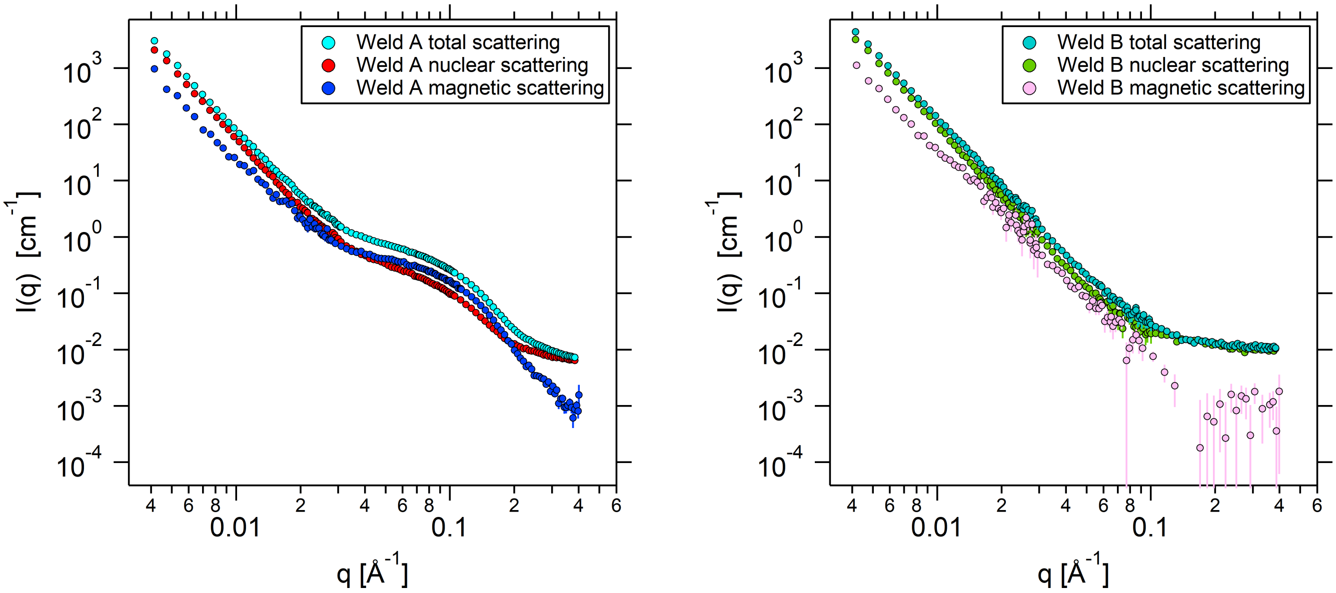

(a) Weld A scattering profiles **(b)** Weld B scattering profiles

Figure 4.6: Graphs showing the total and separated nuclear and magnetic scattering contributions for welds A and B.

4.3.3 SAXS

In order to complement the SANS studies on the long thermally aged welds, the same samples were used in a SAXS/ASAXS study for comparison of standard analysis and model fitting of SAXS profiles, and to provide additional information on precipitate composition through use of the anomalous dispersion effect at elemental absorption edges. Employing ASAXS on the samples and combining the results with previous SANS studies will help to form well-rounded conclusions on the roles of different alloying elements on irradiation damage in commercial nuclear materials.

The real and imaginary contributions to the atomic scattering factor, f' and f", from equation 2.33 have been calculated for the Fe, Cu, Mn and Ni edges. They are presented in Figure 4.7.

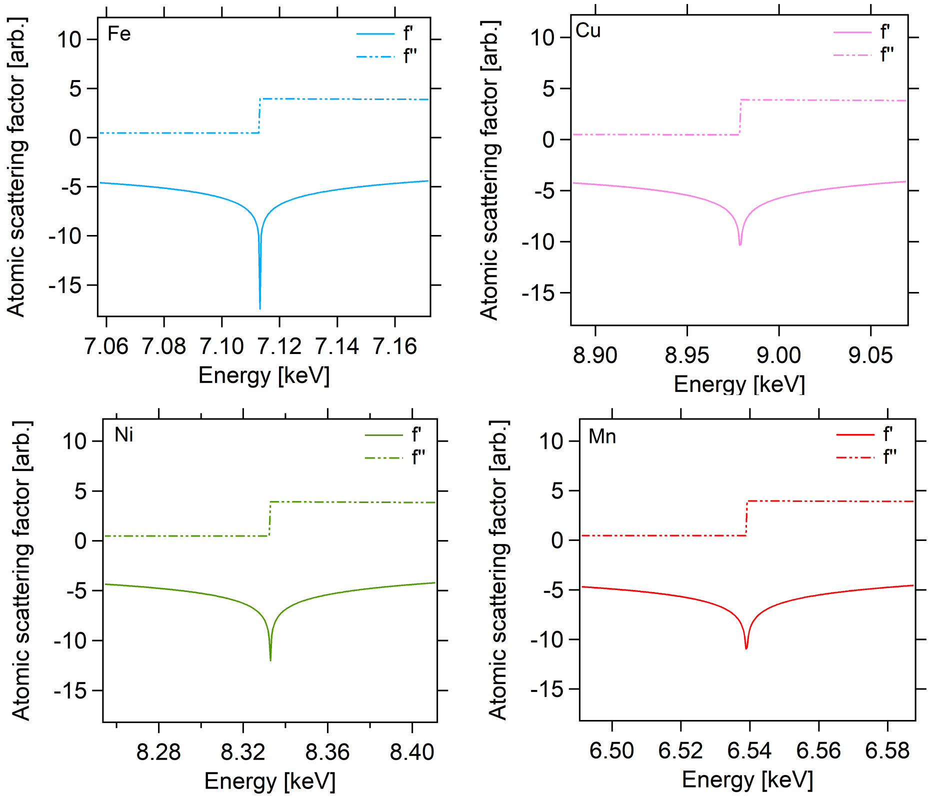

Figure 4.7: The real and imaginary contributions to the atomic scattering factor for the elemental absorption edges in Fe, Cu, Ni and Mn.

This novel technique has the ability to confirm the stoichiometry of thermal ageing induced precipitates in RPV steels, through consideration of the contrast versus energy profiles at each elemental absorption edge. Scanning the incident x-ray energy through elemental absorption edges allows for separation of the resonant contribution to the total small-angle scattering from the respective atoms and so determines the relative numbers of each element contributing to the SAXS profile.

It should be noted that for standard small-angle scattering, whilst x-rays can be complementary to neutron studies on metallurgical samples, neutrons are the preferred technique due to their ability to study bulk samples, which eliminates the troubles associated with preparing thin samples. However, the ability to make use of the anomalous dispersion effect of x-rays is particularly valuable in such a study where neutrons alone cannot resolve exact precipitate compositions in complex alloy systems. More detail on the ASAXS technique is outlined in Section 2.5.1.2, and the sample preparation techniques used are described in Section 3.2.4.

4.3.3.1 Experimental measurements

Three ASAXS beamtimes were completed in total: 12BM at the Advanced Photon Source, Chicago, P23 at Deutsches Elektronen-Synchrotron, Hamburg, and SAXS/WAXS at the Australian Synchrotron, Melbourne. This was to ensure beamtime was allocated and to give additional statistics to the final dataset (since the data reduction process removes differences between instrument configuration and experimental methods allowing for data to be combined). The most consistent and robust data obtained when studying RPV steels with low scattering signals is that from the instrument with the lowest background scattering, for example, minimal air in beam. The ASAXS data used in these works was from the SAXS/WAXS beamline at the Australian Synchrotron, Melbourne [98] as, unlike the other two instruments, the entire system is under vacuum.

A white beam of photons of all energies is produced by the synchrotron. A double crystal Si(311) monochromator selects photons of a specific energy from the white beam, through Bragg reflections and certain levels of harmonics. The single-energy beam is then focussed using a series of apertures, slits and mirrors down to a final beam size of 250 x 25 μm.

The detector used was a 1 m^2 Pilatus 13 2M detector (1280 x 1790 pixels of size 172 x 172 μm). A beamstop was also used to prevent damage by the direct beam with a diode detector installed so the direct beam intensity and sample transmission and thickness can be measured. The detector itself was located within an 8 m evacuated tank with movable sample-detector distance - this allows for a variety of q-ranges to be reached without having to insert tubes of a specific length. The total q range used was $0.07 < q < 0.61$ Å^{-1} ($18.00 > d > 1.03$ nm) to allow for investigation of nanoscale sample features.

The experimental absorption edges were found by scanning through the Mn, Fe, Cu and Ni edges of standard Mn, Fe, Cu and Ni foils of a known thickness respectively, in order to calibrate the Si(311) monochromator. To begin, it was checked that there was no overlap between the required energy range and any higher order harmonics in the monochromator reflections. Then, the transmission as a function of energy through each edge was found in order to isolate the experimental absorption edge energies. The results of this can be seen in Figure 4.8. The experimental edge values were found by fitting an order parameter to the transmission versus energy curves, and are as follows:

- Mn edge = 6.535 keV
- Fe edge = 7.108 keV
- Ni edge = 8.333 keV
- Cu edge = 8.979 keV

Note that the deviation from the theoretical edge energy is 3-4 eV for the Mn and Fe edges due to the monochromator being less stable at lower energies.

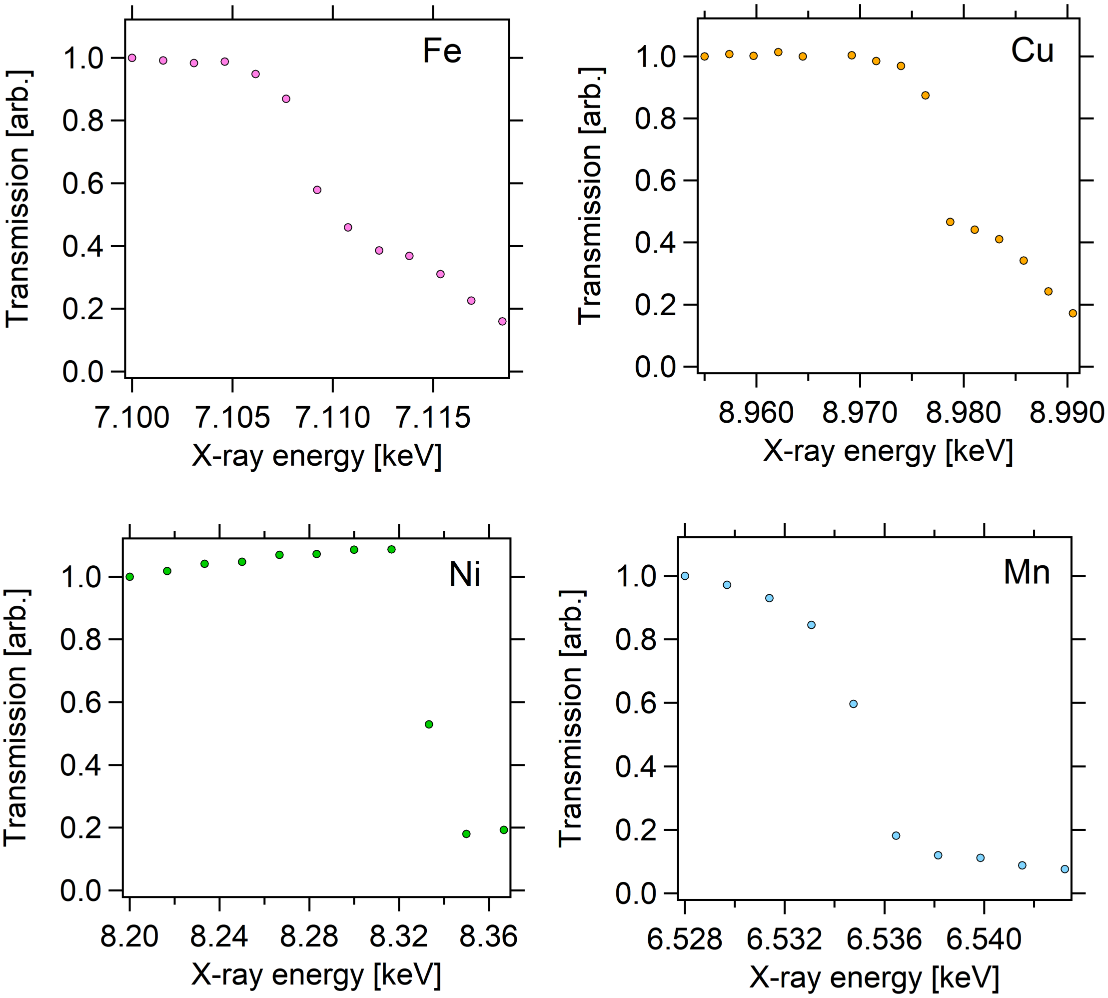

Figure 4.8: Graphs of transmission vs energy through the corresponding elemental absorption edge in Fe, Cu, Ni and Mn foils used to extract the experimental absorption edge energies.

The experimental measurements taken were as follows:

- Calibration of the q-range by scattering measurements of silver behenate with a known lattice spacing spacing.

- Map each sample position in beam and then grid scan to find optimal signal intensity (*i.e.* optimal sample thickness since this is not homogeneous due to the twin-jet polishing sample preparation process). The hole in the centre of each sample was also located, since this has a transmission of 1, and measurements were offset from this.
- Sample scattering at 9 energies through each elemental absorption edge, starting furthest away from the edge and then decreasing in interval (logarithmically) as the edge is approached. It was chosen not to scan through the edge itself since the increased contribution of fluorescence close to the edge drowns out the scattering signal. This was completed for 3 y-positions in total in each sample: 1 in the calibrated position and 1 offset above and below respectively to check if the translation of the sample holder causes displacement of the samples from their mounted positions.
- Sample scattering at an energy far from all elemental absorption edges to obtain traditional SAXS data.
- Empty beam scattering for all energies to allow for the calculation of sample transmission. The empty beam measurements ($\mathrm{I_E}$) were not taken directly after each sample measurement due to experimental time limitations, but since the synchrotron operates in top-up mode any drop in intensity of the beam due to decaying energy of electrons in the storage ring is negligible here.
- Glassy carbon scattering for all energies for calibration of intensity into absolute units.

4.3.3.2 Data reduction and analysis

Before fully reducing the data, all energies through all 4 elemental edges were radially averaged using 360° sectors to give I(q) on an arbitrary scale, as a preliminary investigation of the anomalous dispersion effects and to check that the differences between weld A and B can be observed with SAXS (far from absorption edges). The arbitrary I(q) profiles for weld A and B at 6.809 keV (non-anomalous scattering) are shown in Figure 4.9, showing a clear difference due to thermal ageing. A Porod law has been fitted to weld B to show the sole grain boundary scattering contribution in the unaged sample.

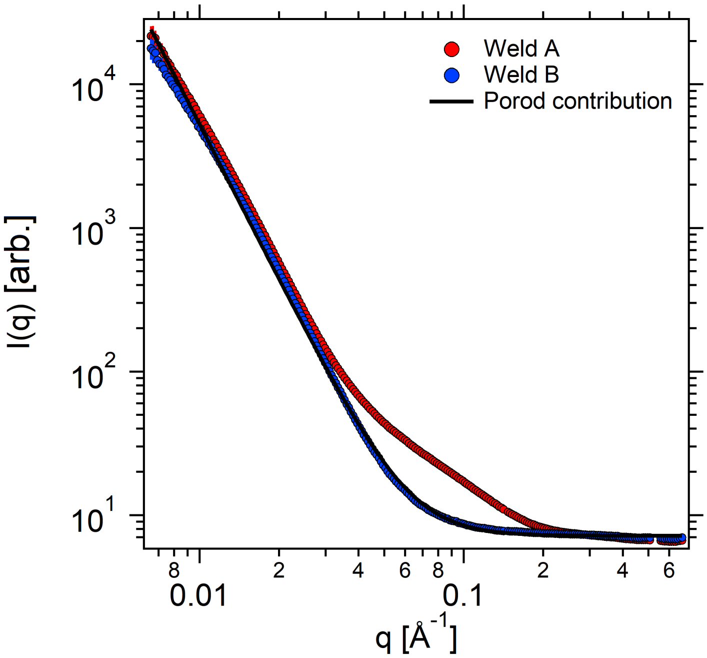

Figure 4.9: Graph showing raw I(q) profiles (arbitrary units) of weld A and weld B at E = 6.809 keV.

In order to get the measured scattered intensity on an absolute scale, corrections are made during data reduction as detailed in Section 3.4.1.2. The calibration sample used is glassy carbon (NIST Standard Reference Material 3600 [110]). The I_0 monitor detector upstream of the sample was not working during the experiment, however the diode detector on the beamstop allowed for the direct beam intensity to always be measured (I_{BS}) despite the presence of a beamstop to attenuate the beam and stop the detector from saturating, hence the sample transmissions were calculated from $\frac{I_{BS}}{I_E}$ instead of the usual $\frac{I_0}{I_E}$. The empty cell transmission could not be measured directly due to the unavailability of the I_0 detector, and is hence assumed to be 1 which is deemed reasonable given that the beam size is 250 x 25 μm so scattering from the sample holder is expected to be minimal. Using the transmissions, the sample thicknesses were corrected for using the Lambert-Beer law. The 2D detector was radially averaged over 360° to extract the 1D I(q) profiles for all energies, masking out the arm of the beamstop and any dead pixels. The data reduction was completed in the Nika software [135], and the analysis using model fitting in the NIST NCNR macros [94] in Igor Pro.

4.4 Results

4.4.1 Metallurgical and mechanical property characterisation

4.4.1.1 Microscopy

Weld B has been studied with a ZEISS Axioskop 50 optical microscope to identify the key microstructural features in an unaged low alloy steel. The sample has been prepared following the standard method outlined in Section 3.2.2. An example micrograph can be seen in Figure 4.10. The microstructure is purely ferritic, with carbides (micron-scale) precipitated out at grain boundaries; no martensite or bainite is present in this particular steel. The average unaged grain size is 9.26 ± 0.94 μm.

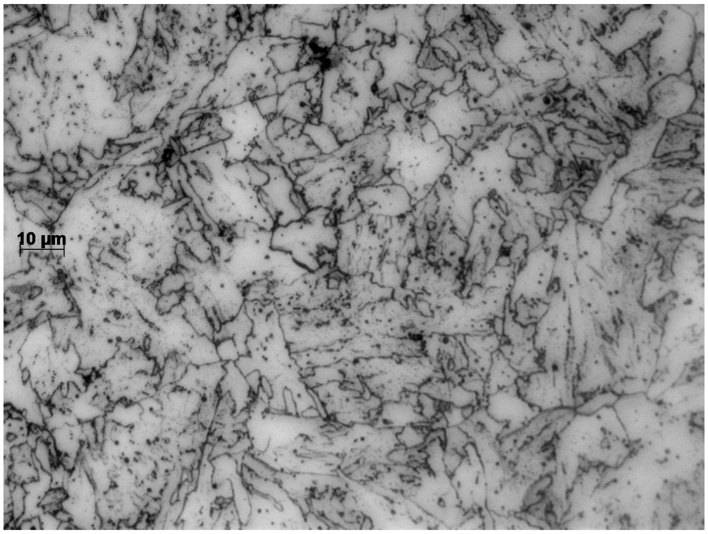

Figure 4.10: Unaged weld material (weld B) optical microscopy to highlight microstructure. Average grain size is 9.26 ± 0.94 μm.

Unfortunately due to the activity of the samples following small-angle scattering experiments, microscopy could not be completed on weld A.

4.4.1.2 Microindentation hardness testing

Vickers hardness microindentation was completed using a DuraScan G5 on both weld steels in order to quantify the effect of the thermal ageing induced precipitation on the hardness. The samples were prepared following the standard method outlined in Section 3.2.1.

The results were found using a 0.1 kgf load and have been averaged from a 8 x 8 grid of indents, giving $H_B = 211.2 \pm 2.0$ Hv and $H_A = 291.2 \pm 2.4$ Hv for weld B and A respectively. This corresponds to an increase in hardness of $\Delta H = 80.0 \pm 4.4$ Hv which has been directly induced by the thermal ageing process. The significance of this hardness increase is discussed in depth in Section 4.5.3.

4.4.2 SANS

4.4.2.1 Standard model-independent analysis

Before modelling complex information in the SANS data, such as contrast, magnetic nature, and the shape and size distribution of precipitates, one should complete some standard analysis in the form of Porod and Guinier plots [77], as discussed in depth in Section 3.4.2.1.

Through fitting of a power law model to the weld A data, one finds the exponents to be 4.170 ± 0.004 and 3.950 ± 0.013 for the nuclear and magnetic scattering respectively. This indicates that the neutron scattering intensity arises from flat 3D interfaces (*e.g.* grain boundaries or larger scale carbides), as expected in polycrystalline metallurgical alloys with a 3D grain structure. This Porod scattering contribution can be directly subtracted from the total scattering to give precipitate-only scattering in weld A, as detailed in Figure 4.11. For weld B, the scattering is purely Porod, with exponents of 4.083 ± 0.004 and 3.954 ± 0.013 for the nuclear and magnetic scattering respectively.

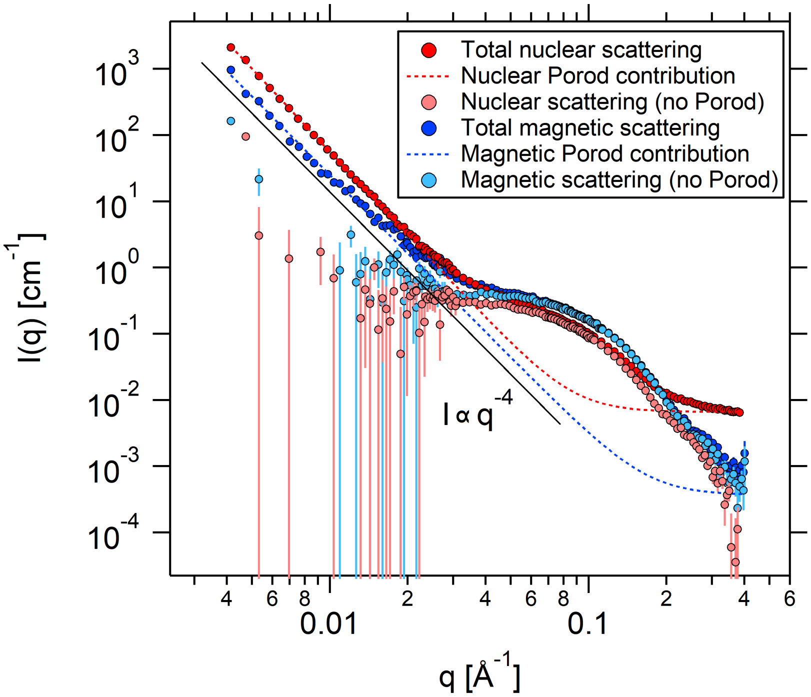

Figure 4.11: Graph showing I(q) nuclear and magnetic total, Porod, and Porod subtracted scattering in weld A. I $\propto$ q^{-4} line is overlaid in black as a guide for scattering from flat 3D interfaces.

The Guinier plot of lnI vs q^2 is valid in the range qR$_q$ $< \sqrt{3}$. It can detail information on the largest scatterers in the system, in the form of the Guinier radius, R$_g$. For both welds, the magnetic and nuclear Guinier radii are R$_{g,M}$ $= 92.59 \pm 2.12$ Å and R$_{g,N}$ $= 87.20 \pm 3.04$ Å respectively. This is consistent with larger scale scatterers in the system, such as micron-sized carbides as observed during microscopy.

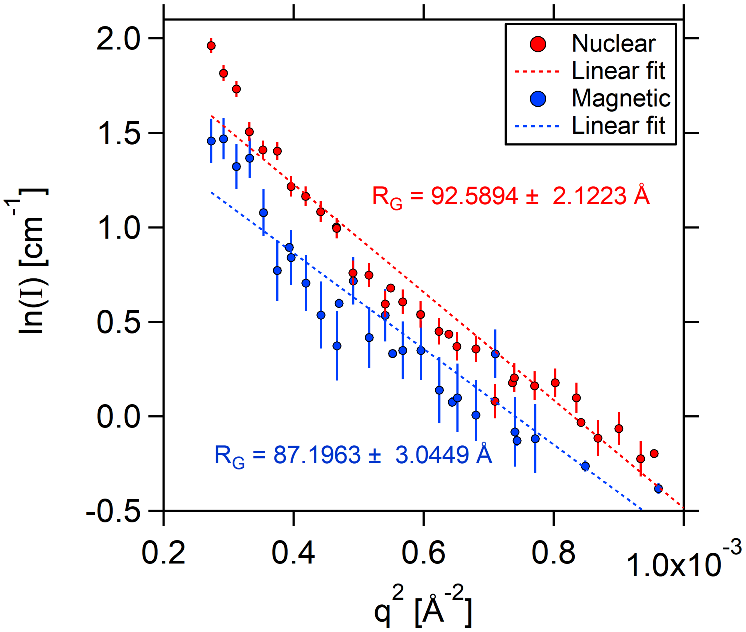

Figure 4.12: Guinier plot lnI vs q^2 for nuclear and magnetic total scattering in weld A. Fitted (dotted) lines and R_g values are included. $R_{g,M} = 92.59 \pm 2.12$ Å and $R_{g,N} = 87.20 \pm 3.04$ Å.

4.4.2.2 Empirical model fitting

Empirically fitting models to the data can extract information on the shape, size, distribution, magnetic nature, composition, and volume fraction of said objects within the matrix. The empirical model fitting of I(q) for weld A and weld B was completed using the NIST NCNR analysis macros in Igor Pro [94].

At low q values, *i.e.* larger length scales, there is a significant contribution to the intensity profile. Owing to their polycrystalline structure, this is Porod scattering, as confirmed by the Porod plot in Figure 4.11. Porod scattering is intensity arising from grain boundaries, which has a power law dependence [75], described by equation 3.13.

At larger q values, it is clear that there is some difference in scattering between the two materials. Under the fair assumption that these are Cu-rich precipitates (as postulated by APT), one can begin with the log-normal sphere model of absolute intensity [31]. The log-normal sphere form factor is derived in Section 3.4.2.2.

Using the knowledge of the system, a sum model can be fit to the data set which combines Porod and log-normal sphere scattering contributions, as seen in Figure 4.13.

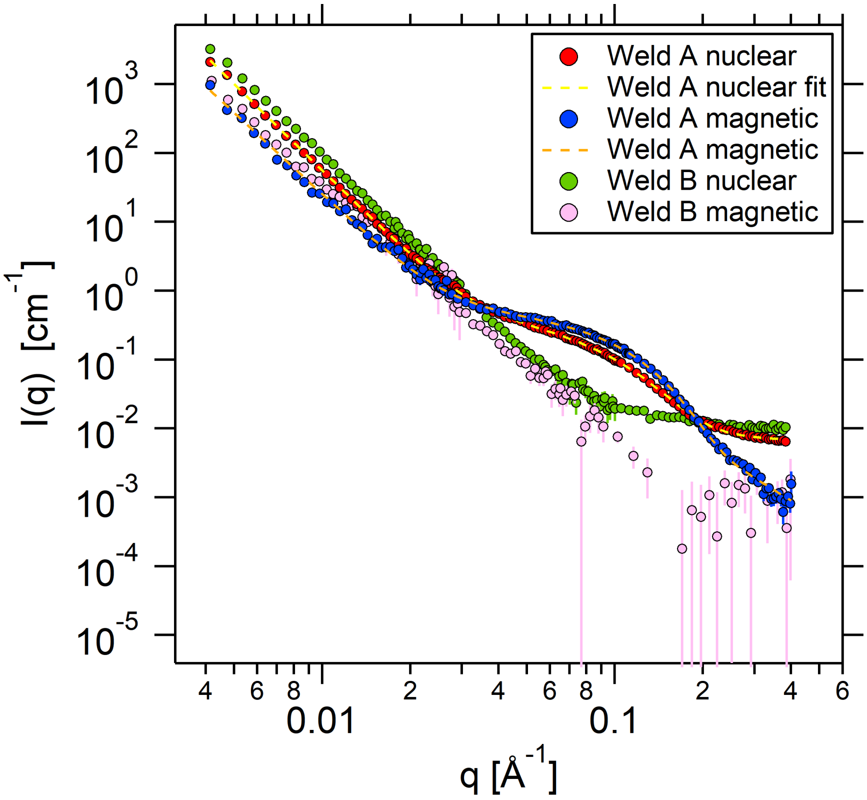

Figure 4.13: Graph showing I(q) nuclear and magnetic scattering in weld A with fitted Porod + log-normal sphere sum models.

In addition, one can subtract the profiles of weld B from weld A to show purely thermally-aged induced microstructural changes. This stark difference is shown in Figure 4.14.

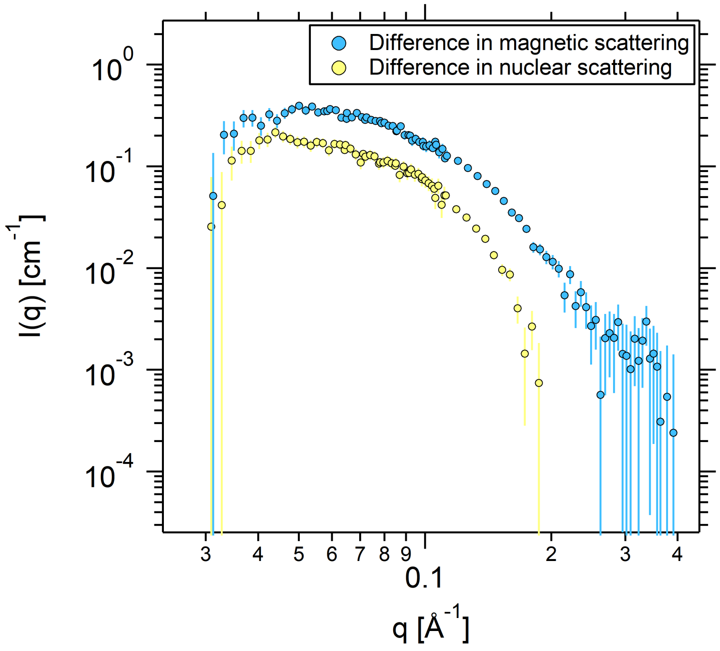

Figure 4.14: Graph showing subtracted weld data.

The log-normal sphere distribution is only present in weld A, since weld B shows no sign of precipitation, hence one can subtract the Porod law from weld A to obtain precipitate-only scattering. The results of this are shown in Figure 4.15.

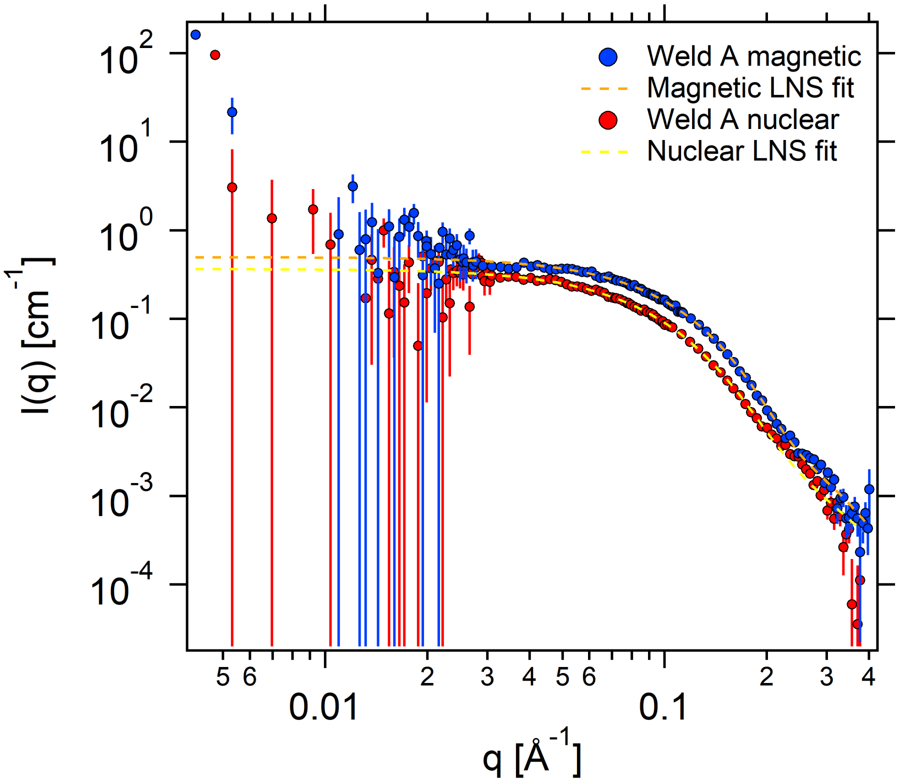

Figure 4.15: Graph showing I(q) nuclear and magnetic scattering in weld A with Porod subtraction.

The results of the fitted log-normal sphere distribution parameters for precipitate-only scattering are shown in Table 4.5.

Table 4.5: Fitted parameters from the log-normal sphere model fitting to Porod-subtracted data. The brackets denote the errors on each value.

Parameter [units]	**Nuclear (error)**	**Magnetic (error)**
Volume fraction [arb.]	0.010 (0)	0.010 (0)
Median radius [Å]	15.905 (0.069)	15.905 (0.0689)
Polydispersity [arb.]	0.285 (0.002)	0.250 (0.002)
$\rho_{\text{precipitate}}$ [Å^{-2}]	5.101 (0.004) x 10^{-6}	1.272 (0.005) x 10^{-6}
ρ_{matrix} [Å^{-2}]	7.791 (0) x 10^{-6}	4.842 (0) x 10^{-6}
Contrast [Å^{-2}]	2.670 (0.004) x 10^{-6}	3.570 (0.005) x 10^{-6}
Background [m^{-1}]	6.503 (3.071) x 10^{5}	7.642 (4.923) x 10^{5}

The median radii for the nuclear and magnetic precipitates have been treated as a linked parameters due to the fact the only difference between nuclear and magnetic scattering is the contrast. The volume fraction has no error since it was a held parameter. The nuclear and magnetic SLDs of the matrix have been calculated and consequently held and so these have no errors either. The holding of these parameters is necessary since the SLDs of the precipitate and matrix and volume fraction are multiplicative in equation 2.42. The mean precipitate radius is 16.486 ± 0.071 Åas calculated using equation 3.21.

The small peak at high q is not fit particularly well by the LNS model, meaning this scattering could be indicative of a core-shell precipitate structure as observed in literature [54, 66]. This is detailed in Figure 4.16.

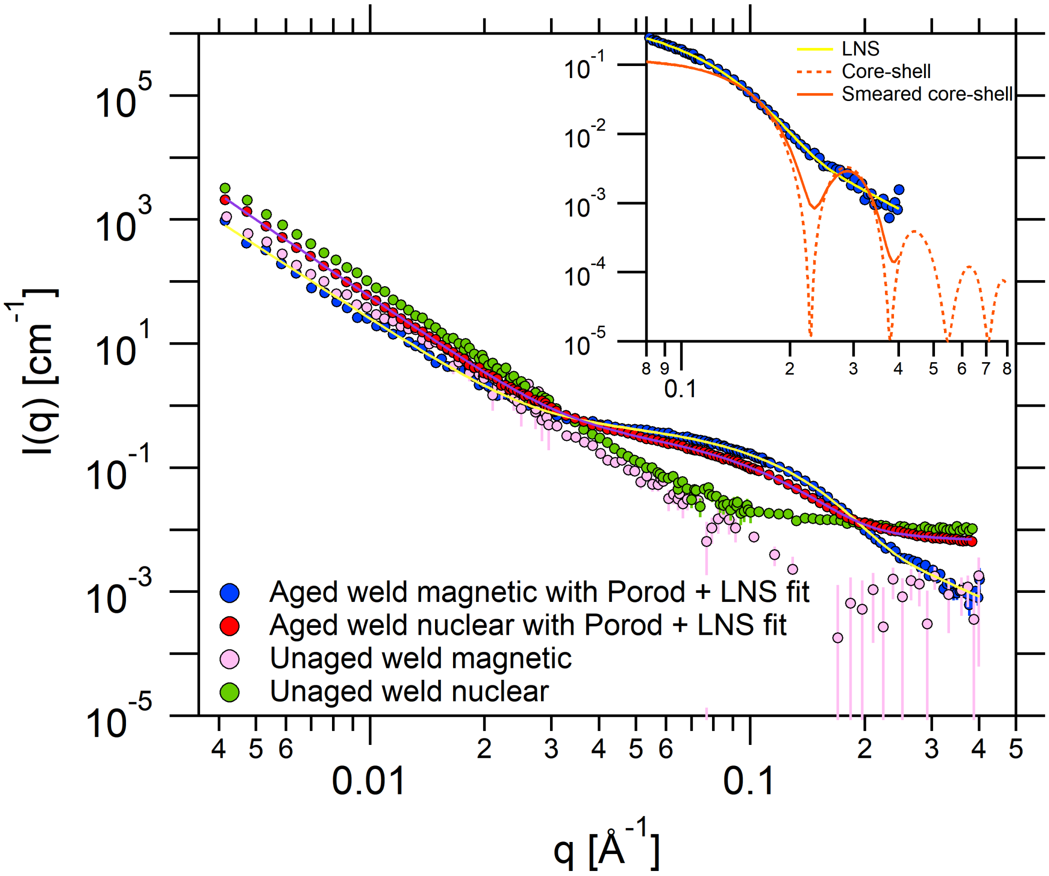

Figure 4.16: Graph showing potential extra high Q core-shell structure.

The extra high q scattering data taken on D22 to investigate the core-shell precipitate structure is shown in Figure 4.17. Unfortunately, a converging empirical model fit could not be obtained. This could be because the fractions of Mn and Ni in the potential outer shell are too low to observe significant contrast changes. It also could be attributed to the inherent noise in high q data due to incoherent background scattering contributions which prevent a form factor model from converging on the coherent scattering data. This could be mitigated by employing SAXS at high q in the future since there is no incoherent background contribution.

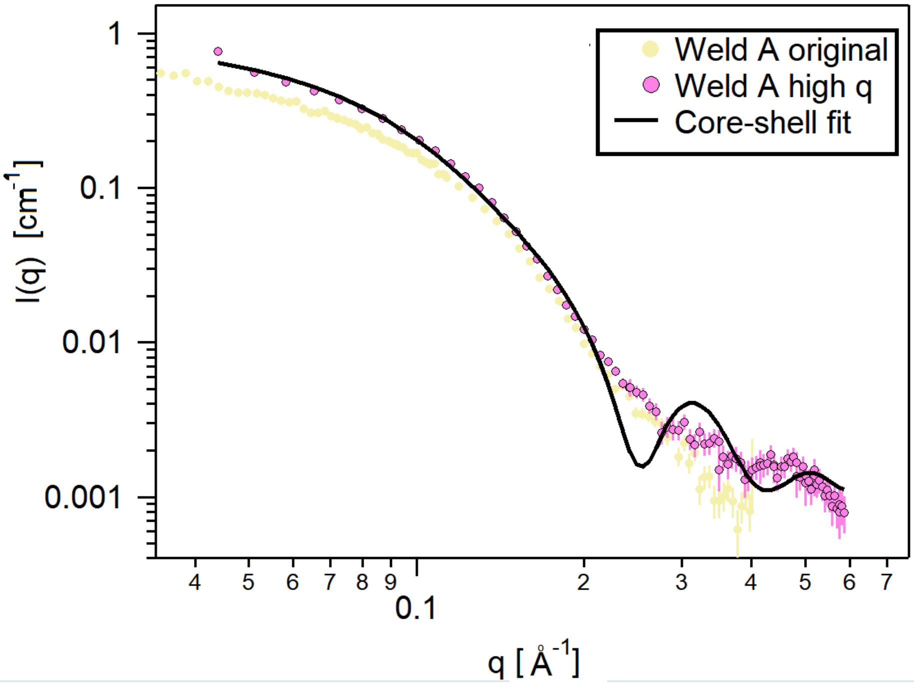

Figure 4.17: Graph showing high q nuclear and magnetic scattering profiles for weld A with an attempted core-shell form factor fit.

4.4.2.3 Maximum entropy fitting

The maximum entropy method in Irena [95] has been used to fit the I(q) profiles of weld A. The results can be seen in Figure 4.18. The mean precipitate radius is 19.826 ± 0.993 Å.

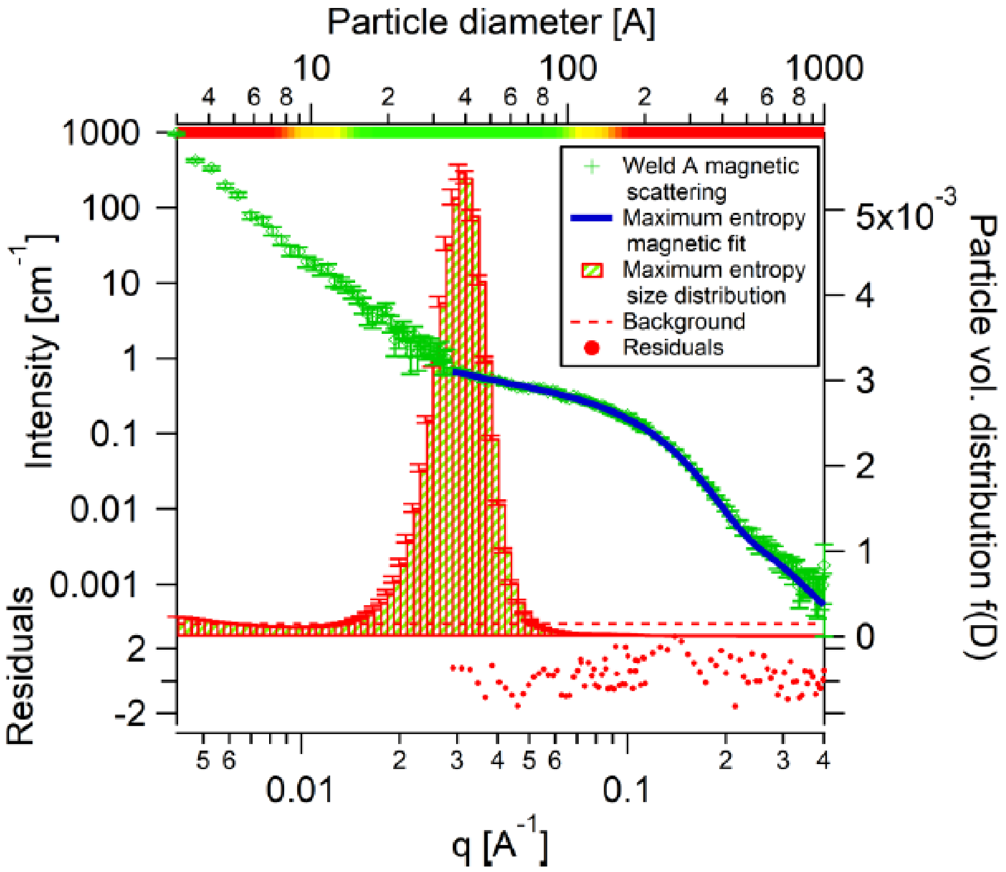

Figure 4.18: Graph showing maximum entropy I(q) fit and size distribution of magnetic scattering in weld A.

4.4.2.4 Monte Carlo fitting

Finally, Monte Carlo modelling for 100 000 iterations was completed on the I(q) data. The results converged to a χ^2 value < 5, and the nuclear and magnetic fits can be seen in Figure 4.19. The precipitate diameters from the nuclear and magnetic profiles are self consistent: $R_N = 41.26 \pm 0.27$ Å and $R_M = 39.90 \pm 2.3$ Å.

The resultant nuclear and magnetic precipitate size distributions can be seen in Figures 4.20 and 4.21 respectively.

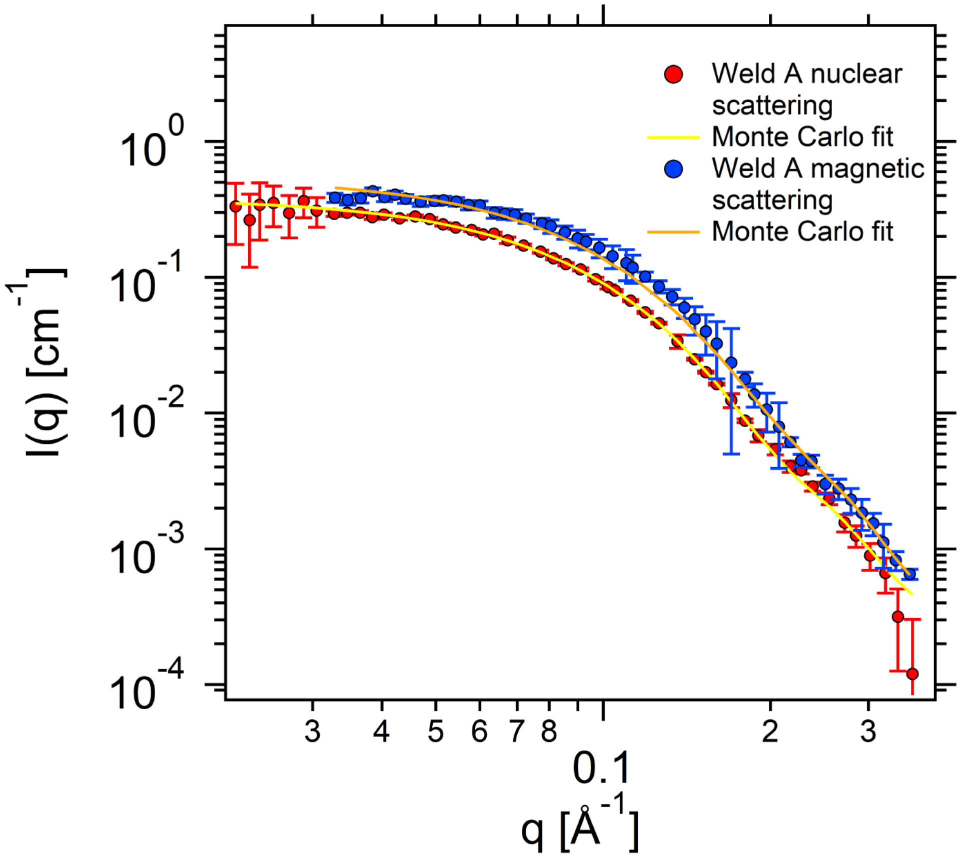

Figure 4.19: Graph showing Monte Carlo I(q) fit of nuclear and magnetic scattering in weld A.

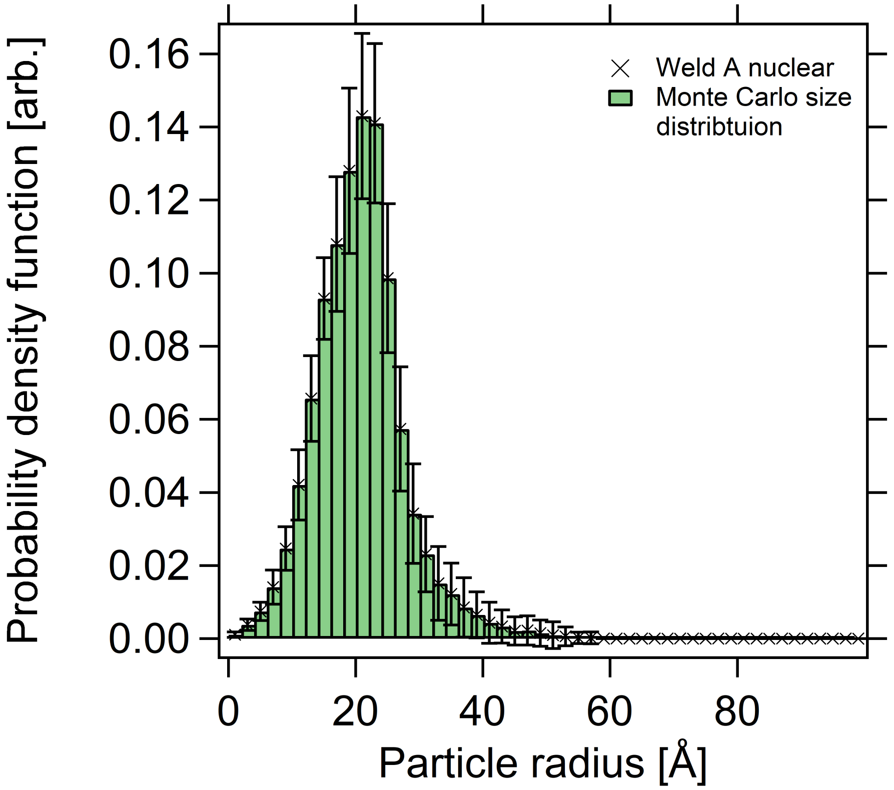

Figure 4.20: Graph showing Monte Carlo fitting and size distribution of precipitates in weld A nuclear scattering.

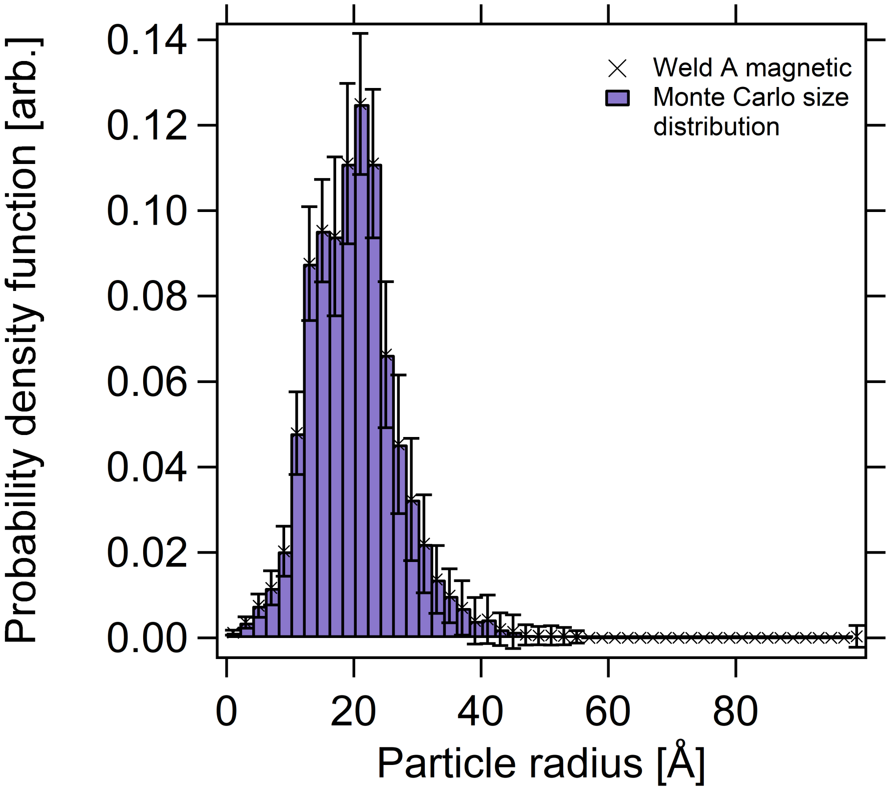

Figure 4.21: Graph showing Monte Carlo fitting and size distribution of precipitates in weld A magnetic scattering.

The implications of the Monte-Carlo and maximum entropy modelling results are discussed in Section 4.5.1.

4.4.2.5 A-ratio compositional analysis

The A ratio derived in Section 3.4.2.3 can either be calculated numerically using the fitted parameters, or more robustly from the raw data. The latter gives the A ratio as a function of scattering vector, which seems more valuable since errors from the fit are not introduced and one can see if there is a change as a function of length scale in the samples, *i.e.* if more than one type of precipitate is present. In any case, all A ratio values shall be compared with reference to the validity of the method by which they were obtained.

It should be noted that in reality, there is a correction factor that must be applied to the term $\frac{I_M}{I_N}$ to give the true A ratio of the precipitates. This factor arises from the calculation of scattering profiles by radially averaging over sectors in GRASP. When choosing the sector configuration, a 35° (0.6 radian) sector leaves out some magnetic signal compared to the use of a 90° ($\frac{\pi}{2}$ radian) sector. The correction factor is given by the ratio of the magnetic scattering integrated over the sector widths:

$$Y = \frac{\int_{-0.3}^{0.3} \cos x^2 dx}{\int_{-\pi/2}^{\pi/2} \cos x^2 dx}$$

Consider the identity

$$\int \cos x^2 dx = \int \frac{1}{2}(1 + \cos 2x) dx$$

$$= \frac{1}{2}\left(x + \frac{1}{2}\sin 2x\right) + C$$

Hence

$$Y = \frac{\left[\frac{1}{2}\left(x + \frac{1}{2}\sin 2x\right)\right]_{-0.3}^{0.3}}{\left[\frac{1}{2}\left(x + \frac{1}{2}\sin 2x\right)\right]_{-\pi/2}^{\pi/2}}$$

$$= \frac{0.582}{\pi/2}$$

$$\therefore Y = 0.37$$

The results for welds A and B can be seen in Figure 4.22.

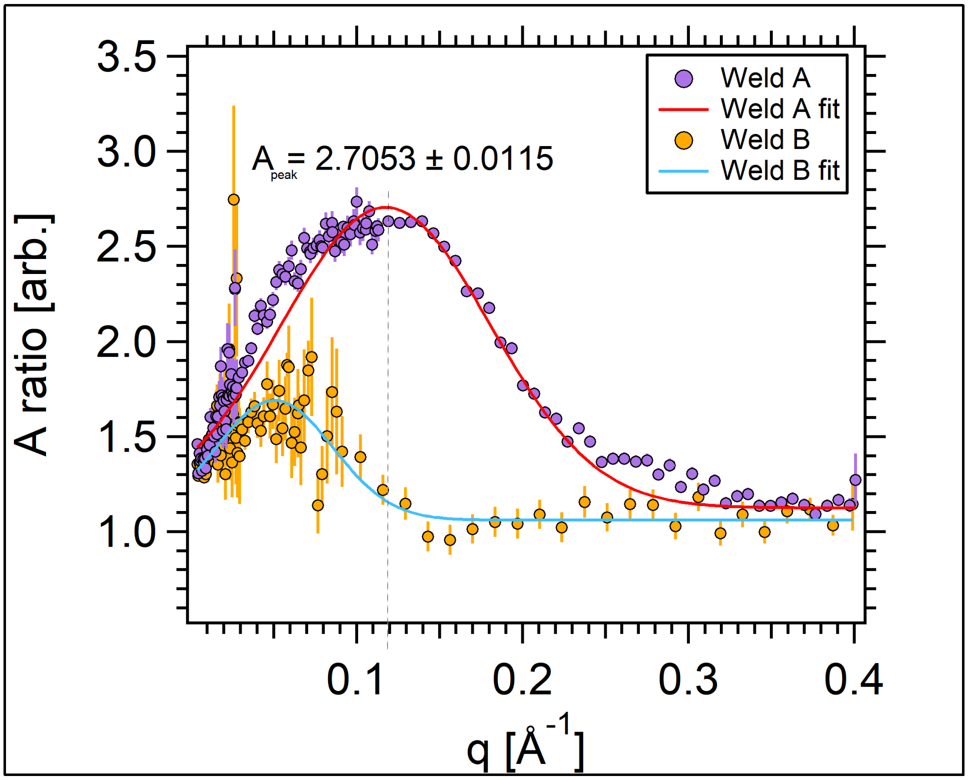

Figure 4.22: Graph showing the raw data calculated A ratio as a function of q, fitted with a Gaussian distribution. The peak at q = 0.11 Å^{-1}corresponds to the length scale of the peak in I(q).

The A ratio vs q from the SANS data shows a clear weld A peak at q = 0.11 Å^{-1}, which corresponds to position of the peak in I(q). From fitting a Gaussian distribution to A ratio(q), a peak value of A ratio = 2.705 ± 0.012 was found. The peak at low q for weld B arises from carbides at larger length scales. This corresponds to micron scale carbide features (radius approximately 9 μm) that have been observed with microscopy.

In the weld A data in Figure 4.22, there is a deviation from the Gaussian fit at q = 0.295 Å^{-1} which could be an extra A ratio peak. This could be indicative of core-shell structure *i.e.* a high A ratio in the core (Cu-rich since Cu has the largest scattering contrast in Fe) and a low A ratio in the shell (Mn-rich since Mn has a negative scattering length which reduces the contrast). This is postulated since the a core shell structure has been observed for similar sample compositions in literature [136], and by a previous APT study on these samples [54]. From fitting a double Gaussian distribution, peak 1 A ratio = 2.697 ± 0.049 (within error bounds of the single peak fit) and peak 2 A ratio = 1.257 ± 0.060.

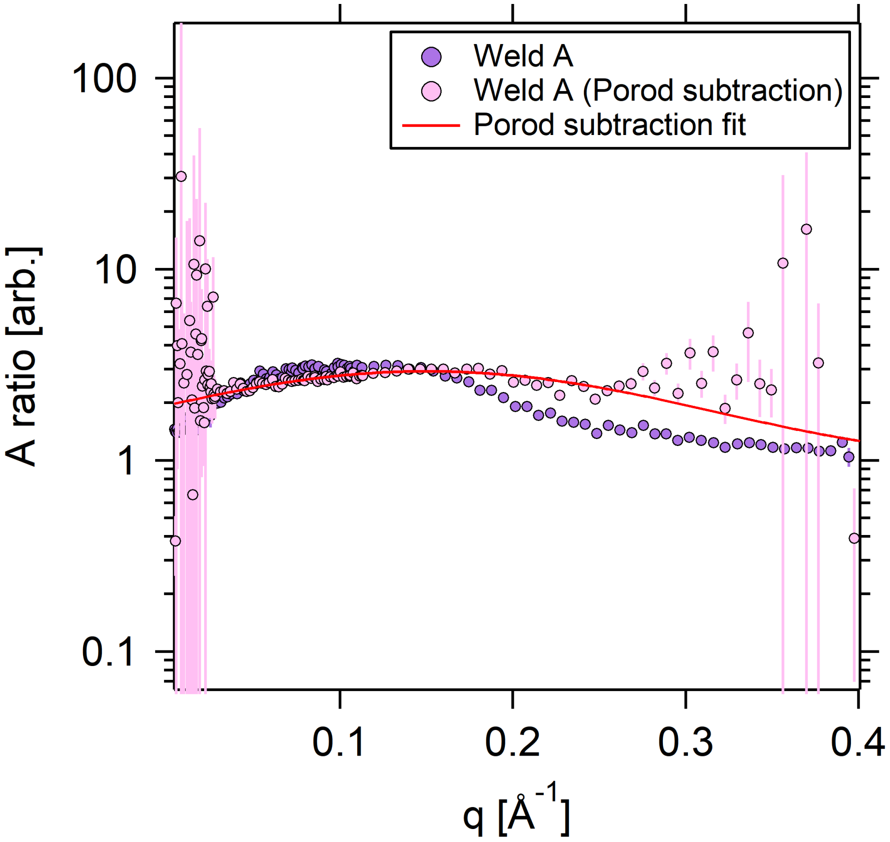

Figure 4.23: Graph showing the Porod-subtracted calculated A ratio as a function of q (pink), fitted with a Gaussian distribution (red). The raw calculated A ratio (purple) is shown for comparison.

To investigate the true nature of this potential second peak, the Porod scattering contribution from grain boundaries fitted during SANS was subtracted from the data to leave precipitate-only scattering. The A ratio(q) was recalculated, as shown in Figure 4.23. Upon doing this, the peak at q = 0.11 Å^{-1} is now much more subtle, but fitting a single peak gives A ratio = 2.921 ± 0.010. Attempting to fit the second high q peak gives very large errors which are unphysical, meaning it is most likely just noise in the data. This implies that the small A ratio peak at high q postulated in Figure 4.22 may just be an artefact arising from the Porod scattering contribution. Hence, the single Gaussian peak fit of A ratio(q) is the best-estimate method, and so the A ratio value = 2.705 ± 0.012.

The A ratio can also be calculated from the contrasts obtained from empirical model fitting. This gives an A ratio = 2.742 ± 0.010, which is statistically consistent with the A ratio value from the raw I(q) data. This suggests that the model fitted contrasts are reliable.

4.4.3 SAXS

4.4.3.1 Empirical model fitting

The SAXS data was analysed to validate the precipitate information obtained from the SANS analysis. The I(q) profiles far from elemental absorption edges were used, to exclude anomalous dispersions.

The matrix contrast, $\Delta\eta$, was calculated using the previously calculated x-ray scattering lengths (Table 2.2). The x-ray scattering length density of a phase in a material, η, is a function of the number densities and bound coherent x-ray scattering lengths of each specific element present, as per equation 2.32 in Section 2.5.1.1.

Hence, for the bulk matrix in weld A (composition given in Table 4.1), the x-ray scattering length density is 6.2635 x 10^{-5} Å^{-2}. Since this is a known value, it can be held constant in the empirical model fitting.

A mean precipitate radius in weld A was found to be 19.57 ± 0.26 Å, which is consistent with the radius obtained through maximum entropy and Monte Carlo fitting of SANS data.

4.4.3.2 Anomalous SAXS analysis

Before any full analysis is completed, the raw unreduced I(q) profiles for the Fe, Mn, Ni and Cu edges were plotted to make an initial comparison and aid the route of analysis going forward. The unreduced scattered intensity of weld A obtained by scanning through the edges can be seen in Figures 4.24, 4.25, 4.26 and 4.27.

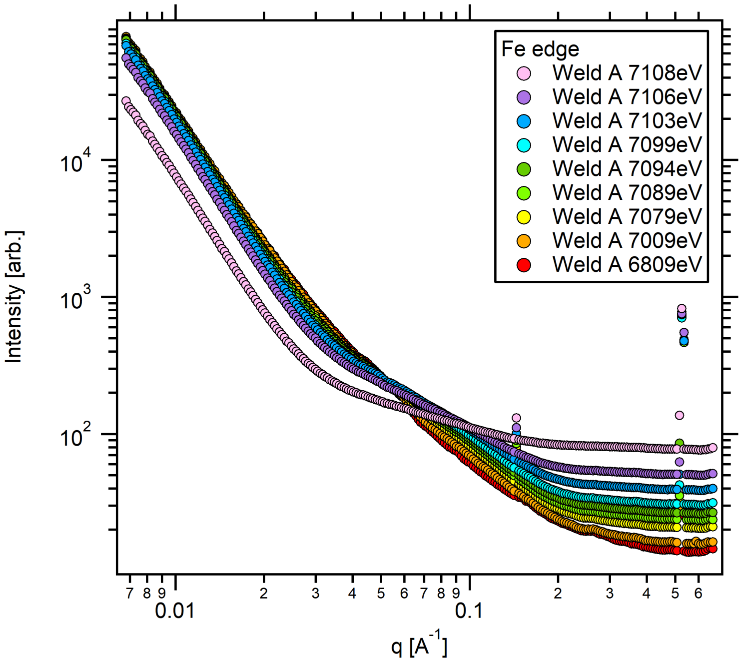

Figure 4.24: Graph showing unreduced ASAXS I(q) [arbitrary units] profiles of weld A at Fe edge.

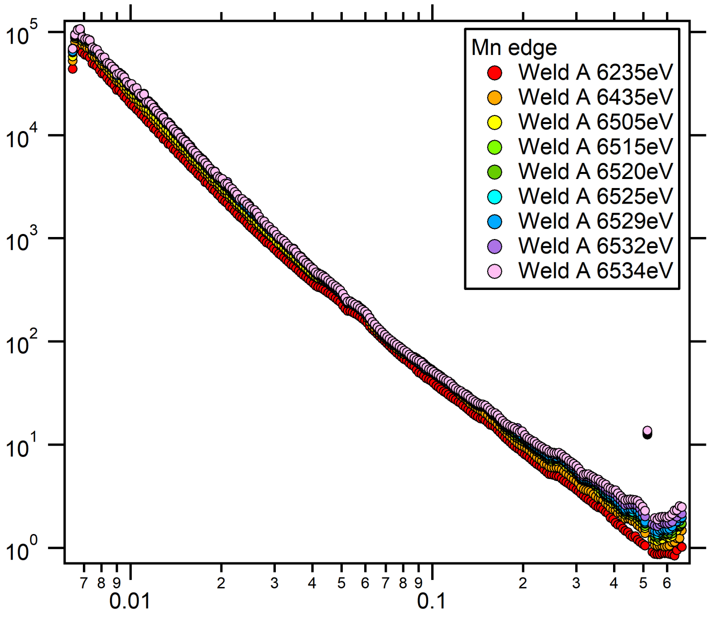

Figure 4.25: Graph showing unreduced ASAXS I(q) [arbitrary units] profiles of weld A at Mn edge.

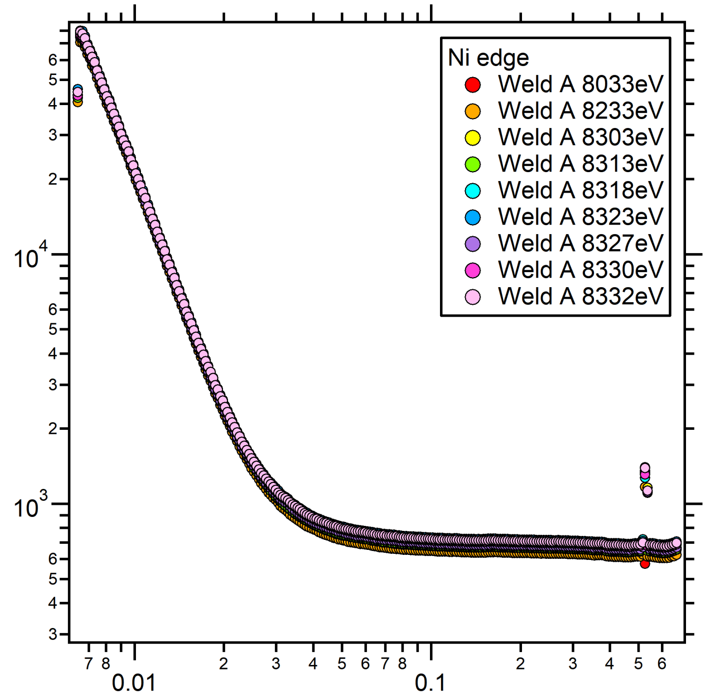

Figure 4.26: Graph showing unreduced ASAXS I(q) [arbitrary units] profiles of weld A at Ni edge.

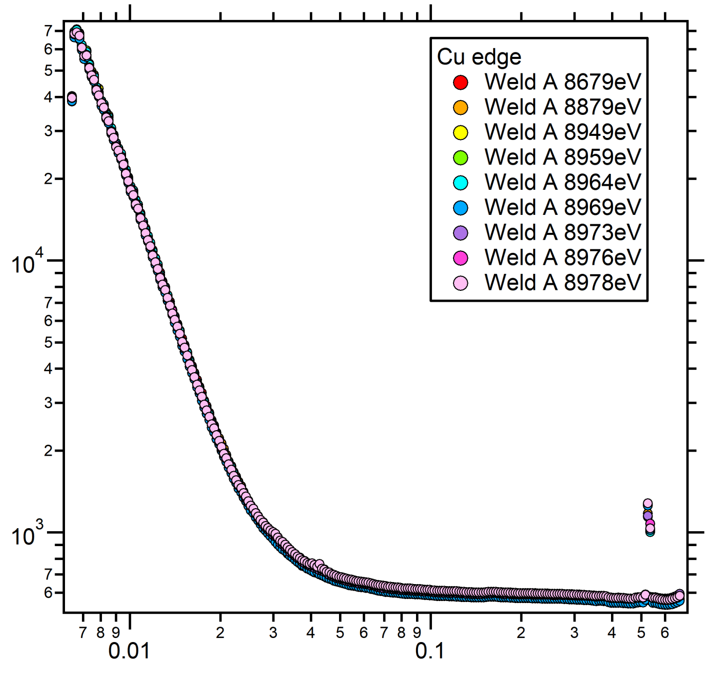

Figure 4.27: Graph showing unreduced ASAXS I(q) [arbitrary units] profiles of weld A at Cu edge.

Due to the known fluorescence phenomena, the fluorescence contribution from the large fraction of Fe atoms in the sample (>95%) increases as incident x-ray energy approaches the Fe edge. This causes the incoherent background at the Fe edge to increase.

The contrast at the Mn, Ni and Cu edges, and hence scattered intensity, is low due to the relative amounts of each element in the matrix. This means that any differences noticed as one scans through each absorption edge are minimal. Also, due to the increasing fluorescence background from Fe atoms that dominates the high q scattering signal, any potential changes with energy are drowned out. Arguably, the most important element fraction to confirm is Fe, so this will form the basis of the ASAXS analysis going forward.

Due to the nature of the ASAXS sample preparation, the sample thickness is not known directly. For the welds, the thickness has been measured experimentally from the transmission: weld A = 25.518 ± 0.900 μm. The reduced Fe edge data can be seen in Figure 4.28.

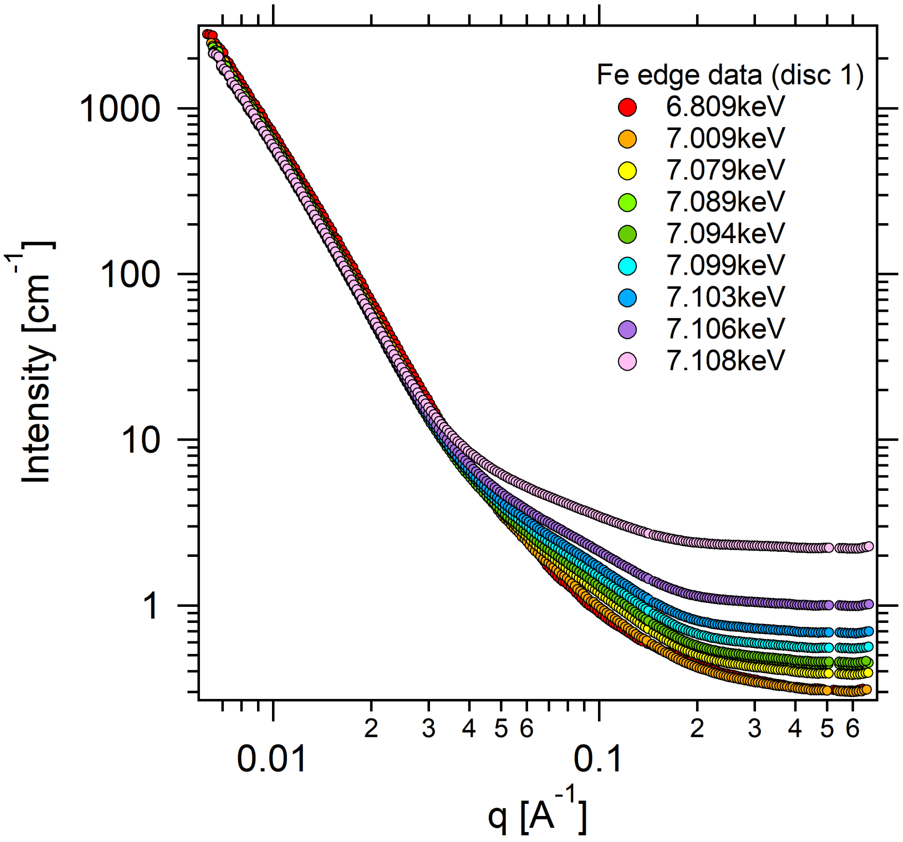

Figure 4.28: Graph showing ASAXS I(q) profiles of weld A at Fe edge.

From the SANS analysis, a combined Porod+LNS model was the best estimate for the precipitates, hence this was also tested in the ASAXS analysis. The contrast in SAXS arises from differences in the electron densities, compared to the contrast from scattering length densities in SANS. The matrix electron density was calculated and held constant in the fit alongside the volume fraction, in order to explicitly obtain the precipitate electron density. This then can be used to calculate absolute volume fraction from the scattering invariant.

In theory, fitted median radius and polydispersity should be the same for the SANS and SAXS data, and so these were held as 15.9045 and 0.2853 respectively. The only thing that will obviously be different is the contrast term; the contrast should change as a function of energy due to the anomalous dispersion of Fe.

The numerically integrated contrast values for each energy can be seen in Figure 4.29. The contrast can be seen to decrease as one approaches the Fe absorption edge. Through fitting of equation 2.35 derived in Section 2.5.1.2 to the $\Delta\eta(E)$ profile through the Stuhrmann method [87], one can extract the Fe content of the precipitate to be $X_{Fe} = 3$ at%.

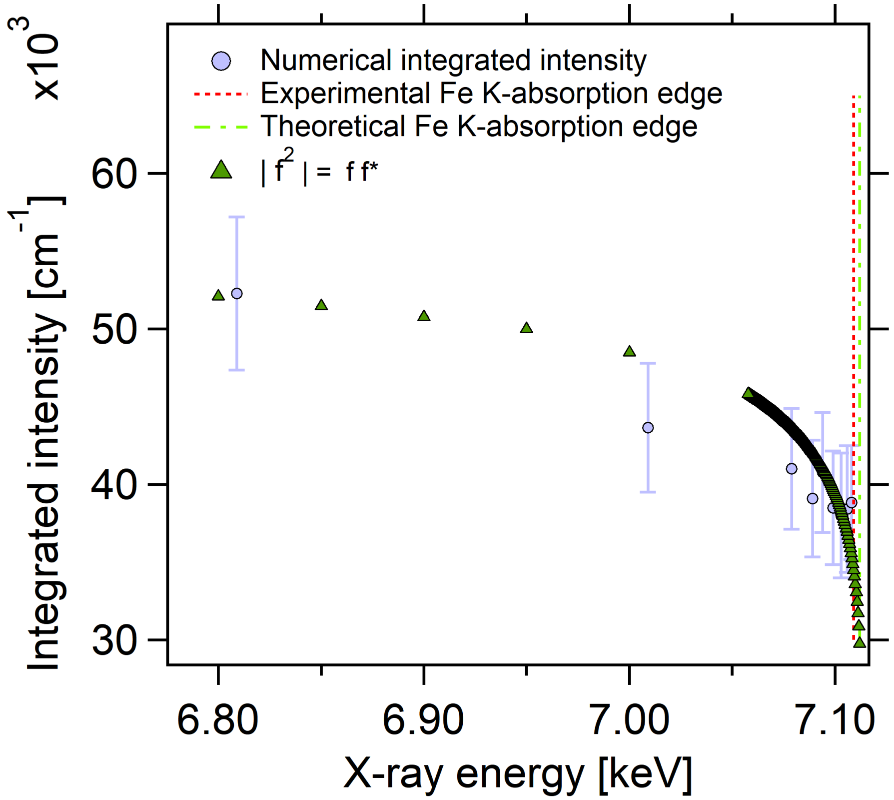

Figure 4.29: Graph showing ASAXS fitted contrast of weld A as a function of x-ray energy at the Fe edge (calculated through numerical integration of the I(q) scattering profiles). The green triangles represent the atomic scattering amplitude.

4.5 Discussion

4.5.1 Shape and size distributions

The precipitates in weld A have been found to be system of polydisperse spheres with a log-normal size distribution. This has been confirmed by maximum entropy and Monte Carlo analysis techniques to ensure no assumptions were projected onto the nuclear and magnetic data sets.

In addition, an increase in the number density and size of precipitates was observed that were not present in the unaged weld material, as documented in other high Ni weld studies [21, 62, 60].

The mean precipitate radii for each analysis method can be seen in Table 4.6. The maximum entropy and Monte Carlo radii are consistent with one another, but the model fitting seems to have underestimated the radius. This is attributed to the deviation of the data from the LNS model at very high q, owing to the potential core-shell structure that could not be confidently resolved in the analysis. Hence, the consistent radii that have overlapping error bounds are the most robust.

Table 4.6: Weld A precipitate radii found using model fitting, maximum entropy method, and Monte Carlo modelling.

Analysis technique	**Mean radius [Å]**	**Error [Å]**
LNS model fitting	16.486	0.071
Maximum entropy method	19.826	0.993
Monte Carlo modelling	20.290	0.185

The nanoscale precipitates induced by thermal ageing at 330 °C for 100 000 hours are spheres with a mean radius of 20.058 ± 0.589 Å and a log-normal size distribution with a polydispersity of 0.267 ± 0.002.

This is fully consistent with the structural information noted by the APT investigation [54].

The presence of a core-shell structure has not been confirmed robustly through the SANS, however due to the reduction in interfacial energy from the congregation of Mn, Ni and Si around the Cu-rich core [127, 56, 67], it cannot be excluded as a likely outcome.

4.5.2 Precipitate composition

Table 4.7 summarises the A ratio values found using fitted contrast parameters and A ratio (q) peak fittings. All results are consistent with one another.

Table 4.7: Summary of A ratio values for precipitates obtained through different methods

Method	A ratio [arb.]	Error [arb.]
Using $\Delta\rho_{N/M}$ from fitting in equation 2.23	2.725	0.001
A ratio (q) peak fitting (single)	2.705	0.012
A ratio (q) peak fitting (double, peak 1)	2.697	0.049
A ratio (q) peak fitting (double, peak 2)	1.257	0.060
Using Fe containing fractions from [54]	4.206	0.010
Using non-Fe containing fractions from [54]	3.978	0.010

The A ratio values from the single and double fitting of the low-q peak are consistent with one another. This suggests the presence of a Cu-rich precipitate. An A ratio of 1.257 suggests that the shell is rich in Mn and/or vacancies, since these are the only elements that when increased in fraction would reduce the precipitate SLD (due to being non-magnetic and the negative and zero nuclear scattering lengths respectively), and thus reduce the A ratio from 2.697. This is consistent with the existence of a Mn-rich shell around a Cu-rich core, where the clustering of Mn, Ni and Si at the precipitate interface reduce the lattice strain and the instability of Cu in Fe. The double peak fitting was discounted as a potential Porod artefact during the analysis and so the single peak fitted value was found to be the most representative A ratio, and hence a core shell precipitate structure could not be confidently confirmed.

Table 4.7 also shows the calculated A ratio values using the APT results from [54] for both non-Fe and Fe containing precipitates. However, one can instantly show that this non-Fe/non-magnetic approximation is not valid in this scenario by comparing the theoretical A ratios calculated using non-Fe precipitate fractions from [54] in equations 2.23 and 3.22 to the experimental A ratios obtained from the SANS data. Even when one treats the precipitates as Fe-containing during APT (which acts to reduce the A ratio value more than non-Fe precipitates), the A ratio calculated from the suggested APT fraction is still too high indicating an overestimation of the Fe content ($>$ 36 at%).

To further highlight this discrepancy, the theoretical A ratios for any Ni:Cu:Mn (non-Fe, non-magnetic) precipitate in a weld A matrix have been calculated by creating a model based on the A ratio equations derived in Section 3.4.2.3 (equations 3.22 to 3.25). All possible A ratio values for all possible precipitate composition ratios of Ni:Cu:Mn have been calculated using the sample matrix composition and plotted in a ternary diagram. The possible precipitate compositions corresponding to the experimentally obtained A ratio value in this work have also been calculated. These possible precipitate compositions are overlaid as blue circles on the Ni:Cu:Mn ternary diagram in Figure 4.30.

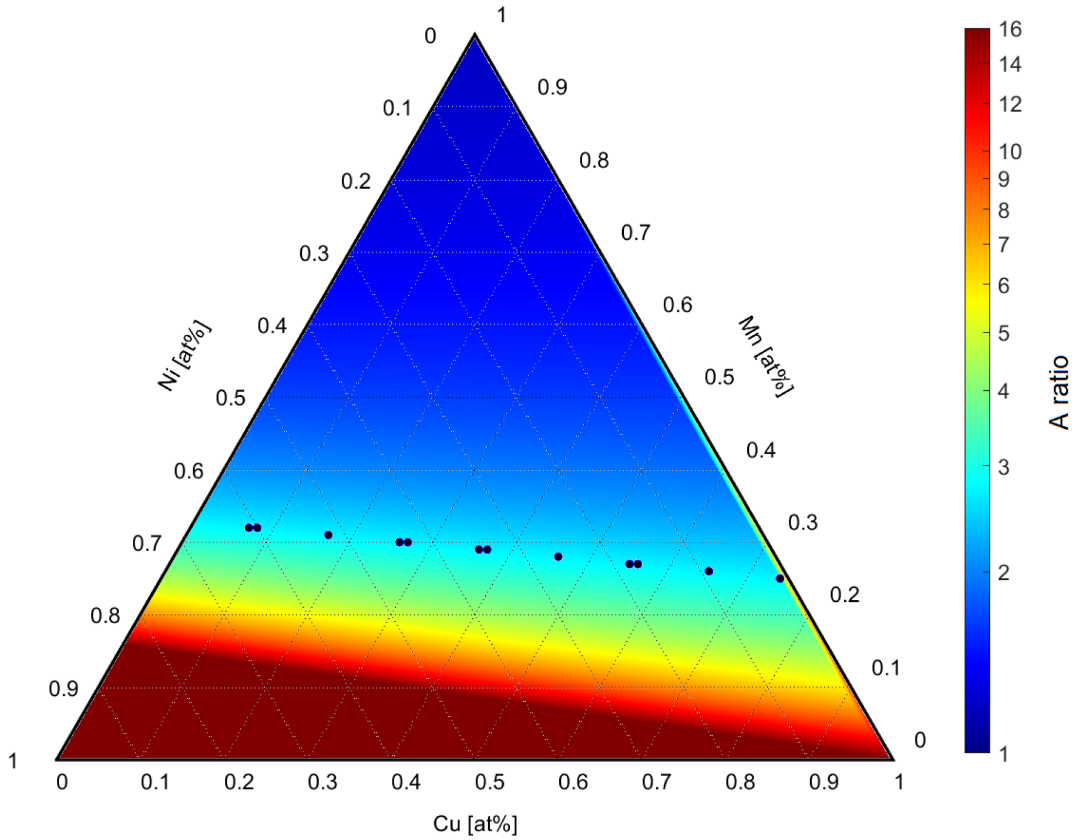

Figure 4.30: Theoretical A ratio ternary diagram for any Ni:Cu:Mn (non-magnetic, non-Fe) precipitate composition in a weld A matrix. Blue overlaid circles highlight the possible precipitate compositions corresponding to the experimental A ratio value of 2.705 ± 0.012.

The A ratio values from APT as defined in Table 4.7 are much higher than the experimental A ratio obtained through SANS. There is no overlap between APT and SANS compositions which directly shows the need for a more complex treatment of the precipitates. Hence, one must consider the presence of Fe and vacancies within the precipitate, and also the role of magnetism.

Using equations 3.22 to 3.25, a model was constructed to calculate the A ratio for all possible vacancy and Fe compositions of the magnetic precipitates. To create the model, the nuclear and magnetic scattering length densities of Cu, Mn, Ni, Fe and Si were calculated for an arbitrary sample volume of

10 000 Å^3. The Cu:Mn:Ni:Si ratios were calculated from the APT results and held constant, and the theoretical A ratio values were computed for all possible Fe and vacancy compositions.

From these theoretical A ratio values, the Fe and vacancy compositions that correspond to an A ratio equivalent to the experimental SANS value experimental A ratio were identified, using the lower bound of errors on calculated A ratio values for conservatism. The results can be seen in Figure 4.31. The black triangles indicate the Fe and vacancy compositions that give an A ratio consistent with the experimental value of 2.705.

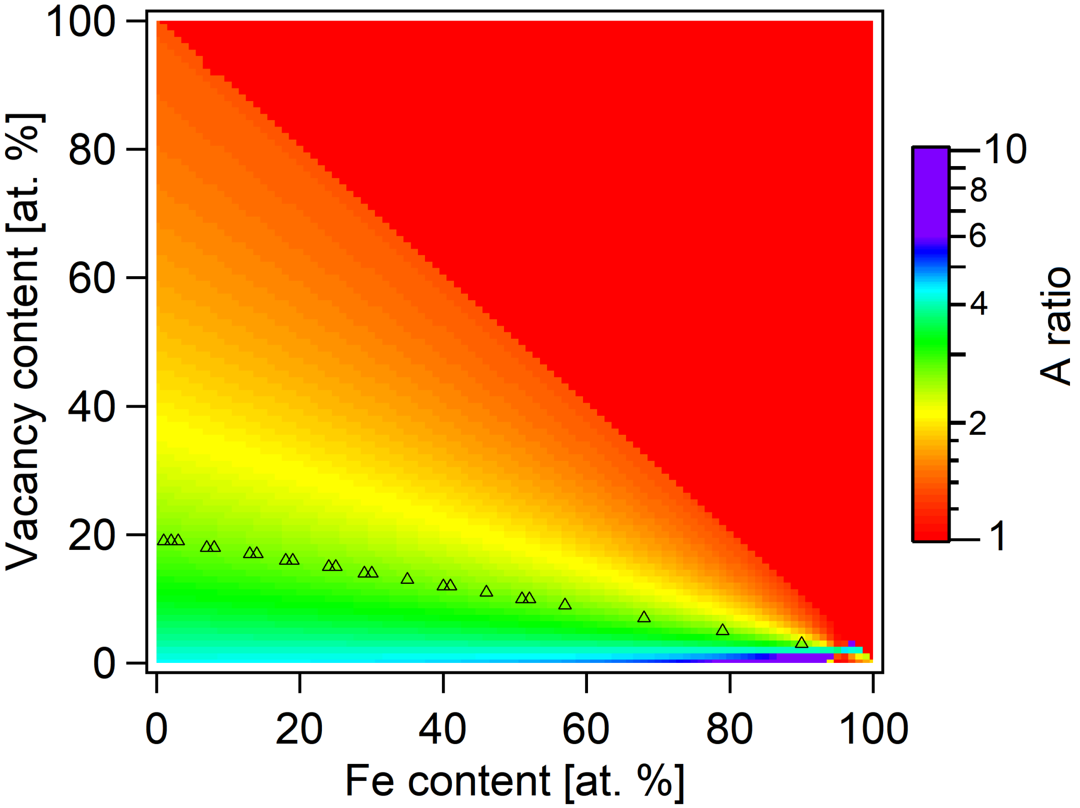

Figure 4.31: Theoretical A ratios for any Fe and vacancy content in a given Cu:Mn:Ni:Si precipitate composition in a weld A matrix. Black triangles overlaid highlight compositions corresponding to experimental A ratio value of 2.705 ± 0.012.

Using the 23 possible Fe and vacancy compositions, the overall precipitate compositions that correspond to the experimental A ratio have been calculated. These are shown in Figure 4.32.

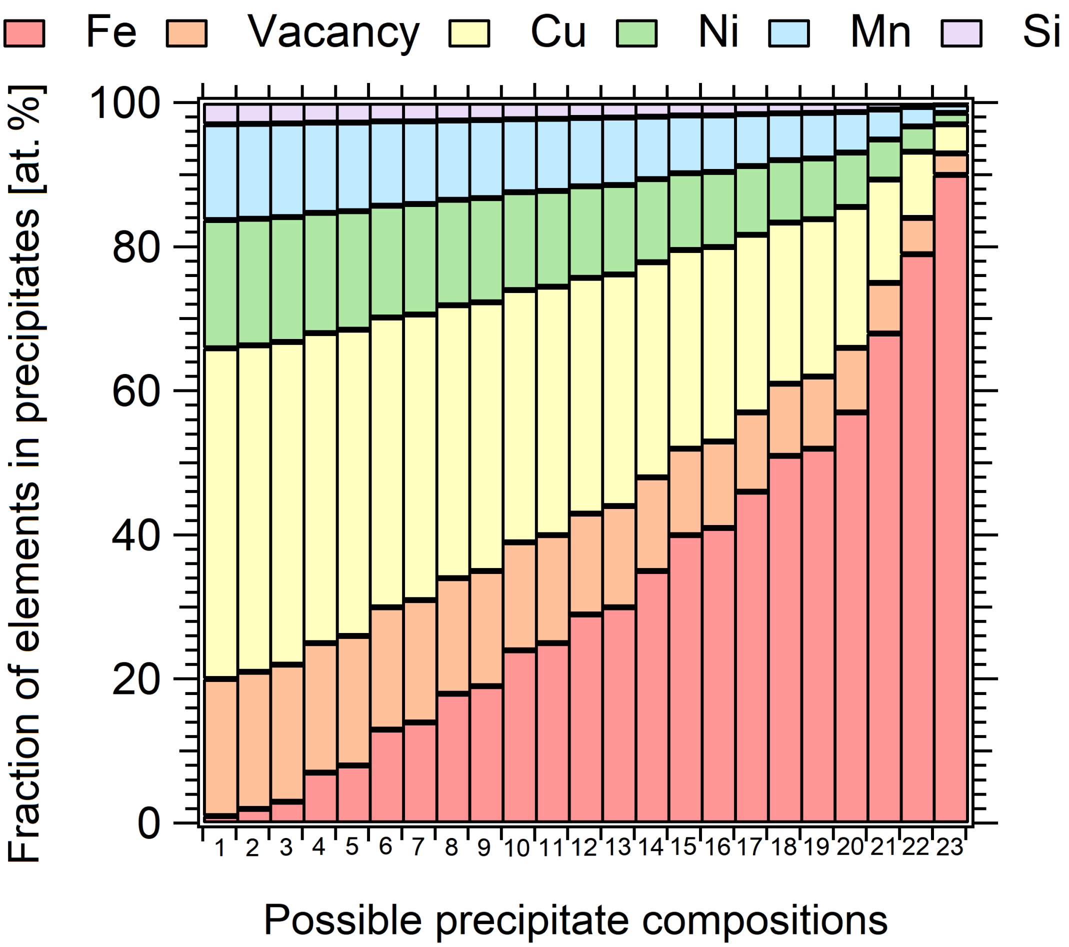

Figure 4.32: Graph showing the 23 possible precipitate compositions in weld A corresponding to the experimental A ratio of 2.705 ± 0.012. Each composition is represented by a vertical bar which shows the fractions of alloying elements present in the precipitates. Each alloying element is represented by a unique colour, and the fraction of each element is equivalent to the height of each colour bar.

From the ASAXS data, the Fe content of the precipitates was found to be 3 at% through fitting of equation 2.35 to the intensity vs energy profile at the Fe edge. The vacancy content corresponding to the experimental A ratio is hence 19 at%.

This finding will impact the way precipitation events in thermally aged RPV alloys are modelled and quantified. It is clear that precipitates cannot be treated as non-magnetic, which is in contrast to a SANS study alone in [22] that suggests no Fe is present in FeCuMnNi model alloys. As such, it has been shown that one must consider the magnetism, Fe and vacancy content of thermal ageing induced precipitates in future studies.

4.5.3 Effect of thermal ageing on mechanical properties

The embrittlement as a result of thermal ageing is encapsulated by the hardening effect of precipitation (a hardness increase of 80.0 ± 4.4 Hv). The presence of nanoscale precipitates in the steel matrix form a direct barrier to dislocation movement [137, 138] which increases the overall hardness. After 100 000 hours, the Cu-rich precipitates have a high number density and are relatively small size. The observed hardness increase for the low alloy RPV weld steel is fully consistent with that observed in the previous APT study [54]. Interestingly, the precipitates were found to have similar structural properties (shape and size) to high Cu RPV steels thermally aged for much shorter ageing times (e.g. 300 hours) [66]. It is important to note that this hardness change caused by temperature exposure alone rivals the embrittlement seen in similar high Cu steels that have been irradiated [50, 67, 118]. This demonstrates the nuanced relationship between temperature, time and the enhancement and acceleration of the precipitation process in a radiation environment.

4.6 Conclusions

The work presented in this chapter is a unique advanced scattering study on precipitation in a low alloy RPV weld steel thermally aged at representative operational reactor conditions (in contrast to the typical elevated temperature/reduced time thermal ageing studies in the literature).

The ageing process has been found to induce a large number of nanoscale precipitates in the high Ni, high Cu RPV steel. The structural precipitate properties have been mapped using SANS, with analysis methods such as maximum entropy and Monte Carlo providing the most consistent results because of the lack of requirement of pre-assumed knowledge of the scattering system. A log-normal distribution of spherical precipitates with mean radius 20.058 ± 0.589 Å was observed which is consistent with the reported precipitate sizes from the APT study. The increase in hardness due to thermal ageing was found to be 80.0 ± 4.4 Hv which is commensurate with documented precipitation hardening observed in similar RPV studies.

The careful analysis of SANS and ASAXS data has highlighted the importance of the consideration of vacancies and Fe in thermal ageing induced precipitates in high Ni RPV steels. Although it may simplify the analysis process, treating precipitates as non-magnetic is a flawed approach, as it excludes Fe within the precipitate and even the magnetism from Ni. It is not conducive with the literature on thermal ageing induced precipitation in Cu-containing RPV alloys for Fe or vacancies to be present [22, 60, 54], but the contribution of vacancy clustering within precipitates is one that cannot be ignored. Moreover, the Fe content of the precipitates obtained during the APT study is an overestimation. The stark differences in A ratio between Fe, non-Fe and vacancy containing precipitates shows this explicitly. The combination of advanced scattering techniques found the average precipitate composition to be 0.03Fe-0.17Ni-0.44Cu-0.13Mn-0.03Si-0.19Vac.

Whilst the findings of this study add a new perspective on precipitation in the long thermally aged RPV weld that could not be obtained through APT, there are additional studies that could be carried out in the future. The neutron and x-ray scattering studies on the samples induced a significant level of activity, meaning that additional post-scattering analysis was not possible. It would be interesting to perform an irradiation study on this alloy composition to investigate the interplay between thermal ageing and irradiation induced precipitation for representative in-service conditions.

CHAPTER 5

THERMAL AGEING INDUCED PRECIPITATION IN FE-CU-MN-NI MODEL REACTOR PRESSURE VESSEL STEEL ALLOYS

5.1 Introduction

Understanding the microstructural evolution of RPV alloys under typical LWR operating conditions is crucial in predicting material integrity over time in-service. In particular, the thermal history plays an important role in nanoscale precipitation that can lead to hardening and hence embrittlement [69, 139]. This is of high relevance in our current nuclear climate where harsh temperature and neutron environments can compromise the mechanical properties of said RPV steel materials over long term operation. The aim of this chapter is to demonstrate how small-angle scattering can be used to study in-situ material transitions and nanoscale precipitation in model low alloy RPV steels . The relationship between alloy composition and thermal ageing induced precipitation is explored in detail.

This chapter presents the results obtained from the thermal ageing and characterisation of precipitation events in multiple model RPV alloys. It shows the contribution that small-angle scattering can make to quantifying properties of thermal ageing induced precipitates. In addition, a novel method of studying precipitation kinetics has been carried out, taking advantage of the ability to perform in-situ thermal ageing measurements due to the long range of neutrons in matter. Magnetic saturation of the RPV alloys has been used to demonstrate how the magnetic nature of neutrons can be exploited to provide compositional information on nanoscale precipitates.

The advantage of studying model alloys is that one can eliminate the trace elements found in commercial alloys that have limited effects on the microstructural evolution during service. This removes a layer of complexity from the characterisation of irradiation damage. The composition of the model alloys were carefully selected based on in-service RPV alloys and previous studies on solubility, precipitation nucleation and growth [18, 20, 45, 140], with only the main elements postulated to have a strong effect on thermal ageing induced damage present (Cu, Mn and Ni). This allows for one to study the effect of particular alloying elements in detail, aiming to elucidate their role in thermal ageing induced precipitation events. The compositions of model alloys chosen in this study can be seen in Table 5.2.

The model alloy samples were aged slightly above the operating temperatures of a light water reactor at 450 °C and 500 °C, with the aim of nucleating and subsequently growing precipitates. These temperatures were chosen so as to achieve precipitation events in an acceptable time scale that are also in an appropriate size range to be detected by SAXS and SANS. The parameters of the scattering instruments employed in this study give a minimum size detection limit below the typical nanometre size range of precipitates induced in in-service alloys [19, 40, 62] ($\approx$ 1 nm), which highlights the usefulness of the techniques for studying such damage events. It should be noted that the timescales of the ageing process in this work (on the order of 10^2 hours) are several orders of magnitude smaller than a lifetime exposure (10^5 hours), however this accelerated ageing process still provides important information on the mechanisms of precipitation and the overall effect on mechanical properties.

The results from SAXS, SANS and hardness testing are presented, focusing on how one can obtain useful information on thermal ageing induced precipitation damage through a combination of experimental methods. The implications of these with respect to the lifetime of such materials under reactor conditions will be considered, and the crucial relationship between thermal ageing and precipitation induced hardening is explored.

5.2 The effect of Cu, Mn and Ni on thermal ageing induced precipitation in RPV alloys: a review

5.2.1 Solubility of Cu, Mn and Ni in Fe

Section 2.2.2 previously introduced the concept of thermal ageing induced precipitation, where the diffusion of solute atoms in the matrix in the presence of vacancies can lead to the nucleation and growth of coherent precipitates [23, 43]. The nature of such precipitation events is coupled with the solubility of certain alloying elements; in the context of RPV steels, the elements of interest are Cu, Mn and Ni within a predominantly Fe matrix.

There have been many studies on the solubility of these elements in an attempt to understand precipitation properties under LWR operating conditions [17, 18, 49]. Despite this, the solubility of Cu in Fe during operation is still disputed in literature, with variations from 0.001 at% to 0.05 at% [16, 72, 141]. In any case, the reported solubility of Cu in Fe is much lower in comparison to other alloying elements such as Ni and Mn [127, 130, 142, 143], as can be seen by comparison of the binary equilibrium phase diagrams in Figures 5.1, 5.2 and 5.3 respectively for Fe-Ni, Fe-Mn and Fe-Cu. In previous thermal ageing studies, the low solubility of Cu has been found to lead to precipitate induced hardening, of which the hardness was found to increase with Cu contents above 0.1 wt% [144].

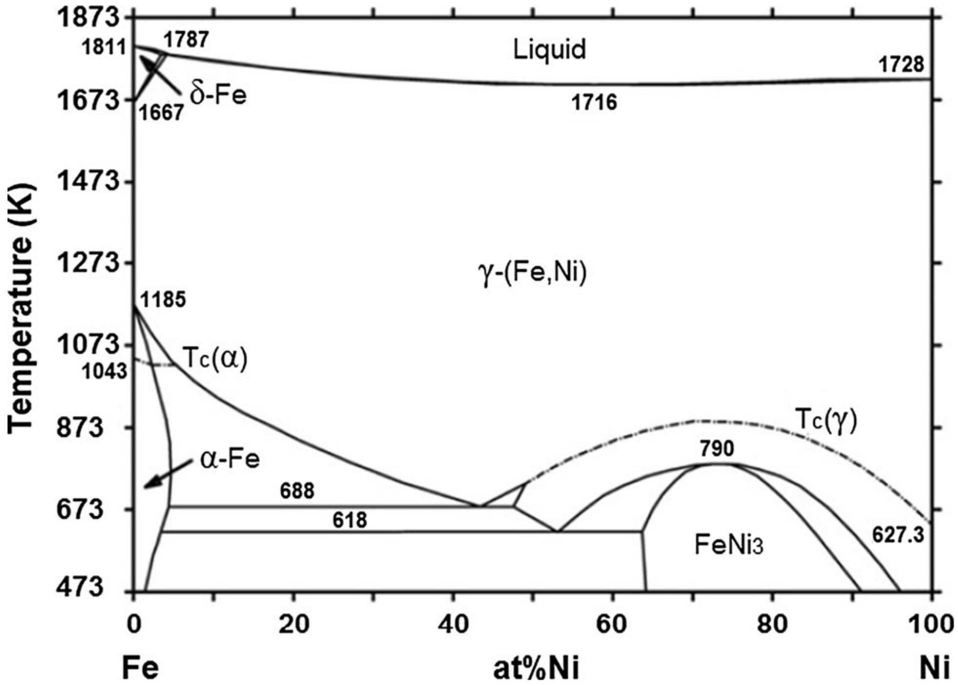

Figure 5.1: Equilibrium phase diagram for binary Ni-Fe system from [142].

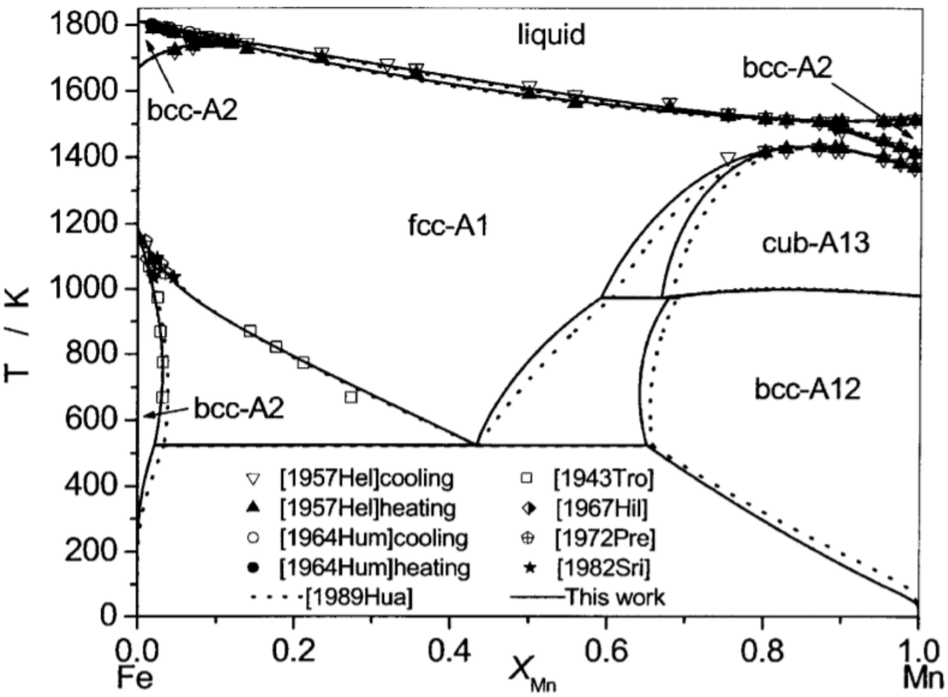

Figure 5.2: Equilibrium phase diagram for binary Mn-Fe system from [143].

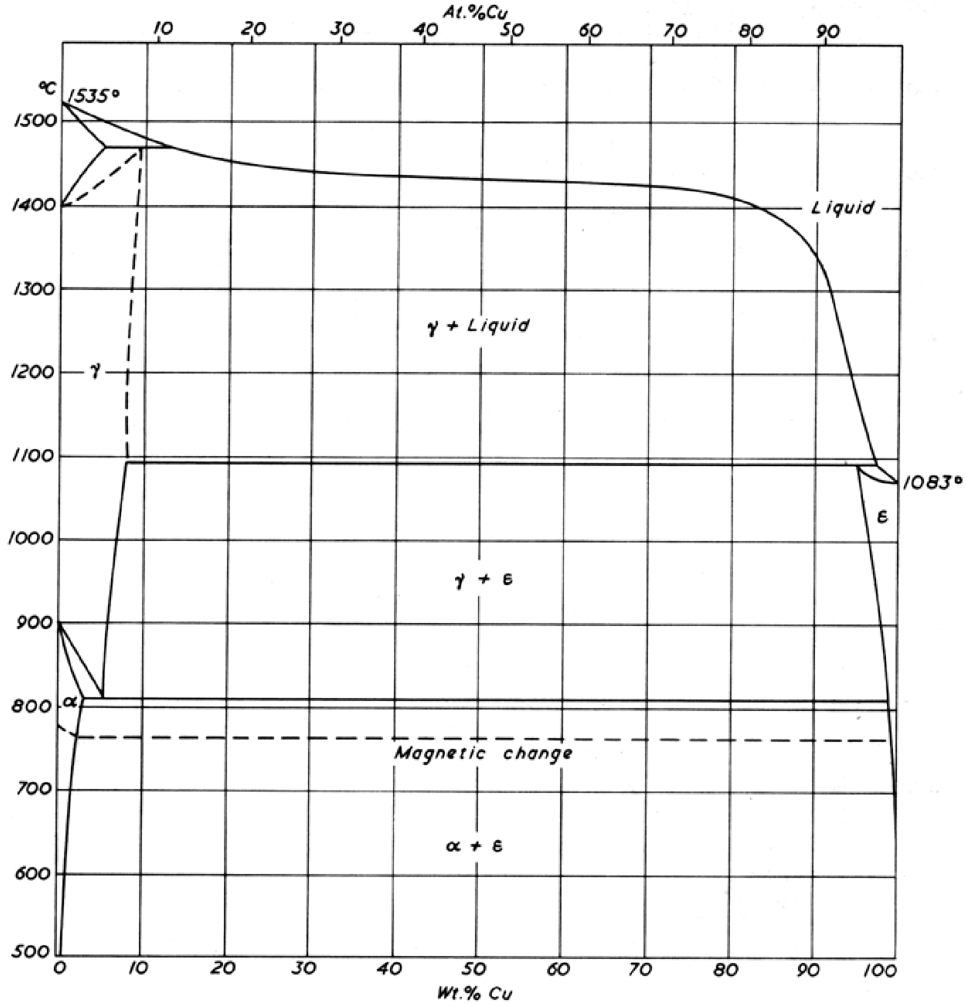

Figure 5.3: Equilibrium phase diagram for binary Cu-Fe system from [145].

The solubility studies and binary phase diagrams have been used as a basis to determine ideal model alloy compositions and thermal ageing parameters to induce precipitation damage in this work. For example, the solubility limits shown in Table 5.1 have been extracted from the binary phase diagram data for consideration in this work.

Table 5.1: Summary of elemental solid solubility limits for consideration in model RPV alloy composition and thermal ageing study, extracted from [142, 143, 145].

Element	**Solubility limit at 330 °C [at%]**	**Solubility limit at 500 °C [at%]**
Ni	3.24	4.83
Mn	3.02	3.79
Cu	0.02	0.74

5.2.2 Thermal ageing of RPV steels

RPV alloys containing Cu have been found to exhibit thermal ageing [47] and irradiation induced [146, 147] precipitates. Many studies have utilised techniques such as APT [14, 52, 66], TEM [45, 72, 112], PAS [46, 57, 148] and SANS [41, 55] in an attempt to quantify the composition and structural properties of precipitates induced in both low and high Cu steels. Combining investigative techniques can allow for a clearer understanding of precipitate behaviour, since each technique has its own set of unique advantages and disadvantages. For example, an APT study on long thermally aged RPV welds found CuMnNi-rich precipitates with a fraction of Fe at 11 at% whilst assuming a 100% precipitate density [54]. The SANS and ASAXS results on the same samples report a fraction of Fe 3 at% and the presence of vacancies at 19 at%. Hence, the use of small-angle scattering is integral for the characterisation of precipitate properties to address shortfalls in other techniques.

There is a documented thermodynamic synergy between Cu, Mn and Ni [144] that leads to precipitation of Mn and Ni in the presence of Cu, despite their relatively high solid solubilities. In order to understand this relationship, thermal ageing induced precipitation in the binary FeCu system must be fully understood as Cu has the lowest solubility and hence drives the initial stages of precipitation.

A binary FeCu thermal ageing study observed nucleation, growth and coarsening of Cu-vacancy precipitates for several ageing times [149]. As ageing time increases, the Cu content of such precipitates was found to increase whilst vacancy content in the precipitates remained the same, indicating that vacancy facilitation is the primary nucleation mechanism and that growth is coupled with a high purity of Cu precipitates [41, 150, 151].

A previous SANS study on irradiated model RPV alloys [50] found that induced precipitates present in Fe-Cu binary alloys were Cu-vacancy clusters with a core-shell structure. The calculated A ratio for the Cu-vacancy ratio in the precipitates is shown in Figure 5.4. The size range (1 to 4 nm) is consistent with those from a similar FeCu thermal ageing study [111]. The thermal ageing induced precipitates in FeCuMnNi model alloys in [47] were found to be enriched in Cu, Mn, and Ni with Cu possibly acting as a nucleation point. This again highlights the synergy between these alloy elements, and the importance of understanding the elemental effects on the precipitation process.

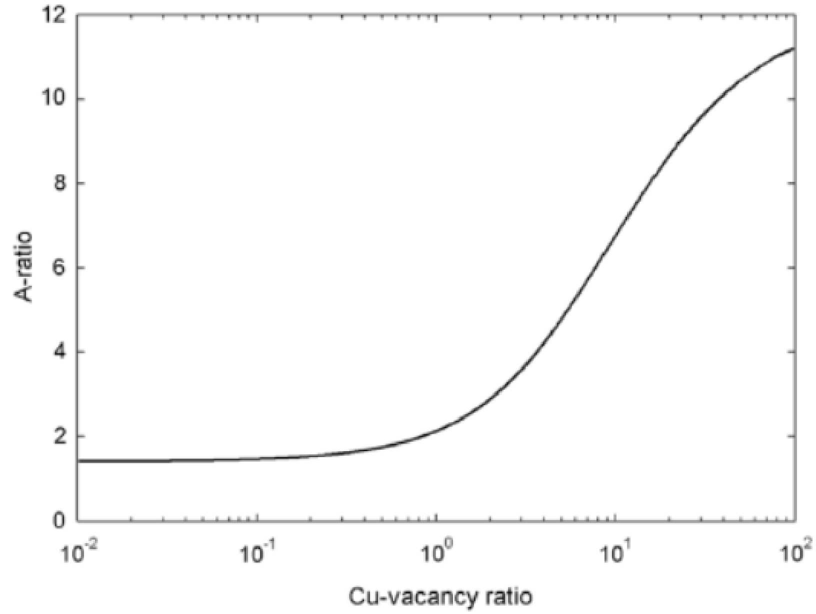

Figure 5.4: Relationship between the Cu-vacancy ratio of a Cu-vacancy cluster in Fe and the A ratio in irradiated FeCu [50].

The main area that requires further study for RPV steel systems is the specific effect of the initial element compositions on precipitate nucleation, growth and composition during thermal ageing, to understand the effect of Mn and Ni on the behaviour of precipitation in the presence of Cu. This has been explored in irradiation studies, such as [48] where it was found that increasing Ni matrix fraction enhances the fraction of Ni and Mn in precipitates. The effect of Mn on the number density of irradiation induced precipitates in FeCu and FeCuMn model alloys was studied in [136]. It was found that the presence of Mn increased the number density of precipitates by a factor of 10. There are limited studies of such effects during thermal ageing, which this work addresses.

This composition effect is closely coupled to the magnetism of such precipitates in RPV alloys. Historically, SANS studies have treated precipitates as non magnetic [40, 125]. This assumption is a simplification designed to aid data analysis. Whilst this may be reasonable for systems containing Cu and Mn, the observed presence of Ni and Fe (ferromagnetic) in thermal ageing induced precipitates [20, 64], coupled with the fact that the majority of the matrix is Fe, means that the magnetism of precipitates in low alloy RPV steels should not be ignored. For example, a recent study [22] employing multiple investigative techniques found that irradiation induced Cu-rich precipitates do not contain a significant amount of Fe. This is a direct contrast to findings from APT studies on both irradiated and thermally aged RPV steels where the Fe content in induced precipitates is considerable [62, 66, 67]. This work will consider the magnetism of precipitates using SANS.

A study by [53] observed precipitates with average radii 1.29 ± 0.38 nm after a high neutron irradiation dose of 5.4 x 10^{18} n/cm^2 in a FeCuMnNi model RPV alloy using APT. In [127], a similar observation was made and in the absence of Cu a late-blooming 'G phase' of Mn-Ni-Si rich precipitates in irradiated RPV alloys was postulated. Additional studies have also focussed on the role of Mn and Ni on precipitation damage in low Cu RPV steels [152].

APT studies have been previously carried out on various neutron irradiated RPV model alloys to study the effect of Mn, Ni and Si of Cu precipitation [48]. Interestingly, the presence of Ni and Mn was found to increase the nucleation of Cu precipitates. The behaviour of such alloying elements under thermal ageing is likely to be different due to the mechanisms of solute atom transport [51, 52]. For example, [47] found that Ni and Mn are present in thermal ageing induced precipitates, but that the number density of precipitates is primarily dependent on the amount of Cu and the ageing time. The distribution of Cu and Ni in induced precipitates in a high Cu RPV model alloy after 13 200 hours at 370 °C is shown in Figure 5.5.

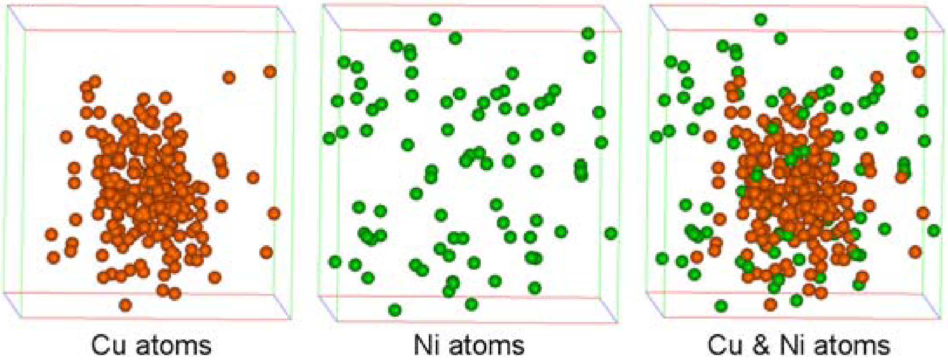

Figure 5.5: Cu and Ni APT fractions in a FeCuMnNi RPV model alloy thermally aged for 13 200 hours at 370 °C [47].

These findings suggest that there are fundamental differences between the compositions of irradiation and thermal ageing induced precipitates, despite documented similarities in the shape and size distributions of such precipitates through both damage mechanisms [13, 20, 53, 61]. Compositional differences are strongly affected by the thermodynamic stability and diffusion mechanisms of different alloying elements in response to high temperature and radiation environments. For irradiation, there are two main types of precipitation damage:

1. Radiation induced: The presence of additional solute atoms can be attributed to irradiation induced interstitials as part of the damage cascade, and clustering of such atoms can occur in spite of equilibrium solubility limits (i.e this is not a thermodynamically driven process).
2. Radiation enhanced: The presence of irradiation induced vacancies in the matrix facilitate the random diffusion of solute atoms [153] and act as nucleation sites.

APT has been used on RPV alloys to investigate the differences between irradiation and thermal ageing induced nanoscale precipitates [21]. Precipitates were induced via thermal aging in a range of high and low Ni RPV weld materials, and then subsequently neutron irradiated. Thermal ageing induced precipitates were found to have higher Cu and lower Mn/Ni fractions than their irradiated counterparts. An increase in the matrix fraction of Ni is observed to also increase the amount of Ni and Mn present in precipitates, as also found in [48], whilst simultaneously reducing the Cu fraction.

An APT study on a low Ni RPV weld thermally aged for up to 100 000 hours at 365 °C found the majority of precipitates to be at dislocations [54]. This can be attributed to the reduction in energy when precipitating in these locations, however it is noted that matrix precipitation has been observed in the same study for a high Ni high Cu long thermally aged RPV alloy due to the relatively large distribution of Cu. The work in this chapter provides compositional and structural information of thermal ageing induce precipitates which can be compared to irradiation induced precipitate properties in similar alloys in literature. This can help elucidate the behaviour of alloying elements at elevated temperatures which is closely coupled to their solubility and diffusion behaviour within a predominantly Fe matrix, and hence their likelihood of matrix precipitation.

In contrast to APT studies that often do not account for vacancies, a study of thermal ageing induced precipitation FeCu model alloys reported that vacancies act as nucleation points for Cu-rich precipitates [154]. In addition, the trapping of vacancies in Cu precipitates and the mobility of such structures was studied and confirmed in [155].

The impact of thermal ageing induced precipitation in RPV welds is strongly dependent on the Cu content. For the long thermally aged high Ni high Cu weld in Chapter 4 (100 000 hours at 330 °C), a hardness increase of 80.0 ± 4.4 Hv was measured, which is in stark contrast to [156] where limited hardening was observed for a high Ni low Cu weld aged for 140 000 hours at 320 °C. The hardness increase obtained from the small-angle scattering study in this work is a 50% increase in hardness, which is wholly consistent with the APT study on the same high Ni high Cu weld in [54].

There has previously been a SANS investigation into the annealing of irradiation induced precipitates in three model RPV alloy samples using an in-situ furnace [56] to study the effect of high temperatures on the presence of irradiation induced clusters. There is an opportunity to elucidate the kinetics of the thermal ageing induced precipitation process in such RPV alloys in a first-of-its-kind in-situ ageing SANS study, as has been employed in this work.

5.2.3 Effect of precipitation on mechanical properties

The presence of precipitates in a sample matrix act to impede the movement of dislocations through which is a primary mechanism of plastic flow. The surrounding local stress fields of such precipitates interact with those from dislocations and result in the bowing of dislocations which leads to an overall increase in hardness and strength that is often coupled with a reduction in ductility. This is analogous to the precipitate hardening technique used in metallurgy to favourably increase the strength of materials.

There are several techniques that can be employed to quantify the effect of identified precipitation on mechanical properties. These include microindentation hardness testing [118, 157], Charpy impact testing to measure the reduction in the ductile-to-brittle transition temperature (DBTT) [158], yield strength tests [159], and fracture toughness tests [160]. The latter three tests require larger samples in comparison to the former and to precipitation property quantification techniques such as small-angle scattering, APT and TEM. The study of thermal ageing and irradiation induced precipitation has limits on sample size set by furnace or reactor space. This means that unless a study is dedicated to a single technique such as DBTT, it is not often feasible to combine precipitate property quantification with multiple mechanical property quantification techniques due to the volumes of specimens required.

The hindrance to dislocation motion can be described through the dispersion barrier hardening model [137, 138] which describes the yield strength, σ_y, as

$$\sigma_y = \alpha G M b \sqrt{N d} \tag{5.1}$$

where α is the barrier strength (1 for Orowan hardening which allows bending of dislocations around the barrier [161]), G is the shear modulus, M is the Taylor factor, b is the Burgers vector, N is the number density of the obstacle, and d is the mean diameter of the obstacle.

Understanding thermal ageing induced precipitation mechanisms and the effect on mechanical properties can unveil adverse alloy compositions for in service loading conditions. Moreover, understanding precipitation properties in reactor steels can lead to the development of new robust materials. For example, [162] has investigated the induction of nanoscale co-precipitation events to enhance the properties of Fe-based alloys.

5.3 Materials and methods

5.3.1 Sample details

A series of RPV steel model alloys have been selected, with varying amounts of Cu, Mn and Ni, to investigate the role of alloying elements on the precipitation process and the effect on mechanical properties. Such model alloy compositions have been chosen by considering various in-service alloy compositions and previous irradiation and thermal ageing studies of RPV steels [14, 22, 53, 61, 140]. Whilst it has been observed in thermal ageing induced precipitates in RPV steels, Si has not been included as an alloying element of interest in this study, since previous works have found that the Si precipitate fraction was comparable to the bulk matrix fraction [48].

The chosen low alloy RPV steels will allow for the investigation of how the ageing time and alloying elements affect precipitation in such alloys, and how this transfers into macroscopic material changes via embrittlement.

After careful selection of required alloy compositions in at%, the model alloys were fabricated in the School of Metallurgy and Materials at the University of Birmingham using a vacuum arc melter.

High purity Fe, Cu, Mn and Ni (>99.9%) in flake form were used during fabrication. The maximum mass of material for a sample fabricated in the vacuum arc melter is 6 g to ensure homogeneity. Using this as a basis, the fractional quantities of each alloying element were calculated and then measured using a high precision mass balance (± 1 x 10^{-4} g) to give the desired atomic fractions. This involved understanding the conversion between required wt% to at% of element i in alloy containing N elements, given by

$$at\%_i = \frac{{}^{wt\%_i}/_{M_i}}{\sum_i^N {}^{wt\%_i}/_{M_i}} \tag{5.2}$$

where M is the molar mass.

The mixture is loaded into a water cooled copper crucible alongside a titanium getter, as shown in Figure 5.6.

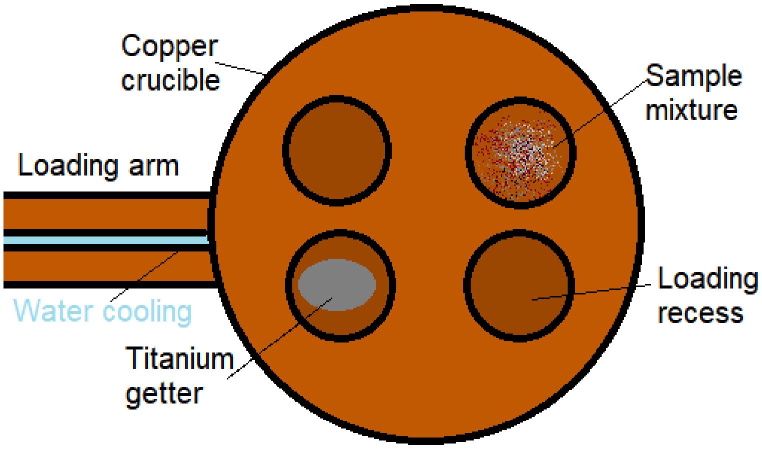

Figure 5.6: Schematic diagram of the vacuum arc melter copper crucible space where the sample mixture is loaded.

The copper crucible is then loaded into the arc melter and sealed with a series of O-rings and bolts. The O-rings were cleaned and greased to ensure a strong seal for vacuum pumping. The sample space is vacuum pumped down and then backfilled with argon to provide an inert atmosphere to minimise impurities in samples.

Personal protective equipment was used to ensure safe operation of the arc melter, including insulated gloves for control of the electrode arm and UV protective goggles. The fabrication was completed with no one except the operator in the vicinity of the equipment since the light emitted from the arc can permanently damage the eyes.

During operation, the tungsten electrode should be moved close enough to the mixture to generate an arc but not so close that it touches it which can contaminate the electrode. Firstly, the titanium getter should be melted using the electrode arc for several minutes to draw any remaining impurities, such as oxygen, from the sample space. Then, the electrode is moved to the sample mixture. The arc formed will melt the mixture (producing temperatures in excess of 2000 °C) and the surface tension pulls the sample into a sphere. Care is taken to ensure that all of the initial mixture is drawn into the sample. The electrode is systematically moved in a figure-of-eight motion over the spherical sample for several minutes to ensure homogeneity. Once complete and solidified, the titanium getter and sample are flipped over using the electrode and the process is repeated five times. Once the process is complete, the sample is allowed to cool in the sealed arc melter for 1 hour to minimise contamination.

EDX was then completed on each fabricated model alloy to confirm compositions using method outlined in Section 3.2.1 and Section 3.3.3. An example spectrum for model alloy 1.3 can be seen in Figure 5.7. The final model alloy compositions in atomic percent are given in Table 5.2.

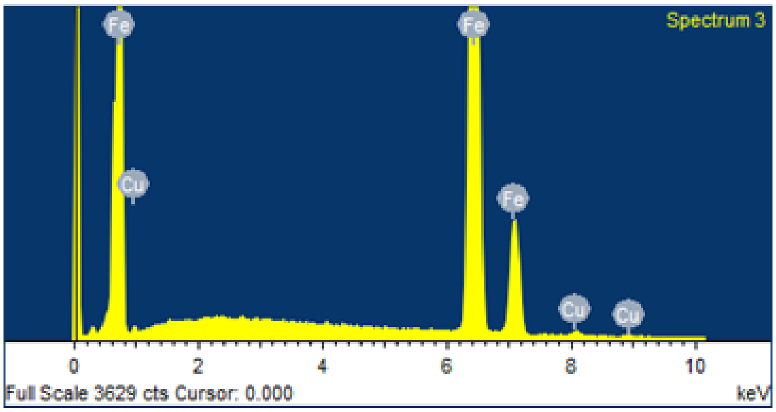

Figure 5.7: EDX spectrum for arc melted sample 1.3.

Table 5.2: Final arc melted model alloy compositions [at%].

Model alloy	Sample number	Density [g/cm^3]	Fe	Cu	Ni	Mn
FeCu	1.1	7.8761	99.80	0.20	-	-
FeCu	1.2	7.8820	99.26	0.75	-	-
FeCu	1.3	7.8874	98.77	1.23	-	-
FeCuMnNi	2.1	7.9048	94.79	0.31	3.33	1.58
FeCuMnNi	2.2	7.9067	94.62	0.25	3.57	1.56
FeCuMnNi	3	7.8995	95.70	1.24	1.73	1.33
FeCuMnNi	4	7.8886	96.19	0.48	1.64	1.70
FeMnNi	5.1	7.9032	94.99	-	3.48	1.53
FeMnNi	5.2	7.9034	95.33	-	3.39	1.28
FeMnNi	6.1	7.9003	92.51	-	4.03	3.46
FeMnNi	6.2	7.9024	92.29	-	4.23	3.47
FeCuNi	7.1	7.9026	97.27	0.73	2.00	-
FeCuNi	7.2	7.9120	96.57	1.24	2.19	-
FeNi	8	7.8958	97.90	-	2.10	-

From here on, samples will be referred to by their numbers, *e.g.* 1.1 AM, 1.1 TA, and 1.1 FA denoting thermally aged (TA), as-made (AM), and in-situ furnace aged (FA) using SANS.

The samples chosen to allow for investigation of the interactions between certain alloying elements of interest on precipitation are shown in Table 5.3. The variability is captured by the use of multiple alloy compositions.

Table 5.3: Summary of samples that allow for comparison of the interaction of alloying elements on precipitate properties.

Element Interactions	**Samples**
Effect of Cu	1.1, 1.2 and 1.3
Effect of Ni on Cu	7.1 and 1.2, or 7.2 and 1.3
Effect of Mn on Ni	5.1 and 5.2
Effect of Mn and Ni on Cu	1.3 and 3
Effect of Mn on Ni and Cu	3 and 7.2
Effect of Ni on Mn (at solubility limits)	6.1 and 6.2
Effect of Cu and Ni on Mn	2.1 and 4
Effect of Cu on Ni	7.2 and 8

5.3.2 Sample preparations

5.3.2.1 Thermal ageing

Due to time restraints imposed by the scheduled small-angle scattering experiments, the thermal ageing process was completed at elevated temperatures to induce the required level of precipitation for investigation. The temperatures were chosen such that they were high enough to sufficiently accelerate the precipitation process but not so high that it compromises the timescales required to obtain a certain size range of precipitates.

Each AM sample was cut in half so a virgin reference sample exists for each model alloy composition for comparative purposes. The thermal ageing process was carried out in a standard furnace, with samples encapsulated in sealed glass tubes filled with argon gas to prevent oxidation. The samples were solution annealed in the furnace at 800 °C for 1 hour and subsequently water quenched to homogenise the microstructure.

Each sample was then thermally aged for the desired time to induce nanoscale precipitation at the chosen temperature using the solubility of elements and the kinetics of the precipitation process to inform the ageing times. The samples were then slowly air cooled to avoid phase transformations through quenching. The ageing conditions used for each sample are shown in Table 5.4.

Table 5.4: Thermal ageing conditions for each arc melted model RPV alloy.

Sample name	Temperature [°C]	Time [hours]
1.1	450	120
1.2	450	71
1.3	450	10
2.1	550	120
2.2	550	120
3	450	120
4	450	120
5.1	550	120
5.2	550	120
6.1	450	120
6.2	450	120
7.1	450	71
7.2	450	10
8	450	71

The ageing times were selected so as to induce precipitates in a size range of 1 to 10 nm to be able to quantify their properties using small-angle scattering. Previous thermal ageing studies on FeCuMnNi alloys have found nanoscale precipitation events to be the most likely over the lifetime of certain RPV low alloy steels [20, 111, 163, 140, 164]. This has been shown in Chapter 4 of this work for the long thermally aged RPV weld steel where FeCuMnNi precipitates were observed with a mean radius of 20.058 ± 0.589 Å after 100 000 hours at 330 °C. Too short an ageing time means that no precipitate nucleation or growth will occur, and conversely too long a time will result in over-ageing of the precipitates, putting them outside the length scales observable from the small-angle scattering instruments.

Samples with similar levels of alloying elements with one varying element were chosen to have the same ageing time so as to highlight the effect of each particular element on the process of thermal ageing induced precipitation.

5.3.3 SAXS

In order to assess the level of induced thermal ageing induced precipitation damage in the model alloys, SAXS and ASAXS were carried out on all of the samples. The SAXS study acted as an aid to identify the extent (if any) of induced damage and to provide shape and size information through model fitting. The ASAXS study, as in Chapter 4 on the long thermally aged RPV weld system, was completed to act as a proof of concept for such material systems and to show the contribution of scattering from each alloying element to the overall SAXS intensity profiles.

Due to the low x-ray energies used in SAXS ($<$ 10 keV), the process in Section 3.2.4 was utilised to produce 3 mm twin jet polished discs that were thin enough to provide sufficient x-ray scattering intensity.

5.3.3.1 Experimental measurements

The SAXS on the thermally aged model alloys was completed during the same three beamtimes mentioned in 4.3.3.1 at 12BM at the Advanced Photon Source, Chicago, P23 at Deutsches Elektronen Synchrotron, Hamburg, and SAXS/WAXS at the Australian Synchrotron, Melbourne. Similarly, the best available data was from the SAXS/WAXS beamline at the Australian Synchrotron, Melbourne [98] as, unlike the other two instruments, the entire system is under vacuum.

The SAXS experiment was completed on all model alloys to primarily indicate the samples in which the ageing process had induced observable microstructural changes. This was carried out at an energy far from the elemental absorption edges (6.809 keV) to obtain typical I(q) SAXS profiles. The SAXS results were then used to inform samples of interest to complete ASAXS on. SAXS results can also be used to confirm concurrence with the structural and compositional precipitate information obtained through SANS.

The experimental setup and measurement process was exactly the same as for the long thermally aged welds in Chapter 4:

- Beam size of of 250 x 25 μm

- 1 m^2 Pilatus 13 2M detector (1280 x 1790 pixels of size 172 x 172 μm)
- Calibration of Si(311) monochromator and elemental absorption edges
- Calibration of q-range using silver behenate powder mounted in kapton tape
- q-range used was $0.07 < q < 0.61$ Å^{-1}
- Locate optimal beam position on each sample
- Scattering measurements at 9 energies through the Fe, Cu, Mn and Ni absorption edges in all as-made and thermally aged model alloy samples
- Scattering measurements at an energy far from all elemental absorption edges for all samples
- Empty beam scattering for all energies
- Glassy carbon scattering for all energies for calibration of measured intensity into absolute units

5.3.3.2 Data reduction and analysis

The standard data reduction method outlined in Section 3.4.1.2 was employed to obtain the SAXS/ASAXS measurements on an absolute scale.

Model-independent analysis was completed to obtain Porod scattering contributions. Then, empirical model fitting was completed on SAXS data for all model alloy samples. ASAXS analysis, as per the method outlined in Section 4.4.3.2, was then completed on samples and elemental absorption edges of interest.

5.3.4 SANS

SANS has been used specifically to investigate the effects of thermal ageing in several RPV model alloys of interest, with details mentioned in Table 5.4. The samples were chosen such that they will allow for an in-depth investigation into the evolution of precipitation through ageing of a material, focusing on example RPV alloy compositions with knowledge gaps on structural and compositional precipitate information and on samples where precipitation was confirmed using SAXS.

As discussed in Section 3.2.3, the samples chosen for SANS are required to have a thickness of around 1 mm to optimise the measured scattering signal. The model alloys of interest were cut using a SiC cutting wheel. Thickness measurements were taken at 8 different points on the surface of each sample, focussing more on the area likely to be illuminated by the neutron beam, and then averaged. The results can be seen in Table 5.5.

Table 5.5: Arc-melted model alloy thicknesses [at%].

Sample name	Thickness [mm] [TA, FA]	
1.3	-	1.282
3	0.935	0.408
6.1	0.256	-
6.2	0.138	-
7.2	1.277	1.425

The SANS experiment took place on the D22 instrument at the ILL, Grenoble. It was split into two main parts with the following aims

1. In-situ thermal ageing study:
    - To induce precipitation damage through thermal ageing.
    - To quantify the evolution of precipitate properties as a function of ageing time.
    - To understand the effect of Cu, Mn and Ni on the kinetics of the precipitation process.
2. Nuclear and magnetic scattering study:
    - To quantify precipitate properties such as shape and size in both thermal aged and in-situ aged model alloys.
    - To investigate the role of magnetism in the precipitates.
    - To better understand the interaction of alloying elements and how their solubility and mobility affects the overall composition of thermal ageing induced precipitation.

5.3.4.1 In-situ ageing measurements

The alloys selected for the in-situ ageing were those with relatively high Cu contents, owing to the time allocated to the SANS study (2 days in total). Sample 1.3 AM was chosen, and hence samples 7.2 AM and 3 AM were also chosen to enable investigation of the impact of Ni and Mn on the kinetics of thermal ageing induced precipitation in the presence of Cu.

The furnace was selected from the ILL sample environment pool, with the specific experimental requirements in mind. Such requirements included the ability to balance the distance between the furnace and the detector window to minimise the air in the beam, and a large enough downstream window to allow for large scattering angles to be measured. The latter is particularly important since the achievable scattering angles set limits on the detectable real-space length scales, which are of the utmost importance when attempting to maximise the probability of observing the precipitates nucleate and grow.

In addition to the above, the furnace must be able to satisfy the temperature range and sample space requirements. The maximum temperature of the furnace was 1000 °C. The sample space was 35 mm diameter x 50 mm height. The furnace is constructed from aluminium with a high vacuum internal environment. This is imperative for preventing oxidation of the model alloys. All of the furnace internals that are illuminated by the neutron beam are made from thin niobium, which is used due to its low neutron scattering cross section.

Slices of 1.3 AM, 3 AM and 7.2 AM were selected and mounted in niobium foil as shown in Figure 5.8. There is no direct thermal contact between the samples encased in the foil. The secure niobium foil was connected to the thermocouples to allow for accurate temperature readings during the ageing process. The foil was attached to the bottom of the sample mount stick using an M8 threaded stud. The sample mount stick, made of niobium (for the length within the furnace) and steel (for the length outside of the furnace), was then inserted into the furnace and the o-rings and flanges were secured to ensure a strong vacuum. The sample stick allowed for 3D positional variation to ensure each sample could be aligned in the neutron beam.

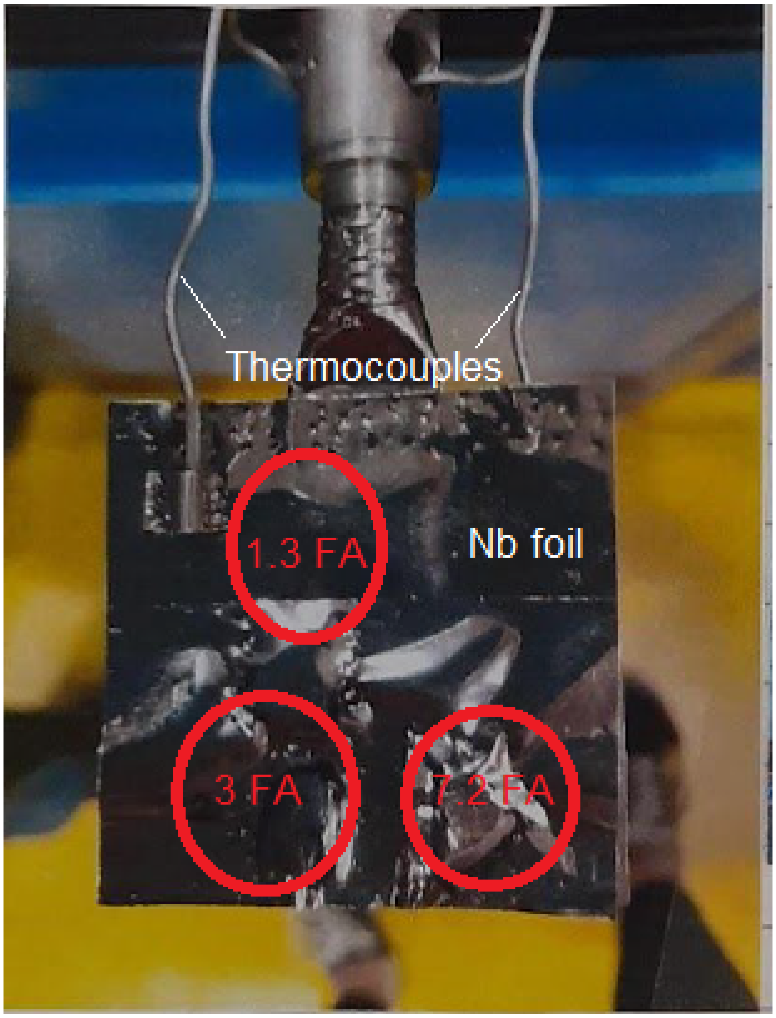

Figure 5.8: Sample setup within the vacuum furnace. Samples 1.3 AM, 3 AM and 7.2 AM were mounted in niobium foil (once ageing started these samples are now referred to as FA rather than AM).

The experimental setup of D22 SANS beamline for the in-situ ageing study is shown schematically in Figure 5.9.

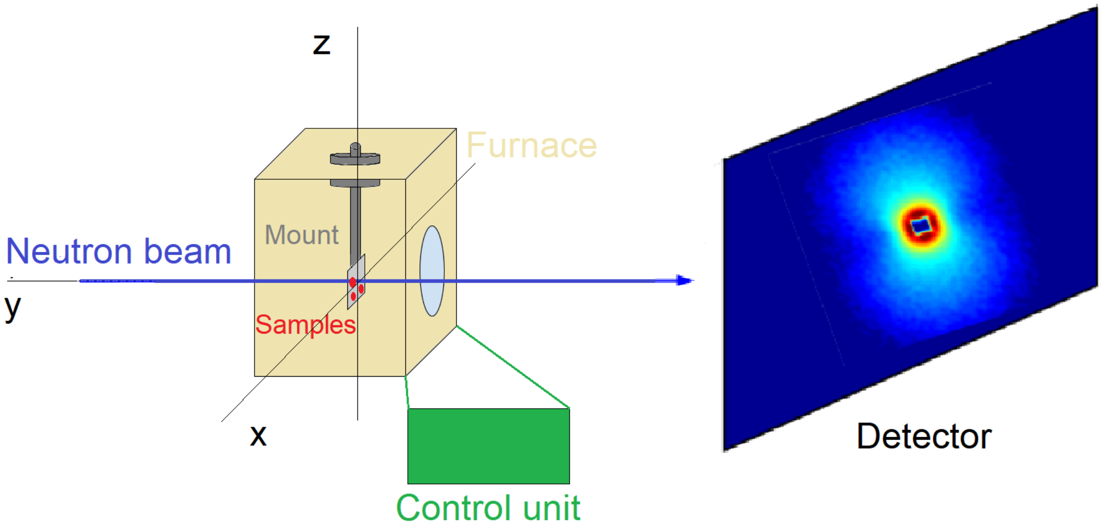

Figure 5.9: Schematic of in-situ ageing experimental set up of SANS instrument, showing samples and furnace.

Due to the efficiency required in timing to ensure that the ageing process was fully captured, the alignment of the samples, setup of q-ranges, neutron measurement times, and estimated time between measurements in each sample had to be carefully considered.

Firstly, the samples were aligned in the x-y plane to obtain coordinates of each that were used in the automated scan process.

Then, the q-ranges were setup to allow for as large a measurable distance range as possible to capture the kinetics of the precipitation process, whilst allowing for enough crossover between the q-ranges, noting the limitations in the maximum attainable q value due to the angle cut-off imposed by the furnace window. The details of the instrument configuration for each q-range is given in Table 5.6.

The sample aperture used was 2 mm diameter, and the wavelength resolution from the time-of-flight calibration was 10%.

Table 5.6: Selected conditions for forming two well overlapped q-ranges on D22 at ILL.

Property [unit]	**Medium q**	**High q**
q range [Å^{-1}]	0.01 to 0.07	0.04 to 0.30
Wavelength [Å]	5.0	5.0
Sample-detector distance [m]	8	2
Collimation distance [m]	8	2.8

The time taken to switch between each q-range was measured so as to optimise the experimental measurements. The approach taken was to measure an exposure for each of the three samples at one q-range, then move to the other q-range and measure again, and then repeat the process for a total ageing time of around 24 hours. This approach allows for incremental measurements of the absolute scattering intensity as a function of ageing time to understand the kinetics of the precipitation process.

The ageing temperature was selected to be 550 °C due to the limited timescales of the beamtime. This temperature choice, from calculations based on theory and experimental data in literature, was a balance between inducing precipitate sizes within the instrument q-range but not on timescales so fast that the evolution would be missed (due to the time taken moving between q-ranges and the ensuring sufficient count times to get reasonable statistics).

The furnace was heated to 100 °C initially where various transmission and scattering measurements were taken. Once the measurement approach was fully planned and automated, the furnace was set to 250 °C where measurements were taken to understand the heating profile of the furnace, and then was set to ramp up to 550 °C where the in-situ ageing measurements began. The time taken to heat the samples from 250 °C to 550 °C was six minutes.

5.3.4.2 Nuclear and magnetic scattering measurements

A homogeneous magnetic field of 0.7 T was applied in the sample plane and perpendicular to the incident neutrons using a pair of magnets mounted in a clamp where the distance between them can be altered, as shown in Figure 5.10. This was done to saturate each sample, allowing for the separation of nuclear and magnetic scattering contributions.

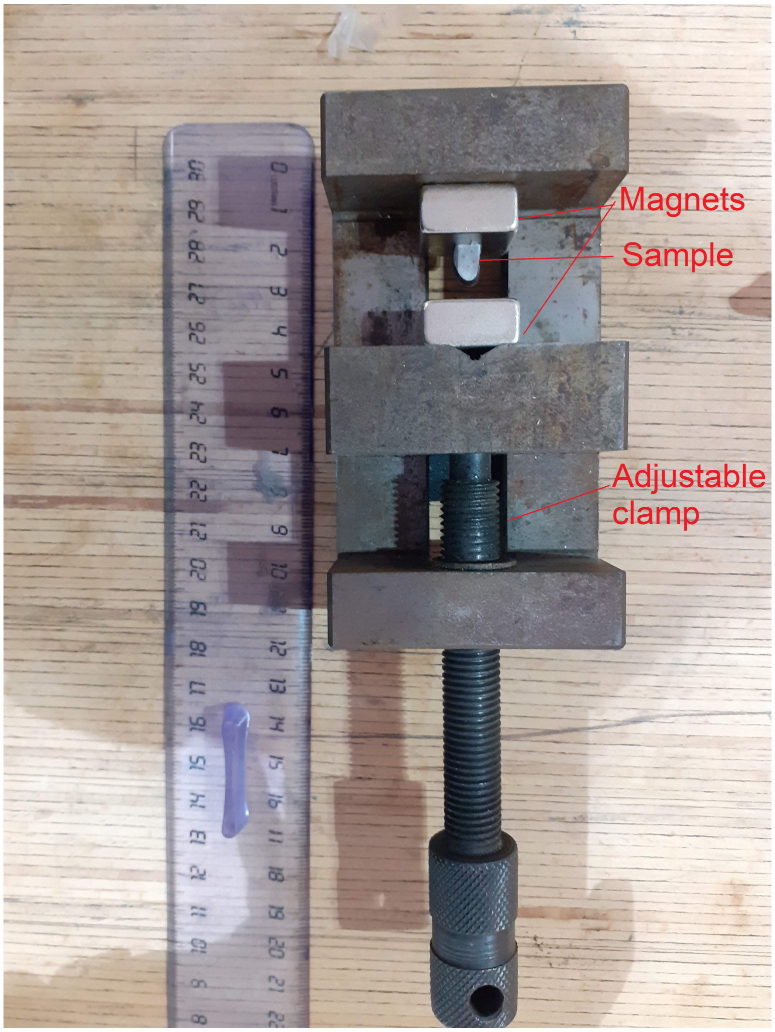

Figure 5.10: Magnet setup to allow for application of a homogeneous magnetic field to each model RPV alloy sample during SANS.

The samples were mounted between the magnets, aligned using a laser, and the final SANS measurements taken were:

- Scattering through a H_2O cell to calibrate the detector.
- Scattering through Cd to correct for electronic background.
- Scattering through each sample and the empty magnet mount in zero field without a beamstop present for transmission calculations.
- Scattering through each sample at each q-range.

5.3.4.3 Data reduction and analysis

The raw data was reduced using GRASP [109] following the process outlined in Section 3.4.1.1 to obtain the absolute scattering intensity profiles. For the in-situ study, where the samples were not magnetised, 360° sectors were used for radial averaging, compared to 35° for the magnetism study.

The anaylsis of the scattering profiles was carried out using MATLAB and IgoPro [165].

In order to overlap the q-ranges for the in-situ ageing study, an understanding of the time difference between each measurement for each sample was imperative. Such information was mapped during the data reduction process to understand which data files were closest together in terms of time between the medium and high q-ranges.

Accounting for the physical change of sample-detector and collimator distances between q-ranges (a few minutes), and the five minute measurement time for each sample, there is around 15 minutes time difference between the medium and high q measurements for each sample. This was judged as acceptable for overlapping and data reduction purposes.

The ageing times recorded are an average of the time spent at each q-range. Since the times to change setup were minimal (order of minutes), this has been deemed as a reasonable method of obtaining in-situ measurements. It should be noted that the recorded total time at temperature is the difference between when the ageing temperature of 550 °C was reached and the start time of the data file, plus the counting time of the data file.

For the magnetism study, the horizontal I(q) profile was subtracted from the vertical I(q) profile, leaving the magnetic scattering.

5.4 Results

The initial SAXS results are presented in Section 5.4.1 to identify the model RPV alloy compositions where thermal ageing precipitation has been successfully induced.

The down-selected samples of interest were then studied using SANS in two distinct investigations. These results are presented in Section 5.4.2.

Finally, the microindentation hardness testing on the RPV model alloys is presented in Section 5.4.3.1.

5.4.1 SAXS

The data was reduced using the method described in Section 3.4.1.2. The absolute I(q) scattering profiles for the model alloys can be seen in the following figures measured at E = 6.809 keV to exclude anomalous dispersions. The scattering profiles for each RPV model alloy were studied to evaluate the effectiveness of the thermal ageing.

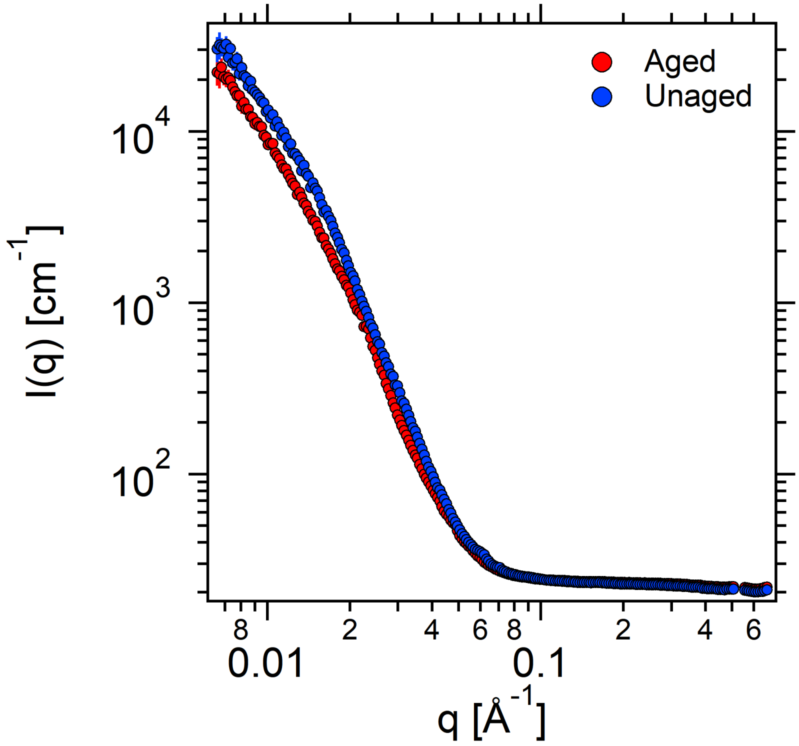

Figure 5.11: Graph showing I(q) scattering profiles for 1.2 AM and 1.2 TA.

For sample composition 1.2, the aged and unaged I(q) profiles are shown in Figure 5.11. At low q, it is observed that the unaged intensity is slightly higher than that in the aged sample. This is likely to be an artefact from the reduction process arising from differences in data normalisation close to the beamstop and is not judged to be significant. In both the unaged and aged samples, the scattering is does not appear to be purely Porod in nature. This should be treated with caution as it could be an artefact from the data reduction, since it is noted that there are minimal differences between samples 1.2 AM and 1.2 TA.

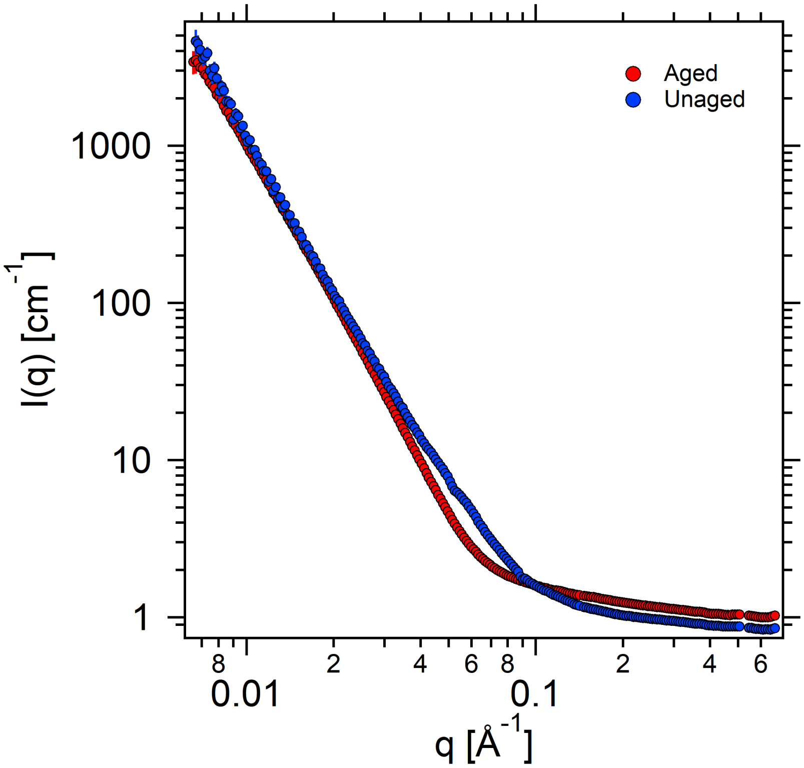

Figure 5.12: Graph showing I(q) scattering profiles for 1.3 AM and 1.3 TA.

The scattering profiles for samples 1.3 AM and 1.3 TA are shown in Figure 5.12. Fitting of a Porod law showed no significant convergence in sample 1.3 TA, indicating the presence of non-grain boundary scattering features. The unaged sample intensity deviates from a Porod law and exceeds intensity from the aged sample in the mid-q range, however this can be attributed to spurious streaks in the detector image from external scattering events. This initial analysis on 1.3 TA is not conclusive and so merits further investigation, for example using ASAXS and SANS, especially since precipitation has been observed in binary FeCu alloys under similar ageing conditions in [163, 22].

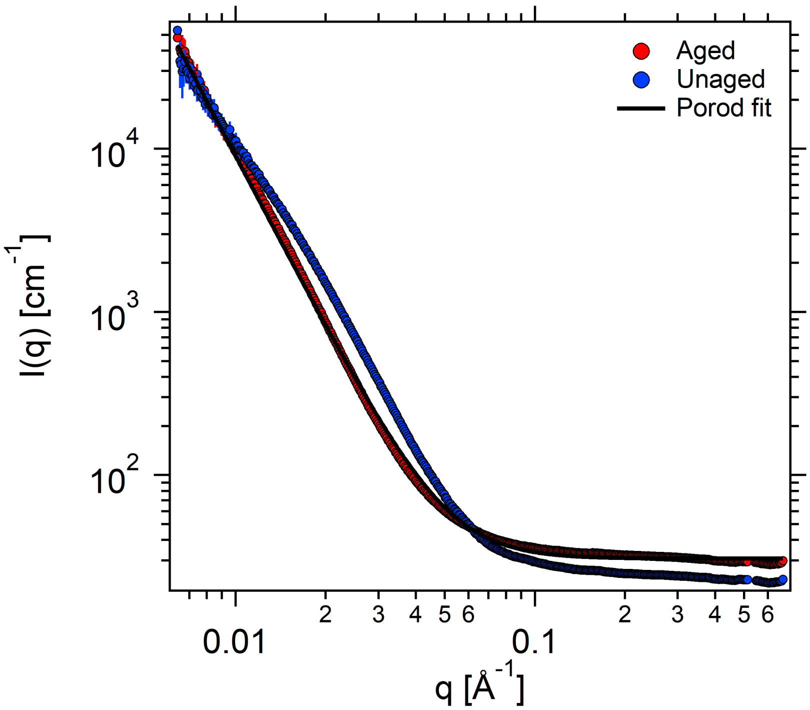

Figure 5.13: Graph showing I(q) scattering profiles for 2.1 AM and 2.1 TA.

There are no observed precipitate scattering events in sample 2.1 TA; the scattering is purely Porod arising from the grain boundaries, as shown by the fitting of a power law with exponent 3.492 ± 0.004 in Figure 5.13. This trend was also observed in samples 2.2 AM and 2.2 TA respectively, owing to the similarity in composition. The unaged sample appears to have a non-Porod scattering contribution at low-q. This is likely an artefact and is not conducive with precipitate scattering in the unaged sample, since the aged counterpart is purely Porod scattering.

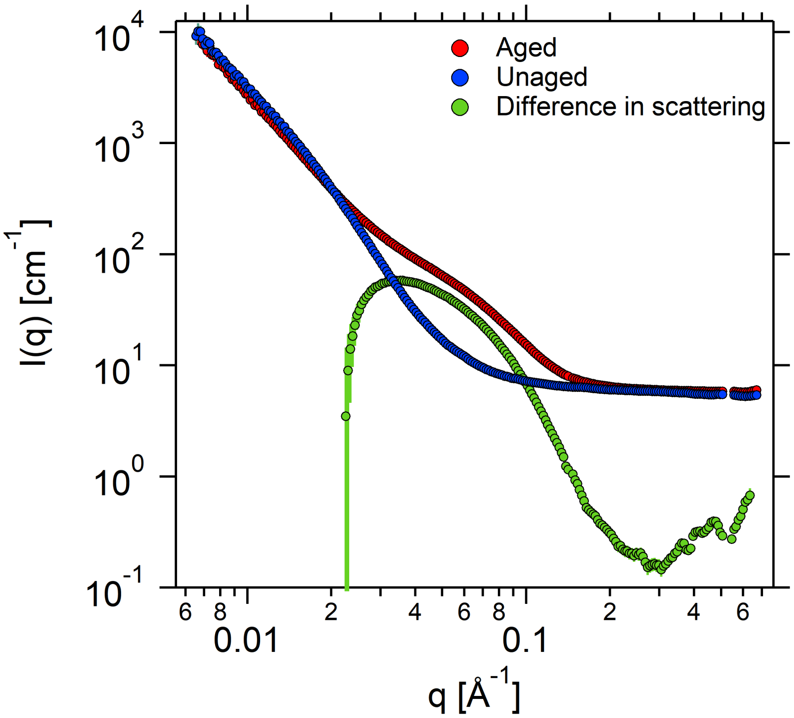

Figure 5.14: Graph showing I(q) scattering profiles for 3 AM and 3 TA.

There is a clear difference in scattering between 3 AM and 3 TA, as shown in Figure 5.14. Sample 3 AM is purely Porod scattering, indicated by a fitted exponent of 3.639 ± 0.005. Subtracting the Porod contribution from 3 TA leaves a clear peak around q = 0.06 Å^{-1}. A peak in the scattering indicates a deviation from Porod scattering that could be attributed to potential induced precipitation events.

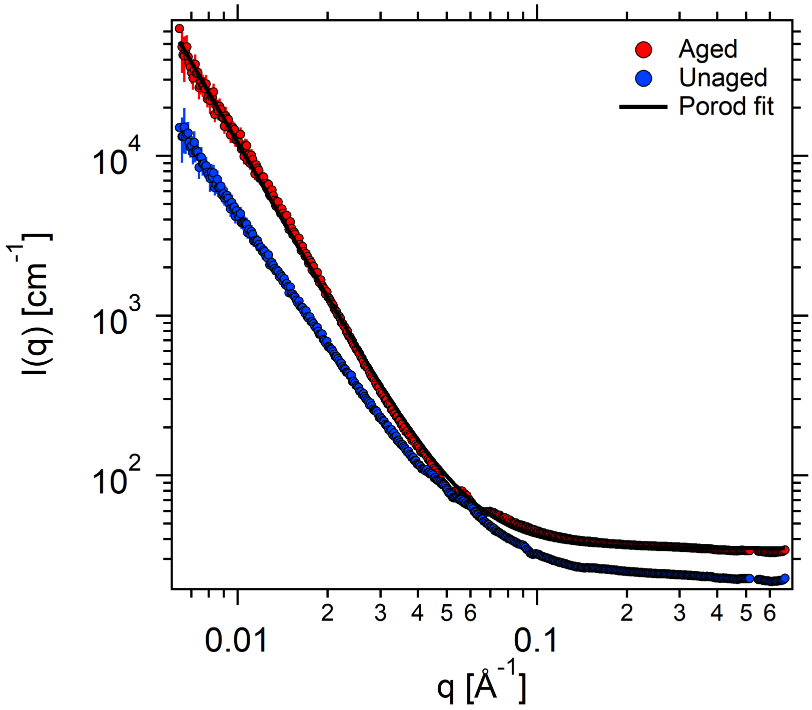

Figure 5.15: Graph showing I(q) scattering profiles for 4 AM and 4 TA, with fitted Porod contribution.

There are no detectable scattering events in sample 4 TA. The scattering is purely Porod arising from the grain boundaries, as shown by the fit in Figure 5.15 with exponent 3.753 ± 0.003.

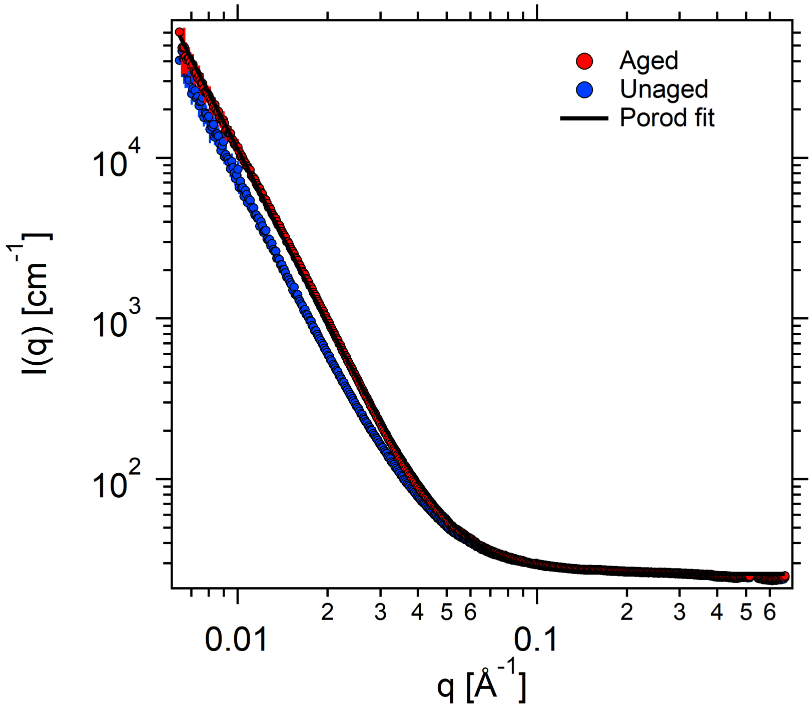

Figure 5.16: Graph showing I(q) scattering profiles for 5.1 AM and 5.1 TA, with fitted Porod contribution.

The scattering of sample 5.1 TA was found to be purely Porod in nature, with a fitted exponent of 3.641

± 0.003, as shown in Figure 5.16. This implies there is no significant precipitation in this sample. The scattering for sample 5.2 TA was found to have the same trend, owing to its similarity in composition and the use of the same thermal ageing parameters.

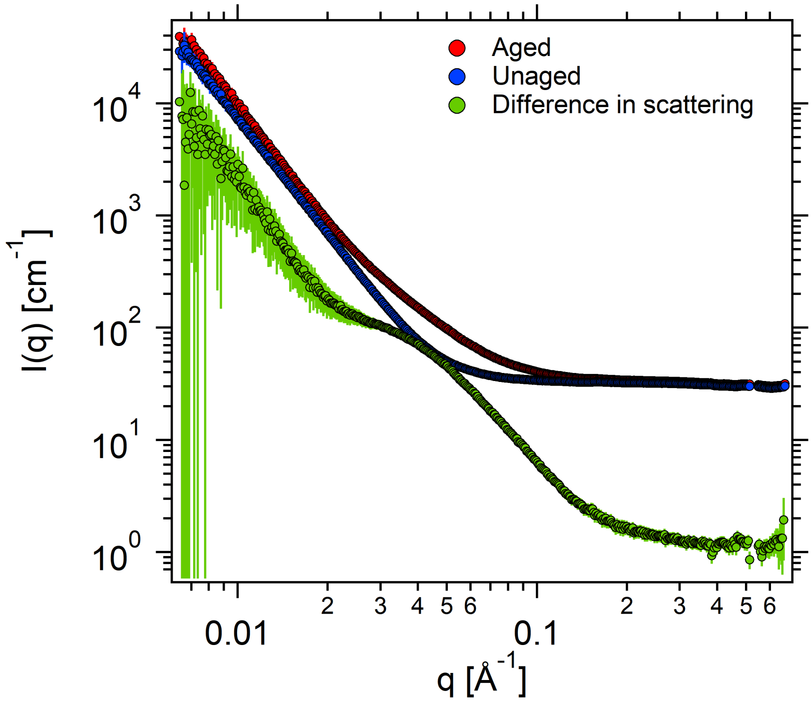

Figure 5.17: Graph showing I(q) scattering profiles for 6.2 AM and 6.2 TA, with fitted Porod contribution.

There is a clear observable difference in scattering between 6.2 TA and 6.2 AM, as shown in Figure 5.17. A Porod law has been fitted to 6.2 AM, with exponent 3.608 ± 0.003, showing purely grain boundary scattering. The thermal ageing induced damage visible in 6.2 TA should be investigated further through empirical modelling. The observed scattering from sample 6.1 TA was very similar, given the closeness in composition and the exposure to the same thermal ageing conditions.

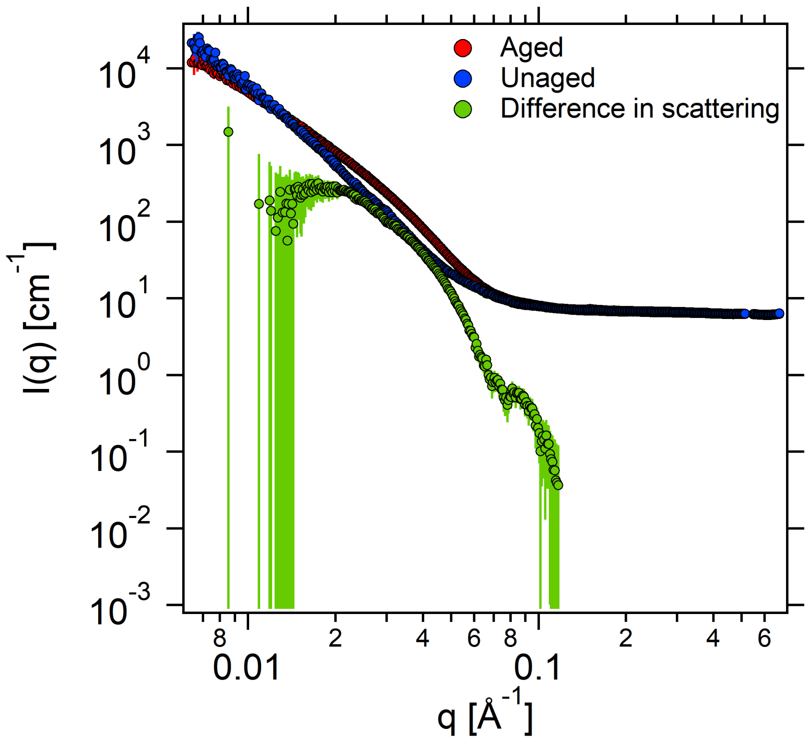

Figure 5.18: Graph showing I(q) scattering profiles for 7.1 AM and 7.1 TA.

There is a difference in scattering between samples 7.1 AM and 7.1 TA, as shown in Figure 5.18. Sample 7.1 AM is purely Porod scattering, indicated by a fitted exponent of 3.558 ± 0.003. The potential thermal ageing induced damage in 7.1 TA should be investigated further through empirical modelling. This should be treated with caution as it is unlikely to observe significant precipitation in sample 7.1 TA when compared to 1.2 TA, due to the solubility of Cu that drives the nucleation process at these ageing conditions [16].

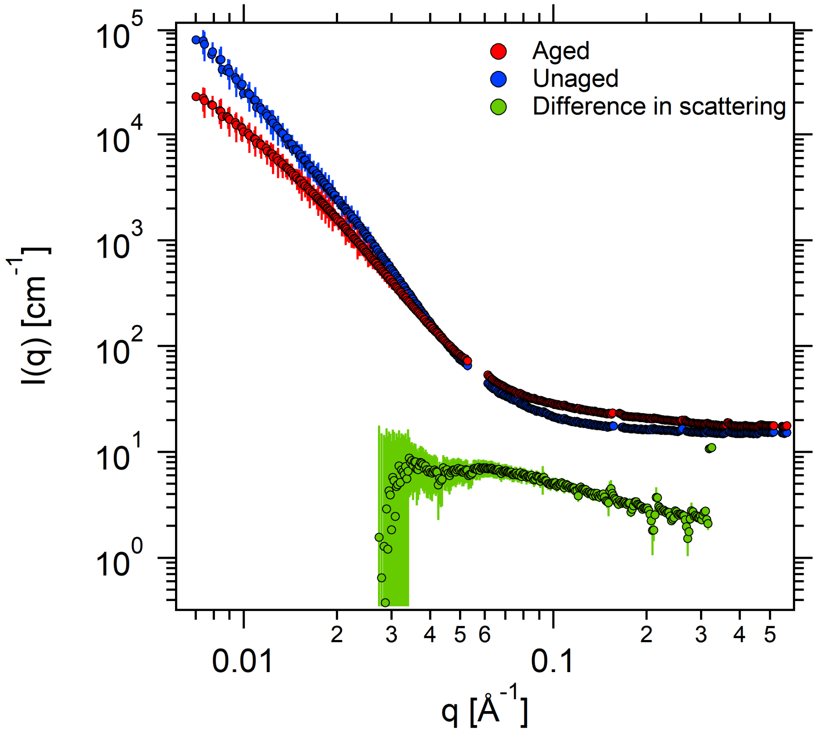

Figure 5.19: Graph showing I(q) scattering profiles for 7.2 AM and 7.2 TA, with fitted Porod contribution.

For sample 7.2 TA, the difference in scattering in the mid q range compared to 7.2 AM in Figure 5.19 warrants further investigation, especially since sample 1.3 TA has been identified as significant. Hence, selection of 7.2 TA for further analysis will allow for a study on the contribution of Ni to thermal ageing induced precipitation in FeCu. The scattering of the unaged sample is Porod in nature, with a fitted exponent of 3.577 ± 0.004.

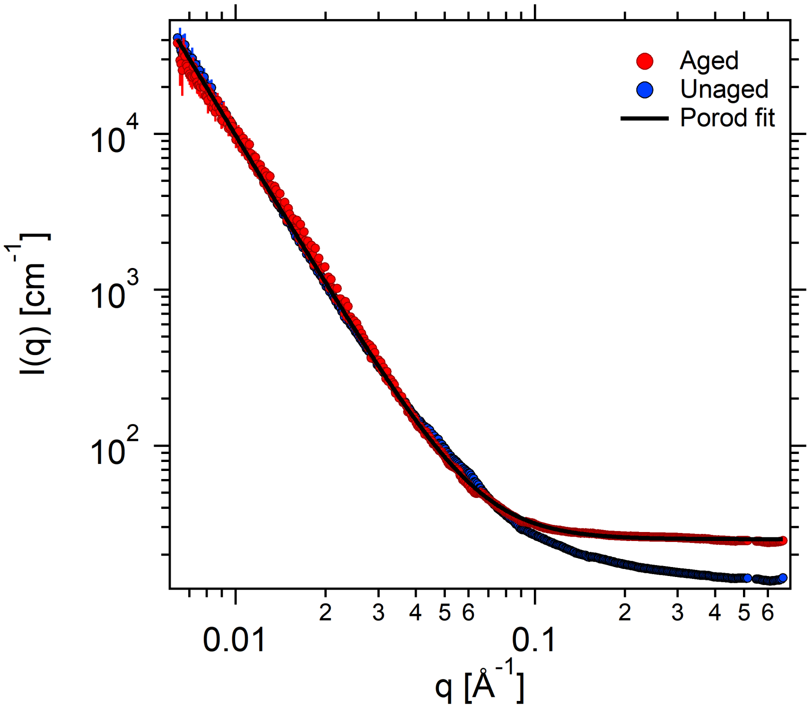

Figure 5.20: Graph showing I(q) scattering profiles for 8 AM and 8 TA, with fitted Porod contribution.

Empirical model fitting to the scattering from sample 8 TA finds no significant evidence of precipitation; the fit is purely Porod with an exponent of 3.671 ± 0.003, as shown in Figure 5.20. Interestingly, sample 8 AM deviates from a Porod fit at high q due to an increased background contribution. This has been investigated and can be attributed to a mismatch during data reduction caused by the difference in thickness between the aged and unaged samples, where the transmission of sample 8 TA is 1.4 times that of 8 AM, meaning the overall 8 AM scattered intensity is lower. Accounting for this and checking for any non-Porod scattering through a log-normal sphere and power law fit to sample 8 AM using the calculated matrix scattering length density, unphysical fitting parameters with unreasonably large errors were found (for example median radius = 0.03 ± 6993 Å, which is outside the minimum observable length scale of 9.38 Å).

The above SAXS results on the thermal aged alloys were used to determine the samples of interest that had significant induced precipitation events compared to their as-made counterparts. The samples with potential non-Porod scattering contributions as were identified as

- 1.2 TA
- 1.3 TA

- 3 TA
- 6.1 TA
- 6.2 TA
- 7.1 TA
- 7.2 TA

Each was then investigated further using empirical model fitting.

The x-ray scattering length density of a phase in a material, η, is a function of the number densities and bound coherent x-ray scattering lengths of each specific element present (previously calculated in Table 2.2 in Section 2.5.2). The matrix scattering length density, η_m, was calculated for each sample of interest using equation 2.32 in Section 2.5.1.1. The results are presented in Table 2.3. Since these are known values, they were held constant in the empirical model fitting.

It was found that for the precipitate-only scattering I(q) profiles (i.e. the Porod-subtracted data) for each sample, the log-normal sphere model to be most representative of true precipitate shape.

For samples 1.2 TA and 7.1 TA where the log-normal model fit parameters are unphysical and have large errors, the effect of Cu and Ni can be investigated using samples 1.3 TA and 7.2 TA instead, where precipitation with higher Cu levels is more clearly observed.

These samples of interest were then investigated further using ASAXS. The data was fully reduced to obtain the scattering profiles as a function of x-ray energy at each elemental absorption edge (Fe, Cu, Ni and Mn). The results are not documented here, since a similar outcome as for the long thermally aged welds from Chapter 4 was observed. Due to the dominance of Fe in the matrix, a significant change in contrast due to anomalous dispersions was only observed at the Fe edge. At the Cu, Mn and Ni edges there was minimal contrast change as a function of x-ray energy and so no compositional information could be reliably subtracted.

The identified set of down-selected model alloy compositions were investigated using SANS to extract structural and compositional precipitate information through an in-situ aging study and the separation of nuclear and magnetic scattering contributions. The SANS results are presented in Section 5.4.2.

5.4.2 SANS

5.4.2.1 In-situ ageing study

Three samples of interest were in-situ thermally aged: sample 1.3 FA ($FeCu_{1.23}$), sample 3 FA ($FeCu_{1.24}Mn_{1.33}Ni_{1.7}$ and 7.2 FA ($FeCu_{1.24}Ni_{2.19}$). Unfortunately a full set of ageing measurements is unavailable for sample 7.2 FA due to a misalignment error with the translatable motors during the experiment. The limited data is shown for comparative purposes only. The choice of these alloys was specific, such that one can directly compare the effect of Ni and Mn on the precipitate properties.

Using the experimental method outlined in Section 5.3.4.1 and 5.3.4.3, I(q) profiles were obtained on an absolute scale for each sample as a function of ageing time. These are shown for samples 1.3 FA, 3 FA, and 7.2 FA in Figures 5.21, 5.22, and 5.23 respectively. The scattering measurements taken at 100 °C are also included to show the Porod-only scattering before the precipitation process had begun. An additional high q scattering measurement (without a corresponding medium q measurement) for samples 1.3 FA and 3 FA at short ageing timescales has been included since they show a clear deviation from the I(q) Porod-only scattering at 550 °C.

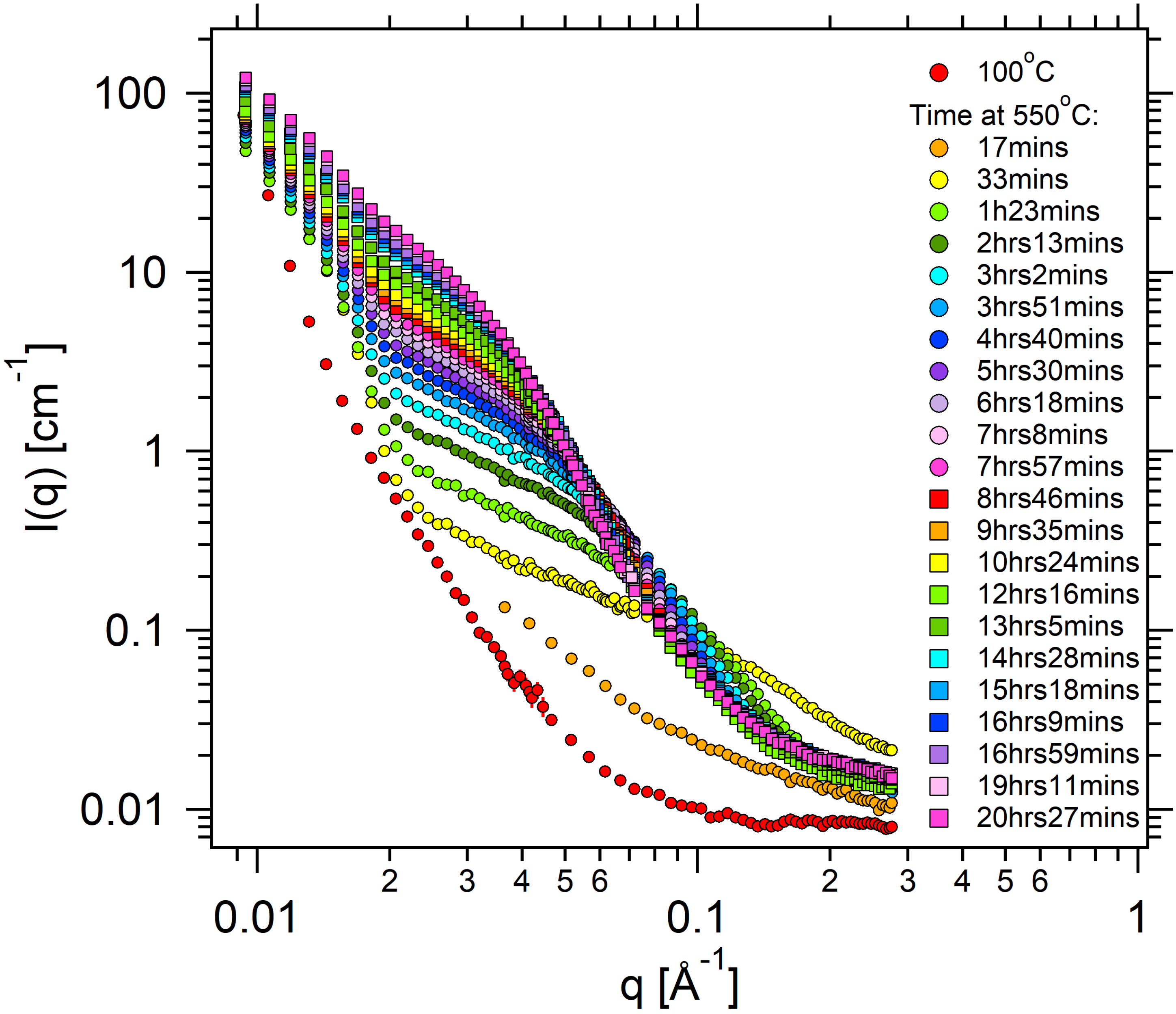

Figure 5.21: Graph showing I(q) profiles for 1.3 FA ($FeCu_{1.23}$) as a function of ageing time at 550 °C.

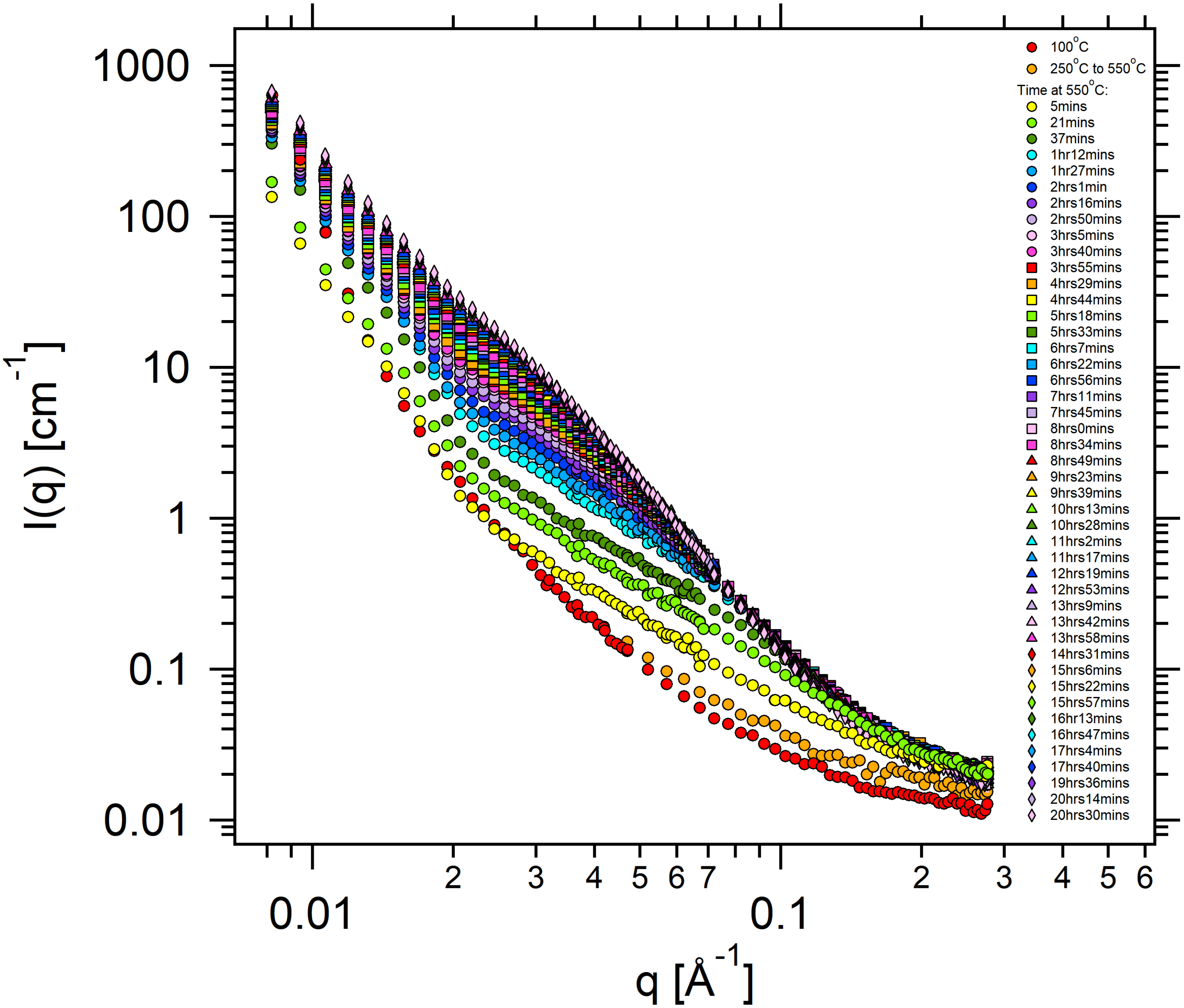

Figure 5.22: Graph showing I(q) profiles for 3 FA ($FeCu_{1.24}Mn_{1.33}Ni_{1.73}$) as a function of ageing time at 550 °C.

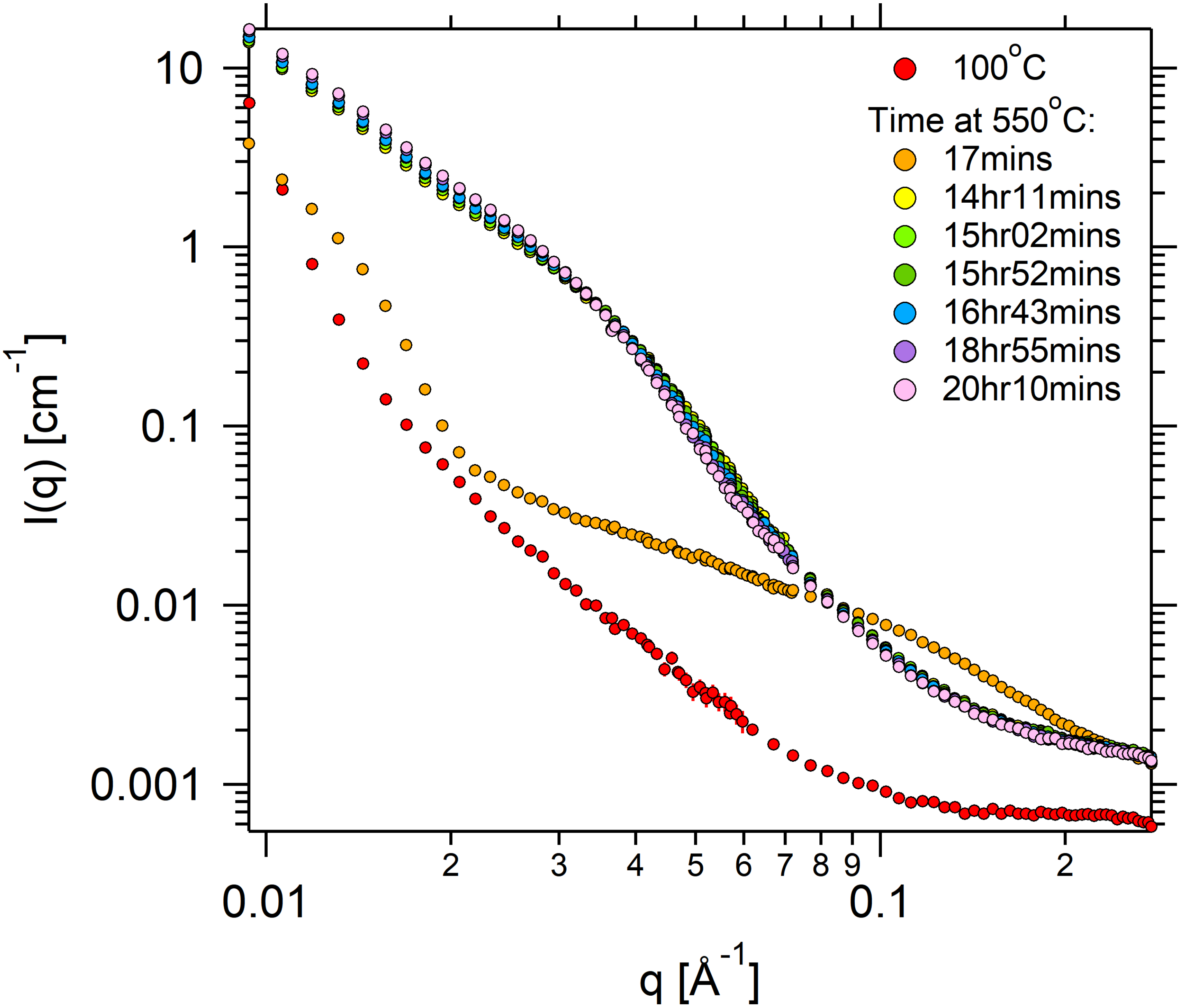

Figure 5.23: Graph showing I(q) profiles for 7.2 FA ($FeCu_{1.24}Ni_{2.19}$) as a function of ageing time at 550 °C. Note that the measurements on this sample are limited due to an experimental misalignment error.

For each I(q) profile for each sample, empirical model fitting was carried out. The process is analogous to that outlined in Section 3.4.2.2, whereby a series of models were fitted to identify the best-estimate option. The log-normal sphere was consistenly the better fitting form factor model; this is reflected in similar small-angle scattering studies on precipitation in FeCu binary systems [111].

Through fitting the 100 °C scattering profiles, and from an understanding of behaviour from similar crystalline steel systems (e.g in Chapter 4), each aged sample was found to contain Porod scattering contributions from the grain boundaries.

There are two options to account for such scattering: subtract the 100 °C profile from each ageing profile, or include the Porod law in each model fit. It was found that the latter was a better choice because it accounts for local changes to grain boundaries specific to the time exposed at the elevated temperature of 550 °C since kinetics are likely to be different there to at 100 °C. As such, the Porod scattering law was combined into the fitting model to simplify the manipulation of the large number of datasets.

Since sample 1.3 FA is a binary FeCu system, the scattering length density of the precipitates and the matrix can be explicitly calculated allowing for the extraction of absolute volume fractions of precipitates. The scattering length densities ρ_p and ρ_m were calculated using equation 2.21, and then held constant during the fit as 6.555 x 10^{-6} Å^{-2} and 8.006 x 10^{-6} Å^{-2} respectively, under the assumption that only Cu precipitates out.

Table 5.7: Fitted parameters from the log-normal sphere model to the I(q) profiles as a function of ageing time for sample 1.3 FA. The brackets denote the errors on each value.

Time [mins]	**Volume fraction [arb.]**	**Median radius [Å]**	**σ [arb.]**	**BG [cm^{-1}]**
33	0.0589 (0.0024)	5.6376 (0.3515)	0.4806 (0.0123)	0.0158 (0.0004)
83	0.0342 (0.0002)	17.4833 (0.1348)	0.2736 (0.0032)	0.0130 (0.0001)
133	0.0370 (0.0001)	21.5034 (0.1063)	0.2614 (0.0024)	0.0133 (0.0001)
182	0.0381 (0.0001)	24.5519 (0.1009)	0.2604 (0.0022)	0.0134 (0.0001)
231	0.0392 (0.0001)	27.1933 (0.0976)	0.2588 (0.0020)	0.0135 (0.0001)
280	0.0395 (0.0001)	29.5853 (0.0967)	0.2566 (0.0020)	0.0136 (0.0001)
330	0.0399 (0.0001)	31.4878 (0.0984)	0.2575 (0.0020)	0.0135 (0.0001)
378	0.0398 (0.0001)	33.5524 (0.1015)	0.2555 (0.0020)	0.0135 (0.0001)
428	0.0391 (0.0002)	35.8126 (0.1062)	0.2462 (0.0021)	0.0134 (0.0001)
477	0.0382 (0.0002)	37.9952 (0.1122)	0.2355 (0.0022)	0.0132 (0.0001)
526	0.0384 (0.0002)	39.8802 (0.1223)	0.2317 (0.0023)	0.0133 (0.0001)
575	0.0364 (0.0002)	42.3468 (0.1325)	0.2187 (0.0024)	0.0128 (0.0001)
624	0.0364 (0.0002)	44.3048 (0.1322)	0.2127 (0.0023)	0.0127 (0.0001)
736	0.0364 (0.0002)	47.8026 (0.1319)	0.2112 (0.0021)	0.0121 (0.0001)
785	0.0416 (0.0003)	48.9773 (0.1333)	0.2151 (0.0021)	0.0136 (7.5281)
868	0.0490 (0.0003)	51.0307 (0.1218)	0.2262 (0.0018)	0.0147 (0.0001)
918	0.0510 (0.0003)	52.0604 (0.1252)	0.2332 (0.0017)	0.0147 (0.0001)
969	0.0530 (0.0003)	53.0455 (0.1247)	0.2358 (0.0017)	0.0148 (0.0001)
1019	0.0544 (0.0003)	54.0073 (0.1292)	0.2419 (0.0017)	0.0148 (0.0001)
1151	0.0585 (0.0003)	57.1663 (0.1284)	0.2440 (0.0016)	0.0149 (0.0001)
1227	0.0605 (0.0003)	58.3959 (0.1297)	0.2467 (0.0016)	0.0150 (0.0001)

For sample 3 FA, ρ_m was calculated as 7.876 x 10^{-6} Å^{-2} and held constant in the fit. Holding the volume fraction constant at an arbitrary value of 0.01 allows for the extraction of the relative ρ_p in the fit.

Table 5.8: Fitted parameters from the log-normal sphere model to the I(q) profiles as a function of ageing time for sample 3 FA. The brackets denote the errors on each value.

Time [mins]	**Median radius [Å]**	σ **[arb.]**	ρ_p **[Å^{-2}]**	**BG [cm^{-1}]**
37	9.3043 (0.3573)	0.5026 (0.0074)	4.57 (0.02) x 10^{-6}	0.0185 (0.0003)
72	13.8451 (0.3573)	0.4552 (0.0074)	4.36 (0.02) x 10^{-6}	0.0205 (0.0003)
87	13.6424 (0.2824)	0.4830 (0.0059)	4.27 (0.01) x 10^{-6}	0.0203 (0.0002)
121	14.9901 (0.2703)	0.4889 (0.0054)	4.13 (0.01) x 10^{-6}	0.0216 (0.0002)
136	13.8873 (0.2876)	0.5252 (0.0060)	4.05 (0.01) x 10^{-6}	0.0206 (0.0002)
170	14.4795 (0.2860)	0.5379 (0.0059)	3.93 (0.01) x 10^{-6}	0.0211 (0.0002)
185	12.5212 (0.3034)	0.5906 (0.0068)	3.81 (0.02) x 10^{-6}	0.0200 (0.0002)
220	13.8523 (0.2920)	0.5736 (0.0062)	3.76 (0.02) x 10^{-6}	0.0212 (0.0002)
235	12.5300 (0.3083)	0.6121 (0.0070)	3.67 (0.02) x 10^{-6}	0.0208 (0.0002)
269	13.7623 (0.3014)	0.5933 (0.0064)	3.66 (0.02) x 10^{-6}	0.0214 (0.0002)
284	12.1802 (0.3184)	0.6384 (0.0074)	3.54 (0.02) x 10^{-6}	0.0201 (0.0002)
318	13.4257 (0.3075)	0.6149 (0.0067)	3.54 (0.02) x 10^{-6}	0.0210 (0.0002)
333	12.0507 (0.3262)	0.6547 (0.0077)	3.43 (0.02) x 10^{-6}	0.0203 (0.0002)
367	12.9886 (0.3206)	0.6379 (0.0072)	3.44 (0.02) x 10^{-6}	0.0206 (0.0002)
382	12.6701 (0.3297)	0.6516 (0.0076)	3.39 (0.02) x 10^{-6}	0.0203 (0.0002)
416	14.3808 (0.3249)	0.6170 (0.0069)	3.47 (0.02) x 10^{-6}	0.0212 (0.0002)
431	13.2260 (0.3402)	0.6476 (0.0077)	3.37 (0.03) x 10^{-6}	0.0199 (0.0002)
465	13.4791 (0.3391)	0.6438 (0.0076)	3.37 (0.03) x 10^{-6}	0.0204 (0.0002)
480	13.3678 (0.3492)	0.6561 (0.0079)	3.30 (0.03) x 10^{-6}	0.0197 (0.0002)
514	13.5736 (0.3520)	0.6513 (0.0079)	3.32 (0.03) x 10^{-6}	0.0197 (0.0002)
529	15.1668 (0.3360)	0.6182 (0.0070)	3.38 (0.03) x 10^{-6}	0.0203 (0.0002)
563	14.9698 (0.3502)	0.6323 (0.0075)	3.31 (0.03) x 10^{-6}	0.0203 (0.0002)
579	14.7935 (0.3657)	0.6437 (0.0079)	3.27 (0.03) x 10^{-6}	0.0198 (0.0002)
613	16.4663 (0.3578)	0.6091 (0.0073)	3.36 (0.03) x 10^{-6}	0.0203 (0.0002)
628	17.2351 (0.3723)	0.6067 (0.0074)	3.35 (0.04) x 10^{-6}	0.0200 (0.0002)
662	17.5236 (0.3632)	0.6013 (0.0072)	3.34 (0.03) x 10^{-6}	0.0205 (0.0002)
677	17.2905 (0.3740)	0.6113 (0.0075)	3.29 (0.04) x 10^{-6}	0.0197 (0.0002)
739	18.0990 (0.3881)	0.6023 (0.0076)	3.31 (0.04) x 10^{-6}	0.0196 (0.0002)
773	19.4413 (0.3738)	0.5732 (0.0070)	3.42 (0.04) x 10^{-6}	0.0200 (0.0002)
789	19.9617 (0.4219)	0.5746 (0.0078)	3.44 (0.04) x 10^{-6}	0.0194 (0.0002)
822	20.3775 (0.4054)	0.5638 (0.0074)	3.46 (0.04) x 10^{-6}	0.0200 (0.0002)
838	20.8769 (0.4274)	0.5663 (0.0077)	3.41 (0.04) x 10^{-6}	0.0196 (0.0002)
871	21.2873 (0.4181)	0.5599 (0.0075)	3.46 (0.04) x 10^{-6}	0.0190 (0.0002)
906	22.4131 (0.4040)	0.5435 (0.0070)	3.49 (0.04) x 10^{-6}	0.0193 (0.0002)
922	23.0159 (0.4487)	0.5371 (0.0077)	3.56 (0.05) x 10^{-6}	0.0186 (0.0002)
957	23.9938 (0.4589)	0.5189 (0.0076)	3.66 (0.04) x 10^{-6}	0.0195 (0.0002)
973	24.1838 (0.4973)	0.5271 (0.0082)	3.61 (0.05) x 10^{-6}	0.0186 (0.0002)
1007	24.1388 (0.4575)	0.5208 (0.0076)	3.61 (0.05) x 10^{-6}	0.0195 (0.0002)
1024	27.5375 (0.5340)	0.4748 (0.0082)	3.87 (0.05) x 10^{-6}	0.0189 (0.0002)
1060	27.6201 (0.5366)	0.4768 (0.0082)	3.85 (0.05) x 10^{-6}	0.0192 (0.0002)
1176	30.6603 (0.6191)	0.4472 (0.0088)	4.01 (0.05) x 10^{-6}	0.0180 (0.0002)
1214	31.0374 (0.6035)	0.4421 (0.0085)	4.02 (0.05) x 10^{-6}	0.0189 (0.0002)
1230	32.0770 (0.6324)	0.4371 (0.0087)	4.03 (0.05) x 10^{-6}	0.0182 (0.0002)

For sample 7.2 FA, ρ_m was calculated as 8.033 x 10^{-6} Å^{-2} and held constant in the fit. As for 3 FA, holding the volume fraction constant at an arbitrary value of 0.01 allows for the extraction of the relative ρ_p in the fit.

Table 5.9: Fitted parameters from the log-normal sphere model to the I(q) profiles as a function of ageing time for sample 7.2 FA. The brackets denote the errors on each value.

Time [mins]	**Median radius [Å]**	**σ [arb.]**	**ρ_p [Å^{-2}]**	**BG [cm^{-1}]**
17	7.6427 (0.2428)	0.4380 (0.0072)	7.083 (0.001) x 10^{-6}	0.0010 (0.0000)
851	50.2589 (0.2048)	0.3245 (0.0023)	6.908 (0.004) x 10^{-6}	0.0014 (0.0000)
902	52.4925 (0.1967)	0.3160 (0.0021)	6.906 (0.004) x 10^{-6}	0.0014 (0.0000)
952	53.7228 (0.2026)	0.3205 (0.0022)	6.882 (0.004) x 10^{-6}	0.0014 (0.0000)
1003	54.9759 (0.2047)	0.3210 (0.0022)	6.879 (0.004) x 10^{-6}	0.0014 (0.0000)
1135	58.7308 (0.2082)	0.3207 (0.0021)	6.846 (0.004) x 10^{-6}	0.0014 (0.0000)
1210	59.7478 (0.2183)	0.3258 (0.0023)	6.821 (0.005) x 10^{-6}	0.0014 (0.0000)

From the fitted paramters in Tables 5.7, 5.8 and 5.9, the mean radius was calculated using equation 3.21.

The radius as a function of ageing time for samples 1.3 FA, 3 FA, and 7.2 FA is shown in Tables 5.10, 5.11 and 5.12 and Figures 5.24, 5.25, and 5.26 respectively.

Table 5.10: Calculated mean precipitate radius as a function of ageing time for 1.3 FA.

Time [mins]	**Mean radius [Å]**	**Error [Å]**
33	6.328	0.396
83	18.150	0.141
133	22.251	0.111
182	25.398	0.105
231	28.120	0.102
280	30.575	0.101
330	32.549	0.103
378	34.666	0.106
428	36.914	0.111
477	39.064	0.117
526	40.965	0.127
575	43.371	0.138
624	45.319	0.137
736	48.881	0.137
785	50.123	0.138
868	52.353	0.127
918	53.496	0.130
969	54.541	0.130
1019	55.611	0.135
1151	58.894	0.134
1227	60.200	0.136

Table 5.11: Calculated mean precipitate radius as a function of ageing time for 3 FA.

Time [mins]	Mean radius [Å]	Error [Å]
37	10.557	0.407
72	15.357	0.400
87	15.330	0.320
121	16.893	0.308
136	15.941	0.334
170	16.734	0.335
185	14.907	0.366
220	16.329	0.349
235	15.111	0.377
269	16.411	0.365
284	14.933	0.397
318	16.219	0.377
333	14.931	0.411
367	15.919	0.400
382	15.667	0.415
416	17.396	0.400
431	16.312	0.427
465	16.583	0.425
480	16.578	0.442
514	16.780	0.444
529	18.360	0.414
563	18.283	0.436
579	18.198	0.459
613	19.822	0.440
628	20.718	0.457
662	20.997	0.444
677	20.842	0.461
739	21.699	0.476
773	22.912	0.450
789	23.544	0.509
822	23.888	0.486
838	24.507	0.513
871	24.900	0.500
906	25.980	0.479
922	26.587	0.530
957	27.452	0.536
973	27.789	0.584
1007	27.645	0.535
1024	30.822	0.610
1060	30.945	0.613
1176	33.885	0.697
1214	34.223	0.678
1230	35.293	0.709

Table 5.12: Calculated mean precipitate radius as a function of ageing time for 7.2 FA.

Time [mins]	**Mean radius** [Å]	**Error** [Å]
17	8.412	0.269
851	52.976	0.220
902	55.180	0.210
952	56.554	0.217
1003	57.883	0.219
1135	61.830	0.223
1210	63.004	0.235

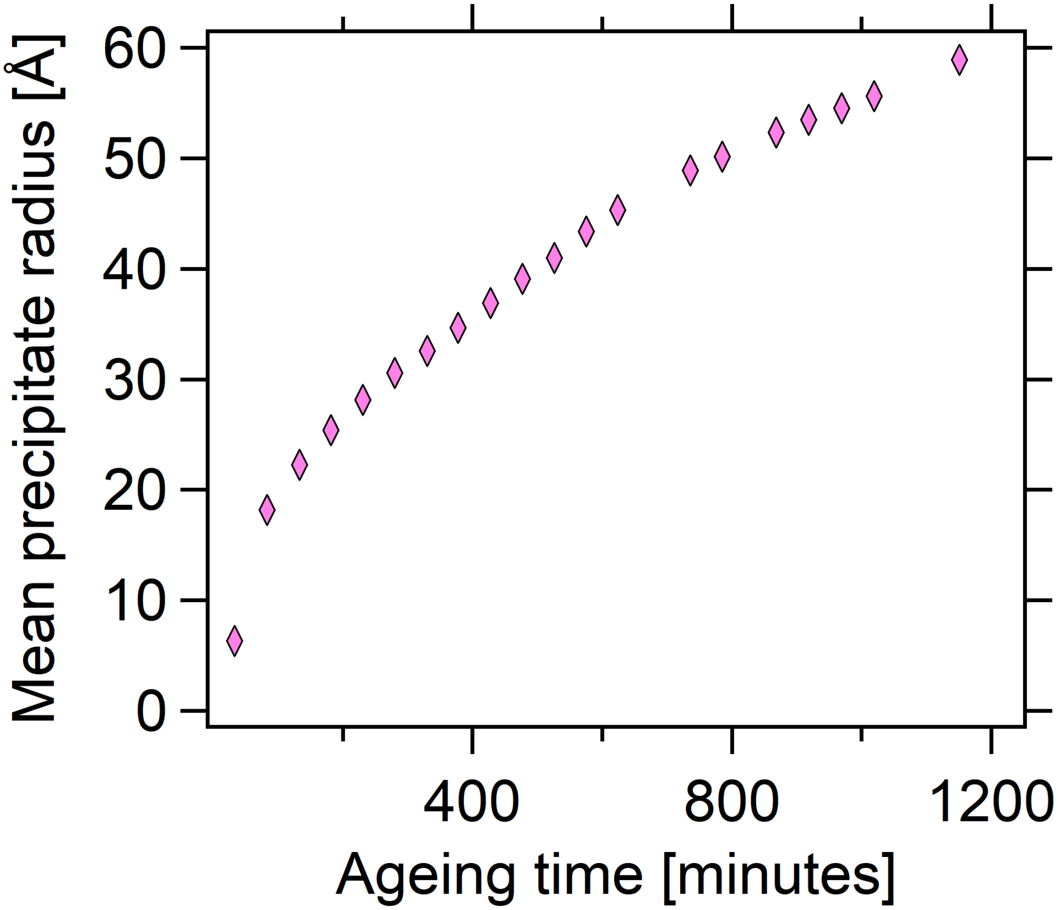

Figure 5.24: Graph showing mean precipitate radius as a function of ageing time for 1.3 FA.

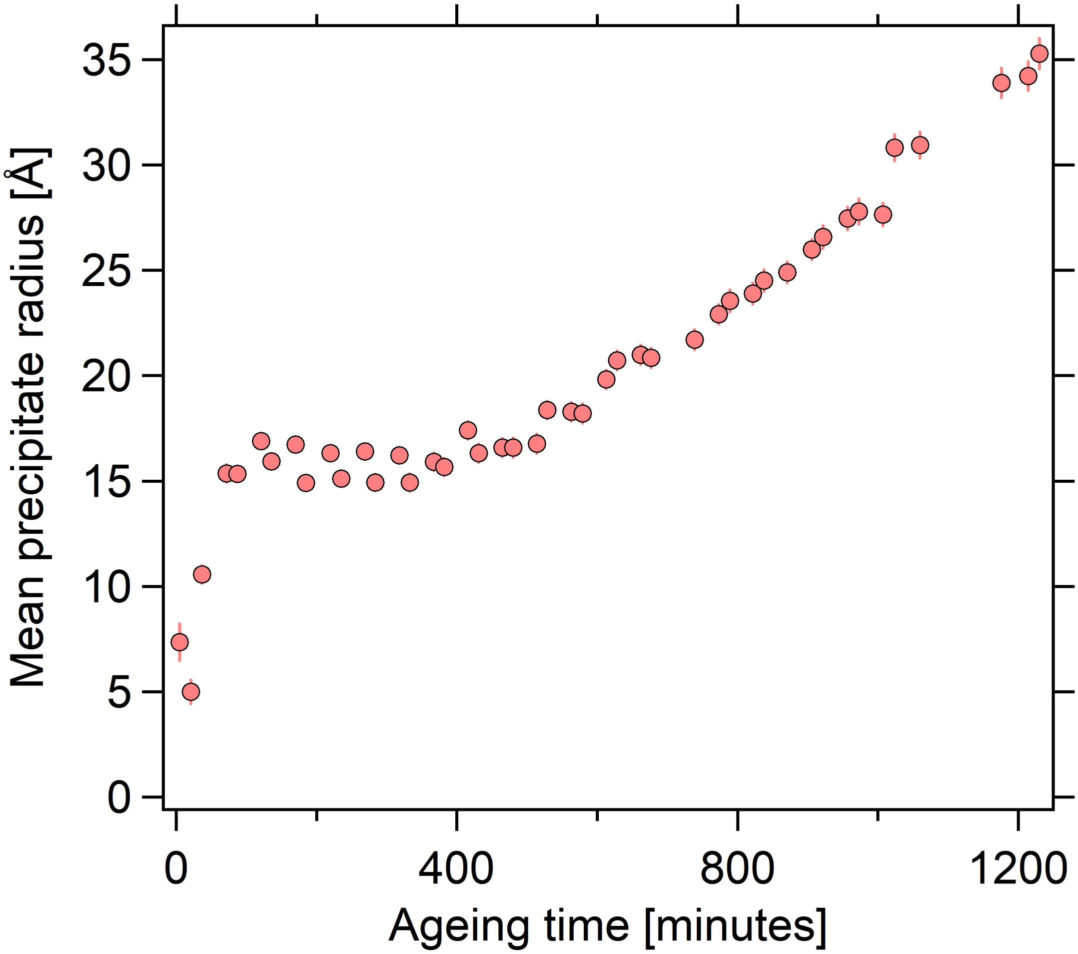

Figure 5.25: Graph showing mean precipitate radius as a function of ageing time for 3 FA.

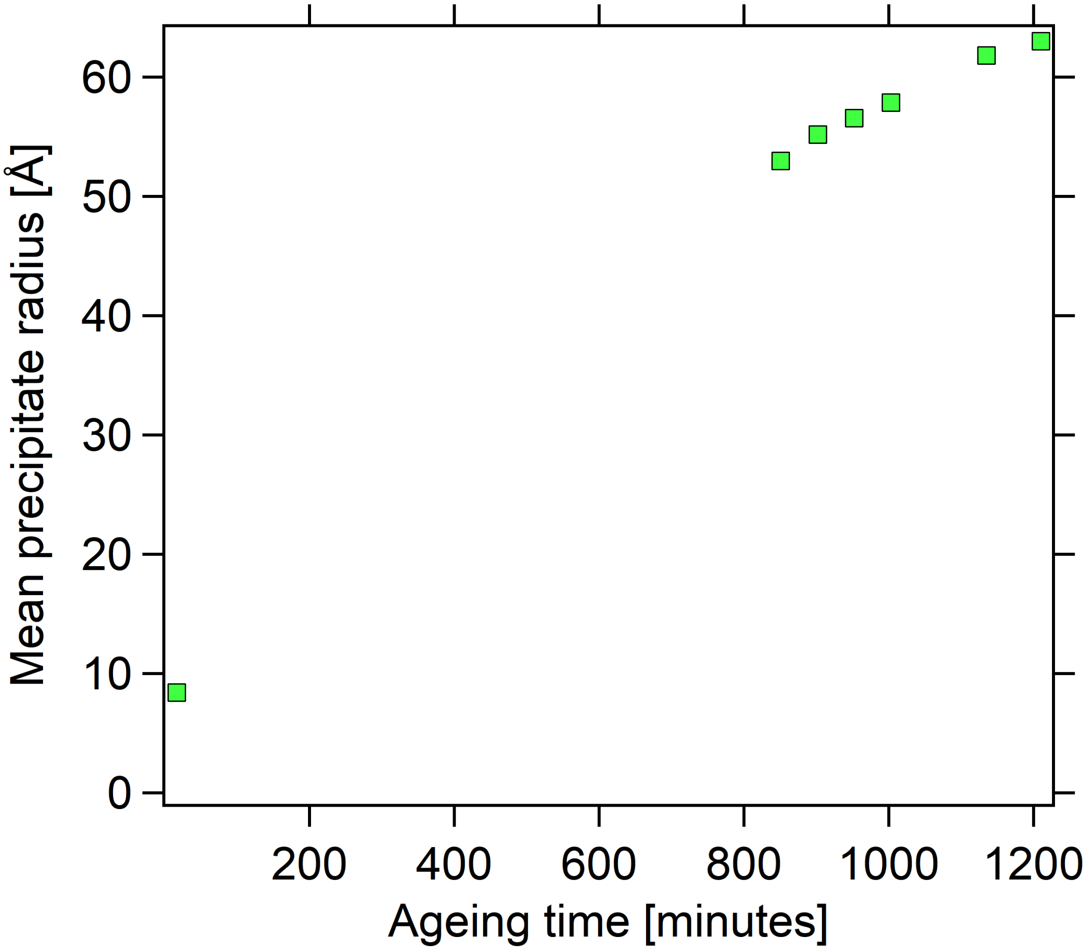

Figure 5.26: Graph showing mean precipitate radius as a function of ageing time for 7.2 FA.

The polydispersity (width of the size disrtibution) as a function of ageing time for samples 1.3 FA, 3 FA, and 7.2 FA is shown in Figures 5.27, 5.28, and 5.29 respectively. The implications of these are discussed in Section 5.5.1.

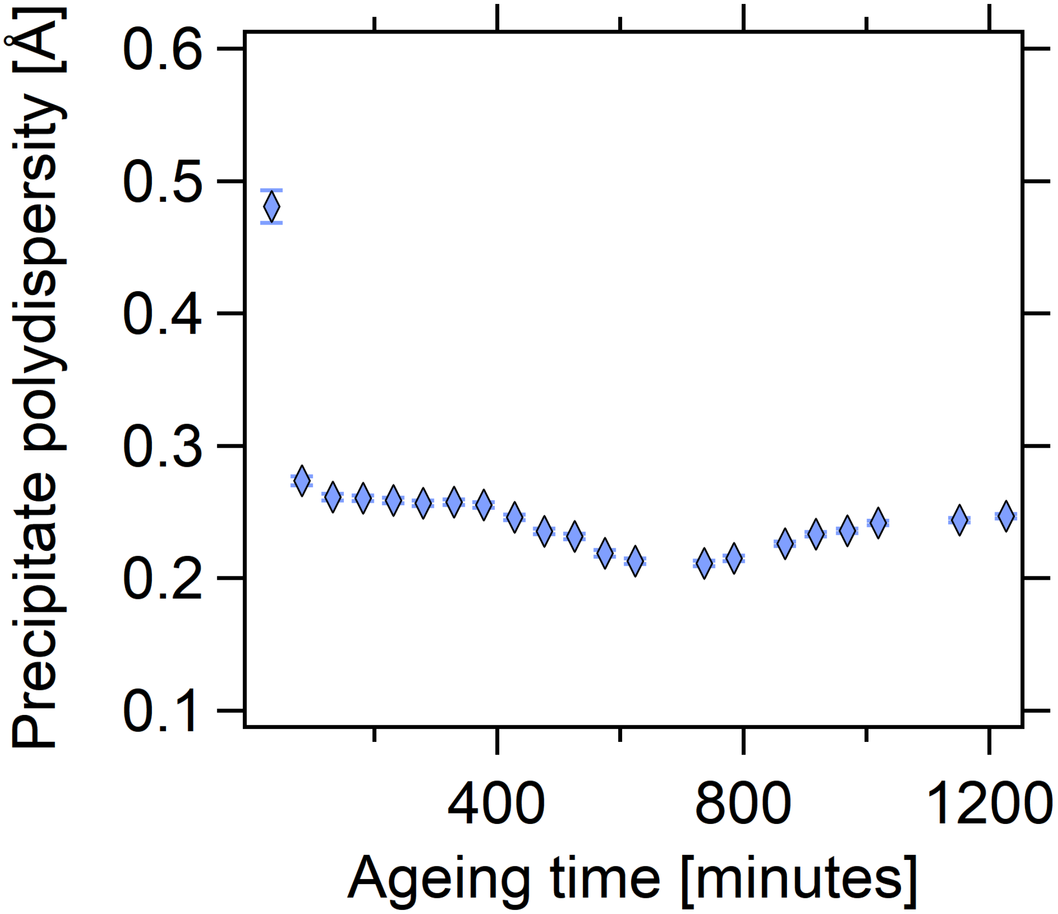

Figure 5.27: Graph showing precipitate polydispersity as a function of ageing time for 1.3 FA.

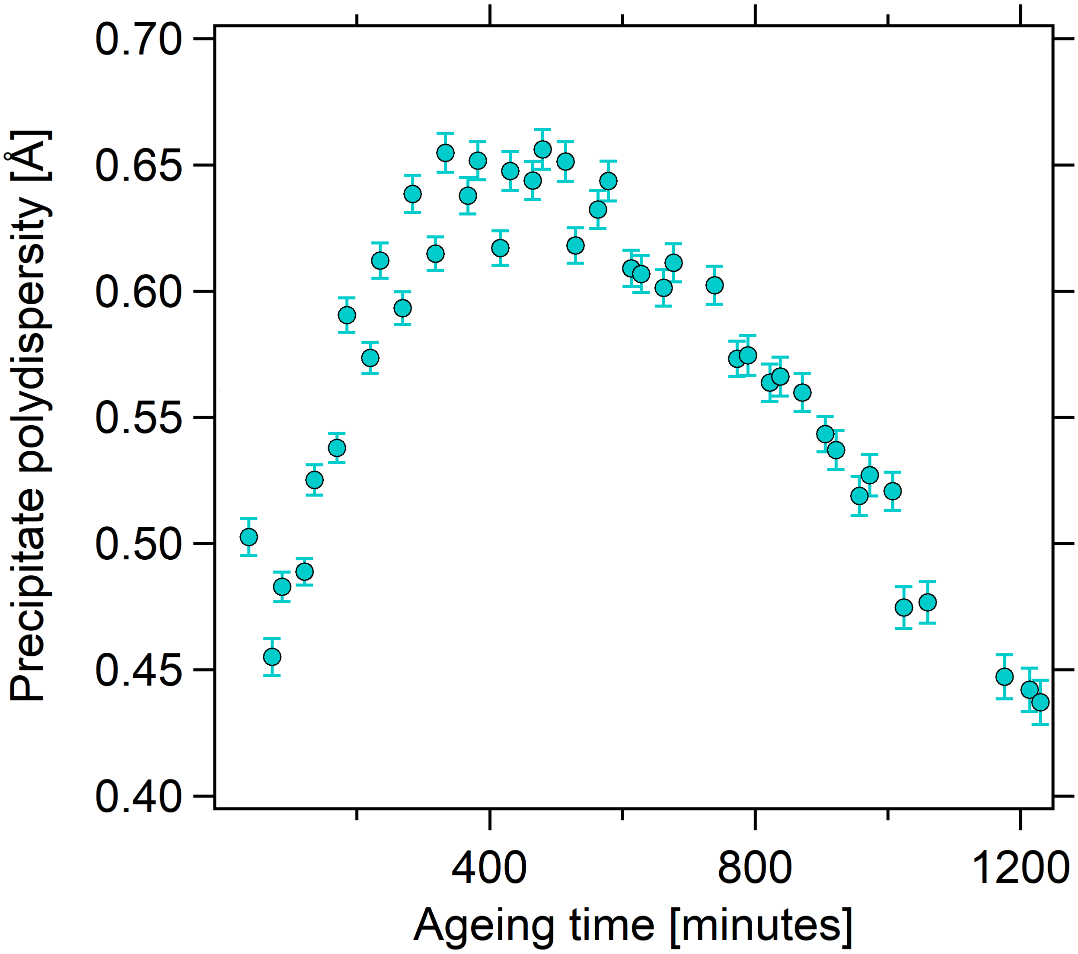

Figure 5.28: Graph showing precipitate polydispersity as a function of ageing time for 3 FA.

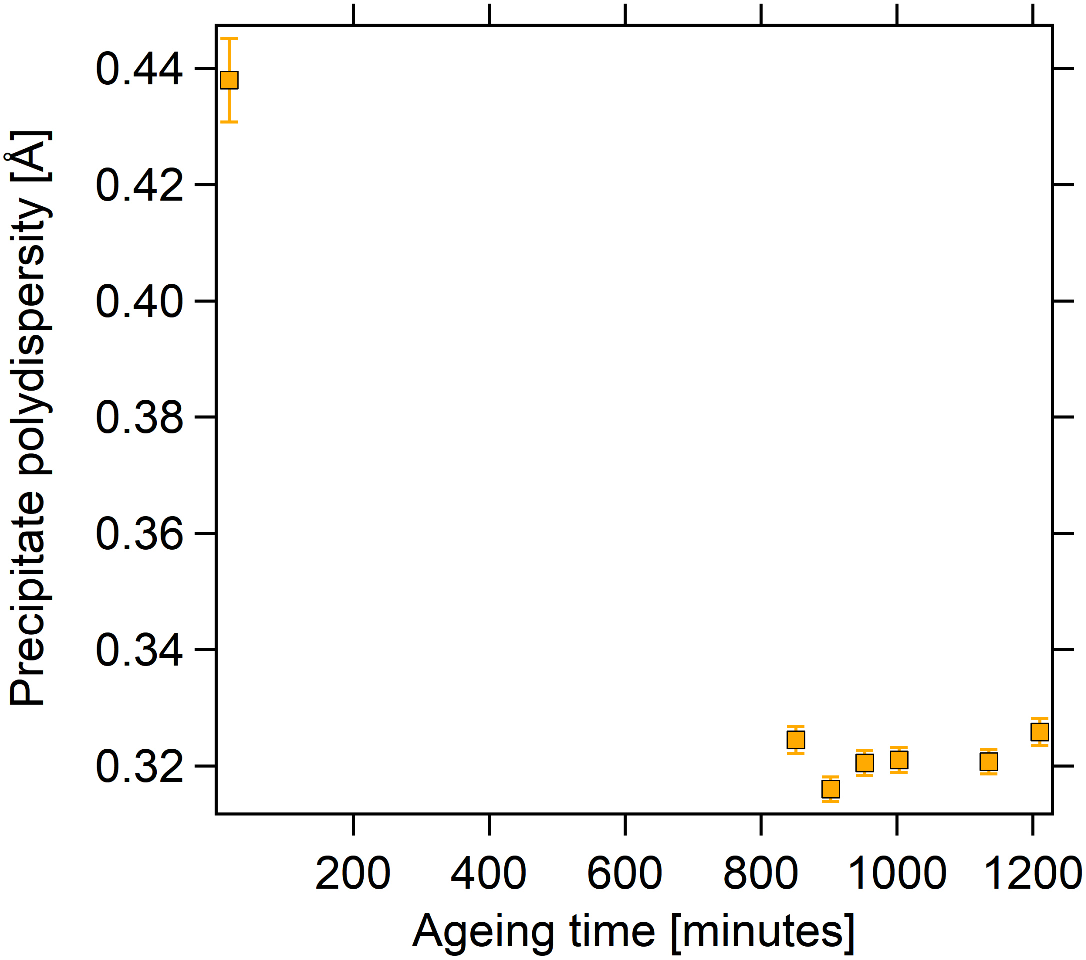

Figure 5.29: Graph showing precipitate polydispersity as a function of ageing time for 7.2 FA.

5.4.2.2 Nuclear and magnetic scattering study

As presented in Chapter 4, the magnetic nature of low alloy steels can be exploited to determine compositional information through the ratio between the magnetic and total scattering intensities. This so-called A ratio can provide information on precipitate composition. This is a particularly valuable tool in this model alloy study where the impact of different alloying elements on thermal ageing induced precipitation events is under review.

In addition, the scattering intensity profiles for each model alloy can provide information on precipitate properties such as size and shape through empirical model fitting.

As discussed in Section 5.4.2.1, there is a clear Porod contribtuion to the scattering profiles of each sample owing to their poycrystalline nature. A combined model that accounts for the form factor of the precipitates and the grain boundary Porod scattering has been used. In each case, mutiple form factor models were used, however the most robust fit was the log-normal sphere model. This is consisten with literature studies on nanoscale precipitates in low alloy RPV steels [139, 164]. This is also consistent with the empirical modelling of the SAXS data presented in Section 5.4.1.

The thermally aged alloy systems of interest where precipitation events have been identified during SAXS and the in-situ ageing study have been selected for this magnetism study. The nuclear and magnetic scattering length densities for the matrix ($\rho_{\mathrm{m,N/M}}$), and precipitates where applicable ($\rho_{\mathrm{p,N/M}}$), have been calculated for each sample using equation 2.21 in Section 2.4.1. The results are presented in Table 5.13 noting that the calculated scattering length densities for sample 1.3 FA are based on the assumption that only Cu precipitates out in the binary system.

Table 5.13: Calculated nuclear and magnetic scattering length densities for the samples of interest with observed precipitation events.

Sample	$\boldsymbol{\rho_{\mathrm{m,N}}}$ [Å^{-2}]	$\boldsymbol{\rho_{\mathrm{m,M}}}$ [Å^{-2}]	$\boldsymbol{\rho_{\mathrm{p,N}}}$ [Å^{-2}]	$\boldsymbol{\rho_{\mathrm{p,M}}}$ [Å^{-2}]
1.3 FA	8.006 x 10^{-6}	4.998 x 10^{-6}	6.555 x 10^{-6}	0
3 (FA and TA)	7.876 x 10^{-6}	4.871 x 10^{-6}	-	-
6.1 TA	7.680 x 10^{-6}	4.747 x 10^{-6}	-	-
6.2 TA	7.681 x 10^{-6}	4.739 x 10^{-6}	-	-
7.2 (FA and TA)	8.033 x 10^{-6}	4.918 x 10^{-6}	-	-

SANS analysis of these samples provides information on the effect of several alloying elements of interest on the thermal ageing precipitation properties, as detailed in Table 5.3.

An analogous method to that employed for the long thermally aged weld study in Section 4.3.2.2 was used to reduce the raw data, including corrections for absolute intensity, radial averaging using sectors, q-range overlapping, and subtraction to separate nuclear and magnetic scattering contributions. The resultant nuclear and magnetic I(q) profiles were analysed using empirical model fitting.

From SAXS, samples were found to contain Porod scattering as expected. This was encorporated into the fitted models. The log-normal sphere model was found to be the best-estimate form factor, consistently producing the lowest chi-squared values with physically realistic fitting parameters. The magnetic and nuclear scattering profiles for each sample were modelled using a global fitting routine that enables linking of certain structural parameters that are the same regardless of the scattering interactions, including median radius and polydispersity.

The global fitting results overlaid on the separated I(q) profiles are shown in the following figures.

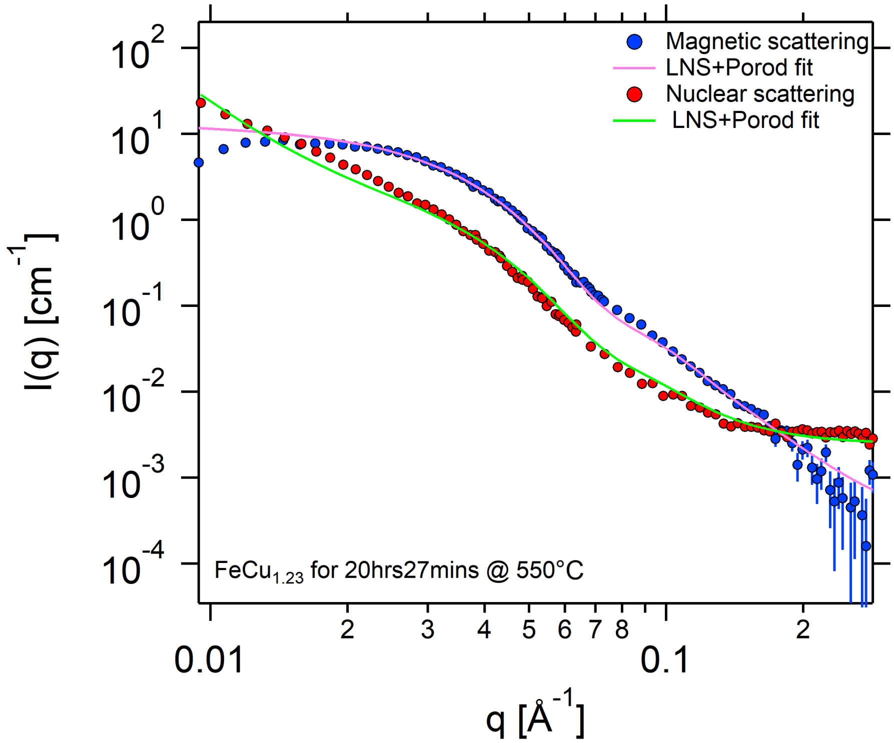

Figure 5.30: Graph showing separated absolute nuclear and magnetic I(q) profiles with fitted log-normal sphere and Porod form factor model for sample 1.3 FA.

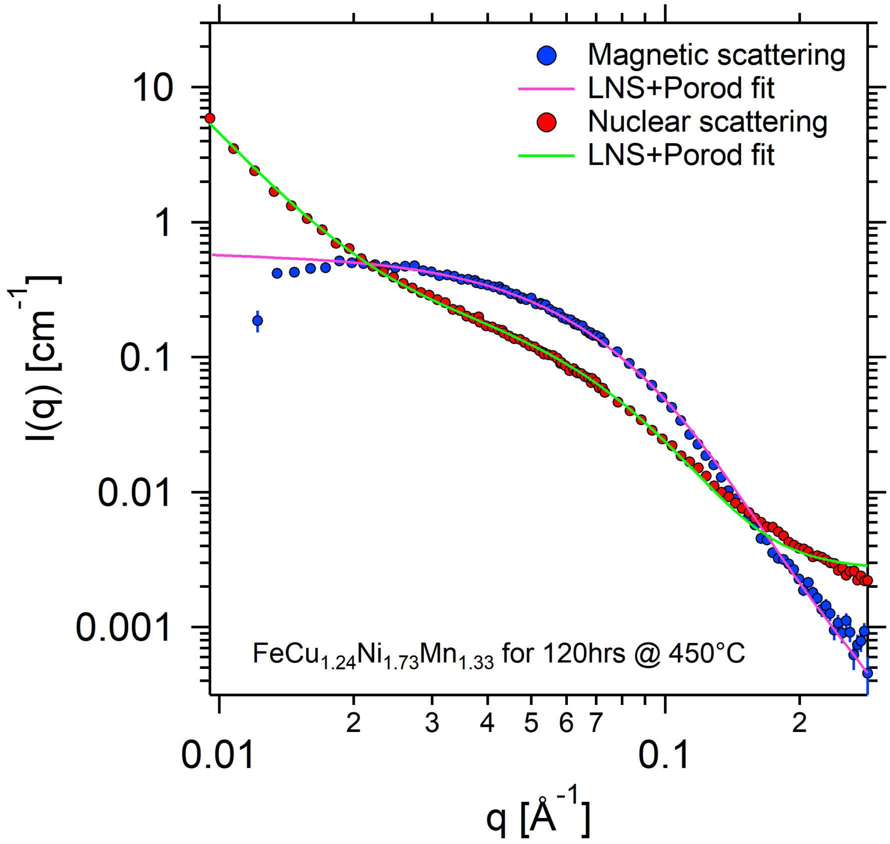

Figure 5.31: Graph showing separated absolute nuclear and magnetic I(q) profiles with fitted log-normal sphere and Porod form factor model for sample 3 TA.

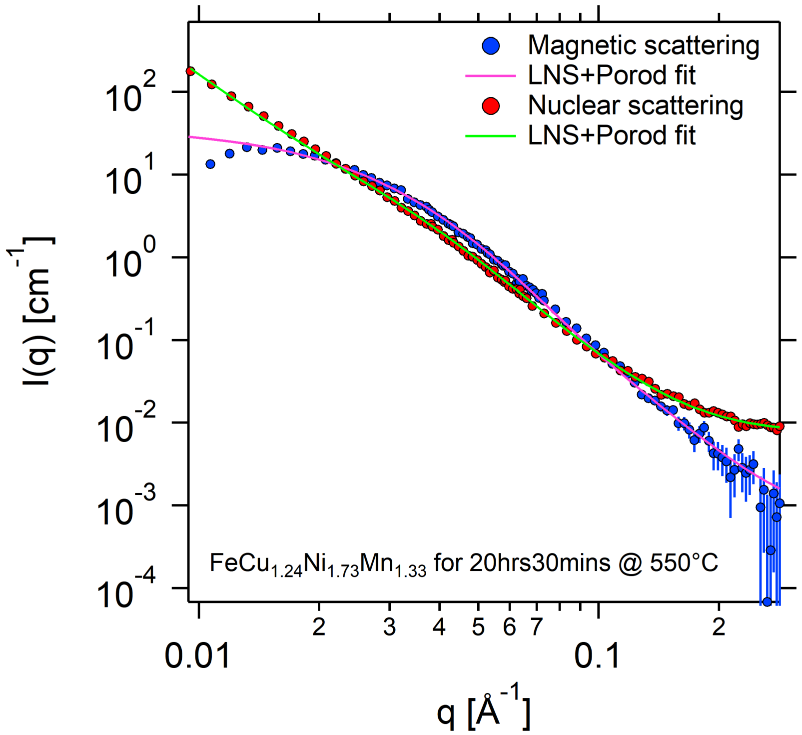

Figure 5.32: Graph showing separated absolute nuclear and magnetic I(q) profiles with fitted log-normal sphere and Porod form factor model for sample 3 FA.

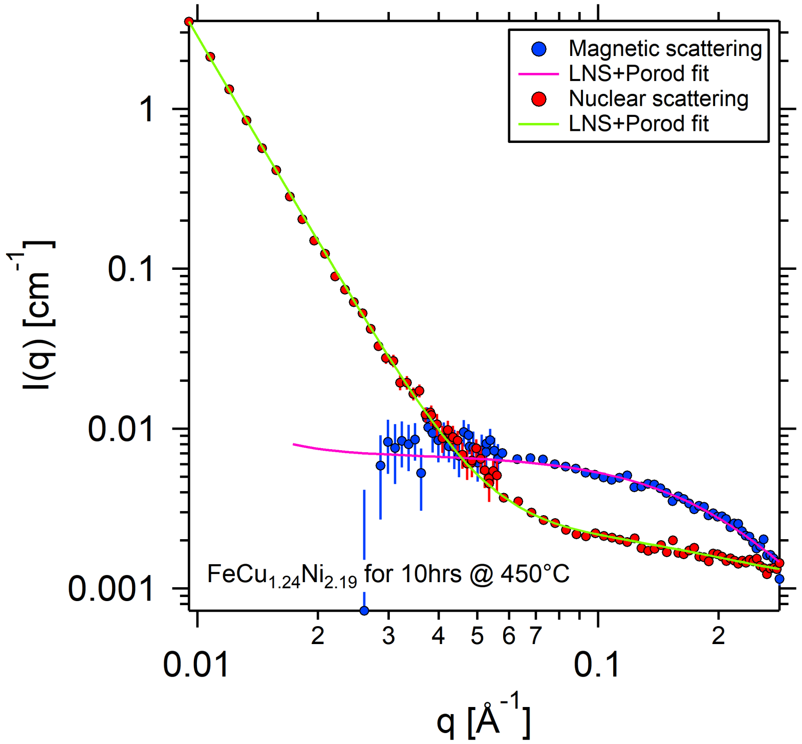

Figure 5.33: Graph showing separated absolute nuclear and magnetic I(q) profiles with fitted log-normal sphere and Porod form factor model for sample 7.2 TA.

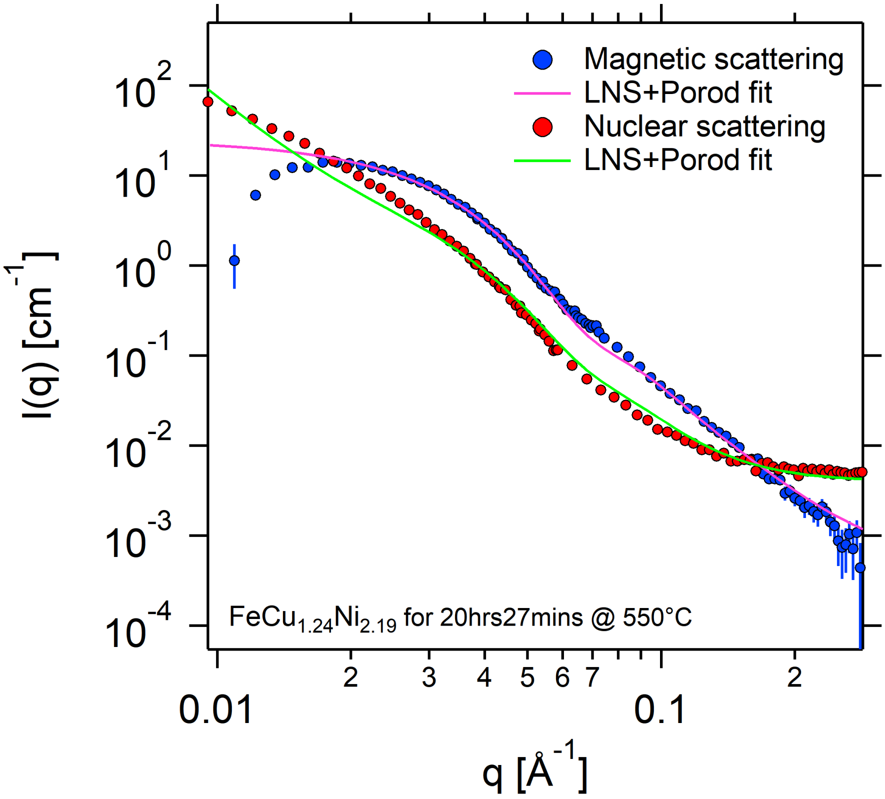

Figure 5.34: Graph showing separated absolute nuclear and magnetic I(q) profiles with fitted log-normal sphere and Porod form factor model for sample 7.2 FA.

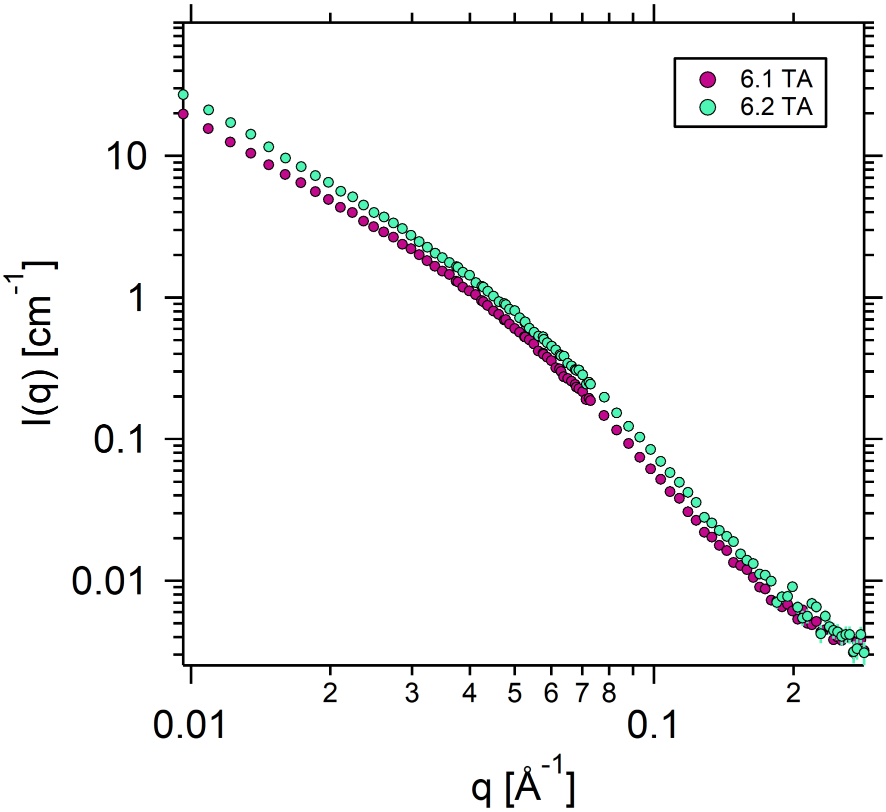

Figure 5.35: Graph showing the total scattering I(q) profiles for samples 6.1 TA and 6.2 TA.

The scattering profiles for 6.1 TA and 6.2 TA are very similar, as shown in Figure 5.35. This is as expected since the only difference between the samples is a small increase in Ni content. This is supported by previous studies [61, 142] where the solubility of Ni in Fe is relatively high compared to other elements such as Cu, which means that it requires relatively longer times at the same temperature to precipitate out. Hence, only sample 6.2 TA will be considered going forward.

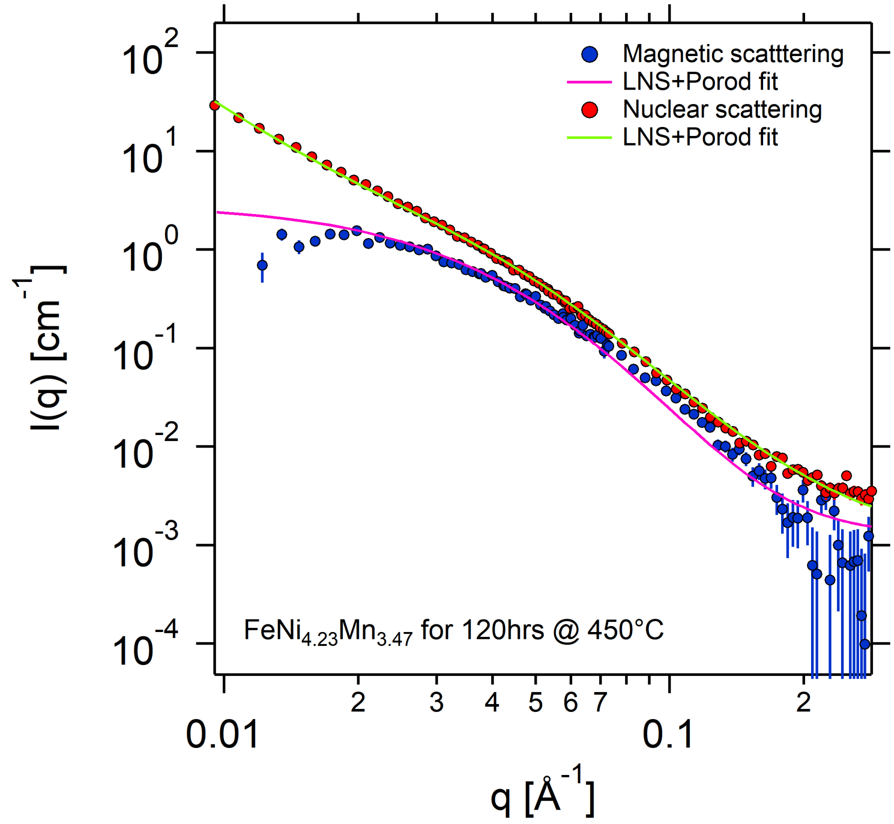

Figure 5.36: Graph showing separated absolute nuclear and magnetic I(q) profiles with fitted log-normal sphere and Porod form factor model for sample 6.2 TA.

Despite being close to the solubility limits, precipitation occurs which is visible from the non-Porod scattering contributions but there is minimal growth observed. This is reflected by the mean precipitate radius of samples 6.1 TA and 6.2 TA compared to their Cu containing counterparts (for example, sample 3 TA).

The precipitate contrast, radius and polydispersity are consistent between in-situ and nuclear scattering profiles (within the same order of magnitude). There is an increased incoherent background level for the in-situ aged samples due to scattering from the furnace itself. Figure 5.37 shows a comparison of the I(q) profiles for sample 3 FA measured from the in-situ ageing and magnetism studies. Table 5.14

shows a comparison of the fitted parameters from the two studies.

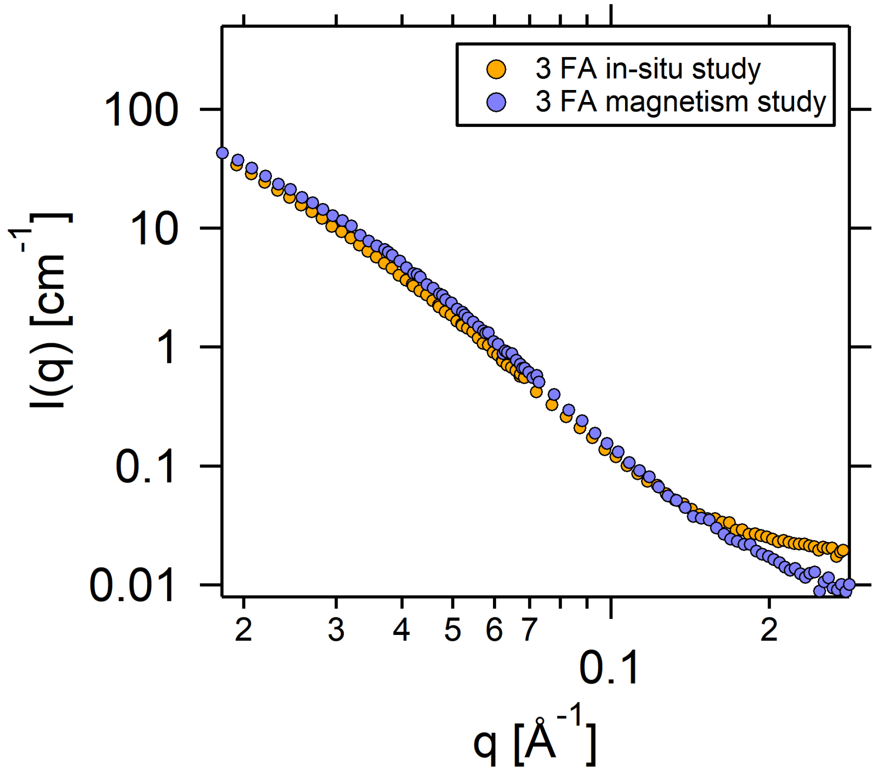

Figure 5.37: Comparison of the I(q) scattering for sample 3 FA from the in-situ ageing and magnetism studies.

Table 5.14: Comparison of key precipitate parameters between the in-situ (IS) and magnetism (M) studies. The brackets denote the errors on each value.

Sample	**Median radius** [Å]	$\boldsymbol{\sigma}$ **[arb.]**
1.3 FA		
IS	58.396 (0.130)	0.247 (0.002)
M	54.020 (0.159)	0.223 (0.002)
3 FA		
IS	32.077 (0.632)	0.437 (0.009)
M	36.889 (0.478)	0.404 (0.005)
7.2 FA		
IS	59.748 (0.218)	0.328 (0.002)
M	58.741 (0.146)	0.223 (0.002)

The overall fitted results are presented in Table 5.15.

Table 5.15: Fitted parameters from the log-normal sphere model to the I(q) profiles for samples in magnetism study. The brackets denote the errors on each value.

Sample	Median radius [Å]	σ [arb.]	$\rho_{N,p}$ [x 10^{-6} Å^{-2}]	$\rho_{M,p}$ [x 10^{-6} Å^{-2}]	BG [cm^{-1}]
1.3 FA	54.020 (0.159)	0.223 (0.002)	6.555 (0)	0 (0)	3.0 (0.1) x 10^{-3}
3 TA	18.203 (0.135)	0.352 (0.003)	9.208 (0.004)	6.949 (0.004)	2.0 (0.1) x 10^{-3}
3 FA	36.889 (0.473)	0.404 (0.005)	5.471 (0.034)	9.181 (0.011)	7.5 (0.2) x 10^{-3}
7.2 TA	11.433 (0.807)	0.280 (0.166)	7.707 (0.030)	6.003 (0.452)	1.1 (0.1) x 10^{-3}
7.2 FA	58.741 (0.146)	0.331 (0.002)	6.276 (0.011)	8.754 (0.005)	4.0 (0.1) x 10^{-3}
6.1 TA	23.862 (0.725)	0.442 (0.009)	5.309 (0.008)	6.411 (0.009)	1.4 (0.1) x 10^{-3}
6.2 TA	22.215 (0.796)	0.459 (0.011)	5.776 (0.036)	6.625 (0.011)	1.3 (0.2) x 10^{-3}

After empirical model fitting, the A ratio quantity was investigated using the scattering data. This is a direct benefit of the magnetism study, where the isolation of the nuclear and magnetic scattering contributions can be used to give compositional information of the scatterers as demonstrated previously for the long thermally aged welds in Section 4.4.2.5. Equation 2.43 was used to calculate the A ratio as a function of q, correcting for the use of 35° sectors during the radial averaging. The results for the model RPV alloys are shown in Figure 5.38.

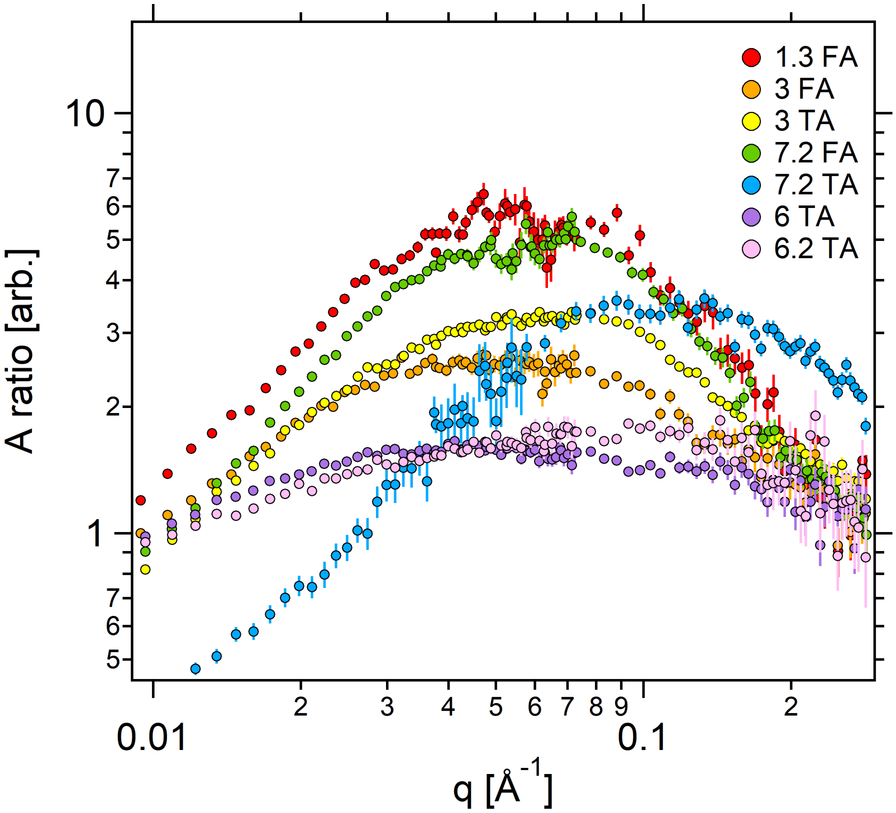

Figure 5.38: Graph showing A ratio as a function of q for the RPV model alloys of interest.

Each A ratio curve was then fitted with a Gaussian model to obtain the peak value and position. The results for each model RPV alloy are given in Table 5.16.

Table 5.16: Fitted A ratio values and reciprocal space position of peak for all model RPV alloys of interest. Values in brackets indicate associated errors.

Sample	**A ratio [arb.]**	**Peak position [Å^{-1}]**
3 TA	3.363 (0.009)	0.061 (0.001)
6.1 TA	1.621 (0.005)	0.049 (0.001)
6.2 TA	1.732 (0.009)	0.074 (0.002)
7.2 TA	3.473 (0.039)	0.113 (0.002)
1.3 FA	5.584 (0.035)	0.052 (0.001)
3 FA	2.666 (0.013)	0.050 (0.001)
7.2 FA	5.212 (0.025)	0.056 (0.003)

The position of the A ratio peak indicates the average size of the precipitates in the system, and the height indicates the average compositional change. Hence, a flatter distribution over the width indicates a smaller variation in composition across the precipitates.

For example, it was found that non-Cu containing alloys 6.1 TA and 6.2 TA have a smaller A ratio range than their Cu containing counterparts. This can be explained by the fact that Mn and Ni have lower solubility in Fe, so they only precipitate out at discrete locations where the energy is reduced, whereas a supersaturation of Cu in the matrix means that the diffusivity is higher and it is more likely to come out of solution at random locations.

The higher q peak position in A ratio for 7.2 TA suggests that the average precipitate size is noticeably smaller than the other RPV alloys. This is supported by the precipitate size extracted using model fitting.

5.4.3 Mechanical property characterisation

5.4.3.1 Microindentation hardness testing

Vickers hardness microindentation was completed using a DuraScan G5 on the model alloys of interest identified during SAXS and SANS analysis in order to quantify the effect of the thermal ageing induced precipitation on the hardness. Due to the similarity in precipitate properties between samples 6.1 and 6.2 TA found from small-angle scattering analysis, only one composition was chosen for hardness testing.

The sample preparation method outlined in Section 3.2.1 was employed. The results were found using a 0.1 kgf load and have been averaged from a 8 x 8 grid of indents, as per the method outlined in Section 3.3.1.

The microindentation hardness testing results are shown in Table 5.17. The calculated errors are statistical since these dominate over systematic errors, such as in the measurement of the indent geometry, due to the variability of hardness across each indent in the grid.

Table 5.17: Calculated hardness with associated error for model alloy samples of interst.

Sample	Ageing time [hr]	Temperature [°C]	Hardness [Hv]	Error [Hv]
1.3	0	0	122.2	1.3
1.3	10	450	151.4	2.9
1.3	20.5	550	159.4	2.5
3	0	0	222.4	4.2
3	20.5	550	245.8	3.2
3	120	450	286.4	4.1
6.2	0	0	298.9	3.2
6.2	120	450	291.6	4.3
7.2	0	0	152	1.6
7.2	10	450	169.3	2.5
7.2	20.5	550	192.4	3.0

5.5 Discussions

5.5.1 Precipitate shape and size distributions

The initial SAXS study presented in Section 5.4.1 was used to identify samples where thermal ageing induced precipitation was successful. This can be linked back to each sample set that allows the effect of each alloying element on precipitation to be investigated.

For example, the SAXS results on the FeCu samples only showed clear precipitation in the highest containing Cu sample, $FeCu_{1.23}$ (1.3 TA). This shows that longer ageing times are needed to investigate the full effect of Cu on precipitate size, since previous literature studies have found that an increase in Cu leads to an increase in precipitate size for the same ageing conditions [111, 157]. Whilst the effect of Cu study was not conclusive for inducing comparative precipitation events, it is noted that binary FeCu alloys are not fully representative of low alloy steels used in RPVs, and hence the role of Mn and

Ni in the presence of Cu is more pertinent.

For the SAXS results on the effect of Cu on Ni precipitation, no precipitates were observed in the $FeNi_{2.10}$ sample (8 TA), and clear precipitation was observed in $FeCu_{1.24}Ni_{2.19}$ (7.2 TA). This precipitation was also confirmed using SANS. This finding is commensurate with the fact that the solid solubility of Ni in Fe is much higher than Cu and hence requires longer times at elevated temperatures to precipitate out of solution, as shown in previous studies [54, 140, 142]. This suggests that the precipitation of Ni in Fe with a bulk Ni fraction below the solubility limit can be facilitated by elements with low solid solution solubility, such as Cu, as found for samples 7.1 and 7.2 TA, where sites of Cu precipitation become nucleation points for elements with lower solubility due to the reduction in energy. This is also reflected by the SAXS findings for samples 5.1 TA and 5.2 TA where no precipitation was observed for FeMnNi in the absence of Cu. Interestingly, a similar trend was observed in 2.1 TA and 4 TA (FeCuMnNi), which suggests that for the same ageing time, an increase in Ni does not correlate to enough of an increase in solubility to nucleate precipitates. This is likely to be because the fraction of Cu present in these samples is not high enough to generate sufficient nucleation points in the ageing time. This is in contrast to an irradiation study [48] where the presence of Mn/Ni was found to increase nucleation of Cu. This shows a clear difference between the mechanisms of nucleation for irradiation and thermal ageing induced precipitation. It would be interesting to study this phenomenon using longer ageing times, or with varying levels of Cu, in future work.

In contrast, there were several model alloys where precipitation was observed using SAXS and then further characterised using SANS. The precipitates were consistently found to be spherical in nature with a log-normal size distribution through empirical model fitting.

For example, the effect of Ni on precipitation in the presence of Cu showed that for the same ageing time, mean precipitates diameters are 6.06 ± 0.04 nm and 6.07 ± 0.02 nm for samples 1.3 FA ($FeCu_{1.23}$) and 7.2 FA ($FeCu_{1.23}Ni_{2.19}$) respectively. This suggests that Cu plays a dominant role in the nucleation and growth of precipitates in comparison to Ni, especially when the bulk fraction of Ni is lower than the solubility limit in Fe. In addition, this precipitate size for high Cu samples 1.3 FA and 7.2 FA is noticabley larger than for the other model alloys which suggests that overageing has occured. This is consistent with a previous study where overaging was observed for $FeCu_{0.8}$ [164] after 30 hours.

The effect of Ni and Mn on precipitation in the presence of Cu showed that precipitate growth is much slower for $FeCu_{1.24}Mn_{1.33}Ni_{1.76}$ (sample 3) in the presence of Mn and Ni compared to $FeCu_{1.23}$ (sample 1.3) for the same ageing time. The mean precipitate size was 6.06 ± 0.04 nm and 3.82 ± 0.05 nm for samples 1.3 FA and 3 FA respectively, found through model fitting. This is similar to trends observed in [20] and [47]. The effect of ageing time on the precipitate size due to the presence of Mn and Ni was confirmed using the in-situ ageing study (discussed further in Section 5.5.3).

The SANS study confirmed precipitation events in 6.1 TA ($FeNi_{4.03}Mn_{3.46}$) and 6.2 TA ($FeNi_{4.23}Mn_{3.47}$) to understand the effect of Ni on Mn in the absence of Cu. These samples have Mn and Ni fractions closer to the reported solubility limits in Fe (Section 5.2.1) than samples 5.1 TA and 5.2 TA. This in itself indicates that a higher matrix Mn and Ni fraction for the same ageing time leads to increased nucleation and growth of precipitates in the absence of Cu, which is consitent with a previous thermal ageing study on high Ni RPV alloys [140]. It is noted that the the precipitates observed were very similar in size and distribution, with mean radius 2.47 ± 0.07 nm and 2.30 ± 0.08 nm and polydispersity 0.442 ± 0.009 nm and 0.459 ± 0.05 nm for 6.1 TA and 6.2 TA respectively. This indicates that whilst a small increase in Cu can impact the induced precipitates as for 3 TA compared to 4 TA, a similar small increase in Ni does not significantly impact the precipitation process in the presence of Mn and absence of Cu. In the future this could be investigated by choosing a larger Ni difference.

The SANS study and in-situ ageing study allowed for the investigation of the role of Mn on precipitation in the presence of Ni and Cu. For the same ageing time and temperature, larger precipitates were observed in sample 7.2 FA (FeCuNi) compared to sample 3 FA (FeCuMnNi), with radii 6.30 ± 0.02 nm and 3.53 ± 0.07 nm respectively. This suggests that Mn suppresses the nucleation and growth of precipitates, which is clearly visible from the in-situ results of precipitate radii as a function of ageing time. This is discussed further in Section 5.5.3 .

The in-situ ageing study allowed for a direct comparison of allow composition on the precipitate size as a function of ageing time. Again, these precipitates were found to be spherical in nature; whilst the core shell structure in FeCuMnNi alloys has been previously reported in APT studies [21, 60], it was not resolvable in this study in samples 3 FA and 7.2 FA. This could be because the incoherent background at high q is damping out any high order I(q) oscillations which often indicate a shell with differing composition to the precipitate core. In addition, the presence of the sample environment set a limit on the maximum achievable q value due to the furnace window angle cut off. This could be investigated further in a separate SANS study that focusses on the high q range without a furnace present.

The change in precipitate size as a function of ageing time confirms the mechanism of precipitation under thermal ageing, where the nucleation of precipitates is facilitated by diffusion of solute atoms and growth is due to solute atoms clustering at nucleation points to reduce their energy. The observed kinetics of precipitation is discussed in more detail in Section 5.5.3.

It is noted that for all samples apart from FeCu, the volume fraction extracted is a relative quantity due to the multiplicative nature of volume fraction and contrast in the differential macroscopic cross section equation. It is only possible to extract the absolute volume fraction of precipitates under the assumption that they are non-magnetic and hence the scattering length density is explicitly known. The volume fraction for sample 1.3 TA was found to be 3.94%. For the same sample composition, the volume fraction was found to increase as a function of ageing time during the in-situ ageing study.

Induced precipitate size is directly linked to the mechanical properties of an in-service material. The implications of this are discussed further in Section 5.5.4 where the precipitate hardening effect is considered. This is important in the development of future nuclear materials where the structural integrity is required to be maintained over their full lifecycles.

5.5.2 Precipitate composition

As mentioned, thermal ageing induced precipitation events have been observed in model alloys 1.3 TA/FA, 3 TA/FA, 6.1 TA, 6.2 TA and 7.2 TA/FA. A map of the model alloy A ratio values as a function of increasing Ni fraction is shown in Figure 5.39. This is annotated with sample compositions and thermal ageing parameters to aid comparison.

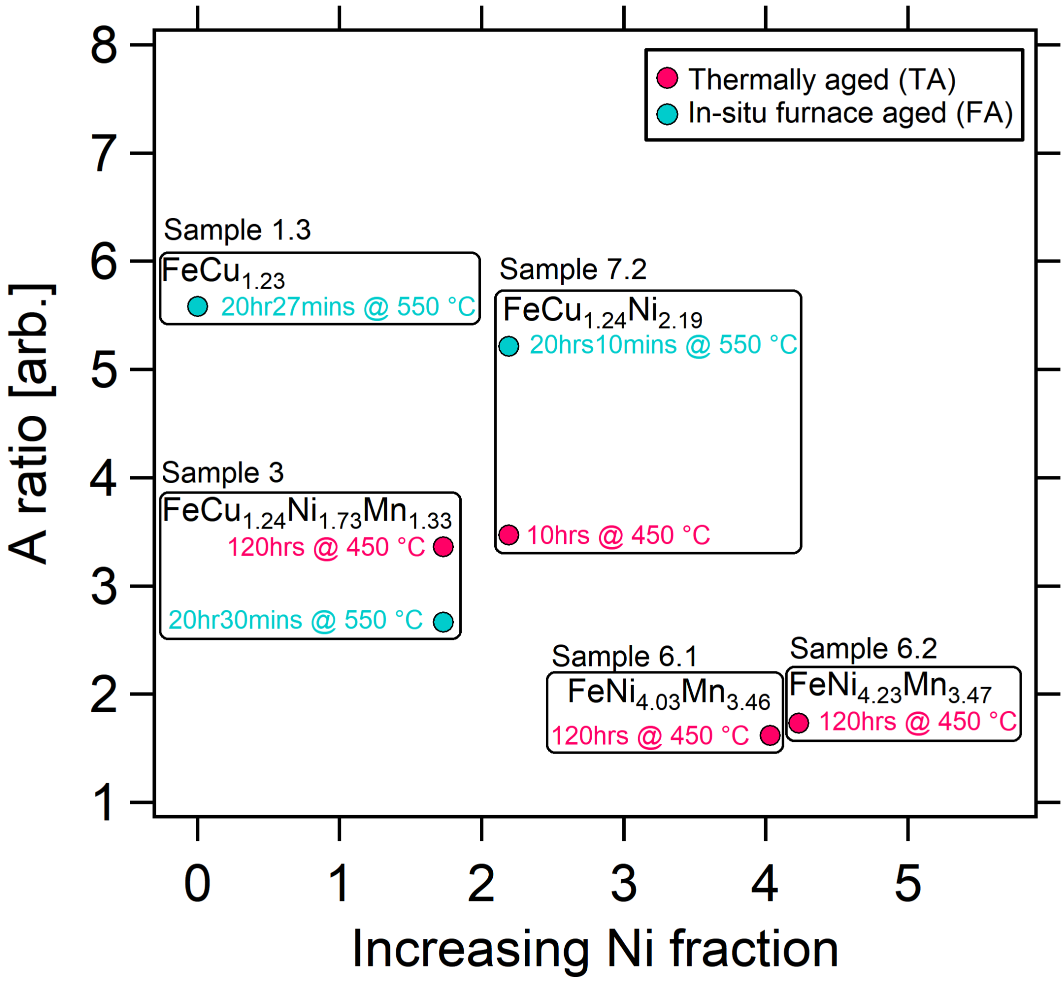

Figure 5.39: Map of the A ratio for model RPV alloys as a function of increasing Ni composition.

Theoretical calculated A ratio values for different precipitate types are shown in Table 5.18. These are not consistent with the extracted A ratio values from the raw data, indicating that there is more than one alloying element that contributes to the precipitate composition.

Table 5.18: Theoretical A ratio values for given precipitate compositions in an example low alloy RPV steel matrix.

Composition	**A ratio [arb.]**
Pure Cu	16.195
Pure Mn	1.195
Pure Ni	14.160
Pure Fe	1.929
Pure vacancy	1.386

Samples with higher Cu content have higher A ratios, since the A ratio for pure Cu precipitates is the highest of the alloying elements included in this study.

The A ratio of sample 3 TA is larger than 3 FA which can be attributed to its longer ageing time, allowing for more Cu to precipitate out of the matrix as observed in [157]. The ageing time is the driving force for the precipitation process since 3 TA was aged for longer but at a lower temperature (450 °C) compared to 3 FA (550 °C) and more precipitation of Cu is seen in 3 TA. This is as expected since at both ageing temperatures the Cu content is above the solubility limit in Fe. This trend is also observed in 7.2 FA which has a longer ageing time than 7.2 TA. This is consistent with more nucleation of Cu precipitates which is facilitated by the presence of Ni. This supports previous studies where Ni has been found to enhance the nucleation process [48].

Interestingly, the A ratio values for samples 3 TA ($FeCu_{1.24}Mn_{1.33}Ni_{1.76}$) and 7.2 TA ($FeCu_{1.24}Ni_{2.19}$) are similar. One may expect that since 3 TA has a longer ageing time than 7.2 TA, it would have a higher fraction of Cu in the precipitates, however this is not clear here. This indicates that the presence of Mn slows the nucleation process during thermal ageing, which is contrasted by irradiation studies [46, 48, 136]. This highlights the differences in mechanisms between irradiation and thermal ageing induced precipitation. This finding can also be explained by the presence of Mn in precipitates 3 TA which acts to significantly reduce the A ratio. This trend is also apparent for the in-situ aged samples (3 FA and 7.2 FA) where for the same ageing time there is a large difference in A ratio values. This means that a shorter ageing time in sample 3 allows the presence of Mn to dominate the A ratio in comparison to the presence of Cu.

The A ratio of samples 6.1 TA ($FeNi_{4.03}Mn_{3.46}$) and 6.2 TA ($FeNi_{4.23}Mn_{3.47}$) are considerably lower than of the other model alloys. This is linked to the absence of Cu and the presence of Mn; low values of A ratio indicate the presence of Mn due to the negative scattering length of Mn. It is noted that the A ratio of 6.2 TA is slightly higher than 6.1 TA, which is indicative of the increased amount of Ni in the matrix available for precipitation. This is consistent with [48] where the increasing Ni fraction in the matrix increases the Ni fraction in the induced precipitates.

It is important to note that multiple combinations of precipitate composition can give the same A ratio value. In addition to the alloying elements of interest, both Fe and vacancies have been observed in thermally aged induced precipitates [24, 60, 155]. It is possible to map the A ratio for varying compositions of different alloying elements in ternary diagrams and use this to identify precipitate compositions that satisfy the measured experimental A ratios within the error range for each model

RPV alloy. Since the magnetic scattering length of Ni is so small in comparison to Fe, precipitates containing Ni have been assumed as non-magnetic and those containing Fe as magnetic. This is reasonable considering the fraction of Fe in the matrix and the fact that the Fe magnetic scattering length is significantly larger than the Ni magnetic scattering length. Hence, all ternary diagrams presented below assume Ni is non-magnetic and that the magnetism arises solely from any Fe within the precipitate.

The FeCu binary system was selected first. Previous thermal ageing studies on FeCu suggest that vacancies and self-solute Fe atoms can also be present in precipitates [24, 51, 53, 60]. Figure 5.40 shows the ternary diagram for a system of Fe-Cu-vacancy precipitates in sample 1.3 FA, with the possible precipitate compositions due to the experimental A ratio value highlighted by the blue circles.

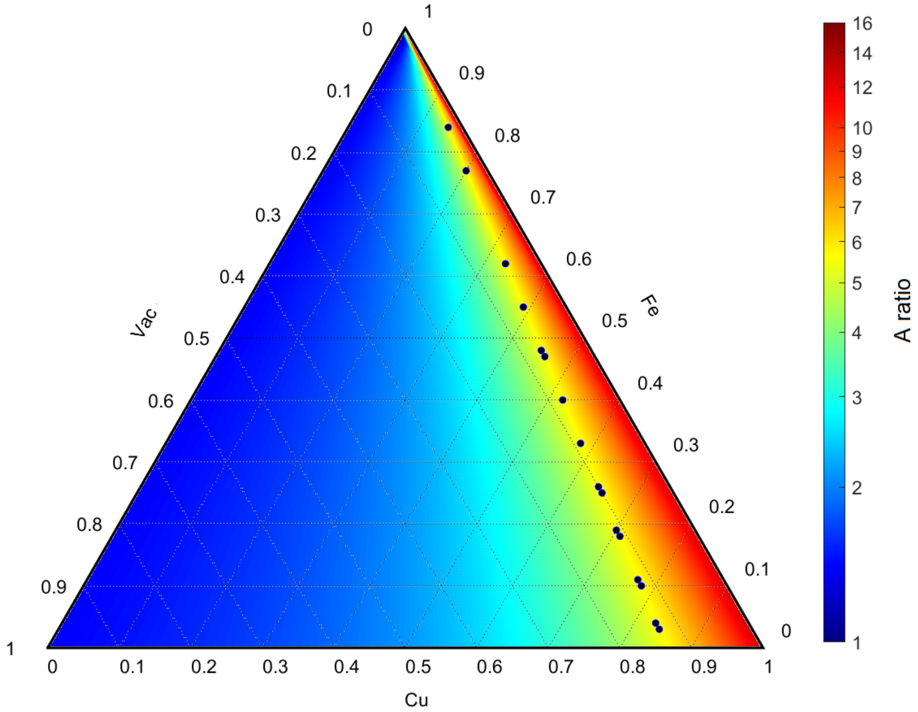

Figure 5.40: Theoretical A ratio ternary diagram for any Fe:Cu:vacancy precipitate composition in a 1.3 FA ($FeCu_{1.23}$) matrix. Blue overlaid circles highlight compositions corresponding to experimental A ratio value of 5.584 ± 0.035 for 1.3 FA.

If one assumes there are no vacancies in precipitates, then the closest combination of Fe and Cu fractions that gives the experimental A ratio is 0.14Cu and 0.84Fe (A ratio = 5.61). This precipitate is majority Fe which is not consistent with literature studies in [22, 72] that found Cu to be the majority fraction of precipitates in an FeCu system. Hence, it can be concluded that there must be vacancies present in the 1.3 FA precipitates. This is concurrent with the facilitation of diffusion of self solute atoms in low alloy RPV steels due to the presence of vacancies [23, 49, 155, 166].

For samples 3 TA and 3 FA, the relationship between Cu, Mn and Ni was investigated since these are the dominant alloying elements in literature [20, 47, 63]. The resultant ternary diagram is shown in Figure 5.41.

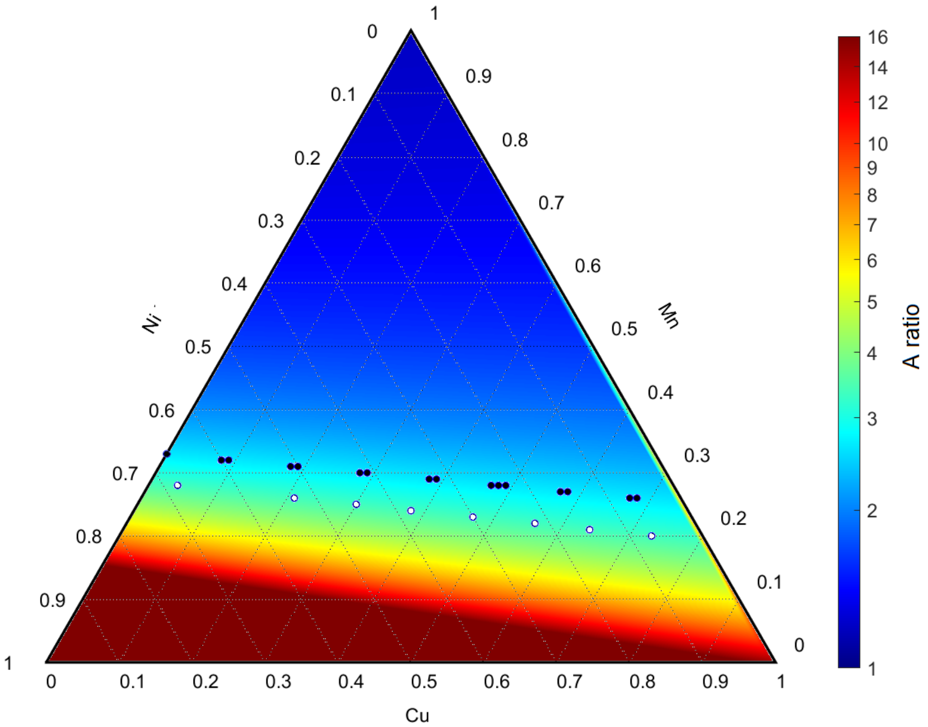

Figure 5.41: Theoretical A ratio ternary diagram for any Ni:Cu:Mn precipitate composition in a 3 TA ($FeCu_{1.24}Mn_{1.33}Ni_{1.73}$) matrix (also equivalent to 3 FA). Blue overlaid circles highlight compositions corresponding to experimental A ratio value of 2.666 ± 0.013 for 3 FA, and white overlaid circles highlight compositions corresponding to experimental A ratio value of 3.363 ± 0.009 for 3 TA.

For thermally aged FeMnNi systems, such as that studied in [140], the presence of vacancies in precipitates has been considered due to their role in the diffusion of solute atoms at elevated temperatures. The resultant Ni-Mn-vacancy ternary diagrams are shown in Figure 5.42 and Figure 5.43 for samples 6.1 TA and 6.2 TA respectively.

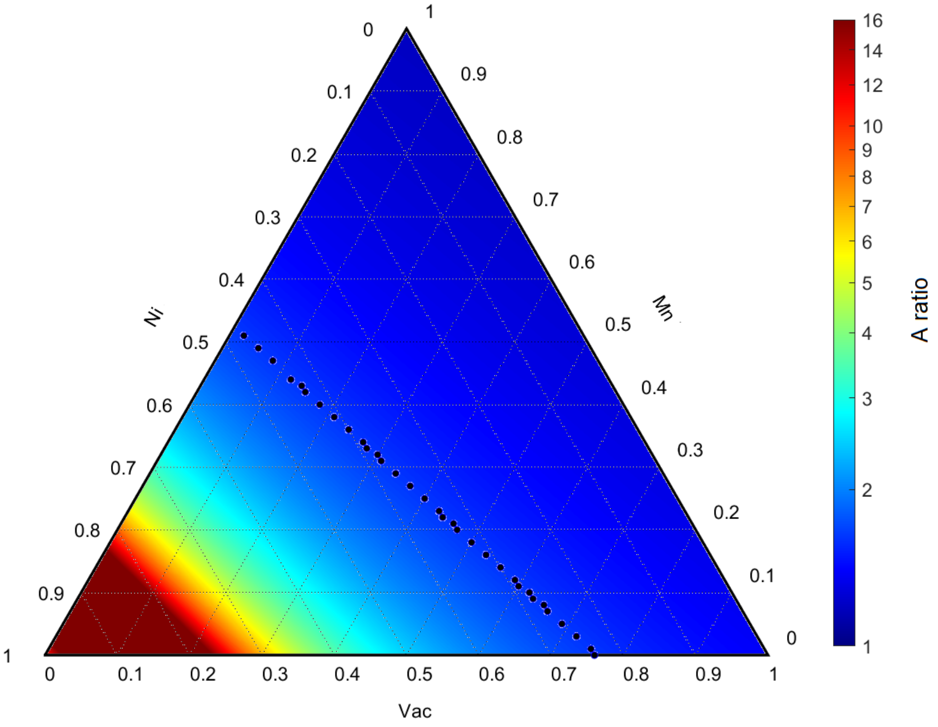

Figure 5.42: Theoretical A ratio ternary diagram for any Ni:Mn:Vac precipitate composition in a 6.1 TA ($FeMn_{3.46}Ni_{4.03}$) matrix. Blue overlaid circles highlight compositions corresponding to experimental A ratio value of 1.621 ± 0.005 for 6.1 TA.

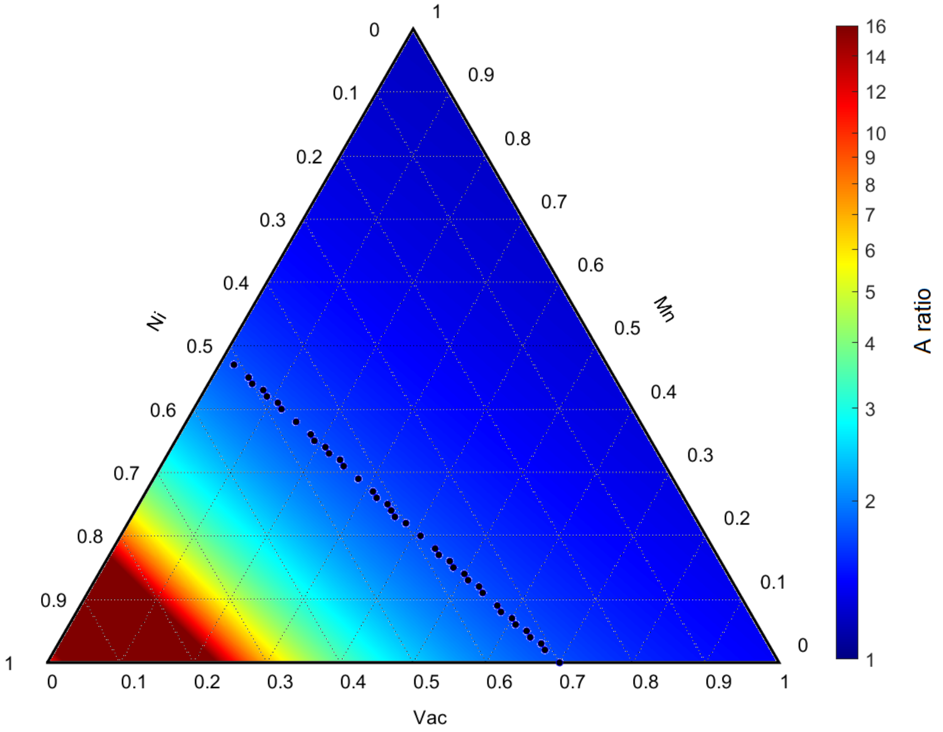

Figure 5.43: Theoretical A ratio ternary diagram for any Ni:Mn:Vac precipitate composition in a 6.2 TA ($FeMn_{3.47}Ni_{4.23}$) matrix. Blue overlaid circles highlight compositions corresponding to experimental A ratio value of 1.732 ± 0.009 for 6.2 TA.

For FeCuNi samples 7.2 TA and 7.2 FA, no theoretical A ratio values for precipitate combinations of Ni-Cu-Fe were found to be in the same range as the experimentally obtained values. This suggests that the precipitates in these samples do not contain Fe, which is supported by [24, 45]. Instead, a ternary A ratio diagram for Ni-Cu-vacancy precipitates is shown in Figure 5.44, with the possible precipitate compositions for samples 7.2 TA and 7.2 FA overlaid.

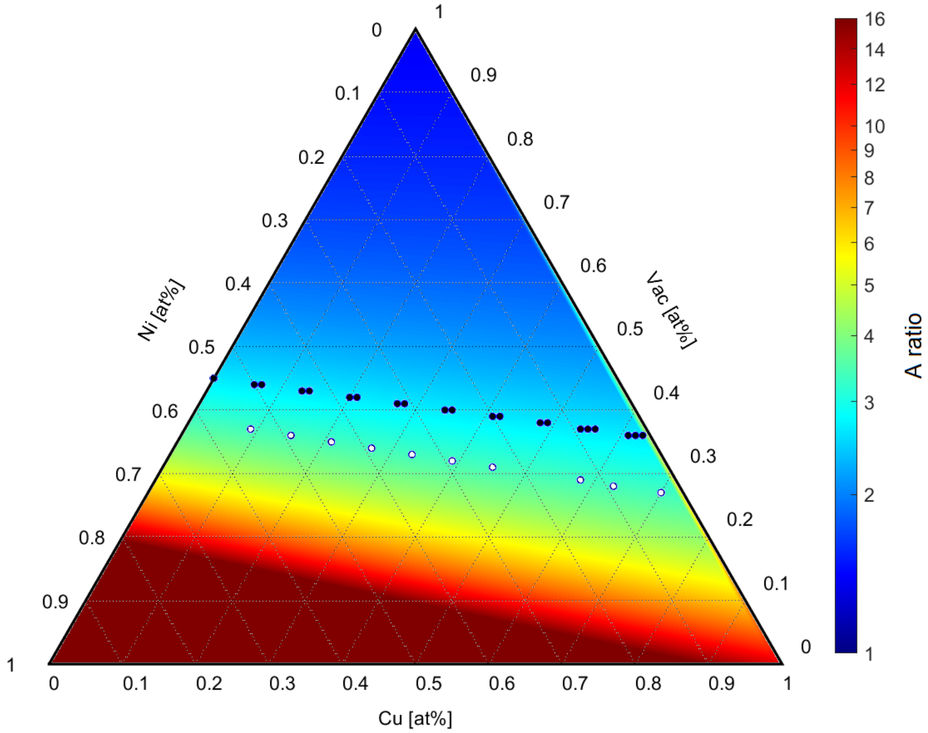

Figure 5.44: Theoretical A ratio ternary diagram for any Ni:Cu:Vac precipitate composition in a 7.2 TA ($FeCu_{1.24}Ni_{2.19}$) matrix (also equivalent to 7.2 FA matrix). Blue overlaid circles highlight compositions corresponding to experimental A ratio value of 5.212 ± 0.025 for 7.2 FA. White overlaid circles highlight compositions corresponding to experimental A ratio value of 3.473 ± 0.039 for 7.2 TA.

It is clear that the presence of Cu, Ni and Mn in the matrix are also present in precipitates. This is supported by several thermal ageing literature studies [47, 53, 62, 68]. The presence of Fe and vacancies is more nuanced. Interestingly, the observed potential Fe fractions from the experimental A ratios in this study are relatively low in comparison to the fractions of alloying elements. This suggests that the amount of Fe present in precipitates is less than observed via APT measurements and in irradiation induced precipitation studies in similar sample compositions where the presence of self interstitials of Fe matrix damage plays an important role for nucleation of precipitates.

These findings show that alloy composition has a stronger effect on thermal ageing induced precipitation than irradiation. Such variations in precipitate composition due to thermal ageing is in contrast to irradiation induced precipitation in studies with similar alloy compositions [50]. This can be described by the different mechanisms of solute migration between the damage processes. It has also highlighted the need for magnetism considerations in such precipitates in future studies. This detail is often omitted, especially in SANS where the omission allows one to extract the apparent absolute volume fraction of precipitates, when in fact it not likely to be representative of the true number density of precipitates in a material.

5.5.3 Effect of alloy composition on precipitation kinetics

The kinetics of precipitation was investigated during the in-situ ageing SANS study in Section 5.4.2.1. The effect of Ni on kinetics in the presence of Cu can be shown through comparison of samples 1.3 FA and 7.2 FA. The effect of Mn on kinetics in the presence of Cu can be shown through comparison of samples 1.3 FA, 3 FA and 7.2 FA. Precipitate size evolution as a fucntion of ageing time for the three model alloys is shown in Figure 5.45.

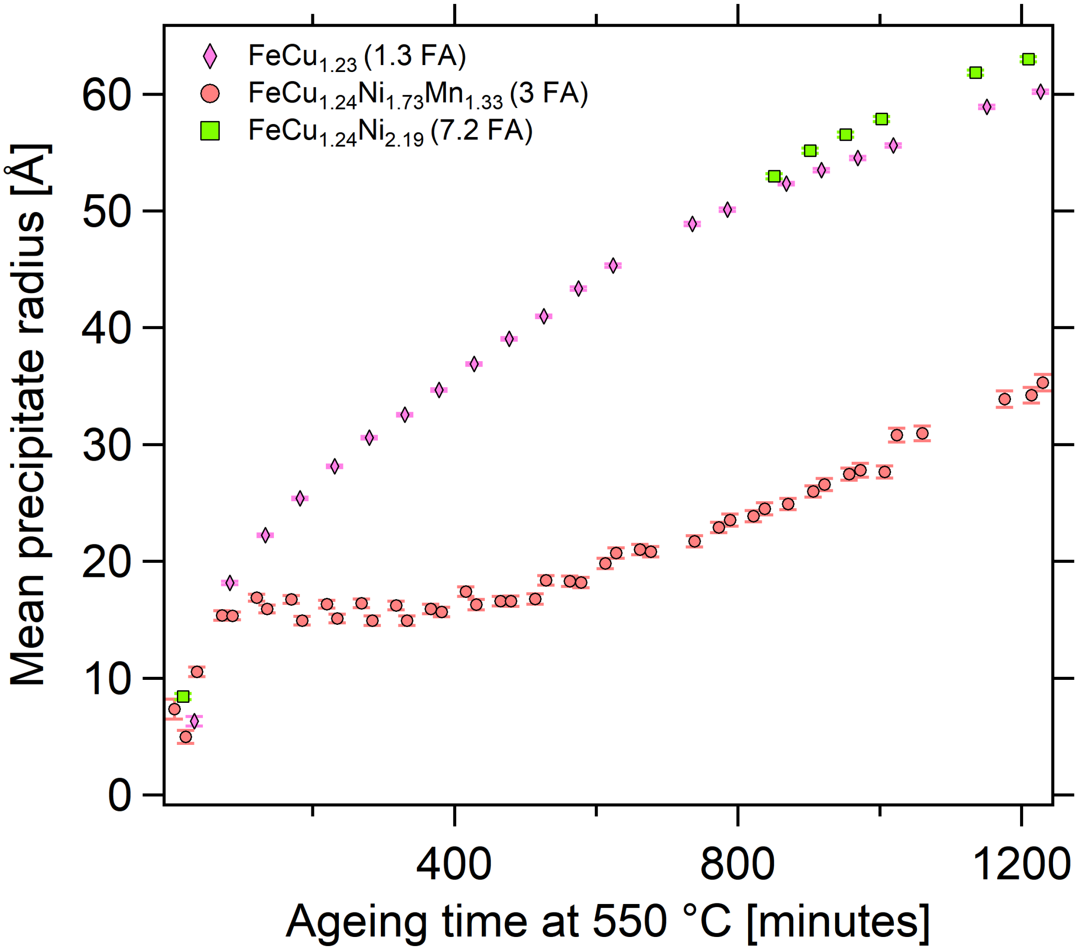

Figure 5.45: Graph comparing evolution of mean precipitate radius as a function of ageing time for samples 1.3 FA, 3 FA, and 7.2 FA.

For all samples, precipitate size changes as a function of ageing time. Nucleation of precipitates is observed almost instantly (less than 1 hour), owing to the high Cu content of these model alloys. Subsequent growth of precipitates is dependent on the alloying element solubility which leads to random solute diffusion and a reduction in energy by clustering at nucleation sites. The growth rate depends on alloying elements present.

Comparing the trends for samples 1.3 FA and 7.2 FA, Ni seems to have a minimal impact on precipitate growth in the presence of Cu. The kinetics of Cu appears to dominate the thermal ageing induced precipitation process, as also found in [167], showing a power law increase of precipitate radius as a function of ageing time. There is no clear evidence of Ni aiding the nucleation process as observed during an irradiation induced precipitation study in [48], however this is primarily due to the lack of in-situ measurements for 7.2 FA at low ageing times as a result of an experimental error.

A plateau period of no precipitate growth is observed between 100 and 400 minutes in sample 3 FA. Whilst growth appears to restart around 400 minutes, the trend is noticeably different to the continuous power law growth observed for the other two samples. This suggests that the presence of Mn within the matrix causes a delay and subsequent suppression of precipitate growth. It would be an interesting future study to understand the role of Mn in precipitate nucleation and growth in more detail. This is particularly pertinent to current and future nuclear materials where Mn is alloyed due to its role in increasing strength and ductility [168].

The polydispersity (width of size distribution of precipitates) changes as a function of ageing time for all three model alloy compositions, as shown in Figure 5.46. This polydispersity evolution provides a more detailed understanding of the precipitation kinetics than size evolution alone, allowing one to deconvolve the nucleation and growth phases. For example, the nucleation process is visible in the first few data points for samples 1.3 FA and 7.2 FA, where there is a noticeably large polydispersity, indicating a wide range of precipitate sizes at low ageing times.

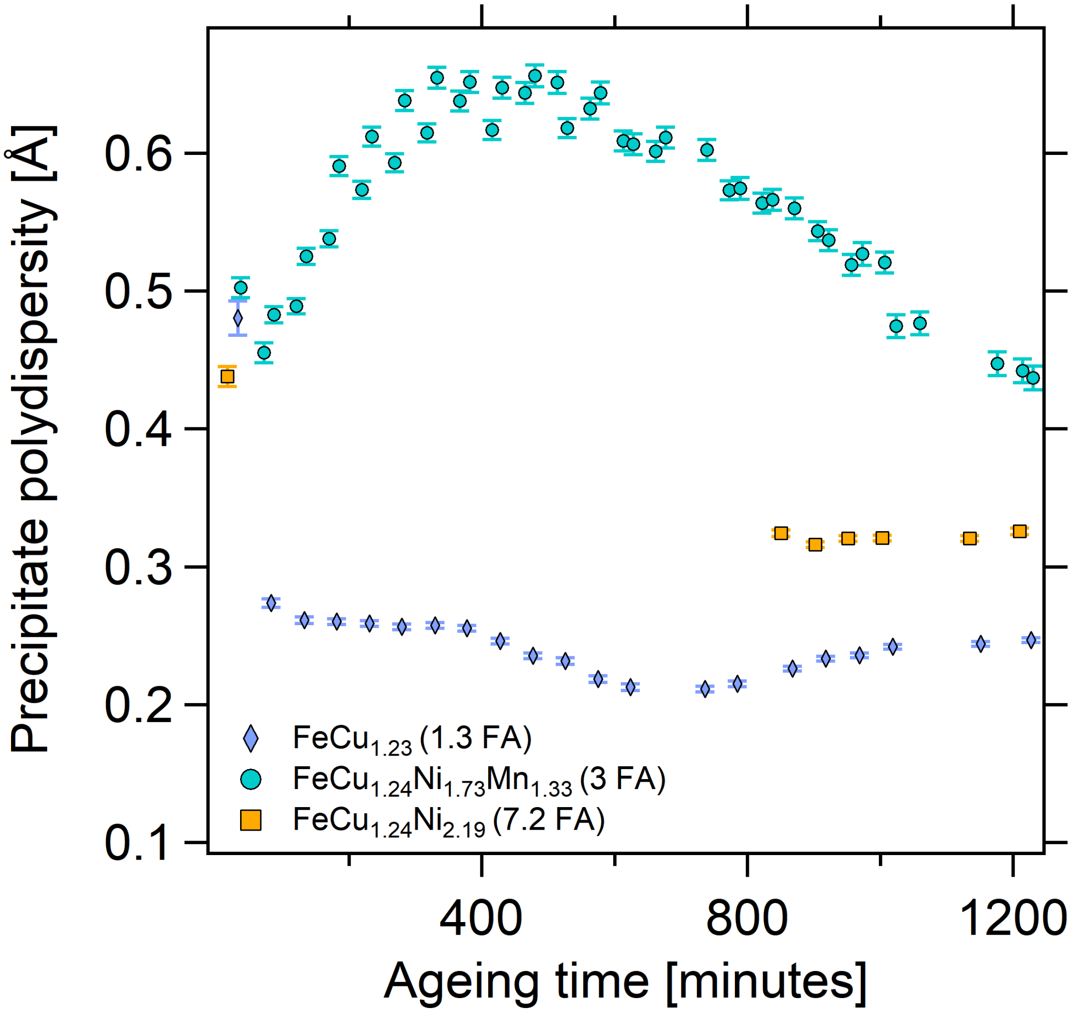

Figure 5.46: Graph comparing evolution of precipitate polydispersity as a function of ageing time for samples 1.3 FA, 3 FA, and 7.2 FA.

The polydispersity is in general much larger for increased alloying element fractions. For sample 3 FA, there is an increase in polydispersity as a function of ageing time up until around 400 minutes. During this time, the mean precipitate radius stays relatively similar in the previously identified plateau region whilst the size distribution widens, suggesting simultaneous nucleation (small precipitates) and growth (larger precipitates). This can be attributed to the presence of Mn. Precipitate growth starts to dominate after the plateau region, which is reflected by the narrowing of the size distribution, where nucleation has slowed and precipitates continue to grow.

Differences due to the presence of Ni are not clear due to the lack of data for sample 7.2 FA, however the trend observed is similar to sample 1.3 FA at higher ageing times.

The mean precipitate radius and size distribution evolution observed for sample 3 FA is the most ideal behaviour out of the model RPV alloys investigated. The presence of Mn in combination with Ni and Cu in RPV steels acts to suppress the growth of thermal ageing induced precipitates, which will lead to a relative suppression of precipitation induced hardening and embrittlement for in service low alloy steels.

5.5.4 Effect of precipitation on mechanical properties

There is not a significant difference between precipitate hardening from irradiation and thermal ageing damage mechanisms, since it is the precipitate structure that determines the degree of hardening [138, 169, 170]. The primary difference between such loading conditions is in the precipitate composition due to the mechanisms of nucleation and growth. The precipitate structure has been found to be consistent between irradiation and thermal ageing [19, 21, 40], where spherical nanoscale precipitates directly impede dislocation motion.

Both irradiation and thermal ageing induced precipitation can lead to hardening and embrittlement of materials. Whilst the mechanisms of inducing such damage may differ, the overall effect is the same; the stress fields of nanoscale precipitates distributed in the material matrix act as a barrier to dislocation movement and hence lead to hardening through impeding plastic flow [170]. During operation, there is likely to be a flow of dislocations under plastic deformation, in addition to other extreme loading that can lead to creep damage and fatigue failures. It is hence important for a reactor material (especially irreplaceable structural components) to be able to withstand such operational conditions, including the production of dislocation loops from interstitials and vacancies induced by interactions with radiation. Hence, precipitate hardening poses a threat to the behaviour of such materials over their lifetime in a reactor.

The overall hardness change measured for each model RPV alloy is shown in Table 5.19.

Table 5.19: Change in hardness for model alloy samples of interst.

Sample	Ageing time [hr]	Temperature [°C]	ΔHardness [Hv]	Error [Hv]
1.3	10	450	29.2	4.1
	20.5	550	37.2	3.8
3	20.5	550	23.4	7.4
	120	450	64	8.2
6.2	120	450	-7.3	7.5
7.2	10	450	17.3	4.1
	20.5	550	40.4	4.7

A map of hardness as a function of ageing time is shown in Figure 5.47. An overall hardness increase is observed for most model alloy compositions as a function of ageing time, however the degree of hardness change differs between samples, even for the same ageing time (for example, sample 3 compared to sample 6.2 after 120 hours). This is also evident when comparing samples 1.3, 3 and 7.2 after ageing for around 20 hours. This trend highlights the strong effect alloying composition has on precipitation induced hardening.

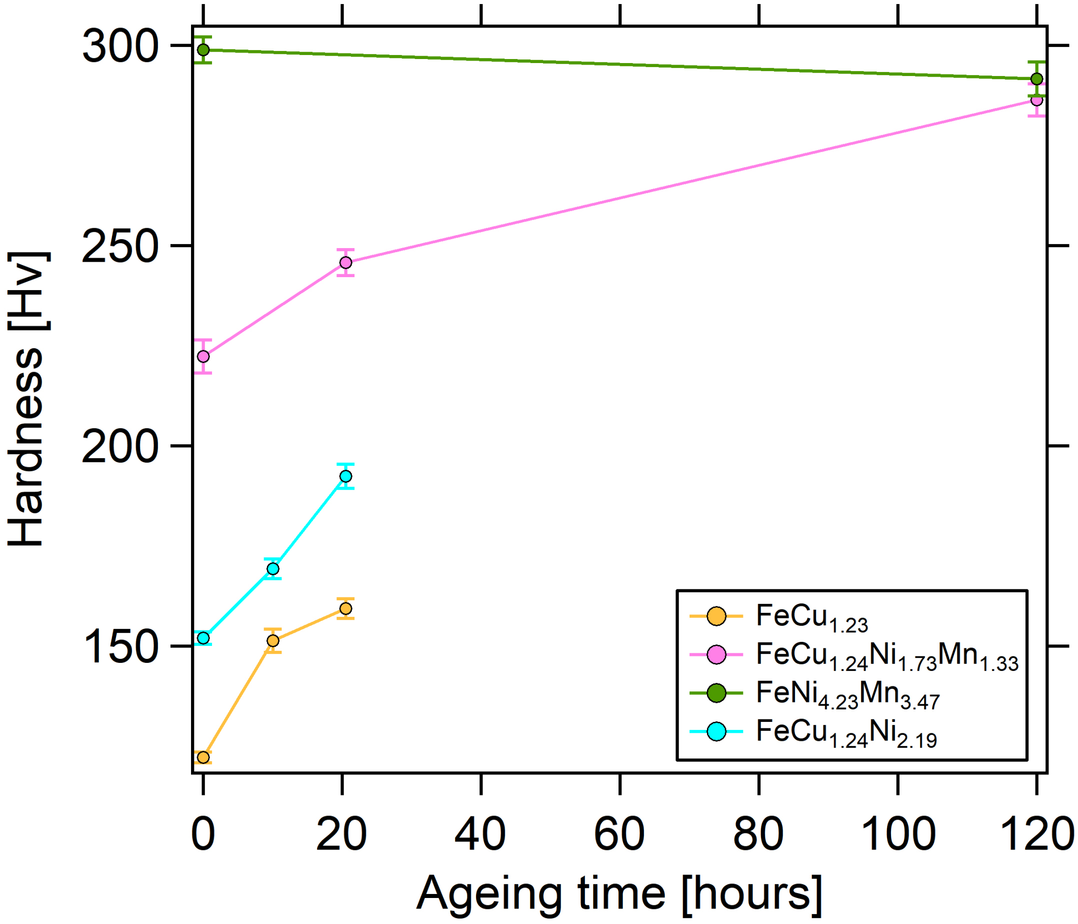

Figure 5.47: Map showing hardness as a function of ageing time for each model RPV alloy with confirmed precipitation events.

Sample 6.2 shows an apparent decrease in measured hardness from ageing for 120 hours at 450 °C compared to its unaged counterpart. However, when accounting for the uncertainty in the microindentation method, both hardness values overlap and so there is not a statistically significant hardness increase for this sample. Moreover, a decrease in hardness with ageing time is not observed in other FeMnNi thermal ageing studies and cannot be explained by precipitate hardening theories. The lack of detectable hardness change in sample 6.2 may also be because the precipitates induced are too small to effectively impede dislocations.

For the model alloys containing Cu, relatively large differences in hardness as a function of ageing time are observed. For sample 7.2 (FeCuNi) and sample 3 (FeCuMnNi), the hardness change also increases with ageing time. The reduction in magnitude of hardness change with ageing time for sample 1.3 (FeCu) compared to these higher order RPV alloys can be attributed to overageing of the induced precipitates, as indicated by the large precipitate size compared to the other model alloys. This is observed in literature [164], where for $FeCu_{0.1}$ peak hardness is observed after thermal ageing for 30 hours at 450 °C and the hardness change is then seen to decrease up to 120 hours. The lower Cu content in [164] suggests that peak ageing will occur at shorter times in this study for sample 1.3, which is consistent with the trend observed after 20 hours ageing for 1.3 FA. The presence of Ni in sample 7.2 increases the range of precipitate sizes in the sample with increasing ageing time compared to the binary FeCu system, meaning there is likely a higher number density of smaller precipitates, hence why the hardness does not begin to plateau off.

It is also noted that the hardness of sample 3 (FeCuMnNi) is much higher initially (and after ageing) than the other counterparts. This is due to the presence of Mn which is alloyed in such RPV steels to improve ductility and strength [168]. The increased initial hardness between sample 1.3 and 7.2 can be explained by the presence of Ni, which is added to ferritic reactor steels to reduce the DBTT [171].

Sample 3 shows an overall hardness increase of 64.0 ± 8.2 Hv after 120 hours at 450 °C. The high Ni RPV weld showed an increase of 80.0 ± 4.4 Hv after 100 000 hours at 330 °C. Whilst these precipitate induced hardness increases are similar, the slightly larger hardness increase for the weld is likely to be because of the larger precipitates (2.01 ± 0.06 nm compared to 1.89 ± 0.01 nm) with larger associated stress fields to disrupt dislocation motion.

5.6 Conclusions

Precipitate damage was successfully induced in a series of low alloy model RPV steels using thermal ageing. By varying the levels of alloying elements of interest from literature, in-situ material transitions were studied to answer key questions on the role of Cu, Mn and Ni on the mechanisms of thermal ageing induced precipitation and hardening.

The properties of induced precipitates were studied successfully using SAXS and SANS. These advanced scattering techniques, in combination, allowed for the identification of precipitate events and the quantification of their key properties, including shape, size distribution, volume fraction and composition. SANS quantified the induced precipitates as a polydisperse system of spheres with a log-normal distribution of radii, with radii ranging from 1.143 ± 0.081 to 5.874 ± 0.015 nm for the different alloy compositions.

An in-situ thermal ageing SANS study using a novel experimental setup was completed by taking advantage of the properties of neutrons. This allowed for a study of the kinetics of precipitation in unaged RPV model alloys to understand the effect of Mn and Ni on precipitate nucleation and growth in the presence of Cu. The samples and experimental set up was chosen to explicitly allow for observation of the real-time thermal ageing induced precipitation in order to understand both the nucleation and growth mechanisms. Precipitates of mean radius 3.689 ± 0.047 nm were induced after 20 hours at 550 °C in the FeCuMnNi sample. The kinetics of the nanoscale transitions were studied, and it was found that Mn suppresses the growth of precipitates in the presence of Cu.

The selection of FeCu, FeCuMnNi, and FeCuNi model alloy compositions allowed for one to understand how mechanisms of precipitation are coupled with the presence (or absence) of certain alloying elements. A further magnetism study using SANS on the in-situ aged and other thermally aged samples was employed to extract the ratio of magnetic to nucler scattering contributions. This so-called A ratio can detail nuances in precipitate composition and the role of Fe and vacancies in the precipitation process which is often contested in literature. Moreover, it allowed for the magnetic nature of the precipitates to be studied.

The hardness was found to increase as a function of ageing time for all thermally aged model alloy compositions, with the largest increase of 64 ± 8.2 Hv observed for the FeCuMnNi system.

There are several improvements and areas of interest that are outside of the scope of this work but that could be investigated as a follow-on step in the future. For example, the RPV alloy compositions where no thermal ageing induced precipitation was observed, such as $FeCu_{0.2}$, could be aged for longer times to increase the likelihood of precipitate formation.

The compositions used where precipitation was induced could be investigated further in a complementary neutron irradiation study. This could be used to challenge the differences observed between precipitate structural properties and compositions by the thermal ageing results in this work and previous irradiation studies in literature on similar, but not exact, model alloy compositions, allowing for a direct comparison. In addition, it would be particularly interesting to investigate effect of Mn in more detail by using a range of FeCuMnNi samples with a varying range of Mn compositions, since this was observed as a driving force for suppression of precipitate growth. To complement the advanced scattering and microindentation results reported in this chapter, additional experimental techniques could be employed that could not be completed during this work due to the activation of the samples induced during the neutron scattering investigations. For structural and compositional information, APT or TEM could be completed on samples, noting that APT is a destructive technique. In addition, the fabrication of larger samples in the future could be useful to allow for mechanical property evolution measurements such as fracture toughness and Charpy impact testing that were limited by sample size in this work. Such samples would need to fabricated using an alternative route, such as a vacuum melting furnace, to ensure the alloys are of sufficient size for investigation by multiple techniques.

CHAPTER 6

IRRADIATION INDUCED PRECIPITATION IN PROT IRRADIATED TUNGSTEN

6.1 Introduction

The aim of this chapter is to highlight the versatility of small angle scattering techniques for the study of irradiation damage mechanisms and nanoscale precipitation in polycrystalline nuclear materials.

The material system in this chapter has been chosen to contribute to current issues facing the nuclear material systems required for future power generation, namely the search for reliable plasma facing materials (PFMs) in fusion reactors. This chapter focusses on quantification of irradiation induced damage in tungsten, analogous to the quantification of thermal ageing induced precipitation in reactor pressure vessel steels presented previously. There is a particular focus on the synergy between precipitation initiated by high temperature exposure (explored in depth in Chapters 4 and 5) and precipitation induced by high energy radiation interactions, both relevant during high temperature irradiation, and so how both can affect the overall material properties.

The work presented here will build on the concept of radiation damage presented in Chapter 2, with a focus on fusion material systems. Specifically, it will discuss the micro-mechanical mechanisms of irradiation damage in PFMs, how one can induce and simulate damage in samples of interest, and the quantification of such irradiation induced microstructural changes. Tungsten and its alloys are feasible candidates for divertor and first wall materials due to their high temperature properties, low sputtering and erosion, relatively low activation (half-lives short than 5 years), high thermal conductivity, and high melting temperature. A study on irradiation induced precipitation in tungsten is presented in this chapter to elucidate the effect of radiation damage on material properties. It includes a novel irradiation configuration for inducing displacement damage, consideration of high energy transmutation and activation reactions, and quantification of the irradiation induced microstructural changes in a SANS study.

6.2 Radiation damage in plasma facing fusion materials: a review

6.2.1 Plasma-facing material requirements

In the current social climate, there is a significant collaborative effort to move away from traditional fossil-fuel based energy sources towards low carbon technologies. To fulfil the energy requirements of a growing global population, multiple low carbon technologies must be combined. This has inspired the field of fusion research over the last 40 years with the aim of developing reliable commercial fusion reactors, which have lower regulatory burdens and generally better public perception than their traditional fission reactor counterparts.

Fusion reactors pose minimal environmental hazards and risk of radiological release since there is no fissile material present as in fission reactors. A particular attraction is the lack of intermediate and high level radioactive waste generated, which reduces future requirements for geological waste disposal facilities and long-term waste storage. The post-operational stage in the life cycle will hence have reduced costs, space requirements and safety concerns compared to fission reactors. It should be noted that some low level waste is inevitable due to the nature of the neutron environment which can still lead to activation of materials.

Current operational fusion reactors are only on a research-scale and there has yet to be any commercial fusion reactors in operation. A large issue here is the efficiency of the reactor system, with regards to the balance between using energy to meet the operational requirements and harnessing the energy released during fusion reaction to generate electricity through turbine driven systems. As it stands, the energy input to generate and maintain the fusion reaction is larger than the energy output. There is a collaborative effort in the scaling up of fusion devices to eventually reach a stage where commercialisation is possible; ITER and DEMO are examples of such efforts. These efforts have been clearly outlined in the EU Roadmap to fusion commercialisation [7], which is currently focussing on material development plans and increasing the understanding of irradiation induced damage in fusion materials that can be documented in an engineering materials database that will store all material properties in response to a fusion reactor environment [172, 173]. The validation of such material properties is an important design consideration for future commercial fusion devices.

Fusion material challenges remain the biggest hurdle to overcome in terms of providing long term energy solutions, largely due to the lack of operational experience on the scales required for commercialisation. Whilst the specific environmental loading experienced by materials is dependent on reactor design, the most onerous loadings that can contribute to material degradation during reactor operation considered for magnetic confinement fusion devices, such as ITER [25], are:

- High energy fusion neutron bombardment, coupled with high neutron fluxes (up to 10^{15} n/cm^{2}s with $E > 1$ MeV)
- High temperature exposure (> 800 °C for plasma facing components)
- High heat fluxes (> 10 MW/m^2)
- High magnetic field exposure to confine the fuel plasma (up to 11 T)

Neutrons are generated during the fusion reaction of the selected fuel type in the plasma of a fusion reactor. Whilst there are many possible combinations of elements that can be used as fuel, the most efficient combination is deuterium (^{2}H) and tritium (^{3}H). This is the fuel type selected for ITER and future demonstration fusion reactors (e.g. DEMO) [25, 174]. The deuterium-tritium reaction is:

$$^{2}\mathrm{H} + {}^{3}\mathrm{H} \rightarrow {}^{4}\mathrm{He}\ (3.5\ \mathrm{MeV}) + \mathrm{n}\ (14.1\ \mathrm{MeV}) \tag{6.1}$$

The neutrons released in this reaction have an energy of 14.1 MeV, which is significantly higher than the mean fission neutron energy (2 MeV) [175]. A comparison of a typical PWR neutron flux distribution and the DEMO first wall is shown in Figure 6.1.

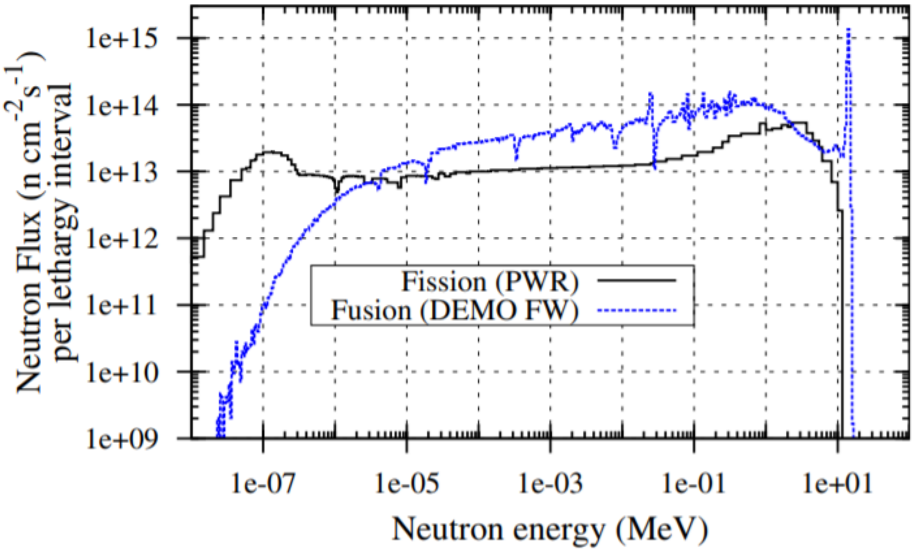

Figure 6.1: Graph showing comparison between the energy spectrum of neutrons for a PWR and the DEMO first wall [175].

High energy neutron exposure can result in threshold transmutation reactions in different materials that can lead to undesirable property changes, such as the production of hydrogen and helium that result in embrittlement. Such effects must be considered in combination with traditional neutron irradiation damage mechanisms.

The superconducting magnets responsible for confining the plasma are subject to a high fast neutron flux. This exposure can result in displacement damage that induces defects in the superconductor material which impacts the critical current and hence magnetic properties [176]. Initially the point defects improve flux pinning, but after a certain damage accumulation the effect reverses [177] and hence the critical current decreases and the stability of the magnet is compromised [178].

Due to the harsh environment, there are a unique set of PFM requirements that must be met so that the environmental loading conditions have a relatively low impact on material properties and overall performance through the life cycle of a fusion reactor.

All PFMs have similar requirements, mostly pertaining to their performance at high temperatures. The primary requirement of the first wall material is to transfer away heat generated through fusion in the fuelled plasma so that electricity can be generated through conventional turbine driven systems. The divertor acts as an exhaust to the tokamak. As such, PFMs must have a high melting point and thermal conductivity to withstand the high plasma temperatures and heat fluxes, and efficiently remove heat from the plasma. PFMs must be resistant to thermal shock and maintain their strength at high temperatures to ensure integrity of the vacuum vessel. In addition, PFMs should have relatively low neutron absorption cross sections to ensure that a sufficient flux of neutrons, generated from the fusion reaction in the plasma, can pass through the first wall to the breeder blanket to allow the device to maintain a tritium breeding ratio > 1. Since typical neutron fluxes are highest at the first wall location, PFMs must have minimised activation and transmutation properties for safety and performance-based considerations. PFMs must also be resistant to erosion and sputtering from interactions with the plasma that can lead to the creation of dust within the vacuum vessel [179, 180].

There are several candidate PFMs that have been of interest over the history of tokamak design and experiments, including beryllium, carbon-based materials, and tungsten. Historically, the first tokamak devices used graphite as a first wall material, including the Joint European Torus (JET) [181]. This was a short-lived choice since the generation of dust due to the low atomic number and hence low erosion and sputtering resistance lead to challenges in safety, waste and decommissioning aspects. The attractive irradiation resistance of carbon-based materials led to the use of carbon fibre composite (CFC) as a divertor material in the JET device, which provided more resistance to sputtering than graphite. The advantages of tungsten over beryllium include the lack of toxicity and the superior resistance of higher heat fluxes, and so tungsten is often favoured as a divertor material. In the ITER like wall (ILW) campaign at JET [182], a tungsten coating was added to the CFC divertor to mimic the plans for ITER, where tungsten tiles are planned to be the initial plasma facing material of the first wall. Tungsten is also a candidate PFM for the divertor which acts as an exhaust to the tokamak and experiences extremely high heat fluxes (up to 20 MW/m^2).

6.2.2 Transmutation reactions in tungsten

PFMs, such as tungsten, are susceptible to degradation of thermal and mechanical properties under high neutron fluences, for example embrittlement and a decrease in thermal conductivity. Hence, the lifetime of the PFCs is a key consideration.

In a fusion environment, pure tungsten has been found to release He as a product of transmutation reactions due to exposure to high energy neutrons [183]. At elevated temperatures, He nuclei can migrate to regions such as grain boundaries or other lower energy defects, resulting in swelling which can subsequently lead to embrittlement. To reduce this effect, tungsten can be alloyed [35, 38, 184].

The transmutation reactions expected in a pure tungsten PFM for ITER have been studied using the Monte Carlo N-Particle (MCNP) transport code [184]. It was found that for 5 and 14 year exposures to fast neutrons in ITER, rhenium, osmium and tantalum are the main elements that significantly increase in concentration (Figure 6.2). The concentrations stated in this study contrast with previous work [28], but the difference can be attributed to the fact that the earlier authors did not account for self-shielding effects in the transmutation calculations.

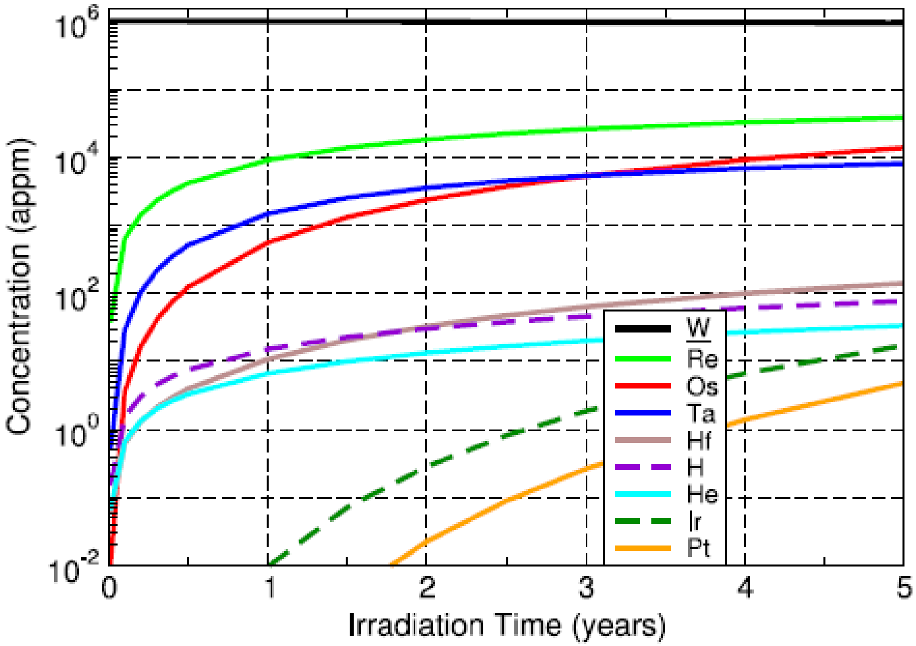

Figure 6.2: Calculated concentration of transmutation elements in pure tungsten, over 5 years, after exposure to fast neutrons[184].

The overall composition of PFMs can change over time as a result of transmutation reactions, meaning the material properties can also evolve. Such property changes as a result of high energy neutron irradiation must be understood and quantified to ensure the PFMs remain reliable over their lifetime in the reactor.

6.2.3 Irradiation induced microstructural changes in tungsten

As discussed in Section 2.2, tungsten exhibits excellent high temperature thermomechanical properties (*e.g.* high thermal conductivity, low ion sputtering, and low erosion) making it an attractive option for use as a PFM in fusion reactors such as ITER or DEMO [184]. For example, it has been suggested to be applied as a protective layer on top of some structural materials for the first wall or as the divertor armour. In either case they prove most useful in regions of high heat flux [183, 185].

Chapter 2 discusses the mechanisms of irradiation damage through bombardment by neutrons. The creation of secondary defects from the precipitation of vacancies and solute interstitials can impede dislocation motion. Studies on transmutation show that production of elements such as rhenium and osmium from the irradiated tungsten can lead to clustering of vacancies and interstitials, leading to precipitate damage in the matrix. This has been explicitly found by [35, 58, 186, 187, 188]. Elucidating the nature of such precipitates as a result of radiation damage is imperative for ensuring integrity of such in-service materials. The current research is heavily focussed on studies on nucleation and growth; there is limited data on the irradiation induced evolution of microstructure of such alloys detailing precipitate size, distribution, shape, and stoichiometry.

For studies of the effects of these damage events, we are typically concerned with imitating damage from fast neutrons (14.1 MeV), as opposed to thermal neutrons in fission irradiation studies. Such damage can be induced using fast material test reactors, accelerator driven neutron irradiation systems, or by using high energy protons, for example 16 MeV protons to induce 1 dpa [37].

Of particular interest from irradiated tungsten studies is the σ precipitates that form when osmium is present in the tungsten matrix [28, 189, 190]. These are introduced as ∼10 nm plate or needle like structures that lie along {110} planes in $W_{1\text{-}x}Os_x$ ($x < 0.05$) and are thought to be the tetragonal σ phase from the equilibrium phase diagram [191]. The resultant microstructure is brittle which is attributed by increased regions of localised strain in the lattice when tetragonal σ is present in BCC tungsten [36]. By contrast, additional studies [185, 188] have found σ precipitates to be *equiaxed*. Examples of the microstructural changes and physical effects observed in WRe and WOs alloys are shown in Figures 6.3 and 6.4.

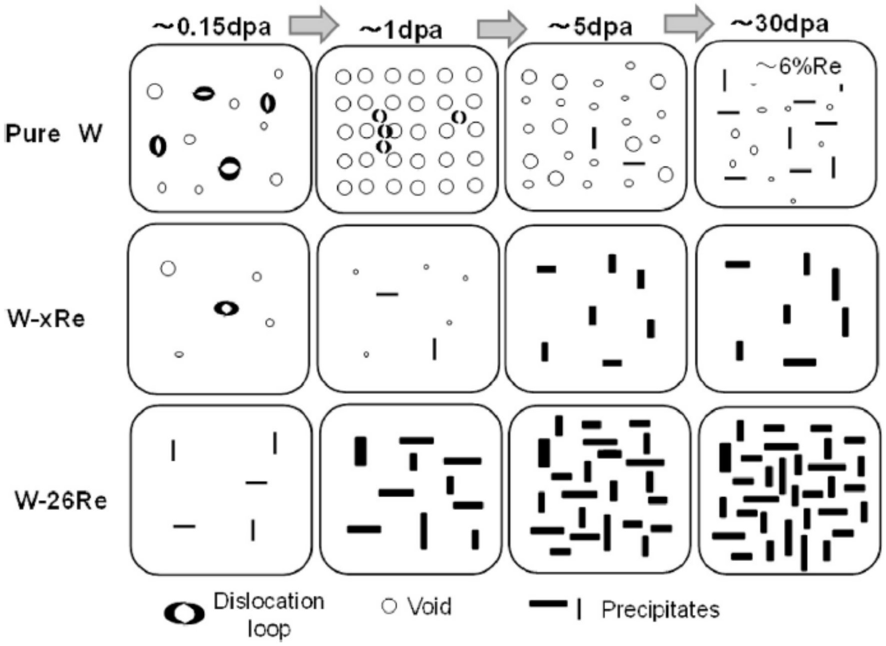

Figure 6.3: Schematic diagram of microstructural features present in W and WRe for a variety of damage levels [27].

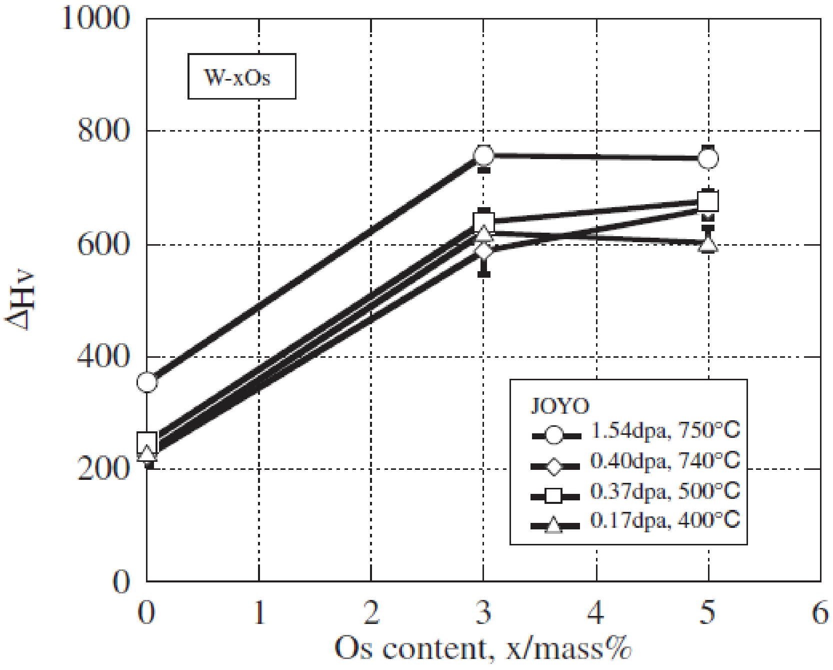

Figure 6.4: Hardness as a function of Os content in $W_{1-x}Os_x$ for a variety of damage levels [189].

By inducing damage in pure tungsten, and aiming to transmute rhenium, one can study such irradiation effects using SANS and quantify the effect on material properties using nanoindentation.

6.2.4 Neutron vs proton irradiation

Neutron irradiation requires long irradiation times (∼years) to reach the desired dose levels as either part of surveillance programmes or in designated test reactor facilities. As a result, this can end up being expensive and time consuming. By contrast, proton irradiation using ion accelerators can reach desired doses on the order of hours, meaning it is a cheaper and faster surrogate. Moreover, proton irradiation allows for the variation of irradiation parameters, such as temperature and pressure, that aren't feasible to alter in a reactor environment [31].

Whilst the irradiation damage mechanisms on the microstructural level are analogous between neutrons and protons due to their equal masses, it is imperative to understand the difference in the damage profiles between the two particles. The charged proton interacts with the electrons of atoms in the irradiated material through the Coulomb interaction. The proton scattering cross section is inversely proportional to velocity, so as the proton slows down the probability of interaction with the electrons increases, which leads to a large deposition of energy as the proton comes to a stop that is described by a characteristic Bragg peak. The uncharged neutron does not interact with the electrons and hence has a long mean free path over which it deposits a constant amount of energy in the irradiated material. As a result, the overall damage profile with penetration depth in the irradiated material is different depending on the irradiation particle, as shown in Figure 6.5. As expected, the neutron damage profile is relatively flat, whilst the proton damage profile is flat at the start of its interaction (plateau region) and then peaks before the proton loses all of its energy over a short range (Bragg peak).

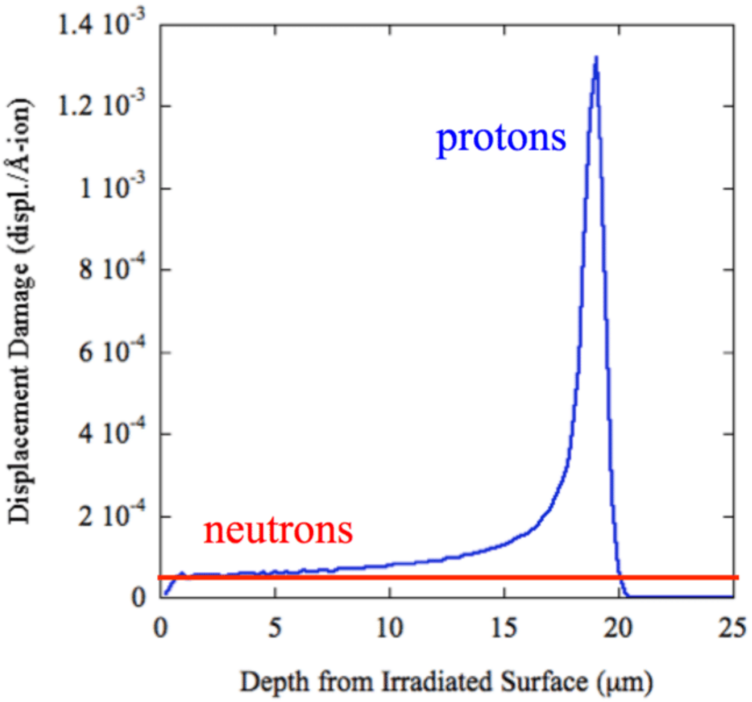

Figure 6.5: Graph showing the comparison of neutron and proton damage profiles in irradiated Fe9%Cr oxide dispersed steel from [192].

Since it is the final state of the material that contributes to its properties, the effects of neutron and proton irradiation can be studied by direct comparison of the induced microstructural damage *e.g.* dislocation loops, precipitates, segregation and vacancies. This means that, despite the differences in displacement damage profiles, proton irradiation can act as a successful alternative to neutron irradiation for such damage studies [11]. This is a well-established method for studying irradiation damage mechanisms, as studied in [193] and [194], hence it was decided to use proton irradiation in this study to induce damage in the tungsten samples.

The evolution of damage can be observed as a function of sample depth during proton irradiation. Tungsten has been selected since it is a candidate PFM and its density means that higher energy protons can be used during irradiation, making it easier to separate the different depth regimes. Through comparison of behaviour at different depths, the evolution can then be used to establish which depth is the most appropriate for simulating neutron damage. Such a question has been addressed for studying irradiation damage in stainless steels [195], however this work will aim to produce a comprehensive comparison of microstructural evolution and material properties for different damage levels in irradiated tungsten.

6.3 Materials and methods

6.3.1 Tungsten samples

To better understand the relationship between irradiation damage and mechanical properties, multiple samples with different induced damage levels are required. Instead of individually irradiating tungsten samples, a stack of 10 individual tungsten foils were used (see justification in Section 6.3.3). The benefit of this approach for proton irradiated samples is that multiple depths along the damage profile (and hence multiple damage levels) can be investigated whilst ensuring that the irradiation conditions are constant for all samples. This is discussed in detail in Section 6.2.4. The ability to irradiate multiple samples at the same time allows for a direct comparison between samples where the only difference is the dpa induced. The foils are numbered as foils 1 to 10, with 1 being the foil closest to the proton beam, and 10 being the foil farthest away.

The tungsten foils were cut into 2.5 cm x 2.5 cm squares from a 50 μm thick as-rolled sheet obtained from Goodfellow [196]. The sheet composition is detailed in Table 6.1.

Table 6.1: Tungsten foil details.

Element	**Fraction [%]**
W	> 99.95
Mo	0.015
Pb	< 0.005
Si	< 0.005
C	0.003
Sn	< 0.003
O	0.002
Fe	0.002
Ca	< 0.002
Cu	< 0.002
Ni	< 0.002
Ti	< 0.002
N	0.001
Mg	< 0.001
H	0.0006

An understanding of the general material properties of tungsten is required for activation, SANS and nanoindentation analysis presented in this chapter. The properties of interest are summarised in Table

6.2.

Table 6.2: Typical properties of high purity tungsten [105].

Property	**Value**
Atomic mass	183.84 u
Density	19.3 g/cm^3
Lattice constant	3.165 Å
Crystal structure	BCC
Melting temperature	3370 °C
Boiling temperature	5900 °C
Young's Modulus	400 GPa
Poisson's ratio	0.28
Yield strength	750 MPa
Emissivity @ 100 °C	0.15
Thermal conductivity (20°C, 200°C, 600°C, 1000°C)	163.3, 146, 128, 117 W/mK
Lattice displacement energy	90 eV [197]

6.3.2 Proton irradiation

In order to reflect the conditions that materials in a high dose environment experience, radiation damage has been induced using the MC40 cyclotron at the University of Birmingham [198].

6.3.2.1 MC40 cyclotron

The MC40 cyclotron is a particle accelerator capable of accelerating a variety of different particles to a range of energies, as shown in 6.3. This versatility means it has applications to many industry sectors in addition to radiation damage studies in nuclear materials.

Table 6.3: Beam properties of the MC40 cyclotron [198].

Ion type	**Energy (N=2) [MeV]**	**Energy (N=1) [MeV]**
^{1}H	3.7 to 10	10.8 to 40
^{2}H	5.4 to 20	-
^{3}He	8 to 28	33 to 50
^{4}He	10.8 to 40	-

The initial ion beam is produced in the presence of an electromagnetic field. The behaviour of the ion beam in the cyclotron in the presence of a magnetic field can be described by the following equation

$$\frac{mv^2}{r} = QvB \tag{6.2}$$

where m is ion mass, Q is ion charge, r is the radius of the circle of motion, and B is the magnetic field strength. Hence, the achievable ion beam energies is wholly dependent on the radius of the cyclotron at which the ion beam exits, R, and strength of the electromagnetic field. The ion kinetic energy at extraction is thus

$$E = \frac{1}{2}mv_R^2 = \frac{R^2Q^2}{2m}B^2 \tag{6.3}$$

In addition, an oscillating voltage is applied across two large electrodes known as 'dees' that causes acceleration of the ion beam as it reaches the gap between the dees. This acceleration frequency can be altered between 14.2 and 28 MHz to achieve the desired beam energy. The harmonic number of the oscillating voltage, N, can be set to 2 or 1 to alter the accelerating frequency and hence achieve the lower and upper energy ranges respectively. The correct energy beam then leaves the system through an ion guide and is lead to the irradiation chamber of interest. This is shown schematically in Figure 6.6. It is noted that the cyclotron is confined in a vacuum vessel to minimise energy losses.

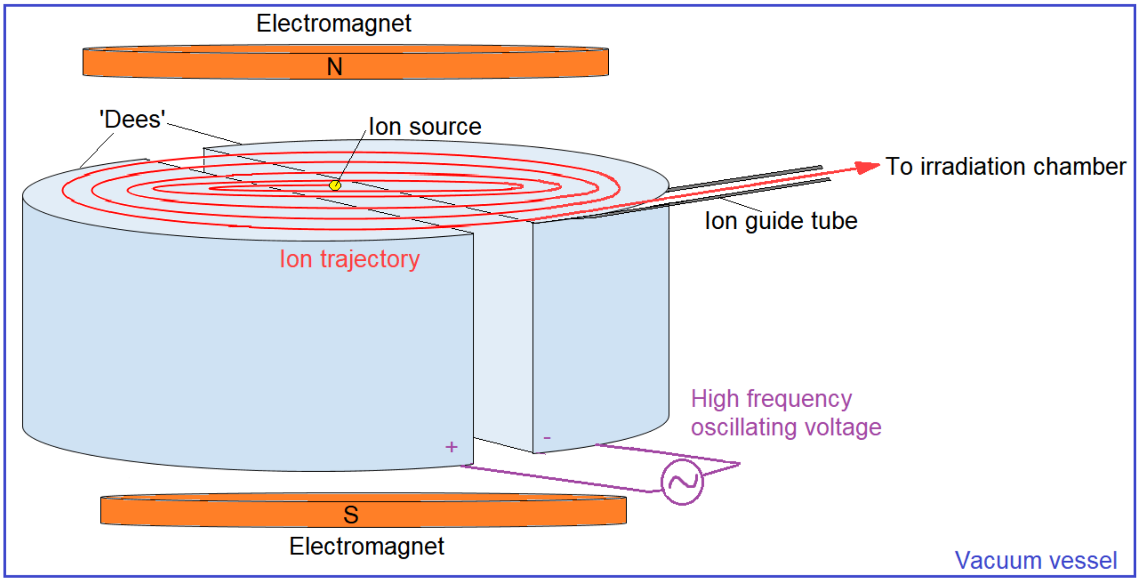

Figure 6.6: Schematic diagram of a cyclotron for ion beam production.

6.3.2.2 Irradiation parameters and setup

In the case of a PFM in a typical fusion reactor, *e.g.* ITER/DEMO, the exposed temperature ranges from 500 °C to 800 °C [12] and irradiation induced precipitation has been observed in tungsten alloys at doses between 0.1 and 15 dpa [59, 188, 189]. These damage levels, alongside fusion energy neutrons, are comfortably achievable within the operational boundaries of the MC40 cyclotron.

The materials irradiation vault at the MC40 cyclotron has a chamber (approximate diameter = 1 m) under vacuum with a removable heater block that is used to mount the foil samples on. The chamber allows for vacuum monitoring, temperature monitoring via thermocouples and an exclusive borosilicate window that allows for mounting of a thermal camera, and a proton aperture for beam shape and size selection. The use of mica washers combined with the presence of a ceramic backplate on the heater block sample mount allows for the samples to be electrically isolated so that the charge deposited can be directly measured (as a proxy for the amount of damage induced). The indium foil acts to increase the efficiency of heat transfer between the heater block and the samples themselves. Schematic diagrams of the irradiation chamber and sample mount are shown in Figures 6.7 and 6.8 respectively. Figures 6.9 and6.10 show photos of the exact setup for reference.

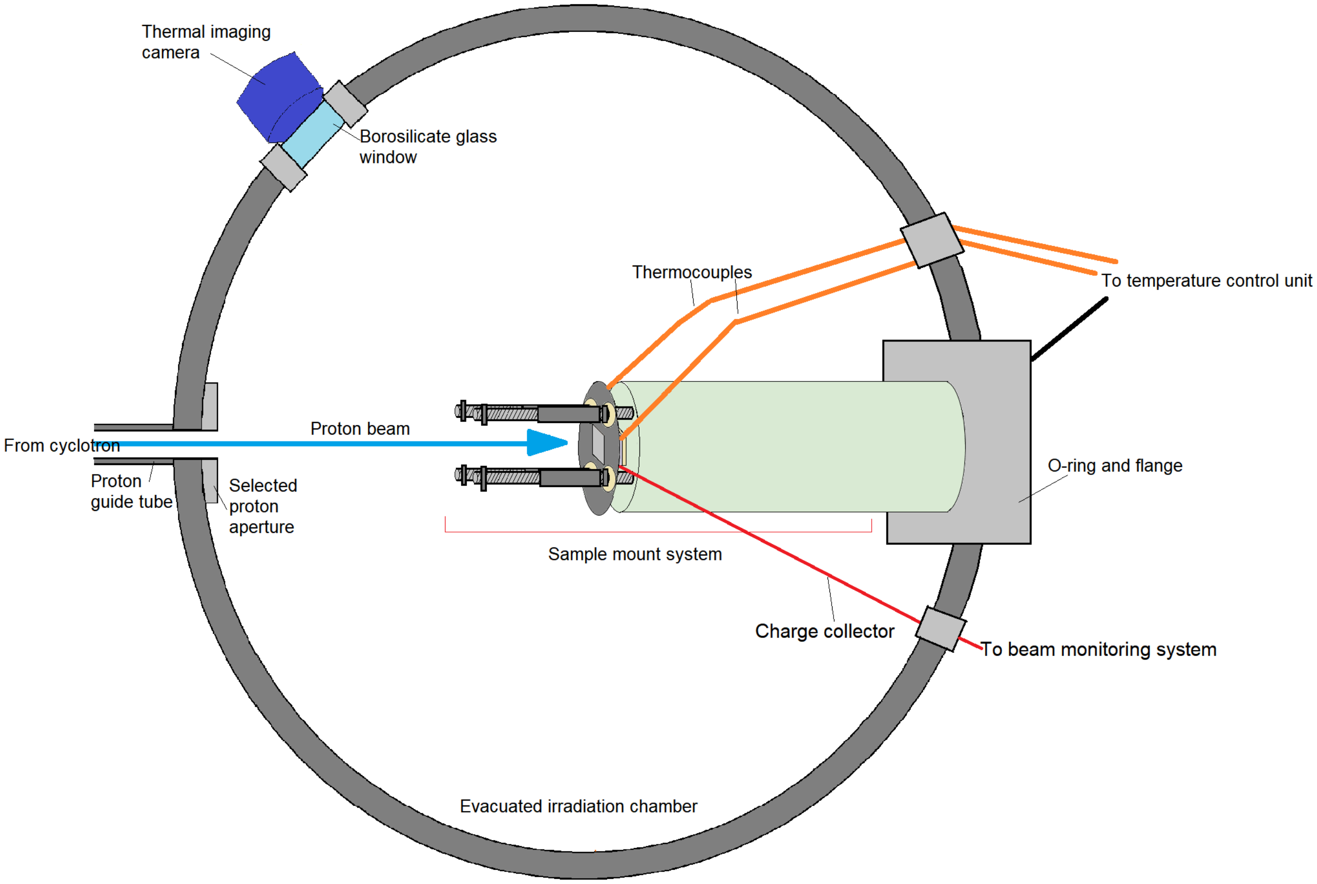

Figure 6.7: Schematic diagram of cyclotron chamber setup.

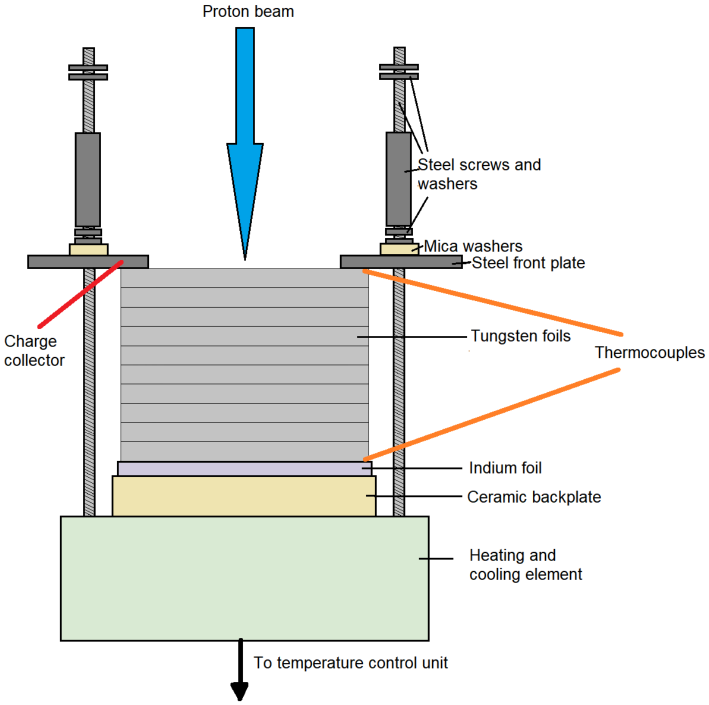

Figure 6.8: Schematic diagram of tungsten sample mount setup.

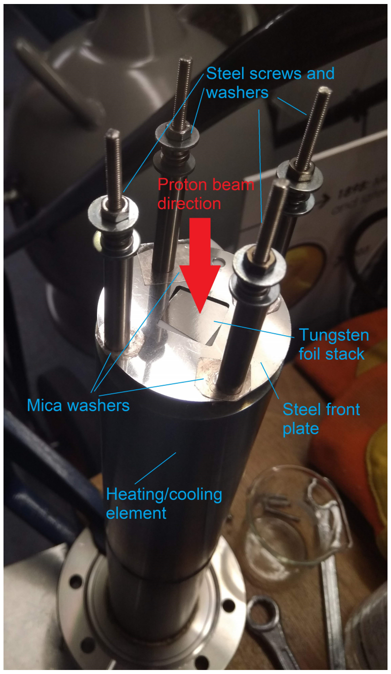

Figure 6.9: Photograph of the tungsten sample mount setup.

Figure 6.10: Photograph of the cyclotron chamber setup.

The properties of the proton beam can be selected to allow for a specific amount of charge to be deposited on the sample. The total charge accumulated on the sample can be measured since the samples are completely electrically isolated from the mount (due to the use of mica washers and ceramic backplate). The accumulated charge is measured by the charge collector probe which is placed between the front plate and foil 1.

The thermocouple on the backing plate was placed in contact with the indium foil to increase the thermal heat transfer coefficient so as to maximise the accuracy of the temperature readings. Since each foil was placed with good thermal contact with its adjacent foils, the thermocouple data over the entire irradiation period was averaged to give an overall estimation of the irradiation temperature. The uncertainty bound on the irradiation temperature is equivalent to the standard deviation of the temperature readings over the total irradiation time. The addition of a thermal camera allowed for independent temperature monitoring of the top foil, which was calibrated to the thermal emissivity of tungsten by the use of black paint.

A study on the simulation of neutron damage with multiple high energy proton beams in tungsten has been investigated in [199]. It was found that there is a subtle offset between correlated neutron and proton energies for inducing damage due to the charged nature of protons, and so the proton energy chosen to best simulate 14.1 MeV neutron damage was 15 MeV.

Table 6.4 shows the parameters used during the irradiation. The aperture used allowed for a rectangular proton beam to be incident on the samples, and the exact location of the incident beam was found by placing a fluorescent disc on the sample mount screws upstream of the foil stack; a photograph of the resultant disc post irradiation is shown in Figure 6.11, where the area of the proton beam can be clearly identified.

Table 6.4: Tungsten sample irradiation parameters.

Parameter	**Value**
Date of irradiation	19.05.2019 and 21.05.2019
Total charge accumulated	0.203 C (1.268 x 10^{18} protons)
Energy of protons	15 MeV
Beam current	4.7 μA
Beam size	6 mm x 5 mm
Beam flux	1.04 x 10^{14} cm^{-2}s^{-1}
Mean sample temperature	509.25 ± 32.41 °C
Vacuum pressure	1.71 ± 0.77 x 10^{-4} Torr
Total irradiation time	9.4 hrs

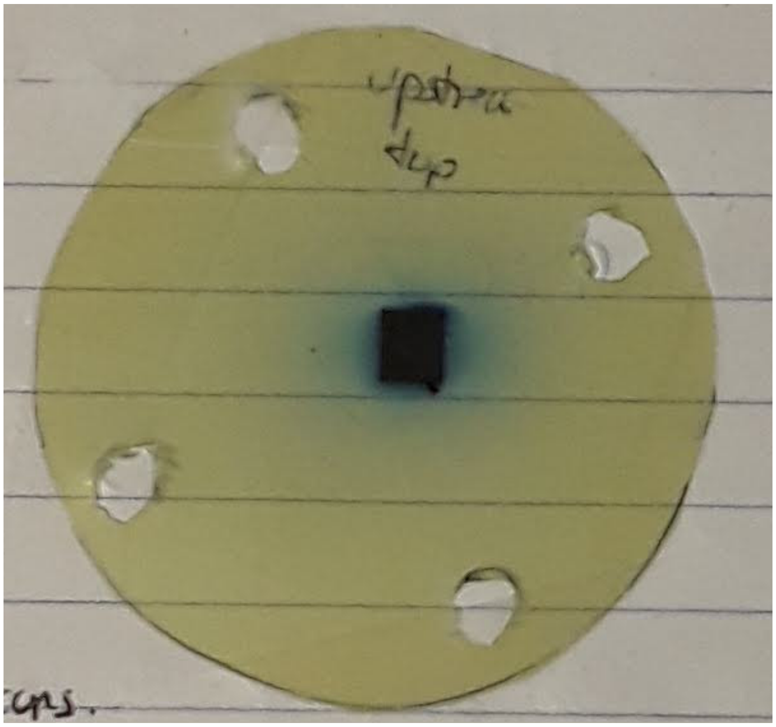

Figure 6.11: Photograph showing the activated disc placed upstream of the sample mount during irradiation. The area of the incident 6 mm x 5 mm proton beam is clearly shown by the dark markings.

6.3.3 Damage calculations

In addition to the above, one must consider the dose needed to induce a certain amount of damage in our samples and to know at which depth the Bragg peak occurs, both of which will be computed using the Stopping Range of Ions in Matter (SRIM) software package [200].

SRIM is a Monte Carlo model of particle transfer and scattering, with the functionality of tracking collision events as a function of depth in a material of choice. Alongside PKAs, SRIM considers target and recoil atom energies, secondary knock-on atoms, and additional scattering phenomena such as ionisation and phonon effects.

The displacement damage theory incorporated into SRIM has been discussed in depth in Section 2.2.1. There are two main calculation options that incorporate the Kinchin and Pease damage model, but there have been several shortcomings found in how SRIM estimates the number of stable defects produced using this calculation method alone [201]. Hence, particular care should be taken when using the SRIM outputs to calculate induced displacement damage.

The SRIM software allows for inputs of ion beam properties such as ion type and energy and material properties such as composition, lattice binding energy, and displacement threshold energy. The lattice binding energy is energy lost by recoiling target atoms when it leaves the lattice. The displacement threshold energy is the minimum kinetic energy required to displace an atom from its lattice site by more than one atomic spacing to form a stable vacancy-interstitial defect pair.

In the case of tungsten, the nominal density of 19.3 g/cm^3 was used. The lattice binding energy for tungsten was set at 0 eV [201] and the displacement threshold energy was set to be 90 eV, as recommended by the American Society for Testing and Materials (ASTM) [197] and supported by molecular dynamics simulations in [202]. The ion properties were set to H$^+$ ions (protons) with an energy of 15 MeV to be consistent with the beam parameters used during irradiation.

The first step, prior to irradiation, is to establish the Bragg depth of 15 MeV protons in pure tungsten. This was used to ensure that the Bragg peak would be captured in the stack of 50 μm foils, allowing for at least one foil where no protons would theoretically reach (essentially unirradiated) to allow for a direct comparison to be made between samples.

Figure 6.12 shows the dependence of the Bragg peak depth in pure tungsten with incident proton beam energy. For 15 MeV protons the Bragg peak is at 328 μm. This has been used to justify the choice of 10 x 50 μm foil tungsten samples to ensure that the full damage profile is covered. The SRIM simulations are hence tracked up to a depth of 500 μm to ensure that the damage in all samples can be calculated. The simulations were ran for 1 x 10^6 protons in total.

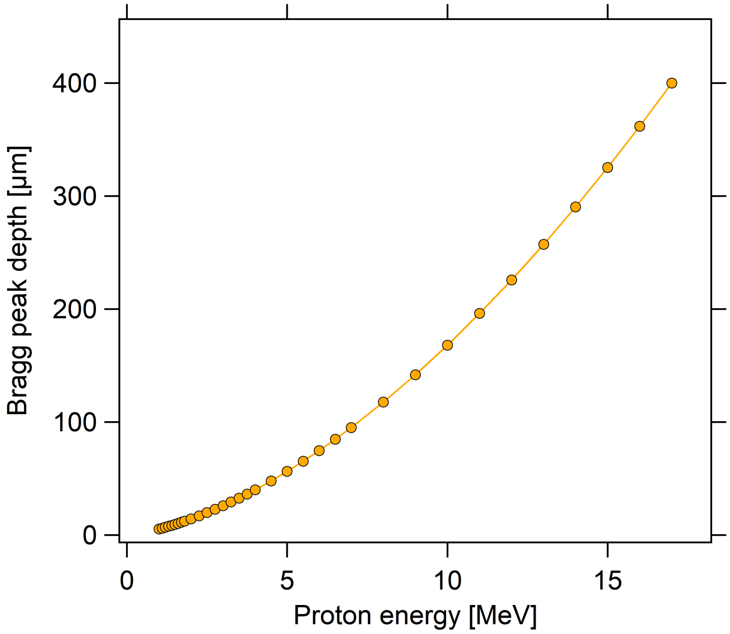

Figure 6.12: SRIM predicted Bragg peak depths in pure tungsten as a function of proton beam energy.

In order to calculate the induced damage via irradiation, the number of vacancies produced per ion as a function of depth is required. This is a direct output of the SRIM simulations. An example of a graphical output of this metric can be seen in Figure 6.13 for 3 MeV protons in a high Cu RPV steel.

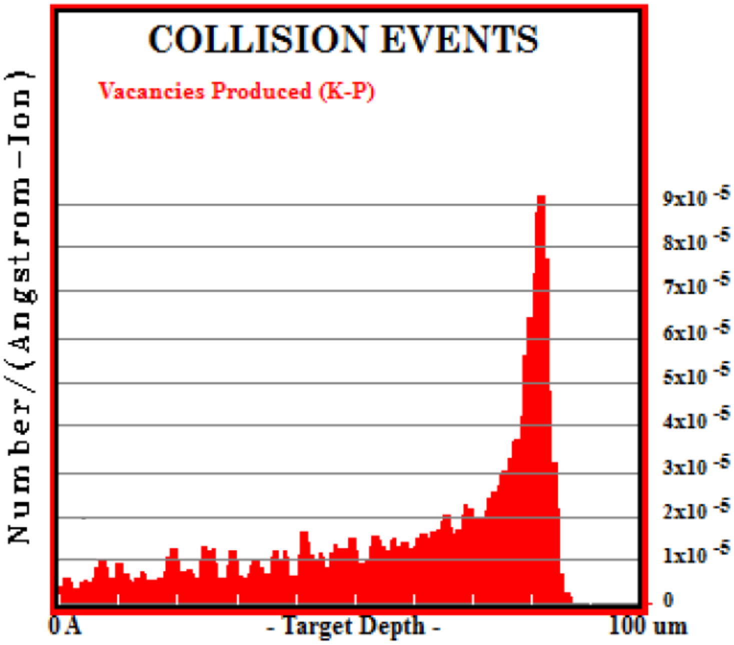

Figure 6.13: Example of simulated Bragg peak in a high Cu RPV steel [31].

The method of calculating the proton irradiation induced displacement damage from the SRIM vacancy output as a function of depth is as follows:

1. SRIM outputs a vacancy.txt file that contains the number of vacancies created by ions and recoil atoms as a function of the depth modelled over. This data can be summed to give the total number of displacements (all vacancies are physical displacements by nature), X, produced by one ion as a function of depth.

2. The total number of displacements per atom, dpa, in the irradiated material can be described by

$$dpa = \frac{X\phi}{N} \tag{6.4}$$

where X is the total output number of vacancies produced by one ion at a certain depth [displacements ion^{-1}length^{-1}] and N is the atomic number density of the incident material [atoms volume^{-1}], given by

$$N = \frac{N_A \rho}{M} \tag{6.5}$$

where N_A is Avogadro's constant [6.022 x 10^{23} atoms mol^{-1}], M is the molar mass [g mol^{-1}], and ρ is the material density [g volume^{-1}].

3. ϕ is the fluence of the ion beam [ions area^{-1}], described by

$$\phi = \frac{Q}{AQ_p} = \frac{T}{A} \tag{6.6}$$

where Q is the amount of charge collected on the material [C], Q_p is the charge of the proton [1.6 x 10^{-19} C], T is the total number of protons deposited on the material [arb.], and A is the area of the incident proton beam [area].

4. Combining the above gives the total damage equation as

$$dpa = \frac{XT}{NA} \tag{6.7}$$

5. This derivation can been confirmed using dimensional analysis of the units in the above equation

$$\frac{\text{displacements}}{\text{atom}} = \frac{\text{displacements ion}^{-1}\ \text{length}^{-1}\ \text{ion}}{\text{atoms length}^{-3}\ \text{length}^{2}} = \frac{\text{displacements length}^{-1}}{\text{atoms length}^{-1}} \tag{6.8}$$

6.3.4 Activation and transmutation analysis

The main limitation in the irradiation process is the amount of damage that can feasibly be induced, due to the requirement of transporting the irradiated samples to the ILL for SANS analysis. In order to package as an excepted package the surface dose rate must not exceed 0.5μSv/hr [65] and there are certain isotopes that carry activity restrictions, as outlined in transport of radioactive material regulations set by the International Atomic Energy Agency (IAEA). It is hence very important to understand the activation and transmutation properties of irradiated tungsten. This ensures that as much damage can be induced as possible whilst not exceeding the regulatory limits, and at the very least that there is enough time between irradiation and transportation to ensure adequate cooling of the samples.

The possible 15 MeV proton induced activation reactions of tungsten have been considered in terms of their cross sections as a function of proton energy. The transmutation reactions from the possible activated isotopes have subsequently been considered, so as to indicate the probability of transmuting certain daughter decay products which may contribute to the overall activity of the irradiated samples [203].

The predicted activation reactions of pure tungsten when incident with 15 MeV protons are shown in Table 6.5. These have been found by considering the cross section for proton interactions with the natural isotopes in pure tungsten (^{180}W, ^{182}W, ^{183}W, ^{184}W, and ^{186}W) and its possible transmuted elements (Os, Re and Ta) from [204]. An example energy dependent cross section of ^{182}W(p,2n)^{181}Re shown in Figure 6.14. Proton interactions with a cross section greater than 1 x 10^{-15} barns have been considered as probable; all other cross sections have been regarded as negligible. The decay chain to stability of each isotope has also been investigated to understand the transmutation reactions relevant to irradiated tungsten. This has been completed using the National Nuclear Decay Chart database [205] and transmutation properties of tungsten simulated using activation code FISPACT-II [206] and TENDL-2015 [207]. The resultant transmutation reactions considered are presented in Table 6.6.

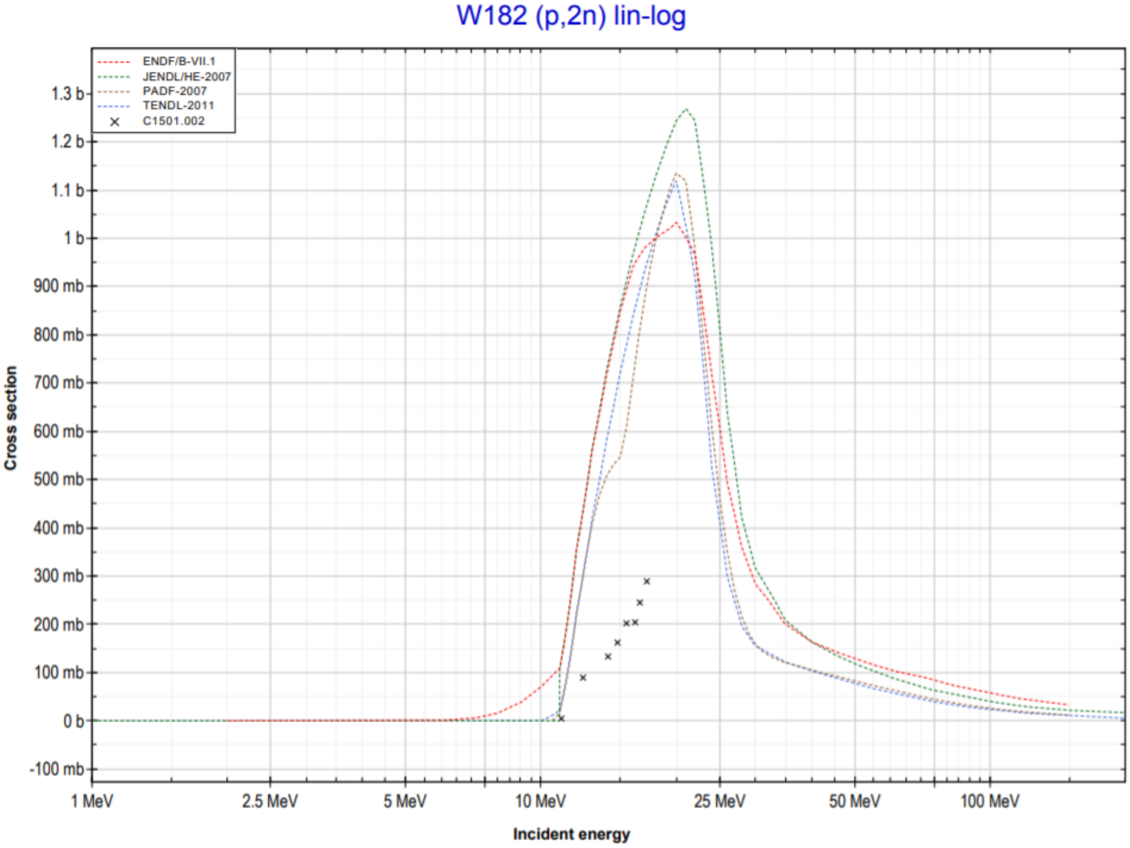

Figure 6.14: Example of energy dependence of the cross section of ^{182}W(p,2n)^{181}Re, from [204].

Table 6.5: Predicted proton induced activation reactions of pure tungsten and its transmuted elements (Os and Re) irradiated with 15 MeV protons.

Proton interaction	Q value [keV]	Cross section [barns]
^{182}W(p,2n)^{181}Re	-10580	15 x 10^{-2}
^{186}W(p,n)^{186}Re	-1363	6 x 10^{-2}
^{186}W(p,d)^{185}W	-4968	1 x 10^{-2}
^{186}W(p,n+p)^{185}W	-7192	1 x 10^{-2}
^{186}W(p,2p)^{185}Ta	-8404	1 x 10^{-14}
^{192}Os(p,n)^{192}Ir	-1829	6 x 10^{-2}
^{187}Re(p,d)^{186}Re	-5135	1 x 10^{-4}
^{187}Re(p,n+p)^{186}Re	-7359	1 x 10^{-4}

Table 6.6: Predicted proton induced activation reactions of pure tungsten irradiated with 15 MeV protons.

Isotope	Half life [time unit]	Decay mode	Probability [%]	Daughter product
^{181}Re	19.9 hr	EC	100	^{181}W
^{181}W	121.2 d	EC	100	^{181}Ta (stable)
^{185}W	75.1 d	β^-	100	^{185}Re (stable)
^{186}Re	3.7 d	β^- / EC	92.53 / 7.47	^{186}Os / ^{186}W
^{186}W	> 2.3 x 10^{19} y	Double β^-	100	^{186}Os
^{186}Os	2 x 10^{15} y	α	100	^{182}W (stable)
^{185}Ta	49.4 min	β^-	100	^{185}W
^{192}Ir	73.8 d	β^- / EC	95.24 / 4.76	^{192}Pt (stable) / ^{192}Os (stable)

These predicted transmutations will be assessed in Section 6.4.1.

To ensure that each sample is safe for transportation, gamma spectroscopy is carried out using a High Purity Germanium (HPGe) detector post irradiation to identify the isotopes contributing to the activity and measure the dose rates. If the predicted transmutations and subsequent activity could exceed transportation limits, the argument to use less energetic protons becomes valid, however not ideal. This is a typical approach when irradiating RPV steels with protons, where the activity of Co-60 transmuted from Fe isotopes dominates the overall dose profiles and so transmutation of this is limited by limiting the proton beam energy to 5 MeV [31].

The presence of a high purity germanium crystal with a large depletion volume allows for the creation of electron-hole pairs when incident with a photon. The detection of charge is directly proportional to the energy deposited within the crystal. The benefit of using such a detector over a scintillation counter, such as a NaI, is the high energy resolution. The detector resolution and efficiency must be quantified and accounted for during analysis of the measured spectra in order to obtain accurate quantification of active isotopes and overall dose rate.

The detector energy resolution, R, can be calculated as

$$R = \frac{FWHM}{E} \tag{6.9}$$

where FWHM is the full width at half maximum of the detected photopeak, and E is the energy of the detected photopeak.

The detector efficiency accounts for the efficiency of the crystal to detect gamma rays. It is a function of the detector properties and the energies of the incident gamma rays. Efficiency can be defined by two metrics:

1. Intrinsic efficiency, ϵ_{int} - the ratio of the number of photons detected to the number of photons incident on the detector, described by

   $$\epsilon_{int} = \frac{4\pi}{\Omega}\frac{\dot{N}}{A\Gamma} \tag{6.10}$$

   where A is the source activity and Γ is the branching ratio. $\dot{N}$ is the rate of gamma rays interacting with the Ge crystal given by

   $$\dot{N} = \frac{N_t - N_b}{t_l} \tag{6.11}$$

   where N_t is the total counts detected, N_b is the background counts, and t_l is the detector live time. Omega is the solid angle between the source and detector face, given by

   $$\Omega = 2\pi\left(1 - \frac{d}{\sqrt{d^2 + a^2}}\right) \tag{6.12}$$

   where d is the distance between the source and the detector face, and a is the radius of the detector face.

2. Absolute efficiency, ϵ_{abs} - the ratio of the number of photons detected to the number of photons emitted by the source, described by

   $$\epsilon_{abs} = \frac{\Omega}{4\pi}\epsilon_{int} \tag{6.13}$$

The intrinsic efficiency accounts for the geometry of the detector setup, whilst the absolute efficiency removes any geometric dependence. Hence, the absolute efficiency should be used so as to not underestimate the total source activity.

The activity that each photopeak contributes to the total source activity, A, can be found using

$$A = \frac{\dot{N}}{\epsilon_{abs}} \tag{6.14}$$

The estimated dose rate, D, in μSv/hr can be found using

$$D = \frac{AE_{\gamma}}{6r^2} \tag{6.15}$$

where A is the activity in MBq, E_{γ} is the photopeak energy in MeV, and r is the distance from the source in m. This method was primarily used to estimate the dose rate after certain periods of time post-irradiation to successfully plan shipment of samples to the location of the SANS experiment. The dose rate can also be explicitly measured using a hand held gamma dose meter. This was used periodically to ensure the dose was reducing at an appropriate rate to allow for SANS analysis.

6.3.5 SANS

6.3.5.1 Experimental measurements

The SANS experiment was carried out on the D22 instrument at the ILL, Grenoble. This instrument has been used in previous chapters for quantifying precipitation events in other nuclear materials.

Since tungsten is non-magnetic, the experimental setup is relatively standard in that no sample environment is required. The individual foils from the irradiated foil stack were loaded into a 2D translatable sample mount, as shown in Figure 6.15. The samples were removed from their shielding container and care was taken to measure the contact and distance dose rates before handling of the samples, through liaising with the dedicated Health Physics department. The contact dose rate was above the limit for handling, so samples were manipulated using long tweezers and with an active effort to work quickly and efficiently to limit exposure time.

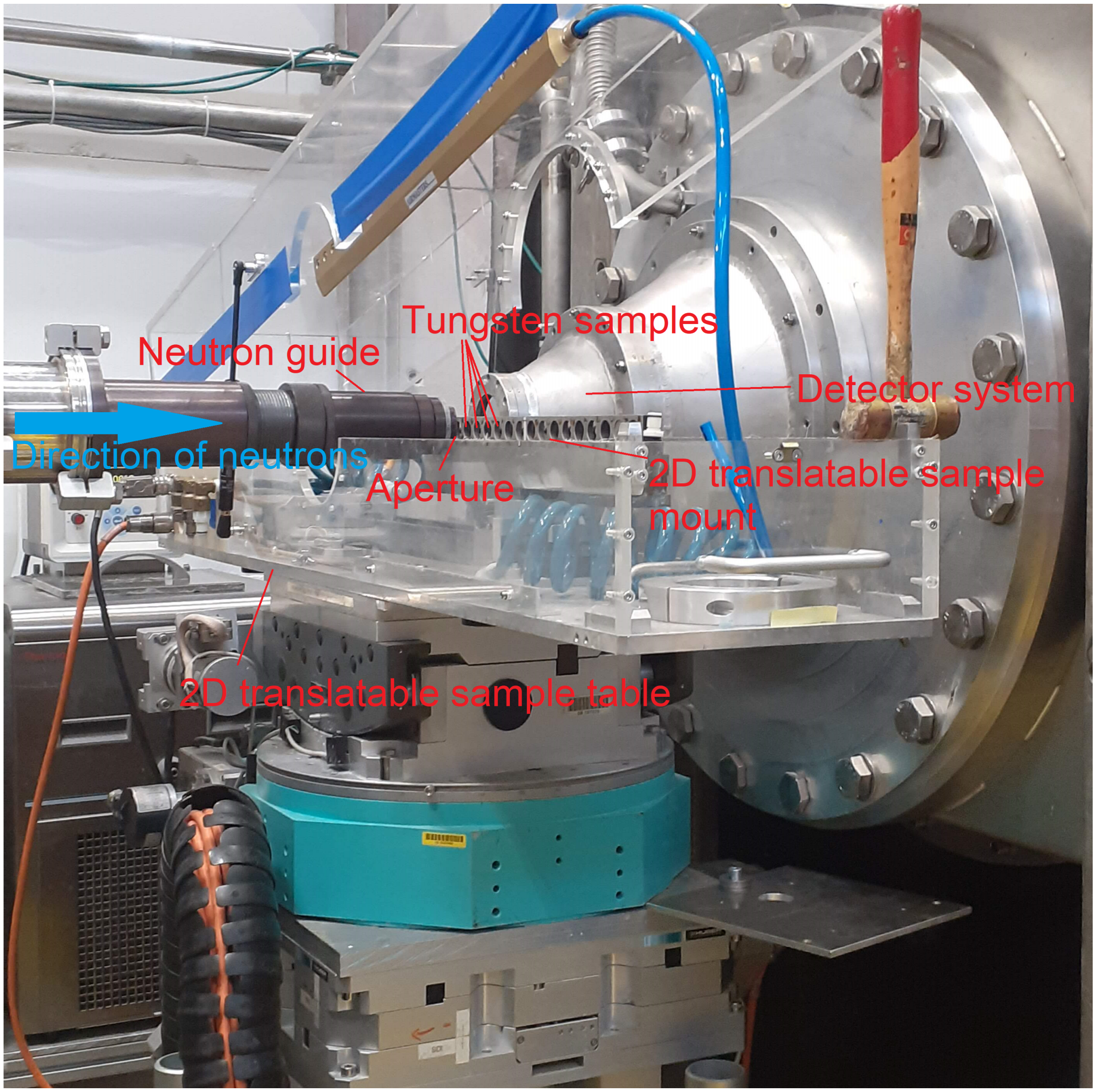

Figure 6.15: Sample space area of D22 SANS instrument with 2D translatable sample mount used to mount the required tungsten and calibration samples.

Each position on the sample mount either contained an irradiated tungsten foil mounted between two Al rings (including foil 10 at the back of the irradiation stack located beyond the Bragg peak), or the required samples for data corrections. The SANS measurements taken were:

- Scattering through a H_2O cell to calibrate the detector.
- Scattering through Cd to correct for electronic background.
- Scattering through an empty Al ring for transmission calculations.
- Scattering through each tungsten foil sample at two q ranges.

The experimental setup parameters used to achieve two well-overlapped q ranges are presented in Table 6.7. The q ranges were selected to be able to observe scattering events on the nanoscale (1.58 nm $<$ d $<$ 33.07 nm).

Table 6.7: Selected experimental conditions for forming two well-overlapped q-ranges.

Property [unit]	**Medium q**	**High q**
q range [Å^{-1}]	0.019 to 0.118	0.053 to 0.397
Wavelength [Å]	5.0	5.0
Sample-detector distance [m]	4.0	1.4
Collimation distance [m]	4.0	2.8

On some of the irradiated samples, there is surface oxidation present due to the combination of poor vacuum conditions in the cyclotron chamber and elevated temperature exposure during irradiation. It is imperative to distinguish between probing the surface oxide and probing the true bulk sample, since it is difficult to deconvolve the individual contributions from the measured scattering intensity.

Due to the importance of probing the correct area of each sample, significant care was taken in the alignment process to ensure that the correct sample area was chosen. To aid with alignment and to ensure that only the irradiated part of each of the samples was probed, a laser was used during sample alignment. In addition, the neutron beam size was selected to be smaller than the proton irradiation beam size. The diameter of the neutron beam aperture was set as 5 mm, compared to the 6 mm square proton beam aperture used during irradiation, allowing for the complete separation of induced damage and the unirradiated sample matrix. This is shown schematically in Figure 6.16.

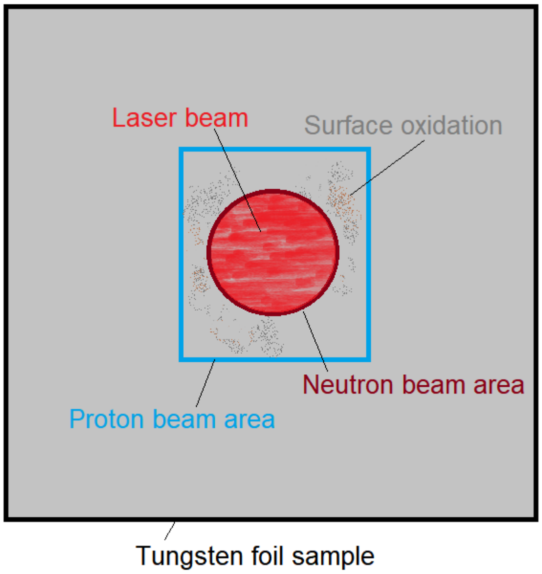

Figure 6.16: Schematic of tungsten foil sample surface illuminated by neutron beam.

6.3.5.2 Data reduction and analysis

The standard data corrections discussed in Chapter 2 were applied to the raw scattering profiles for each q range to obtain the total scattering intensity for each foil over the range 0.019 $Å^{-1}$ to 0.397 $Å^{-1}$.

As discussed, experimental care was taken to ensure that the neutron beam was smaller than the irradiated area so that only irradiation damaged aspects of the samples were probed and to avoid surface oxidation areas to prevent contamination in scattering profiles. Additional measurements of the unirradiated region were obtained for each sample so as to distinguish the best option for extracting precipitation-only damage in each foil.

There are three data reduction options to obtain such precipitation-only damage:

1. Subtraction of the scattering intensity from the unirradiated area of the foil from the overall irradiated area scattering profile.
2. Fitting and subsequent subtraction of the Porod scattering contribution from the overall scattering profile, removing grain boundary contributions.
3. Subtraction of the scattering intensity from the foil that lay beyond the Bragg damage peak that

is essentially unirradiated (foil 9) from the overall irradiated area scattering profile.

The Porod scattering of the irradiated area is equivalent to the Porod scattering of the unirradiated area in each foil sample. This is as expected since the Porod contribution in such metallurgical samples arises from grain boundary scattering. As a result, options 1 and 2 above are analogous.

Figure 6.17 shows the Porod scattering contribution in foil 7 with the highest induced damage.

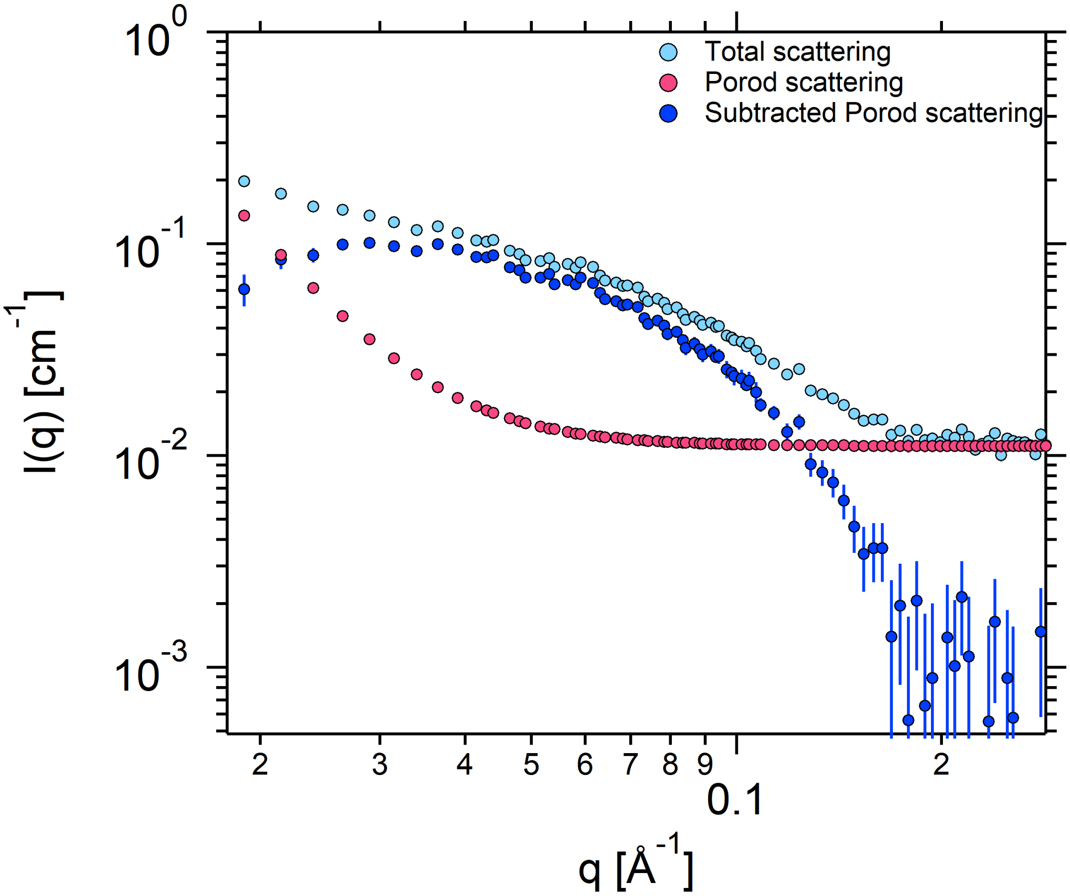

Figure 6.17: I(q) total, Porod and Porod subtracted scattering of tungsten foil 7.

A comparison between the Porod scattering subtraction and the unirradiated foil subtraction is shown for all samples in Figure 6.18.

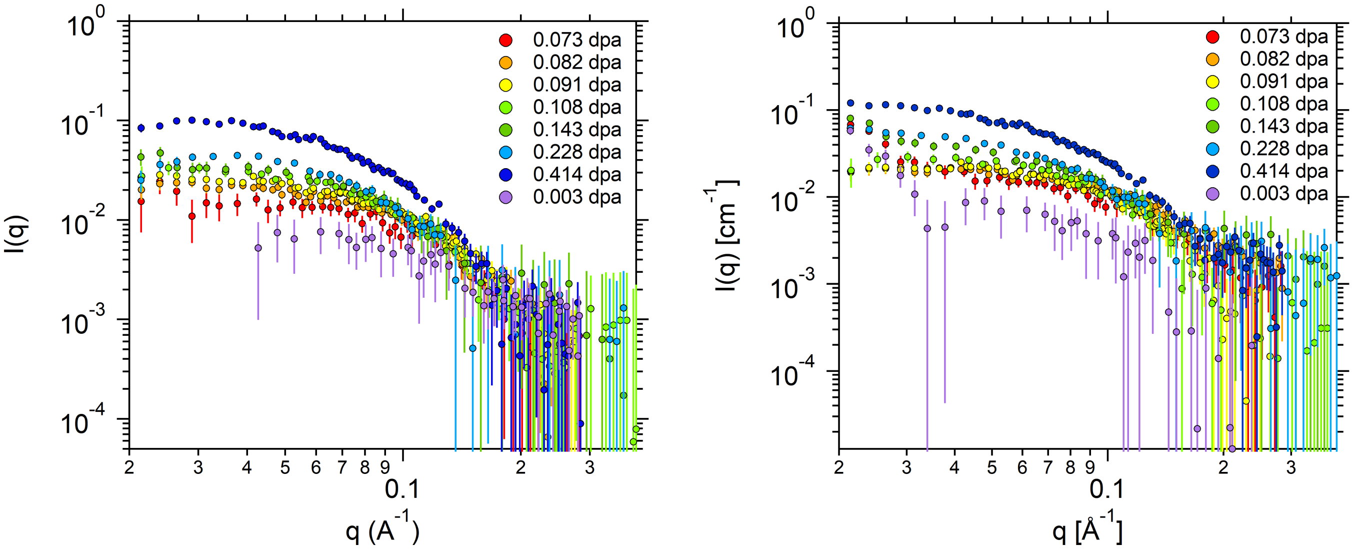

(a) Scattering profiles of foils 1 to 8 with individual Porod subtraction

(b) Scattering profiles of foils 1 to 8 with foil 9 Porod subtraction

Figure 6.18: Comparison of subtraction methods to obtain precipitate-only scattering.

Whilst the two subtraction methods provide relatively similar results, it has been concluded that the Porod scattering contribution should be subtracted from the overall scattering intensity for each foil to obtain the precipitate-only scattering. This is preferred since it accounts for a direct deconvolution of the scattering from precipitates and the scattering from grain boundaries within each foil. In addition, the blanket subtraction of foil 9 scattering may mask any subtle variability between samples.

6.3.6 Nanoindentation hardness testing

Nanoindentation hardness testing has been used as a technique to complement SANS to quantify mechanical property changes due to matrix damage and precipitation induced during irradiation. This has been chosen over microindentation hardness testing where the indent depth is on the micron scale due to the nature of the thin tungsten foils used in this work (50 μm). Continuous stiffness measurements have been used to extract the evolution of elastic modulus and hardness as a function of displacement damage in the irradiated tungsten samples. The indenter tip used during the nanoindenter was a Berkovich tip.

Due to the complexity of the indentation technique and small length scales involved, there are several experimental factors that may contribute to uncertainty in the calculated projected contact areas and hence hardness and elastic modulus measurements. Some examples include:

- Calibration of indenter position relative to the sample surface - since the modulus and hardness measurements are directly related depth of the indent, a reference measurement of the vertical position of indenter tip at the surface of the sample must be made using a small initial contact load. This is one correction that must be made during data analysis to ensure that the small indentation left behind after this initial load does not contribute to the depth of the final indentation.
- Calibration of indenter deflection - the deflection of the nanoindentation instrument can be determined through calibration measurements of indents in a known material, such as fused silica [208].
- Geometry of indenter tip - since the nanoindentation measurements are dependent on the area of the indenter, any deviations from the expected tip geometry will affect the calculated hardness and elastic modulus values. To account for this, the indenter tip is calibrated in a material where the elastic modulus is known (e.g. fused silica) and an area function for the contact is obtained that can be used during data analysis.
- Thermal drift - due to the small length scales involved, temperature fluctuations can play a role in depth measurement results by causing differing amounts of thermal expansion in the nanoindenter instrument. Whilst measuring the unloading cycle, the thermal drift of the indenter itself is measured. The unloading curves are then corrected by the indenter drift when analysing the data.
- Pile ups and sink ins - depending on the material properties, two phenomena can often occur that can either respectively overestimate or underestimate the true contact area of the indenter: pile up and sink in. Such effects are shown schematically in Figure 6.19.
- Surface roughness - surface roughness will impact the indenter tip contact area within the sample and can hence affect the measured hardness and elastic modulus. First and foremost, this can be counteracted by ensuring samples are well polished prior to nanoindentation. Often, since nanoindentation is designed for measuring small sample volumes, this is not feasible. In such cases, the effects of surface roughness can be limited by choosing an indentation depth that is significantly higher than the variation in surface height of the sample.

- Indentation size effect - a common material phenomenon that can compromise the validity of hardness measurements is that the hardness can change as a function of indent depth. This indentation size effect can be attributed to the role of dislocations in response to the plastic flow of the material under load, such that at low depths (few hundred nm) the material hardness increases [209, 210, 211]. Hence, it is important to ensure that the hardness values are only obtained at sufficient indent depths where hardness is independent of depth.

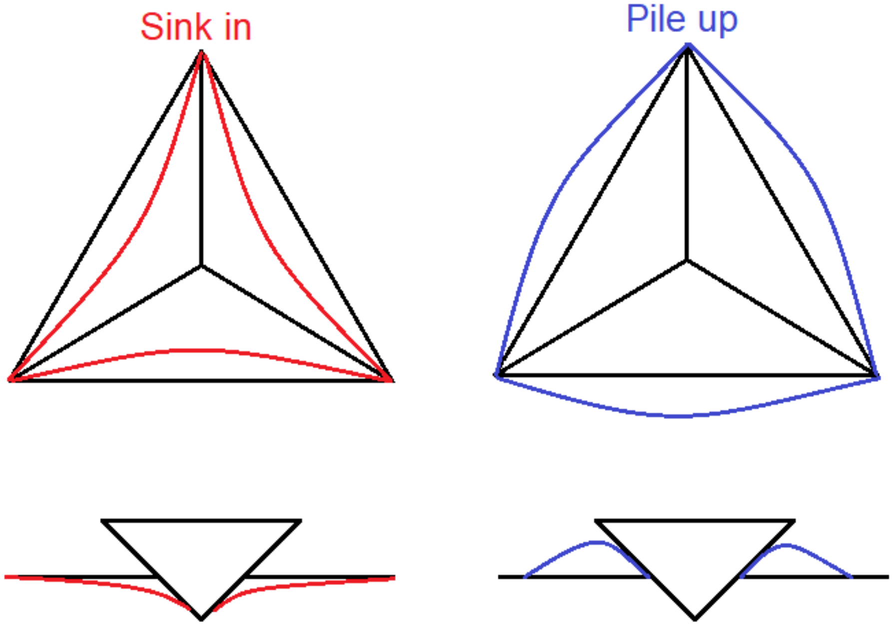

Figure 6.19: Schematic diagram of sink in (red) and pile up (blue) phenomena compared to the expected projected contact area of a Berkovich indenter (black) during nanoindentation.

The thin foil samples were mounted onto an aluminium stub using crystal bond glue. Since the elastic response of the sample is measured during nanoindentation, the thickness of the crystal bond glue should be minimised to avoid measuring the elastic response from the glue and aluminium stub. An initial feasibility test was completed on an unirradiated foil to determine the effects of surface roughness and probing of the underlying sample mount materials.

The appropriate indenter calibrations were completed to be used in the post-experimental analysis of the nanoindentation data. This included calibration of the indenter tip using fused silica to obtain the indenter deflection and tip contact area function, and obtaining the reference displacement where the indenter tip is in contact with each sample.

A schematic diagram of the sample line dissection of indents is shown in Figure 6.20. Sampling in such a way allows for any between sample variability to be captured, since the the unirradiated and irradiated parts of each sample can be studied. A photograph of the nanoindenter head and sample mount stage is shown in Figure 6.21.

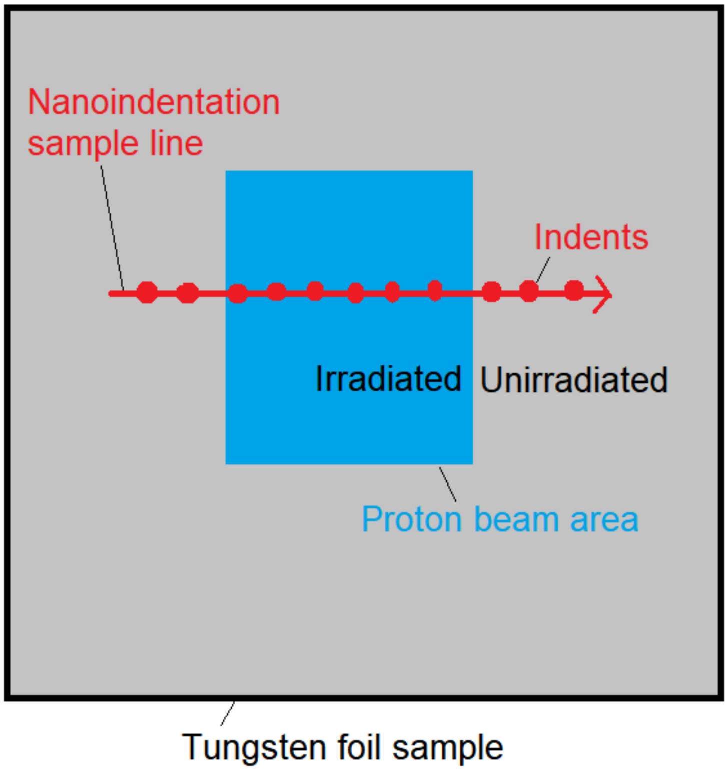

Figure 6.20: Schematic diagram of the measured area of interrest during the nanoindentation of each tungsten sample. The irradiated and unirradiated regions are highlighted, along with an example indentation sampling line.

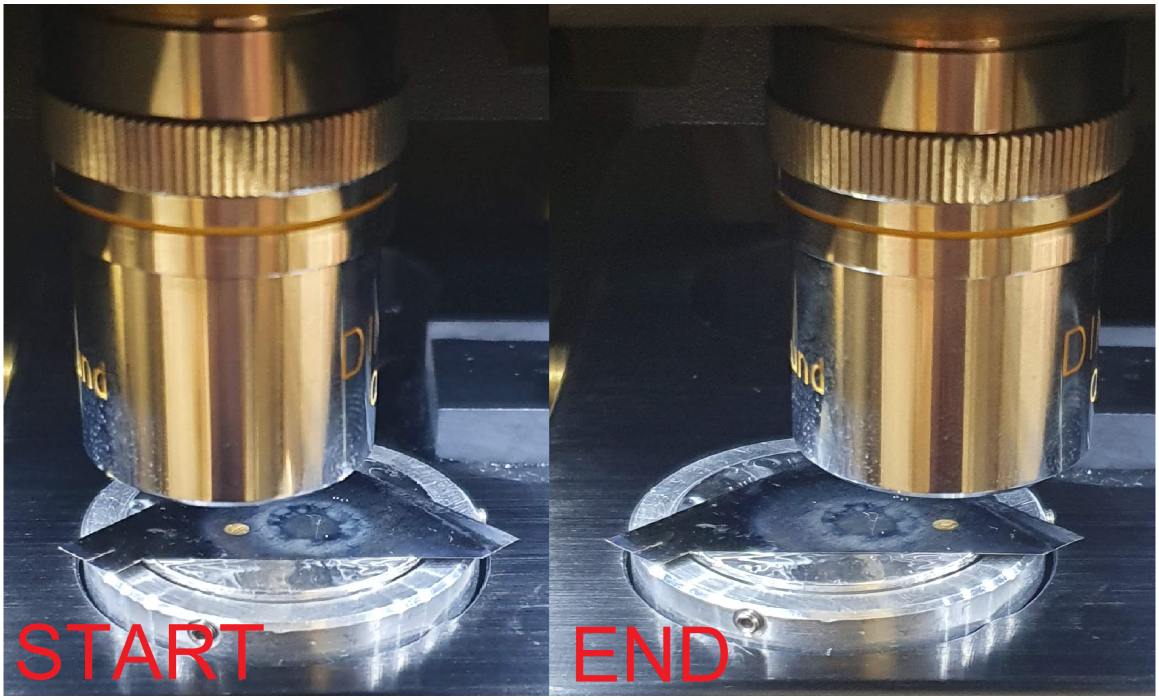

Figure 6.21: Photograph of nanoindenter sample stage showing the start (left) and end (right) of the indentation measurement line in Foil 7. The illuminated area highlights the position of the Berkovich indenter tip.

The sample was mounted to ensure there was enough clearance between the tip and sample to allow for measurements to be taken. A microscope and 2D translatable sample mount table allowed for the sampling line to be selected.

During measurements, the threshold drift rate of the indenter tip was set to 0.05 nm/s, meaning the indentations will only start once the thermal drift rate has dropped below this value. It should be noted that the instrument only waits a certain amount of time for the thermal drift to drop below the threshold value before beginning the measurements anyway. As a result, particular care should be taken during data analysis to check that the thermal drift is below the threshold value.

The indentation depth limit was set to 1 μm due to the thickness of the foils (50 μm). This was chosen to ensure that the deformation upon unloading of the indenter tip is purely elastic, where the equation 3.4 for elastic modulus is valid.

The strain rate used was 0.5 s^{-1}. The surface approach distance was 10 000 nm with an approach velocity of 40 nm/s. The harmonic oscillation frequency of the indenter was set to 45 Hz and the depth harmonic was 2 nm.

The number of indents made across each sampling line was selected as a balance between enough indents to have significant statistics and a large enough distance between each indent to ensure that there are no overlaps of the plastic zones (step size > 50 μm). The sampling details for each tungsten sample are shown in Table 6.8. The parameters vary between foils to ensure that the indentation line fully crosses the tarnished surface. The sample with the highest damage level (foil 7 due to the location of the Bragg peak at 328 μm) has a large number of indents in the irradiated area to increase the statistics. This was achieved by taking multiple passes of the sampling line. It is noted that foil 9 is a sample with no induced displacement damage due to its location in the proton damage profile. Foil 10 was not investigated since it is the same as foil 9 in terms of its exposure, i.e. no displacement damage since all the protons have lost their energy by foil 8.

Table 6.8: Number and incremental distance of nanoindentation measurements taken for each tungsten sample.

Foil	**Number of indents**	**Distance between indents [μm]**	**Sampling line length [mm]**
1	60	150	9.0
2	31	300	9.3
3	60	200	12.0
4	30	350	10.5
5	60	200	12.0
6	60	200	12.0
7	180 (3 passes of 60)	200	12.0
8	60	200	12.0
9	75 (5 passes of 15)	150	7.0

6.4 Results

6.4.1 Activation and transmutations

The transmutation and activation results presented here were used to inform imperative safety and transport considerations for SANS and nanoindentation studies on the irradiated samples. They were also used to calculate whether any Re or Os had been transmuted during irradiation, since this informs the SANS analysis to understand whether Re/Os precipitates could form in the pure tungsten matrix.

From Table 6.6, the transmutation reactions identified to be induced during 15 MeV proton irradiation were those with the highest expected cross sections as follows:

- ^{182}W(p,2n)^{181}Re
- ^{186}W(p,n)^{186}Re
- ^{186}W(p,d)^{185}W
- ^{186}W(p,n+p)^{185}W

The isotopes of interest in irradiated tungsten with their associated activity limits, as set by the IAEA transport of radioactive material regulations, are shown in Table 6.9.

Table 6.9: Activity limits of tantalum, tungsten and rhenium isotopes for the posting of solid radioactive samples, as set by the IAEA.

Isotope	**Activity limit [TBq]**
^{178}Ta	10
^{179}Ta	1000
^{182}Ta	10
^{178}W	5
^{181}W	30
^{185}W	0.8
^{187}W	0.6
^{188}W	0.3
^{184}Re	10
^{186}Re	1000
^{188}Re	100
^{189}Re	100

When the samples had sufficiently cooled post-irradiation, HPGe spectroscopy was performed using the process outlined in Section 6.3.4. A live time of 600 s was used. The resultant spectrum for foil 7 with subtracted background is presented in Figure 6.22.

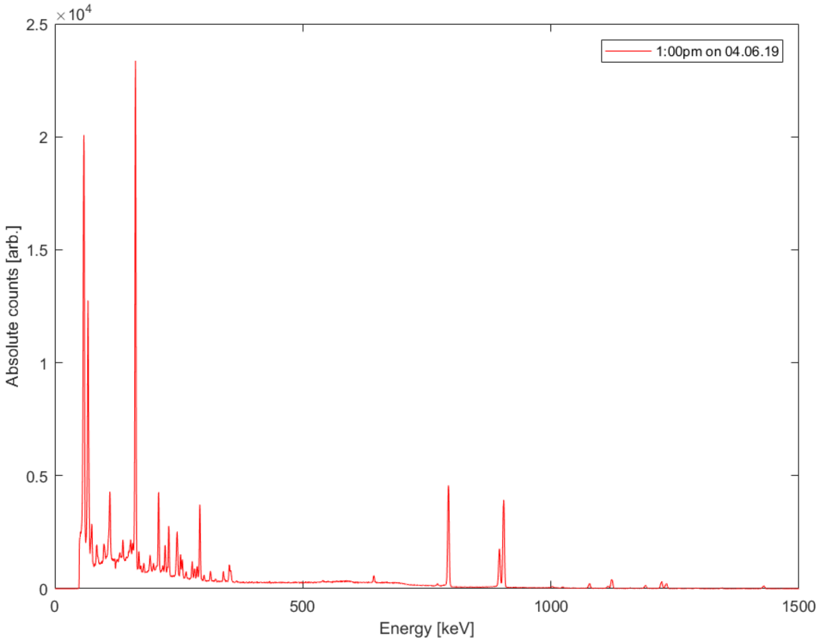

Figure 6.22: HPGE spectrum of counts as a function of energy in irradiated tungsten foil 7 with background subtractions.

Each photopeak from the spectrum was fitted with a Gaussian function written in MATLAB to estimate the centroid and FWHM energies and total area beneath each resolvable peak. An example of the photopeak fitting process is shown in Figure 6.23. These fitted parameters were then used to calculate the detector resolution and efficiency as a function of photopeak energy using equations 6.9 and 6.13, as presented in Figure 6.24 and Figure 6.25 respectively.

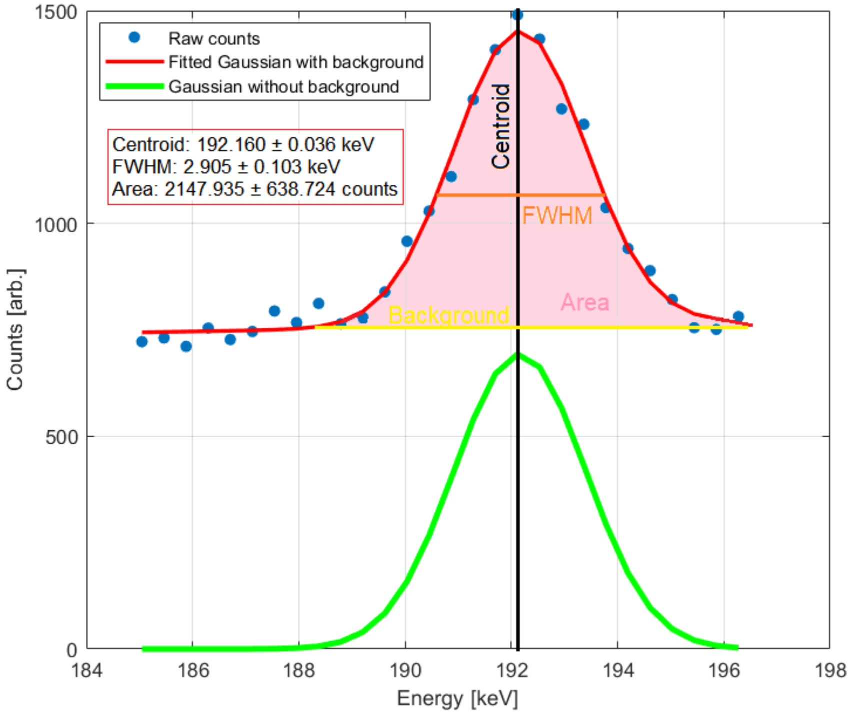

Figure 6.23: Example photopeak from HPGe spectrum of irradaited tungsten foil 7 with fitted Gaussian function (red) and key parameters highlighted as: peak energy (black), FWHM (orange), area (pink) and background (yellow).

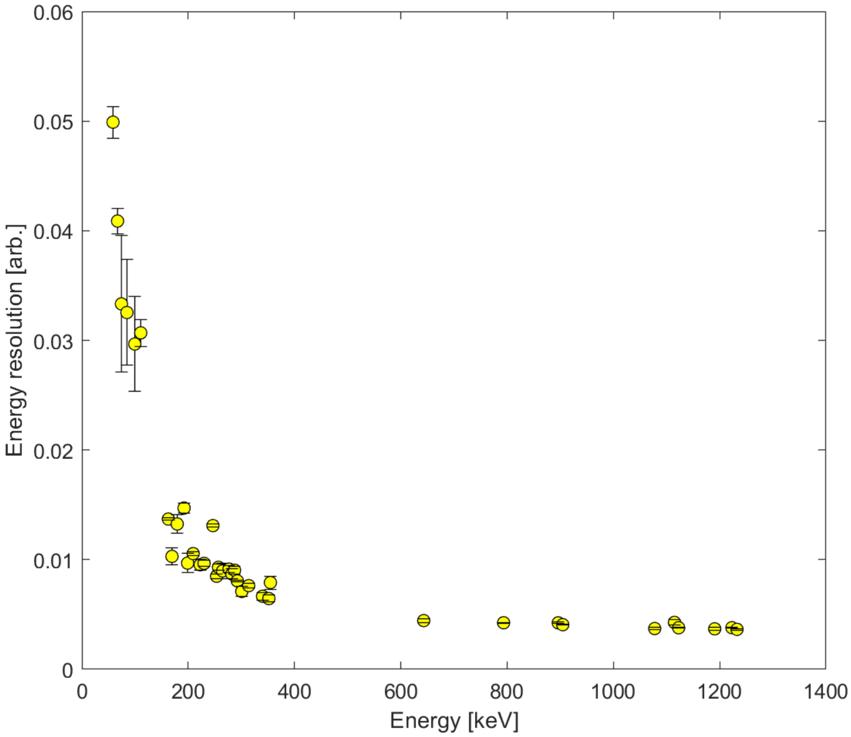

Figure 6.24: Calculated HPGe detector resolution as a function of photopeak energy.

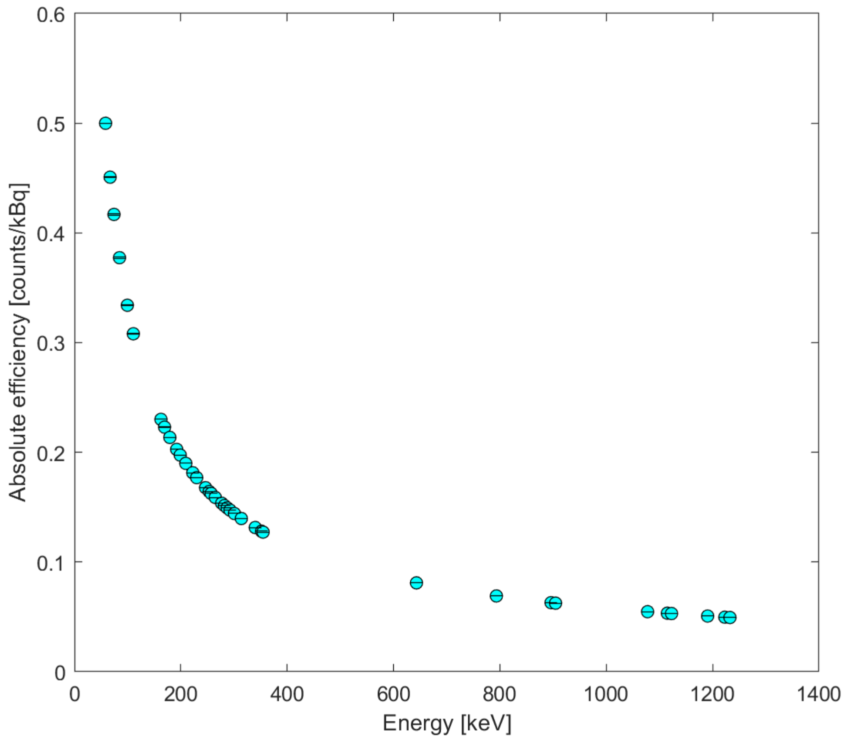

Figure 6.25: Calculated absolute HPGe detector efficiency as a function of photopeak energy.

Using the fitted photopeak parameters from the spectra, the activity contributions of each photopeak were calculated using equation 6.14. The results are shown in Figure 6.26.

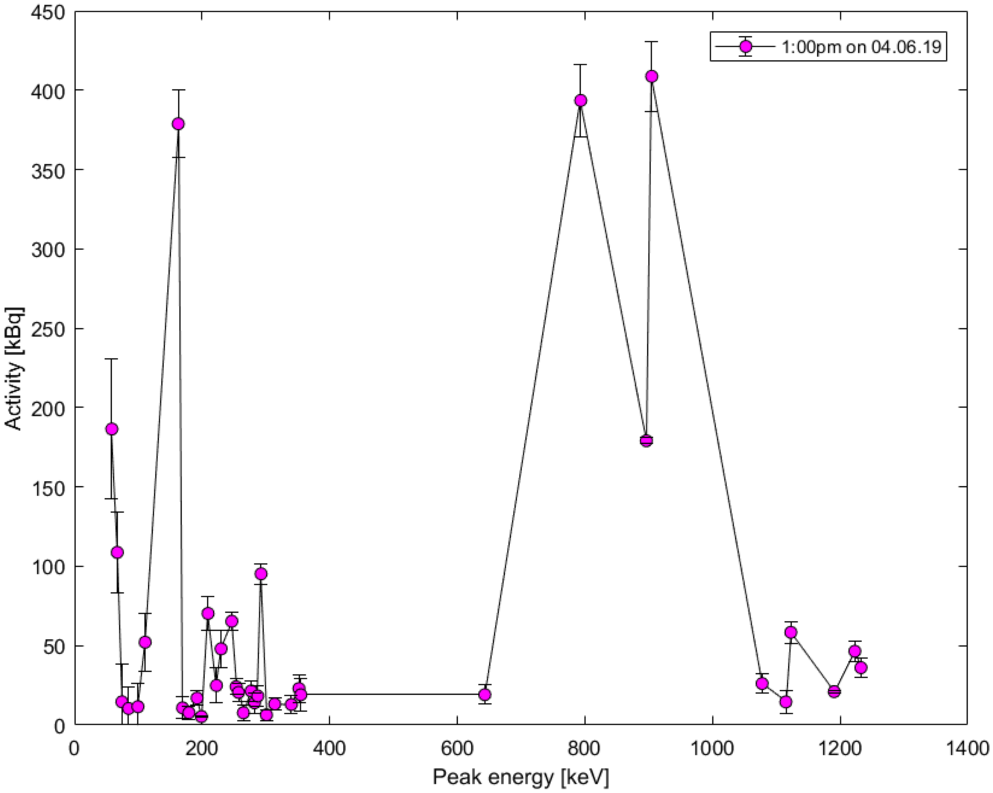

Figure 6.26: Calculated activity as a function of photopeak energy for all irradiated tungsten samples.

Using this spectrum of photopeaks and the common transmutation reactions of tungsten, all of the possible transmuted isotopes present in the irradiated samples were obtained. Through a process of elimination, the most likely contributors to each photopeak were computed. There are several photopeak energies that could be attributed to multiple transmuted isotopes and conversely, some isotopes have an exclusive photopeak that is not present in the decay profiles of other isotopes. The resultant isotopes found to be present in the irradiated tungsten samples are shown in Table 6.10. The low energy photopeaks (below 100 keV) can be attributed to lead isotopes present from the HPGe shielding setup, for example ^{189}Pb(IT).

Table 6.10: Isotopes detected in irradiation tungsten samples using HPGe spectroscopy.

Isotope	**Decay mode**	**Half life [time unit]**
^{189}Re	β^-	24.3 hr
^{184}Re	EC	35.4 d
^{183}Re	EC	70.0 d
^{182}Re	β^+	14.4 hr
^{181}Re	EC	19.9 hr
^{182}Ta	β^-	114.7 d
^{183}Ta	β^-	5.1 d

Despite the high initial activity from rhenium isotopes, the majority of the detected photopeaks can be attributed to threshold proton reactions that result in the stable isotope at the end of the decay chain to be tungsten, such as ^{182}W(p,2n)^{181}Re. This reaction has the highest proton induced cross section. The only reaction identified with sufficient likelihood with 15 MeV protons that can transmute stable rhenium is ^{185}W β^- decay to ^{185}Re with a half-life of 75.1 days. The unique characteristic photopeak of this decay compared to the other possible decay pathways has an energy of 125.4 keV. Despite the errors on fitted values and the known energy resolution of HPGe detector, no photopeaks of this energy were detected, suggesting that the total proton charge accumulated during irradiation was not high enough to induce significant transmutation of tungsten to rhenium. This can be tested explicitly using SANS through the relationship between scattering intensity and elemental contrast.

The total activity and dose rates from all of the foils as a function of time post-irradiation were calculated using equation 6.15. The corresponding results are presented in Figure 6.27 and Figure 6.28 respectively.

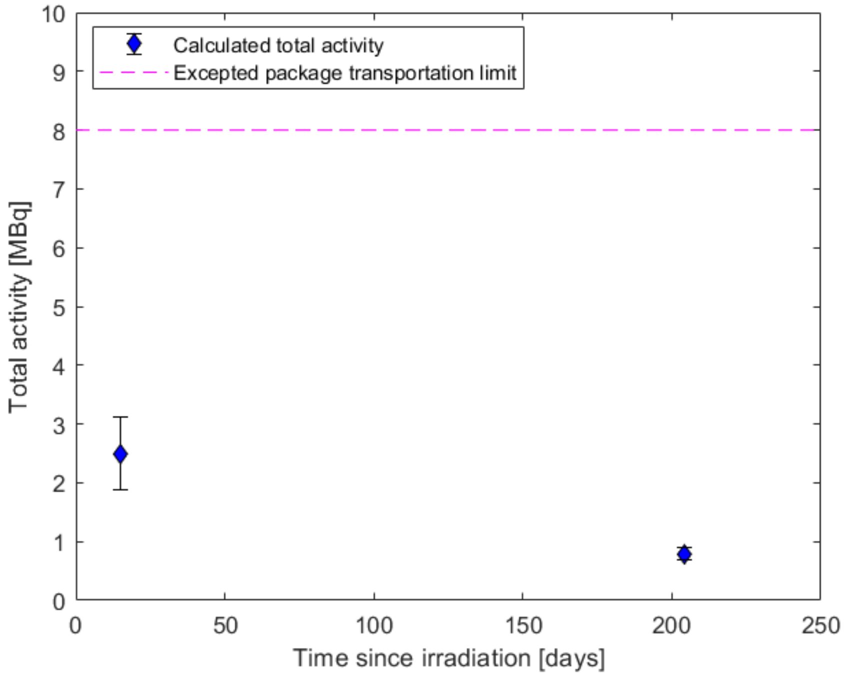

Figure 6.27: Calculated total activity as a function of time post-irradiation for all irradiated tungsten samples (blue) relative to the IAEA excepted package transportation activity limit for tungsten, tantalum and rhenium isotopes (pink).

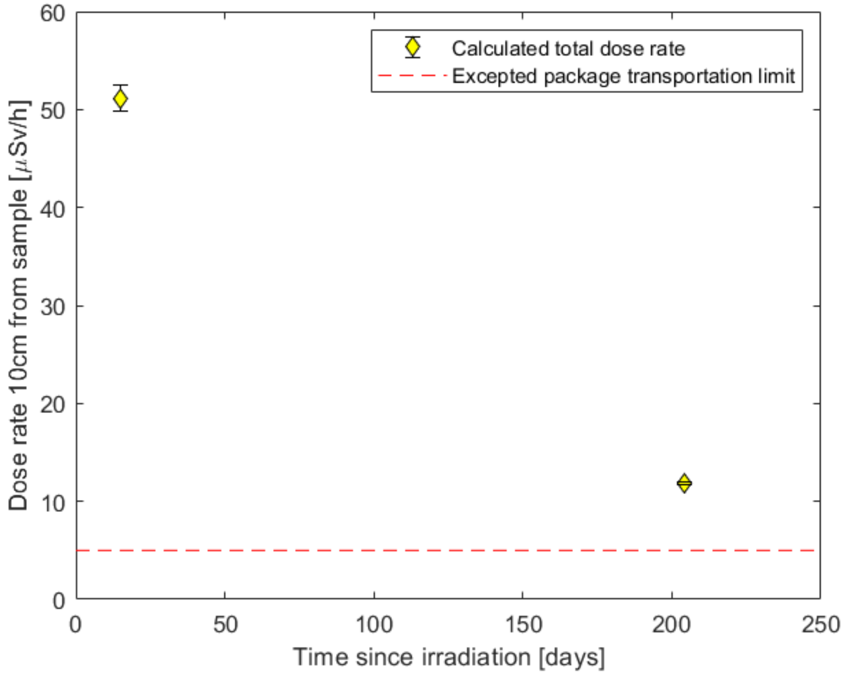

Figure 6.28: Calculated total dose rate as a function of time post-irradiation for all irradiated tungsten samples (yellow) relative to the IAEA excepted package transportation dose rate limit (red).

The total induced activity is below the transportation limit for the transmuted tungsten, tantalum and rhenium isotopes of interest outlined in Table 6.9. This allowed for the irradiated tungsten samples to be sent as an excepted package to the ILL for SANS analysis as soon as the dose rate on the surface of the package had reduced below the 5 μSv/hr limit. This was achieved by packing the samples into a heavily shielded container made of tungsten. This container was then packed into a large cardboard box filled with dense packing material. The dose rates on the surface of the package were measured to ensure compliance with the regulations and the appropriate labelling was included. The consignment package was sent to the ILL for SANS using a dedicated radioactive transport courier company.

6.4.2 Induced damage

The SRIM simulation results of 15 MeV protons in pure tungsten are presented here. The recoil atom paths are shown in Figure 6.29.

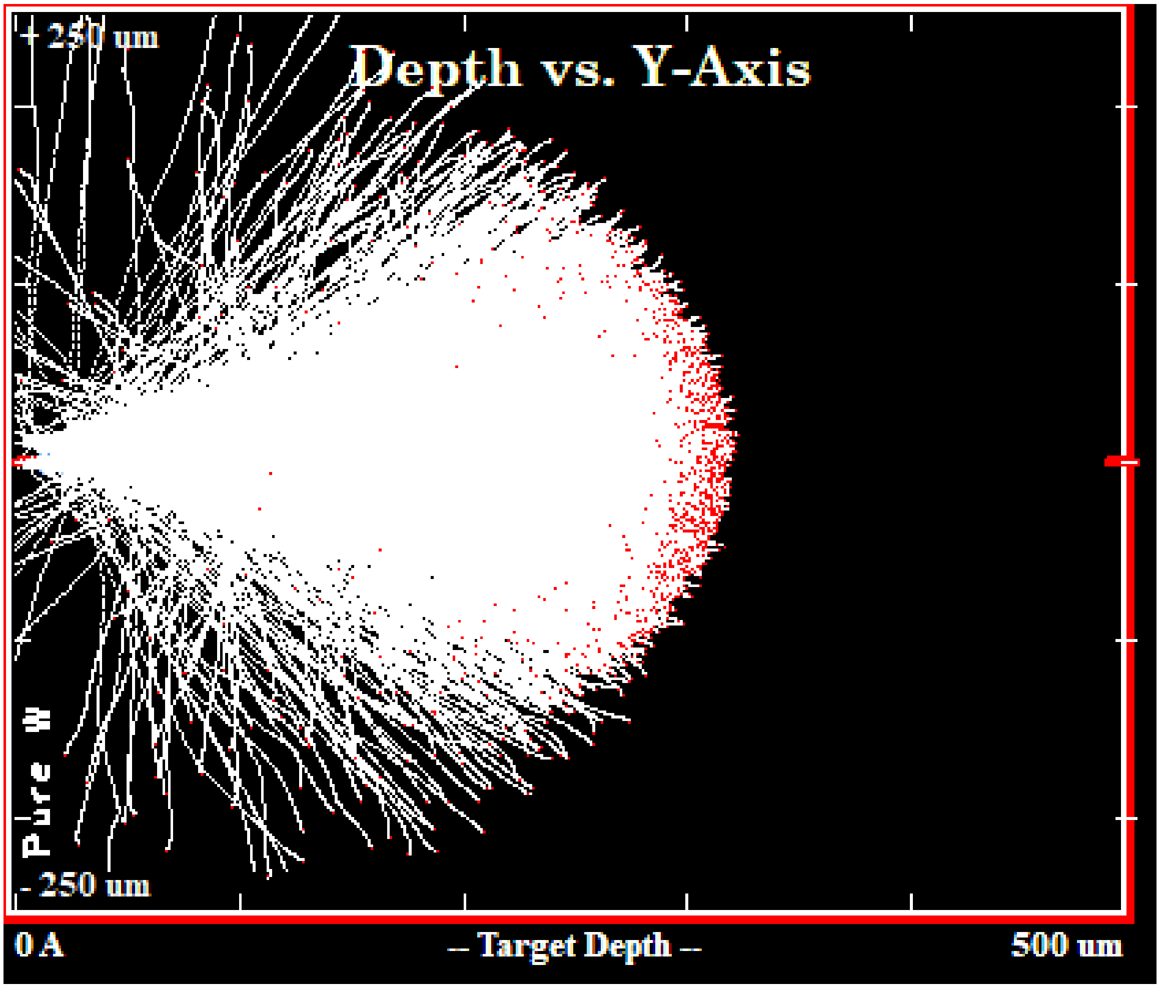

Figure 6.29: Simulated damage cascade in pure tungsten irradiated with 15 MeV protons showing the PKA trajectories.

The method of calculating induced displacement damage from Section 6.3.3 has been used. The SRIM outputs of vacancy data from simulations with 1 x 10^6 15 MeV protons have been used to obtain dpa as a function of depth into pure tungsten. The resultant damage profile with each foil depth is shown in Figure 6.30. These results were then averaged over the foil depths to obtain the peak and mean induced dpa in each sample during proton irradiation.

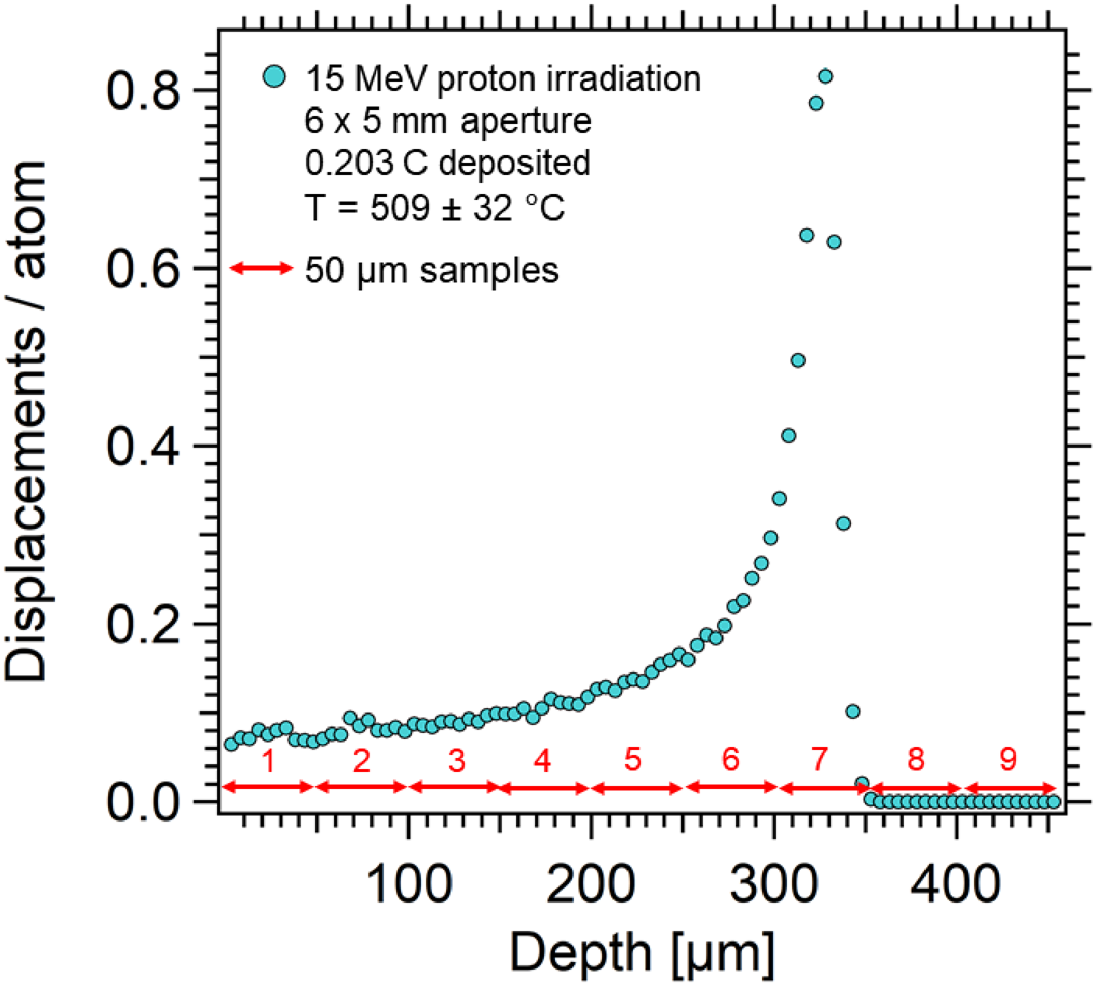

Figure 6.30: 15 MeV proton irradiation induced displacement damage as a function of depth in tungsten, with each foil sample overlaid. Key irradiation parameters are noted.

Table 6.11 shows the peak and mean displacement damage induced by proton irradiation of the tungsten samples. The average damage is used as a parameter for the remainder of this chapter since it is the most representative metric of the damage induced in each foil.

Table 6.11: Calculated peak and average displacement damage induced in each tungsten foil sample during irradiation.

Foil	Peak induced damage [dpa]	Average induced damage [dpa]
1	0.083	0.073
2	0.094	0.082
3	0.100	0.091
4	0.118	0.108
5	0.166	0.143
6	0.296	0.228
7	0.815	0.414
8	0.003	0.003
9	0	0
10	0	0

6.4.3 SANS

6.4.3.1 Empirical model fitting

The experimental methodology discussed in Section 6.3.5.1 highlights the challenges with obtaining reliable results on irradiated foil samples. Particular care was taken to ensure that the neutron beam was smaller than the irradiated area so that only irradiation damaged aspects of the samples were probed, and to avoid surface oxidation areas to prevent contamination in scattering profiles. Additional measurements of the unirradiated region were obtained for each sample so as to distinguish the best option for extracting precipitation-only damage in each foil.

The resultant precipitate-only scattering intensity distributions for each foil after the appropriate data reduction methods (calibration, transmission correction, background subtraction, and Porod subtraction) are shown in Figure 6.31.

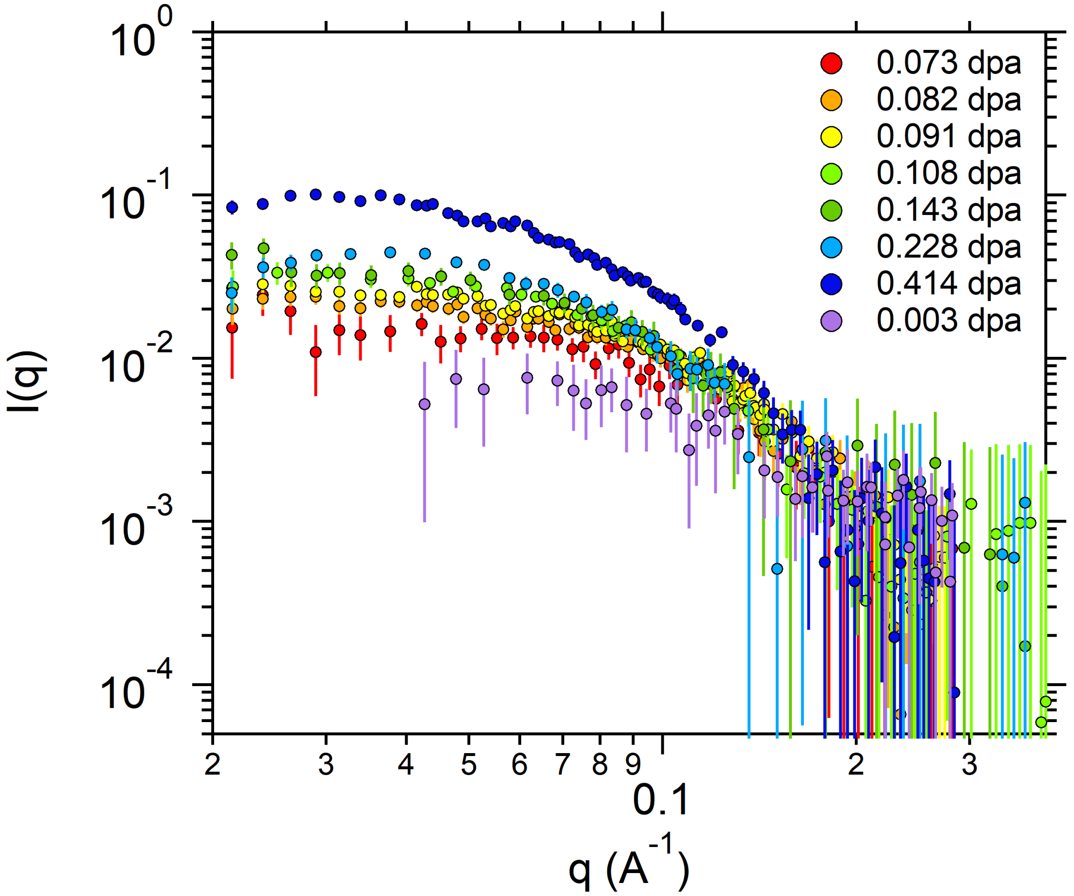

Figure 6.31: I(q) precipitate-only scattering from each W foil over the Bragg peak damage range.

The fitting process utilised is analogous to that discussed in Section 4.4.2.2 and in analyses of other nuclear material systems.

The tungsten system is relatively straight forward compared to the RPV alloy steels studied using SANS in Chapters 4 and 5 since it has a single phase matrix with other elements only present as impurities. The initial unirradiated material composition is presented in Table 6.1, however the impurity levels are so low that their contribution to the overall neutron scattering intensity is likely to be negligible in comparison to the background scattering. As a result, it has been assumed that the unirradiated sample matrix is pure tungsten.

Section 6.4.1 presents the transmutation calculation results. It has been assumed that due to the damage levels induced during irradiation (peak of 0.820 dpa) that the level of rhenium and osmium transmutation is not high enough to produce significant quantities of either in the matrix to precipitate out. This is supported by TEM studies that only observe rhenium precipitation in irradiated pure tungsten with 4 at% Re transmuted in the matrix [27, 36, 37, 189], or at induced damage levels greater than 5 dpa [35].

This hypothesis has been tested by assuming the presence of rhenium precipitates within the tungsten matrix during the fitting process, with ρ_p calculated as 6.2541 x 10^{-6} Å^{-2} and ρ_m = 3.0805 x 10^{-6} Å^{-2}. It was found that the contrast from such rhenium precipitates does not fit the data well and supports the assumption that there is not enough transmuted rhenium to form precipitates at the damage levels induced in this study. As a result, the irradiated sample matrix should be modelled as pure tungsten.

Previous irradiation damage studies in tungsten only observe self or solute interstitial precipitation events at damage levels greater than 1 dpa. All matrix damage at levels below this has been shown to be as vacancy clustering (analogous to interstitial clustering to form precipitates) which produces nanometre scale voids.

Overall, the best estimate scenario for the irradiated samples is to model the matrix composition of pure tungsten and the detected scattering objects as voids. In this case, the absolute volume fraction of the induced voids can be extracted since the scattering contrast is known.

Recapping equation 2.21 from Chapter 2, the nuclear scattering length density for a system can be calculated using the elemental number densities and bound coherent scattering lengths. The scattering length densities of the components of interest are presented in Table 6.12. These scattering lengths will be held constant during the model fitting process since they are known parameters.

Table 6.12: Nuclear scattering lengths [79] and calculated scattering length densities for the modelled elements of interest.

Element	**Scattering length [fm]**	**Scattering length density [10^{-6} Å^{-2}]**
Tungsten	4.860	3.073
Vacancy	0	0

The incoherent macroscopic scattering cross section of the scattering system scan be calculated to check that the data has been correctly reduced and is as expected using equation 2.44 derived in Section 2.6.2.

For pure tungsten with σ_{incoh} = 1.63 barns and $\mathrm{V_m}$ = 1.58 x 10^{-23} cm^3/mol, the measured incoherent differential cross section is equal to 0.008204 cm^{-1}. This is in agreement with the total background scattering intensity in Figure 6.32 (no separation of void and grain boundary scattering). It is also clear from Figure 6.32 that the incoherent scattering background is consistent across all samples, which supports the conclusion that no rhenium is present in the matrix.

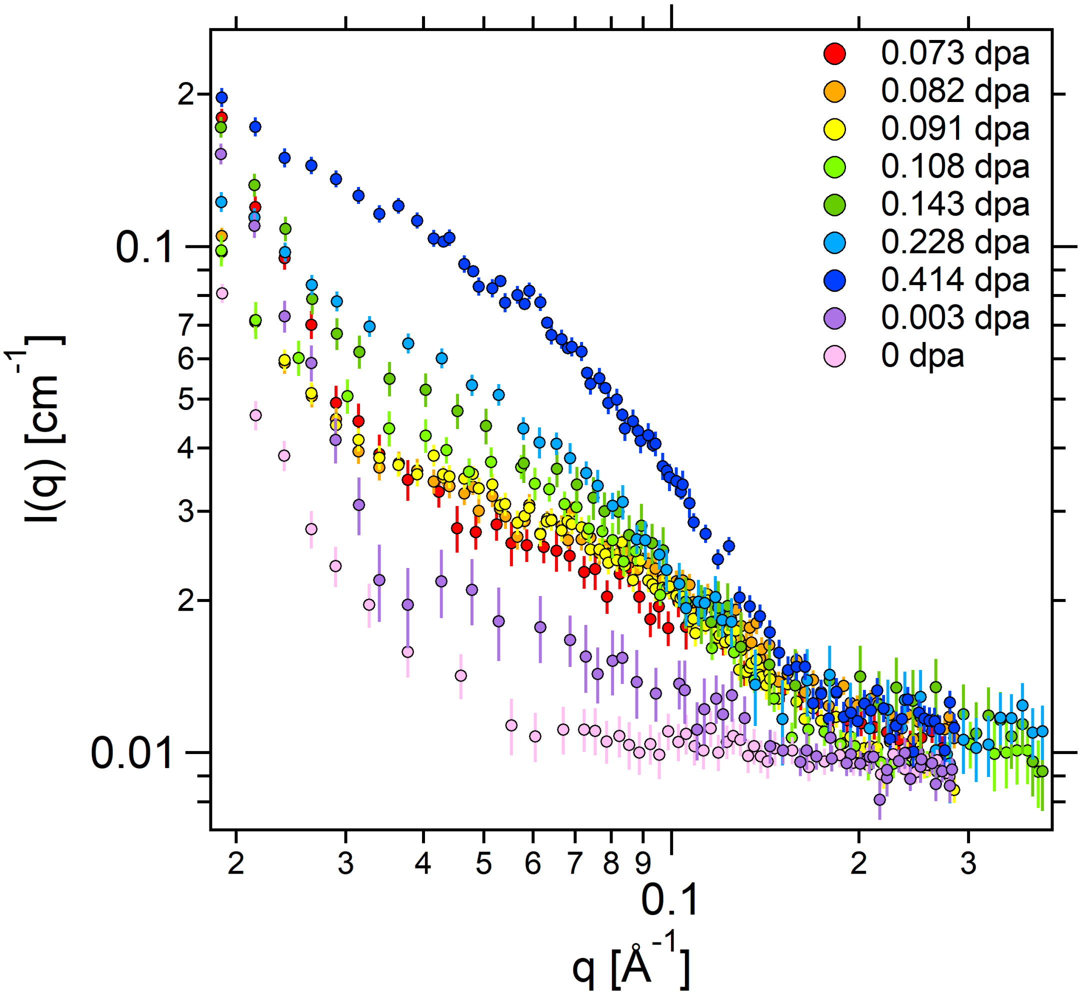

Figure 6.32: I(q) total scattering from each W foil over the Bragg peak damage range.

It is clear from Figure 6.30 that the sample with a depth beyond the Bragg peak received no irradiation damage, as expected. This is reflected by the purely Porod-like scattered intensity, which arises from grain boundaries within the sample, and the fact that there is no visible contrast from any scattering objects. The fitted parameters of the Porod scattering to the sample with no induced irradiation damage is shown in Table 6.13. Going forward, the void-only scattering will be modelled for the 8 samples over the damage range 0.003 to 0.414 dpa.

Table 6.13: Table of fitted power law model parameters for the tungsten foil with no induced irradiation damage (0 dpa).

Model parameter [unit]	**Value (uncertainty)**
Coefficient [arb.]	3.16 (0.25) x 10^{-8}
Power [arb.]	3.77 (0.31)
Background [cm^{-1}]	0.009 (0.001)

A variety of scattering object form factors were used to obtain the best structural representation of the voids in each sample:

- Log-normal distribution of spheres, as observed in TEM literature at the damage levels achieved [27]
- Normally distributed monodisperse spheres
- Monodisperse ellipsoids
- Polydisperse ellipsoids
- Cylinders

Each model was fitted to foil 7 with the highest peak in scattering intensity for the comparative form factor modelling.

The log-normal sphere model shows best form factor fit for all tungsten foils to the void-only scattering profiles, as shown in Figure 6.33.

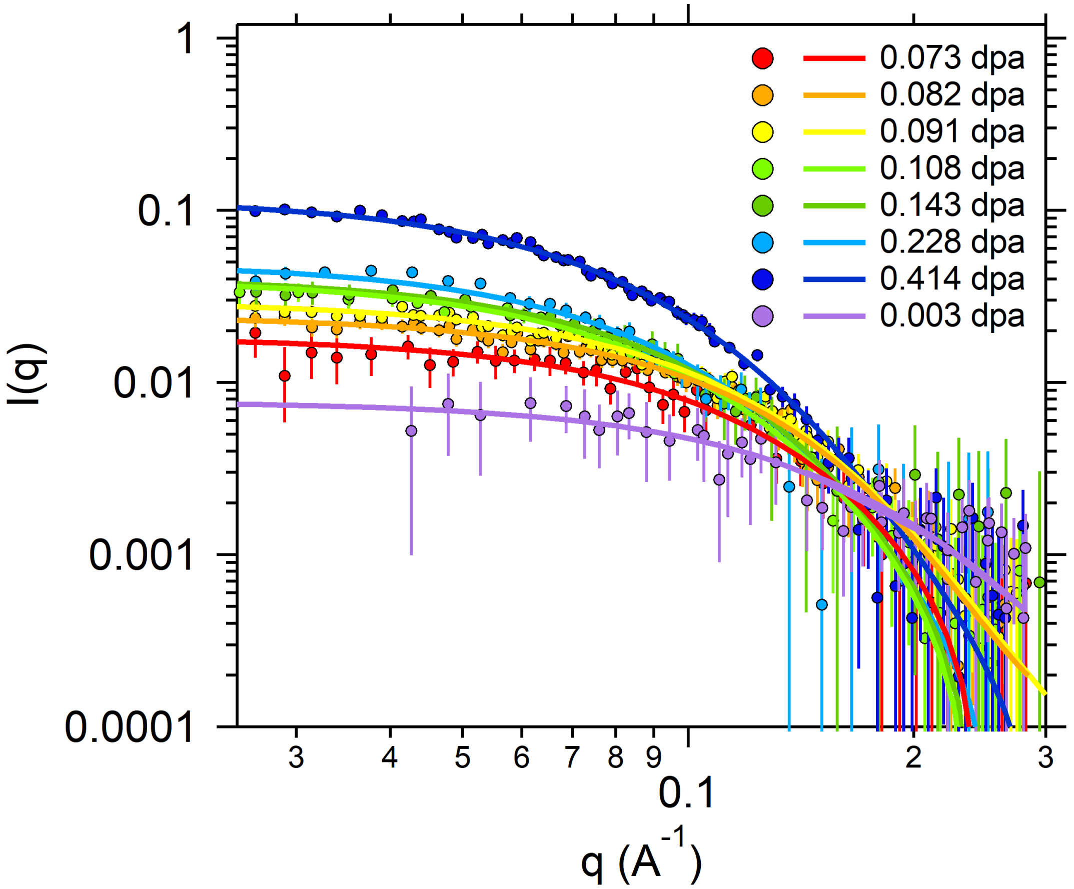

Figure 6.33: I(q) void-only scattering (circles) fitted with log-normal sphere form factors (solid lines) for each tungsten foil over the Bragg peak damage range.

Recapping from Section 4.4.2.2, the mean radius of spherical scatterers with a log-normal distribution can be calculated from the medius radius and polydispersity of the distribution (equation 3.21).

The overall fitted log-normal sphere void parameters for each foil are presented in Table 6.14.

Table 6.14: Table of fitted log-normal sphere parameters for each tungsten foil with associated errors in brackets. The fits were completed by holding the calculated contrast values $\rho_{\text{void}} = 0$ Å^{-2} and $\rho_{\text{matrix}} = 3.0725$ x 10^{-6} Å^{-2} constant.

Sample	Volume fraction [arb.]	Median radius [Å]	Polydispersity [arb.]	χ^2
Foil 1	0.0010 (0.0002)	10.999 (0.679)	0.306 (0.498)	0.57
Foil 2	0.0011 (0.0002)	13.392 (2.278)	0.252 (0.059)	0.74
Foil 3	0.0012 (0.0002)	12.611 (1.953)	0.289 (0.047)	0.73
Foil 4	0.0011 (0.0001)	13.191 (0.438)	0.324 (0.462)	0.57
Foil 5	0.0011 (0.0004)	14.322 (2.494)	0.298 (0.137)	0.49
Foil 6	0.0013 (0.0001)	14.824 (0.469)	0.343 (0.117)	1.40
Foil 7	0.0019 (0.0001)	17.563 (1.016)	0.275 (0.020)	1.05
Foil 8	0.0011 (0.0021)	7.038 (2.730)	0.348 (0.465)	1.38

The mean void radius and its associated uncertainty for each sample can be calculated from the fitted model parameters using the log-normal sphere form factor equation. Recapping from equation 3.21, the mean void radius is a function of the median radius and the polydispersity as

$$R_{mean} = \exp\left(\mu + \frac{\sigma^2}{2}\right) \tag{6.16}$$

where $\mu = \ln(\mathrm{R_{med}})$.

The uncertainty on the mean void radius can be calculated by propagating the uncertainty associated by the fitted $\mathrm{R_{median}}$, $\exp(\mu)$, and polydispersity, σ, values using the general uncertainty propagation equation. This gives the uncertainty as

$$\sigma(R_{mean})^2 = \left(R_{mean}\,\frac{\ln(R_{median})}{R_{median}}\,\sigma(R_{median})\right)^2 + \left(R_{mean}\,\frac{s^2}{2}\,\sigma(s)\right)^2 \tag{6.17}$$

noting that the uncertainty of a parameter is denoted by σ(parameter).

Table 6.15: Table of calculated mean void radii and uncertainties for each tungsten foil.

Mean foil damage [dpa]	Mean void radius [Å]	Uncertainty [Å]
0	0	0
0.003	7.479	3.144
0.073	11.525	1.899
0.082	13.824	2.360
0.091	13.148	2.045
0.108	13.884	2.269
0.143	14.971	2.678
0.228	15.723	0.805
0.414	18.241	1.060

As displacement damage increases, the size of voids induced in the tungsten samples increases, as shown in Figure 6.34. The average damage per foil has been used in this comparison instead of the peak damage due to the bulk probing properties of neutrons.

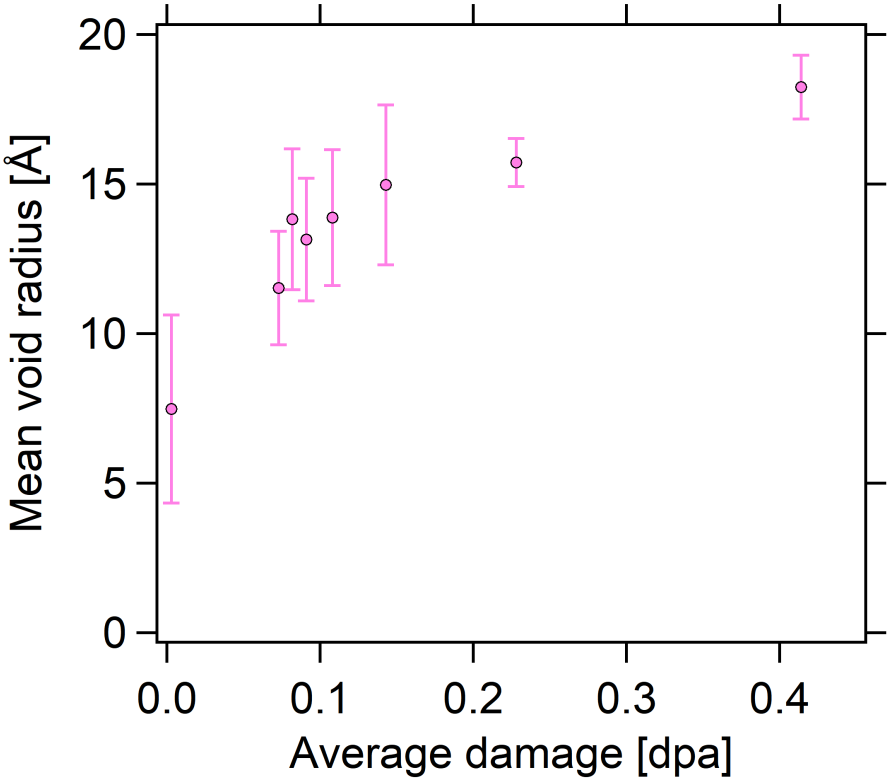

Figure 6.34: Mean radius of voids as a function of induced damage in irradiated tungsten.

The volume fraction of the voids as a function of damage is shown in Figure 6.35.

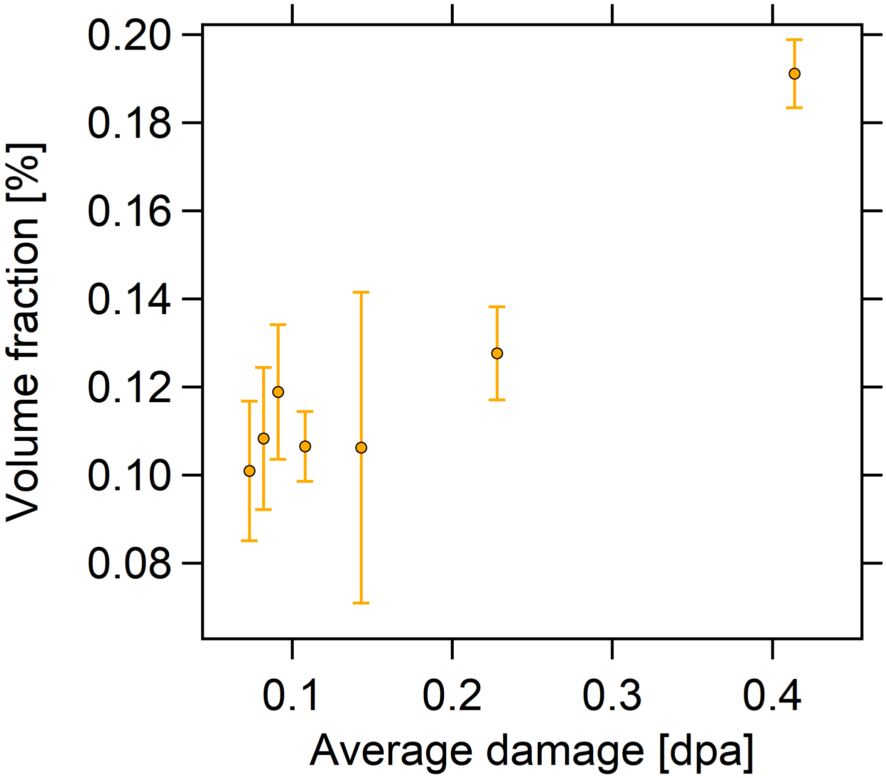

Figure 6.35: Volume fraction of voids as a function of induced damage in irradiated tungsten.

6.4.4 Nanoindentation

The necessary corrections discussed in Section 6.3.6 were applied to the data, including the geometry correction factor, initial contact indent depth, thermal drift of indenter, area function of indenter tip, and indenter deflection. Then, equations 3.6 to 3.8 were used to calculate the elastic modulus and hardness values for each sample.

From analysing the experimental data, measurements from foils 2, 3, 4, 6 and 8 were deemed to have large uncertainties, despite corrections, due to surface roughness effects and thermal drifts higher than the threshold values. As a result, they have not been included in the final nanoindentation results. Despite this, useful indentation data from the remaining foils (1, 5, 7 and 9) is still sufficient to cover the areas of interest across the Bragg peak damage profile - two samples from plateau region, one from the peak and one with no induced damage. Load-depth curves for foils 5 and 7 are presented in Figure 6.36.

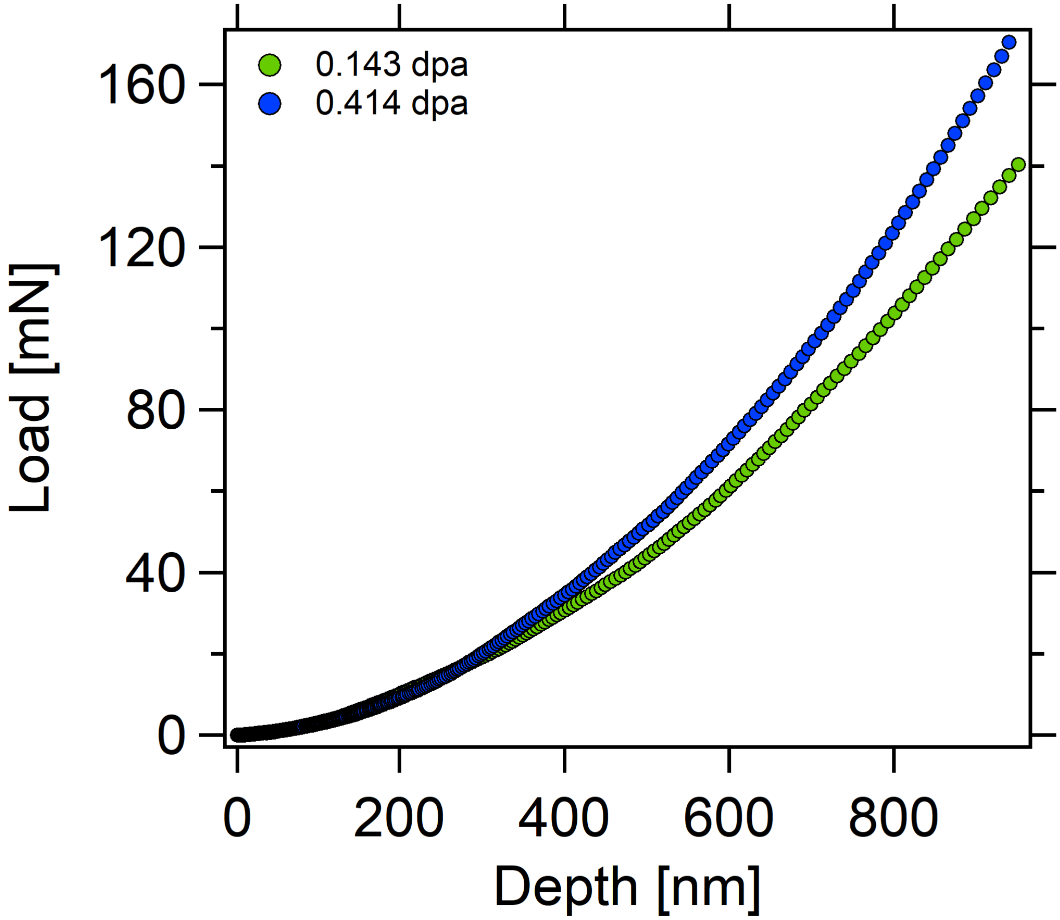

Figure 6.36: Comparison of applied load as a function of indent depth in the irradiated regions of foil 5 and foil 7.

The hardness and elastic modulus for each foil was calculated from the load-depth indentation profiles between depths of 700 nm to 900 nm. Choosing these depths ensured that purely elastic behaviour was probed during unloading to be able to reliably extract the elastic moduli. It also ensured that the indentation size effect would not contribute uncertainty to the calculated hardness values, since at these length scales the hardness was found to be independent of indent depth, as shown in Figure 6.37.

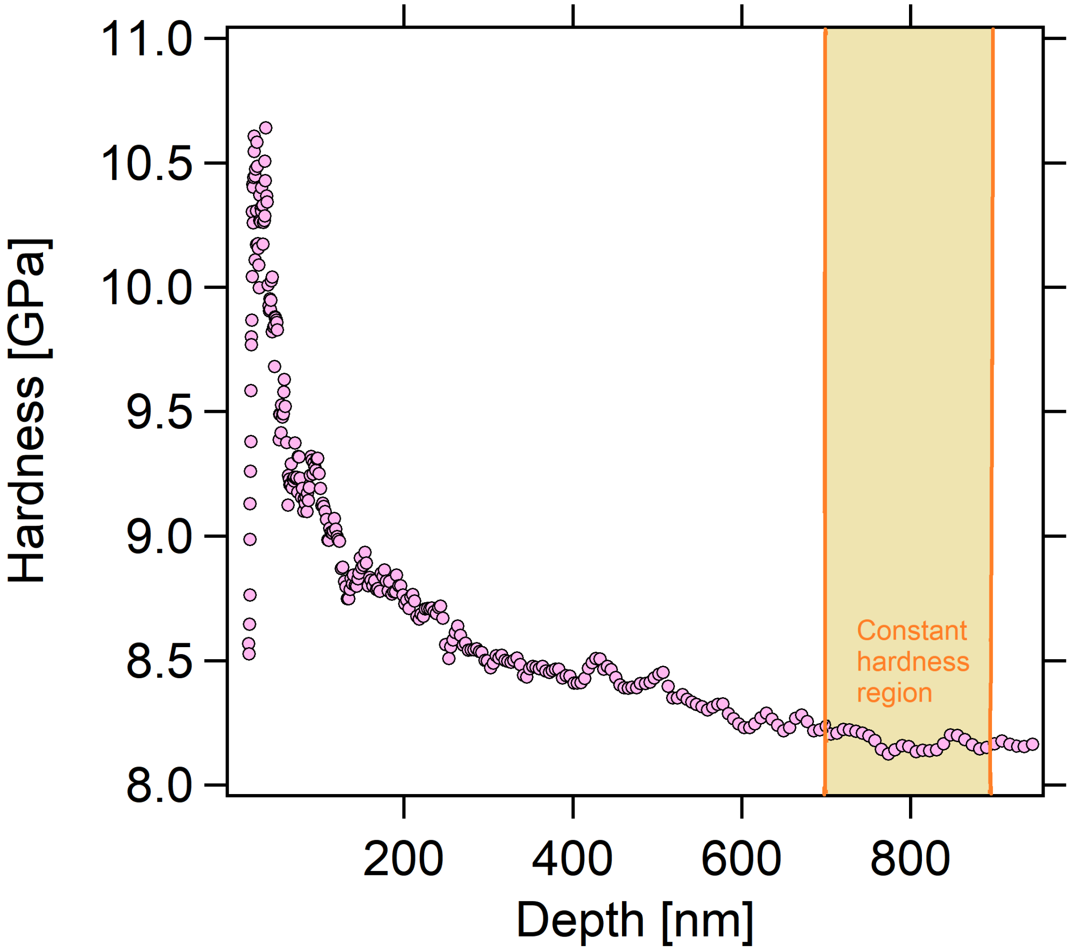

Figure 6.37: Calculated hardness as a function of indent depth in unirradiated tungsten. The indentation size effect can be seen at low tip depths, where hardness is not independent of indent depth.

Despite the initial feasibility test, it was found that the thickness of the crystal bond glue varied between samples due to the thin nature of the foils. In addition, it was found that in some samples the modulus of the underlying glue and aluminium stub were being probed in addition to the sample modulus.

To avoid overestimation of hardness values between samples due to such uncertainties, the data analysis must be qualitative only. This approach considers the change in hardness due to irradiation induced damage in each sample by comparing hardness values in the unirradiated and irradiated regions of each individual foil, rather than a comparison between the absolute hardness values in each foil. Hence, the hardness as a function of sampling line distance across each sample has been presented for such a qualitative comparison. Interestingly, this highlights the useful nature of the sampling line approach to obtaining the indentation data. It also removes potential within-sample variabilities due to irradiation temperature differences. The resultant hardness as a function of distance across the sample for the foils of interest are presented in Figure 6.38. It is noted that the absolute values presented should not be considered due to the aforementioned uncertainties.

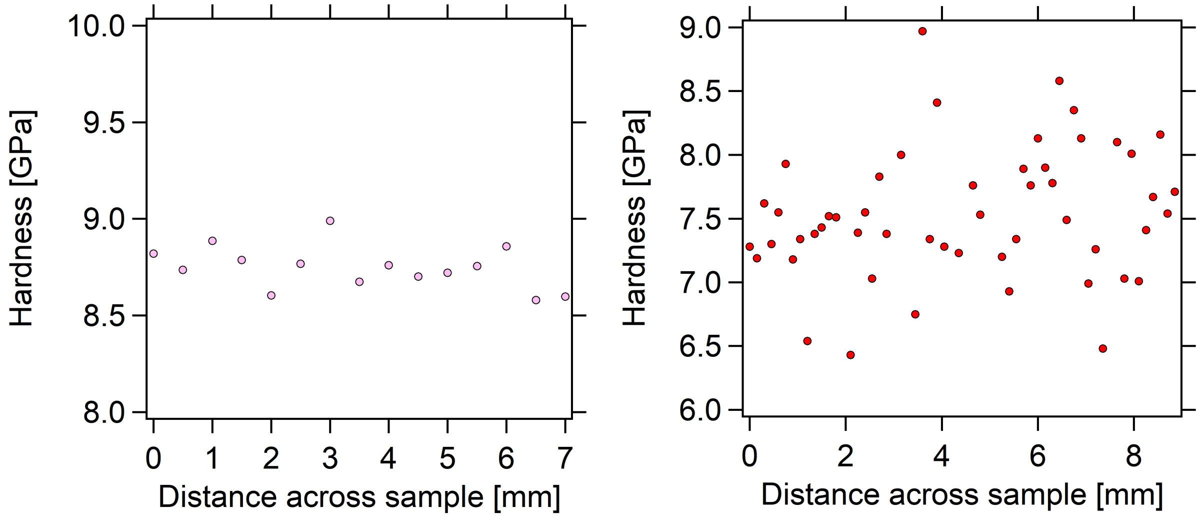

(a) Unirradiated (b) 0.073 dpa

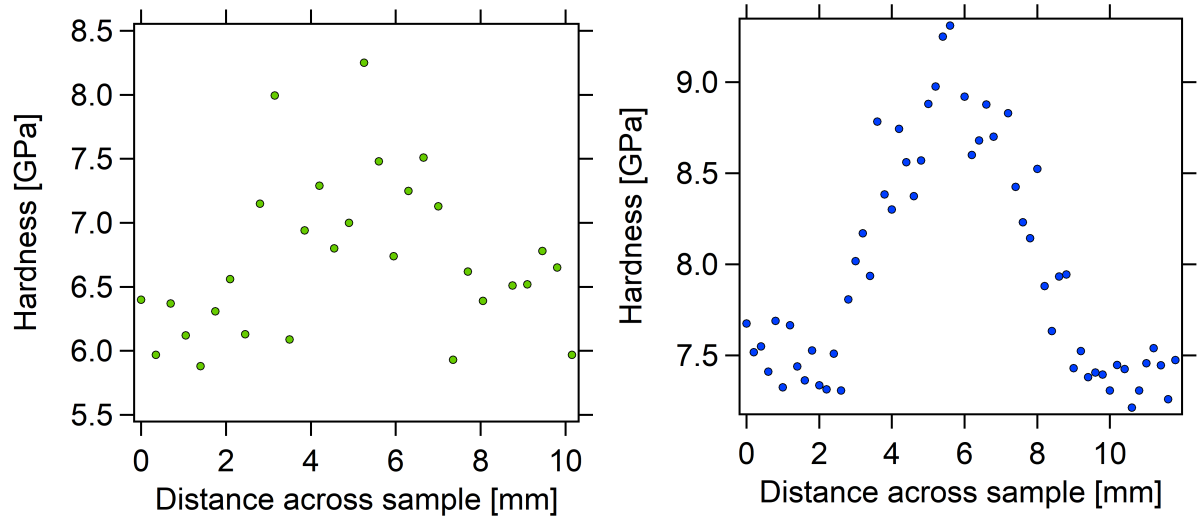

(c) 0.143 dpa (d) 0.414 dpa

Figure 6.38: Hardness as a function of distance probed across sample for samples with varying induced displacement damage.

The hardness obtained as a function of sampling distance during nanoindentation is superimposed with the illuminated area during proton irradiation in Figure 6.39. The peak-shaped behaviour can be attributed to the rastering of the proton beam during irradiation, such that the proton flux is highest in the centre of the beam. The hardness values in the irradiated and unirradiated regions are respectively averaged to provide a mean irradiated and unirradiated hardness for each foil. The implications of hardness change as a function of damage are presented in the discussion section.

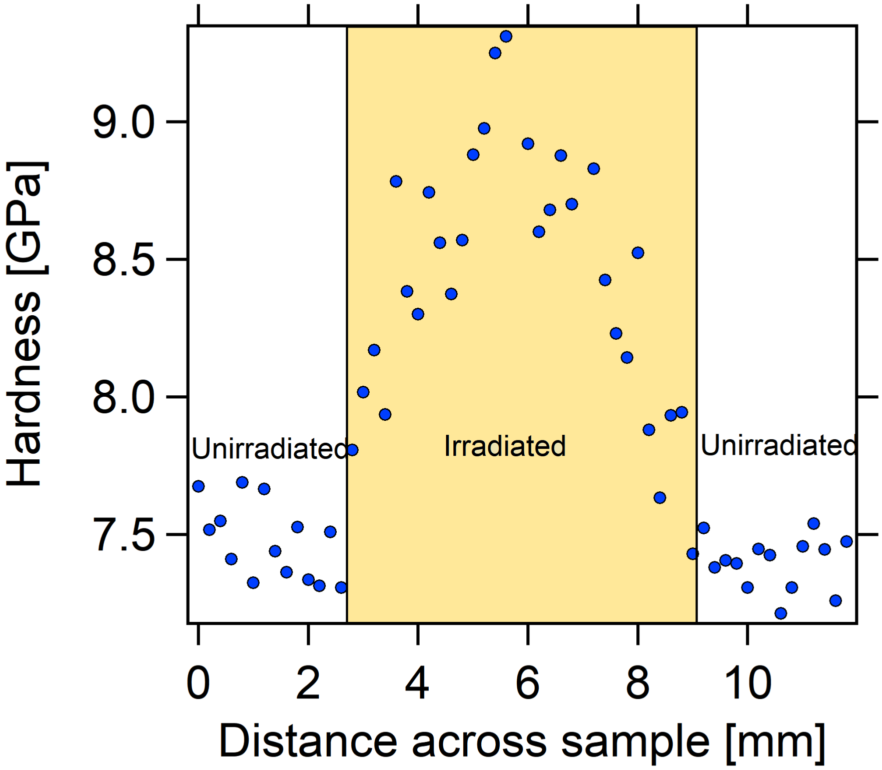

Figure 6.39: Hardness as a function of distance across sampling line in foil 7, with proton beam area superimposed (yellow).

6.5 Discussions

6.5.1 Transmutation and activation of tungsten

From damage simulations and calculations in Section 6.4.2, the maximum displacement damage induced in the tungsten samples was found to be 0.820 dpa. Using the calculated activity spectrum from the samples in Section 6.4.1, it was concluded that there was not enough damage induced for significant quantities of transmuted rhenium to favour precipitation of rhenium in the tungsten matrix. [35]

induced displacement damage in tungsten and tungsten rhenium alloys up to 30 dpa. They noted that in pure tungsten, sufficient levels of rhenium to influence the precipitation process are only transmuted at damage levels over 5 dpa. The level of rhenium at which such precipitation events are observed has been found to be 4 wt%.

Unfortunately, the damages achieved in this study were primarily limited by beamtime requirements and the international transport of radioactive materials. In both these cases, the timescales were the predominant factor in the effective inducing of displacement damage in the tungsten samples.

Interestingly, despite the relatively low damage levels, the tungsten samples remained above the excepted package transportation limits for almost one year. This can be attributed to the high cross sections of proton induced reactions such as ^{182}W(p,2n)^{181}Re which, through their decay pathways, generate isotopes that have relatively long half lives (months) compared to the order of hours of other threshold reactions. Hence, transmuted unstable isotopes ^{183}Re,^{184}Re and ^{182}Ta contributed most to the overall post-irradiation sample activity. This is an important consideration for any future proton irradiation studies in tungsten and its alloys, since it imposes practical limitations on the irradiated sample properties.

6.5.2 Effect of damage level on precipitate shape and size distributions

Through analysis of the precipitate-only scattering profiles, it has been concluded that the unirradiated sample matrix remains as pure tungsten. This is supported by the initial purity of the as-received samples, where the impurity concentrations are so low that their contribution to the total neutron scattering intensity is likely to be negligible compared to the level of incoherent background scattering arising from the tungsten atoms.

Previous TEM studies on irradiated tungsten have observed rhenium precipitation in samples induced with damage greater than 5 dpa [27, 35]; in contrast, the damage levels achieved during irradiation in this work only reached a peak value of 0.82 dpa. In combination with the findings presented in Section 6.5.1, calculation of the scattering length density and incoherent background of the scattering objects has shown that the scattering objects are voids rather than self or solute interstitial precipitates. The formation of such microstructural features during irradiation arises from matrix damage from the primary knock-on atom, with subsequent vacancy channelling and clustering to form larger coherent void structures.

Neutron damage is likely to not differ across the sample due to the bulk penetrating nature of the radiation. Hence, it is imperative that, if proton irradiation is being used as a comparison to the observed results from [27, 36, 35, 37, 58, 189] using neutron irradiation, one is able to fully separate the damage in each region of the Bragg peak. The method of proton irradiation adopted during this work has allowed for a direct deconvolution between the nature of damage at different proton depths within samples. As such, the void properties as a function of damage can be explicitly obtained in a shorter period, with more control over other environmental loading conditions such as pressure and temperature, compared to more traditional neutron irradiation techniques. The discussions presented here assume that a qualitative comparison can be made between the microstructural state of irradiated tungsten samples in previous TEM studies and the information obtained through SANS analysis.

The form factor of the void scatterers has been investigated through empirical model fitting of the SANS scattering intensity, I(q), data. The fitting of several form factor models found the most consistent form factor with the lowest χ^2 value to be the log-normal sphere model. All other models used either produced unphysical void parameters or had large uncertainties in the fit. It has been judged that a log-normal size distribution of spherical scatterers is the most likely representation of the shape of the voids within the irradiated tungsten. This is wholly consistent with the form factors of such voids observed in TEM studies at similar damage levels [27, 193].

The observed voids in tungsten have been found to increase in radius and volume as a function of increasing irradiation damage, as shown in Figure 6.34 and Figure 6.35 respectively. This is wholly consistent with the fundamental understanding of damage mechanisms in polycrystalline metals exposed to radiation, where the channelling of vacancies can lead to clustering and precipitation into larger void structures to reduce the free energy of the system. Such void structures are of particular interest in this work since the elevated temperatures achieved during irradiation favour increased mobility of defects in the atomic lattice.

A proton irradiation study in pure W and W-5wt%Ta observed void formation at high temperatures (800 °C and 1000 °C); the voids in pure tungsten continue to grow in size past 0.2 dpa with a mean radius of 5.7 ± 0.6 μm at 0.5 dpa [193]. [189] found that at higher damage levels than achieved in this work (up to 1.5 dpa), the void radius trend saturates, with a declining growth rate, and to minimise the free energy further a void lattice structure is generated. Past this damage level, void shrinkage begins to occur as the transmutation of the tungsten matrix into rhenium and osmium isotopes favours nanoscale precipitation events with needle like structures.

Since small-angle scattering allows for probing of bulk material properties on the nanoscale, it can provide a more reliable picture of the microstructual state compared to volume limited techniques such as TEM. The conclusion that at the damage levels achieved in the study the scattering objects are a distribution of voids, the volume fraction of such voids can be found explicitly. This is a large benefit of using SANS to study such a binary system where the scattering contrast is definitive.

The observed volume fraction increase of voids with increasing damage level can be attributed to the increased density of vacancy matrix damage induced by the primary knock on atoms. This is also seen consistently in other irradiation induced damage studies in tungsten [27, 36, 37, 58, 186]. In addition, it was found that the whole distribution of voids increased in size for increasing displacement damage levels, reflected by the relatively constant void polydispersity across each sample from the fitted scattering intensity form factors (Table 6.14).

6.5.3 Induced hardening and embrittlement

As discussed in Section 6.4.4, nanoindentation itself can induce dislocations in the material due to plastic flow.

During nanoindentation of polycrystalline metals with a Berkovich indenter, the initial contact is elastic and behaves in a Hertzian manner. At a certain depth, the mateiral will experience an elastic-plastic transition at the onset of plasticity. This transition can lead to a sudden increase in displacement of the indenter with no change in load and is known as the pop-in phenomenon [212, 213, 214]. Pop-in is a direct result of nucleation of dislocations; in an unirradiated material the nucleation is homogenous and occurs at shear stresses close to the material strength, whilst in irradiated materials the nucleation is heterogenous due to the presence of secondary lattice defects. Since the number of secondary defects, such as voids, increases with induced irradiation damage, the pop-in phenomenon is more prevalent for materials subject to high doses [215].

Inspection of the irradiated tungsten nanoindentation data shows clear pop-in events for all damage levels. Figure 6.40 shows such phenomena in the load-depth curves for several irradiated samples.

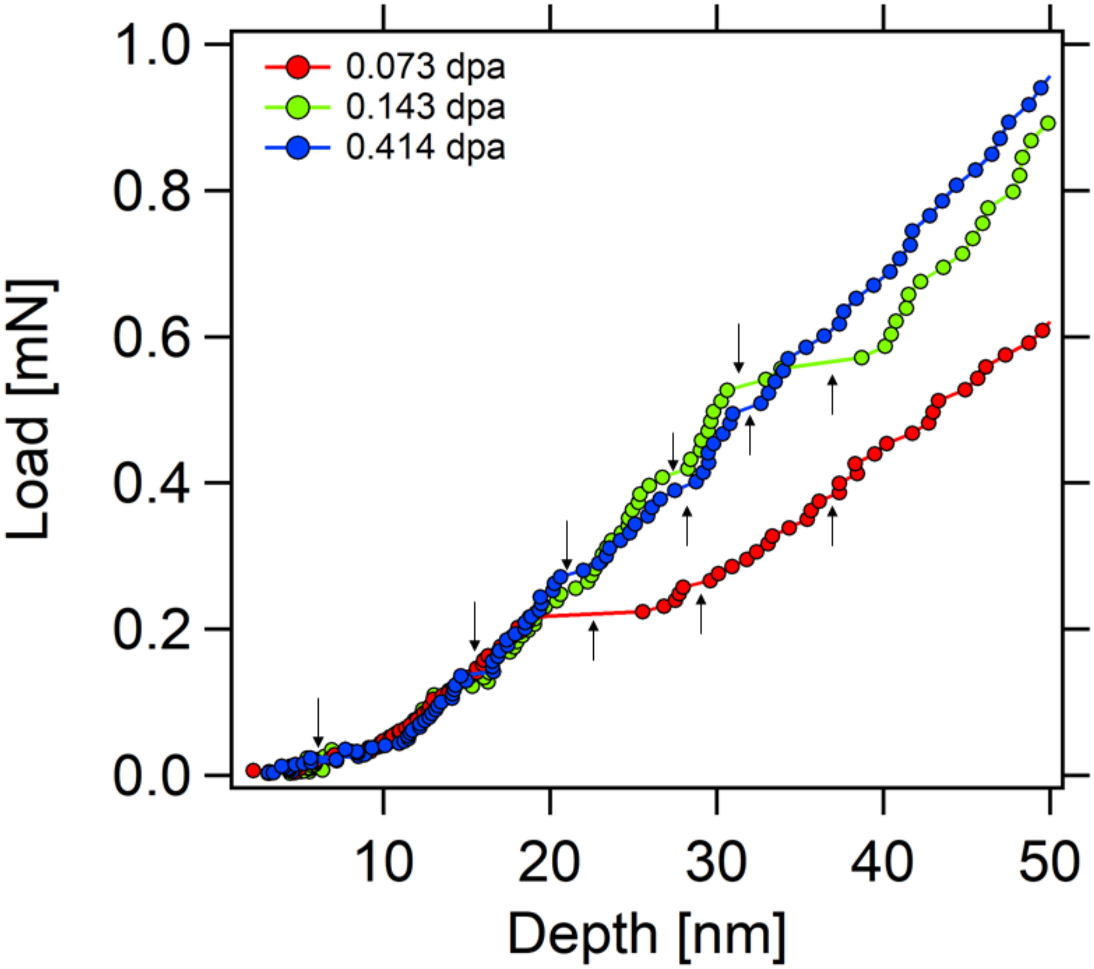

Figure 6.40: Applied load as a function of indent depth at low depths in irradiated samples showing pop-in phenomena.

The presence of void structures induced during irradiation leads to an increase in dislocation density due to mismatches in the underlying crystal structure. The implications of this is an increase in hardness as a direct response to exposure to high energy protons.

Through analysis of the raw nanoindentation data, the hardness and Young's modulus of each irradiated sample was obtained (Section 6.4.4). A qualitative change in both material properties provides information on the mechanisms of irradiation damage in tungsten and how it may affect performance.

The measured, uncorrected elastic moduli were lower than the expected tungsten Young's modulus

(400 GPa from [105]). This suggests that the elastic moduli of the underlying substrate materials of the sample mount are being probed, such as the crystal bond glue and aluminium stub. Whilst this is significant for the elastic modulus calculations, the validity of the hardness results is not affected. The indenter depth was set as 1 μm so that the fraction of the sample thickness probed is less than 10 percent. From this, it is reasonable to assume that there is a minimal effect of the substrate hardness on the hardness measurements [216].

The surface effects have been considered during the nanoindentation analysis, leading to exclusion of certain foils from the final dataset due to erroneous behaviour that has been attributed to the presence of oxide on the sample surface. In addition, surface roughness must be accounted for. Large surface roughness means that the indenter tip is not in full contact with a flat surface and so the calculated projected area may be larger than the true contact area with the sample. If the indent depth is comparably larger than the surface roughness parameter, such surface roughness effects can be overcome [104]. As such, a relatively large indent depth was employed during the nanoindentation of the tungsten foils, due to the feasibility issues with polishing active samples.

The majority of the challenges associated with ion-irradiated nanoindentation is that the damage is concentrated near the surface in the form of a Bragg peak due to the mean free path of the ion in the material of choice [217]. Examples of such challenges are shown schematically in Figure 6.41. Previous nanoindentation studies on ion irradiated Fe-9%Cr oxide dispersed steels by [218] faced significant challenges when selecting an appropriate indenter depth that was

- Shallow enough to avoid probing of the unirradiated bulk that can underestimate hardness.
- Deep enough to overcome the indentation size effect and the surface roughness attributed to surface sputtering during irradiation, both of which can overestimate hardness.

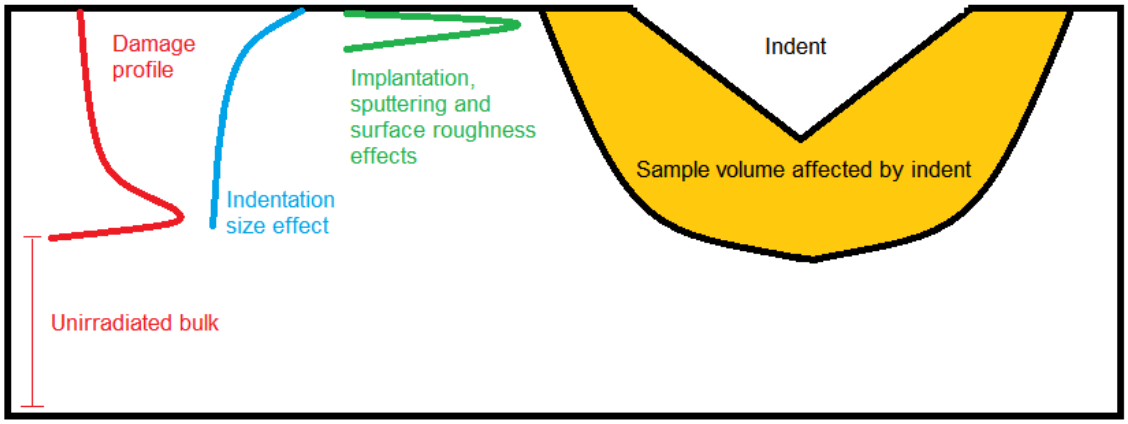

Figure 6.41: Schematic of the various effects to consider during nanoindentation of ion irradiated metallic samples. Adapted from [217].

Such challenges were overcome in this study through the irradiation setup of a stack of tungsten samples, where each thin foil represents a specific region of the Bragg damage peak. Since nanoindentation results are depth sensitive, the indenter depths required to probe hardness in the elastic zone and where surface roughness is negligible can be offset by a drastically changing damage profile as a function of sample depth, leading to large uncertainty in obtained results and even possibly probing the unirradiated bulk instead. A specific advantage of the irradiation setup in this study is that damage is induced across the full depth of each foil and so there is no unirradiated region that can be probed by large indenter depths. As a result, the indenter depth chosen in this study was such that the surface roughness impact and indenter size effect is negligible.

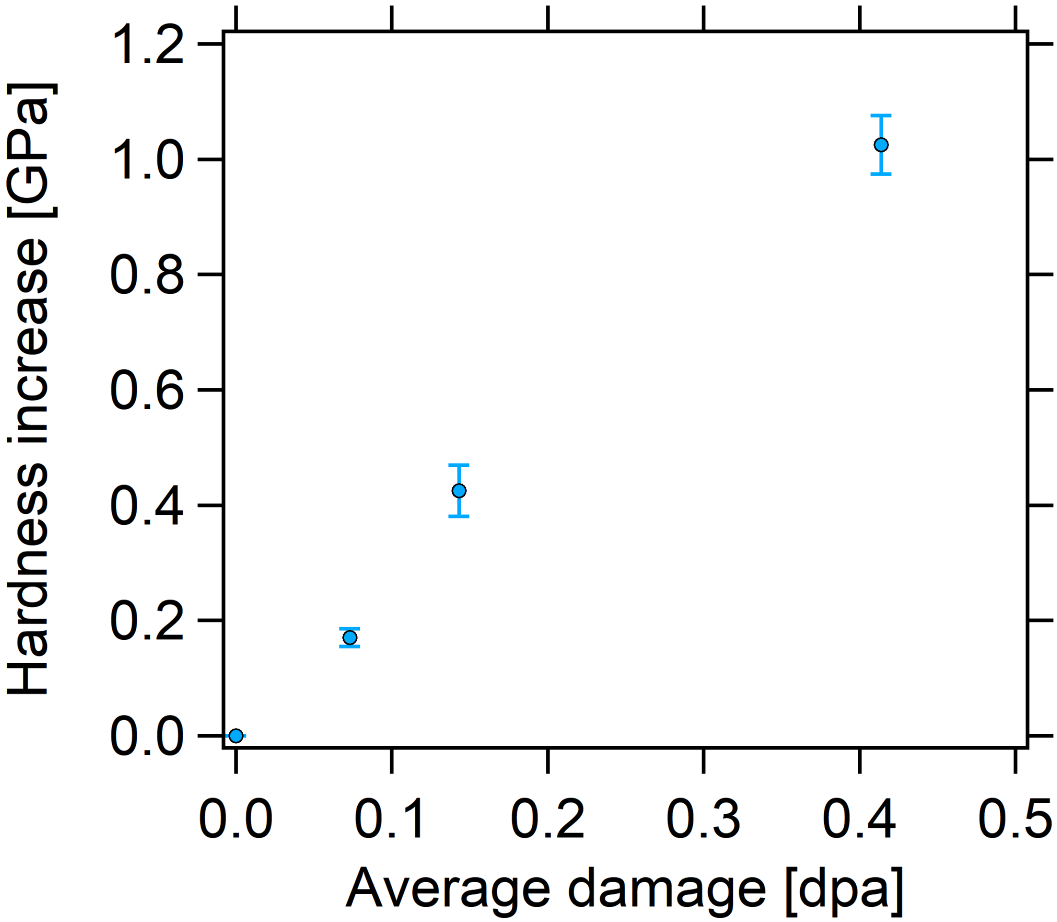

Figure 6.42: Change in hardness as a function as a function of induced damage in irradiated tungsten.

Figure 6.42 shows the irradiation hardening observed in tungsten as a function of damage. This can be fully attributed to hardening caused by the matrix damage itself rather than any indentation size effect hardening. It is clear that the largest irradiation induced hardness change is observed for the sample with the most induced damage. This is supported by the relatively large volume fraction and radii of induced void damage present in comparison to tungsten samples with lower induced damage levels obtained through SANS. The void size increase with damage follows the same trend as the hardness; both have a saturating exponential growth rate with increasing damage. These trends are consistent with other literature studies on nanoindentation of irradiated polycrystalline metals [215].

Mechanistically, the void distribution induced by the primary knock-on atoms and consequential damage cascade through the tungsten matrix provides significant barriers to dislocation motion. This has been observed in [219] and [220], where the void number density and size significantly increased following irradiation, leading to an irradiation hardening effect quantified using nanoindentation. In addition,

[189] found an approximate increase in hardness of 200 Hv for pure tungsten irradiated to damage levels below 1 dpa, with the hardness change increasing to 400 Hv for damage up to 1.5 dpa. This is consistent with the findings of this study, where for tungsten with 0.4 dpa of induced damage, the hardness increase was found to be 1.03 GPa (104.6 Hv). Such irradiation induced hardening in tungsten poses several challenges to the lifetime of tungsten as a plasma facing component in a fusion reactor, namely those associated with ensuring sufficient structural integrity and thermal shock resistance.

6.6 Conclusions

The development of reliable PFMs in the international endeavour of fusion reactor commercialisation for energy output has been a considerable research effort over the last 30 years. Tungsten has been considered as a potential first wall and/or divertor material to meet the onerous requirements of a plasma facing material within the fusion device. Such requirements include maintenance of structural integrity over its lifetime in the reactor ($\sim$10 years), minimal transmutation, low activation, low tritium retention, low erosion and sputtering, thermal shock resistance, and the ability to maintain its thermal and mechanical properties at high temperatures.

Exposure to the plasma, high magnetic fields, high temperatures and a high flux of high energy neutrons can provoke material property evolution over the lifetime of a PFM such as tungsten. It is imperative for the development of reliable PFMs that the property evolution of tungsten is understood across all of the loading conditions experienced over its lifetime. The current state of literature surrounding irradiated tungsten presents several gaps surrounding induced Re and Os transmutation events, quantification of irradiation damage using bulk techniques as a complementary tool, and the effect of irradiation induced defects on mechanical properties.

The work presented in this chapter has focussed on how the exposure to a harsh radiation environment can impact the microstructural evolution of tungsten and induce irradiation hardening and embrittlement. The nature of the induced secondary defects was identified, and the macroscopic effect of induced secondary defects on mechanical properties such as hardness was also assessed.

A custom proton irradiation setup was designed to obtain a range of samples with varying levels of damage in a single irradiation run. Such a setup ensures consistent environmental conditions for each sample where the only difference is the induced damage. This is a specific advantage of using proton irradiation over neutron irradiation to study such damage in PFMs since the parameters can be more closely controlled. Using this setup, pure tungsten was successfully irradiated for 9.4 hours using 15 MeV neutrons at 509.25 ± 32.41 °C to average damage levels ranging from 0 to 0.414 dpa (peak of 0 to 0.815 dpa) to simulate the expected peak neutron energy from the ^{2}H + ^{3}H fusion reaction (14.1 MeV).

The majority of irradiation induced damage studies in tungsten have used TEM as a method of quantifying the precipitation events, which is limited by its ability to only probe a specific sample area. The work presented in this chapter presents a novel small-angle neutron scattering study on irradiated tungsten. It demonstrates the robust nature of using such analysis techniques to quantify bulk irradiation damage.

Evidence has been obtained that suggests that the level of induced damage leads to the generation of vacancies and voids within the tungsten matrix. This is supported by TEM studies on irradiated tungsten. The presence of voids are of particular interest when considering interactions of the first wall or divertor materials with the plasma itself. Ideally the PFM would have low sputtering properties to minimise erosion, co-deposition and dust production within the tokamak. The presence of voids can lead to embrittlement, but can also act as tritium trap concentration sites that favour tritium permeation and retention in the component [221, 222, 223].

At damages up to 0.414 dpa, the voids were found to have a spherical shape with a log normal size distribution. Alongside void shape, SANS has allowed for quantification of the effect of displacement damage on void size and volume fraction, with radii and volume fraction ranging from 0.748 nm to 1.824 nm and 0.10 % to 0.19 % respectively with increasing damage.

The change in hardness was obtained as a function of damage using continuous stiffness nanoindentation. The custom irradiation setup was invaluable for such quantification where:

1. More common lower energy proton irradiation in different material systems results in surface level damage only. The high energy protons allowed for increased penetration within the tungsten to obtainable nanoindentation depths.

2. The tungsten foil sample stack allowed for different regions of the Bragg peak to be investigated,

with each foil having a full irradiated bulk.

It was found that the irradiation induced hardening effect increased with increasing damage levels, with the largest increase measured as 104.6 Hv for 0.414 dpa.

Despite the aforementioned successes, there are some shortcomings in this work that can act as areas to be improved upon for future work. For example, the damage levels achieved in this study were primarily limited by beamtime requirements and the international transport of radioactive materials. In both of these cases, the timescales were the predominant factor in the effective inducing of displacement damage in the tungsten samples. Inducing higher levels of damage (> 5 dpa) may lead to significant transmutation of rhenium in tungsten, which ultimately will initiate solute interstitial precipitation events in the matrix rather than void precipitation. If such high damage levels are unfeasible, then a variety of unirradiated W_xRe_{1-x} alloys could be used as a starting point. For these future studies, TEM or APT could be used in combination with SANS as such techniques were not feasible in this work due to the very high activity and long half-lives of the transmuted elements in the tungsten samples.

If a similar irradiation setup is adopted in the future, there is the potential to use slightly thicker samples. This can be balanced by using W_xRe_{1-x} alloys or altering the energy of the proton beam. It should be noted a balance must be struck between samples remaining thin enough to allow for different parts of the Bragg damage peak to be available through the irradiation stack, but thick enough to not have issues of probing elastic moduli of underlying sample mount materials. Increasing the thickness sufficiently could allow for a comparison of absolute values between foils rather than within-foil comparisons of hardness between irradiated and unirradiated foil regions. It would also be interesting to vary the irradiation parameters used, for example the temperature to understand the thermodynamics of the precipitation process, or the proton energy to investigate the nuances of using proton irradiation to emulate the in-service neutron irradiation of PFMs.

The tungsten samples could have been polished to reduce effects of surface roughness in nanoindentation, allowing for more accurate results; this was limited by the sample activity in this study. Moreover, the pile-up effect could be examined in more detail using SEM techniques, noting that this will likely be required to be carried out at a dedicated facility such as the MRF that can handle radioactive samples. Moreover, the completion of TEM on the active samples at such a facility could be an interesting extension of this work. Due to the nature of the tungsten samples, this was unfortunately outside of the scope of this thesis.

There are several other candidate PFM systems aside from tungsten that could be investigated in the same way as this study. For example, similar principles could be applied to tantalum or vanadium alloy systems to investigate their property evolution under irradiation.

Finally, there is a large field of research dedicated to neutron-induced transmutation and bubble formation in PFMs. SANS is a robust tool that could be used to study the coupling of induced void or precipitate damage with hydrogen and helium transmutation in material systems of interest. This is of particular importance when considering trap concentrations for tritium migration and retention in PFMs that can lead to fuel management and waste issues.

CHAPTER 7

CONCLUSIONS

This work contributes to the current knowledge gaps surrounding irradiation and thermal ageing induced precipitation damage in various nuclear materials. It demonstrates how advanced scattering techniques can be combined to provide vital insight into nanoscale material transitions, which is essential in the research and design of reliable nuclear materials.

A study of precipitation in a high Ni RPV weld thermally aged for 100 000 hours at 330 °C was presented to show how advanced scattering techniques can be used to add value to data obtained from other investigative techniques. Thermal ageing induced precipitation damage was confirmed using SANS. The extracted structural properties were found to be consistent with the APT results: a distribution of polydisperse spherical precipitates with a mean radius of 2.006 ± 0.059 Å confirmed through a variety of scattering analysis techniques. The core-shell structure suggested by the APT study was investigated in a dedicated high-q SANS experiment but was not explicitly identified. The magnetic nature of neutrons and the use of anomalous x-ray dispersions in the vicinity of elemental absorption edges allowed for additional insight into the disputed role of Fe and vacancies in precipitates and the magnetic nature of the induced precipitates. The precipitates were found to have an A ratio of 2.705 ± 0.012 and an average composition of 0.03Fe-0.17Ni-0.44Cu-0.13Mn-0.03Si-0.19Vac, in contrast to APT studies that often overestimate the Fe fraction and SANS studies that disregard precipitate magnetism. Microindentation testing quantified an increase in hardness of 80.0 ± 4.4 Hv attributed to the thermal ageing induced precipitation damage.

An advanced scattering study of thermal ageing induced precipitation damage in a series of model low alloy RPV steels was completed to investigate in-situ material transitions and to test the current understanding of the role of Cu, Mn and Ni on the mechanisms of thermal ageing induced precipitation and hardening. A series of model low alloy RPV steels were fabricated and thermally aged. SAXS was used to compare the as-made and thermally aged samples; the thermal ageing process was found to have varying levels of success owing to the effect of solubility and thermodynamic stability of certain alloying elements in a Fe matrix. A first-of-its-kind ASAXS investigation was carried out to provide a comprehensive study of the induced precipitate compositions. Due to the relatively low alloy fractions in comparison to the predominantly Fe matrix, the observed contrast changes as a function of energy at the elemental absorption edges of Cu, Ni and Mn in the model RPV samples were not significant. The anomalous dispersions were so small that accurate compositional information could not be resolved. SANS was used to extract the magnetic to nuclear scattering ratio, and whilst a single average precipitate composition was not distinguishable, it provided a down-selection of possible precipitate compositions for each model alloy. SANS also quantified the induced precipitates as a polydisperse system of spheres with a log-normal distribution of radii, with radii ranging from 1.143 ± 0.081 to 5.874 ± 0.015 nm for the different alloy compositions.

A novel in-situ ageing SANS study on FeCu, FeCuNi and FeCuMnNi used the long-range nature of neutrons to understand the effect of Mn and Ni on precipitate nucleation and growth in the presence of Cu. Precipitates of mean radius 3.689 ± 0.047 nm were induced after 20 hours at 550 °C in the FeCuMnNi sample. The kinetics of the nanoscale transitions were studied, and it was found that Mn suppresses the growth of precipitates in the presence of Cu.

The hardness was found to increase as a function of ageing time for all thermally aged model alloy compositions, with the largest increase of 64 ± 8.2 Hv observed for the FeCuMnNi system. The results of this study allowed for a comparison to previous thermal ageing and irradiation damage studies on precipitation mechanisms in similar low alloy RPV steels.

A novel irradiation setup was designed to induce varying levels of displacement damage and transmutation in a set of thin high purity tungsten foils. The tungsten was successfully irradiated for 9.4 hours using 15 MeV neutrons at 509.25 ± 32.41 °C to average damage levels ranging from 0 to 0.414 dpa (peak of 0 to 0.815 dpa) to simulate the expected peak neutron energy from the deuterium-tritium fusion reaction (14.1 MeV). High purity gamma spectroscopy and the physics of radioactivity were used to obtain the induced transmutation and activation within the irradiated samples to allow for safe transport for analysis. The key transmuted elements identified were ^{181}Re, ^{183}Re, ^{184}Re and ^{182}Ta.

The majority of irradiation induced damage studies in tungsten have used TEM as the investigative technique. The first ever SANS investigation on irradiated tungsten was completed during this work to provide bulk quantification of precipitation events. The damage induced was identified as a system of polydisperse spherical voids with a log-normal size distribution, owing to the matrix damage mechanisms and the lack of significant transmutation of Re to favour Re-rich precipitates. The radii and volume fraction of voids were found to increase from 0.748 nm to 1.824 nm and 0.10 % to 0.19 % respectively as a function of displacement damage. Nanoindentation was used to quantify the irradiation induced hardening effect, where the largest hardness increase was observed for the peak irradiated sample ($\Delta H_{0.4\ \mathrm{dpa}} = 104.6$ Hv).

The irradiation induced precipitation study in high purity tungsten shows the versatility of SANS for the investigation of any type of precipitation events. This is key for understanding irradiation and thermal ageing induced damage as it provides a single technique that can study precipitation regardless of its initiating mechanisms and allows for comparisons to be drawn between the two. Both damage mechanisms are key for nuclear materials research due to the onerous reactor operating environment. Moreover, this understanding is valid across the whole nuclear industry, with the simultaneous importance of operational safety justifications, life extension, qualification of materials for use in future reactor designs, and even the development of novel materials that are more resistant to precipitation induced hardening and embrittlement.

The findings of this thesis provide invaluable contributions to the understanding of nanoscale induced microstructural changes that occur in nuclear fission and fusion materials subject to harsh temperature and radiation environments. The evolution, and hence degradation, of mechanical properties with thermal ageing and irradiation induced precipitation damage has been quantified, with a fundamental mechanistic understanding of the precipitate damage process provided by advanced scattering investigations. Overall, this work has shown how precipitation damage in a variety of nuclear material systems can be investigated using advanced scattering techniques. Key nuclear materials challenges across all stages of the material lifecycle have been addressed, including life extension considerations for reactor pressure vessel steels in generation III and III+ light water reactors, the development of degradation-resistant materials for advanced fission reactors, and the qualification of materials for the design, and eventual commercialisation, of fusion reactors.

CHAPTER 8

FUTURE WORK

This work has identified several areas of interest that are outside of the scope of this thesis, but that would nonetheless be exciting to investigate in further studies.

In Chapter 4, a long thermally aged high Ni RPV weld was studied and the structural and compositional information of the induced precipitates was extracted using SANS and ASAXS. Whilst this forms a direct contribution to understanding of precipitation in the welds that could not be obtained through APT, there are additional studies that could be carried out. For example, due to the activity of the samples after neutron and x-ray exposure, TEM was not possible. In the future, TEM could be used to quantify any additional induced microstructural changes. It would also be interesting to perform an irradiation study on this alloy composition to investigate the interplay between thermal ageing and irradiation induced precipitation for representative in-service conditions.

For the thermal ageing of RPV model alloys presented in Chapter 5, there were several RPV alloy compositions where no thermal ageing induced precipitation was observed. For such samples, longer ageing times could be used to increase the likelihood of precipitate formation and hence form additional conclusions on the role of Cu, Mn and Ni on thermal ageing induced precipitation. In addition, the in-situ ageing SANS study could be repeated for other alloys of interest, and for longer ageing times. A high-q focussed SANS experiment could be used to study the potential core-shell nature of the precipitate systems, which was limited by the experimental configuration used in this work.

As for the RPV weld, it would be interesting to investigate the model RPV alloy compositions used where precipitation was induced further in a complementary SANS study on neutron (or proton) irradiation samples. The effect of annealing on such irradiation induced precipitates could also be investigated using SAS. It was found that Mn has a particularly strong influence on the precipitation process, which could be studied in more detail by using a range of model RPV alloys with varying fractions of Mn to quantify the impact on the precipitation kinetics and structural properties.

The damage levels induced in tungsten in Chapter 6 were limited by the requirement to transport the samples to international facilities for scattering analysis. Whilst some transmuted rhenium was identified after irradiation, the amount was not significant to induce rhenium dominant precipitates, and the damage level was not high enough to induce significant self solute precipitation of tungsten. Instead, at the peak level of 0.414 dpa the induced damage observed was a network of voids. Inducing higher levels of damage ($>$ 5 dpa) may lead to more significant transmutation of rhenium in tungsten, which ultimately will initiate solute interstitial precipitation events in the matrix rather than void precipitation. If such high damage levels are unfeasible, then a variety of unirradiated W_xRe_{1-x} alloys could be used as a starting point. It would also be interesting to vary the irradiation temperatures to understand the thermodynamics of the precipitation process, or perhaps irradiate using a range of proton energies to better understand how proton irradiation can act as a surrogate for neutron irradiation of PFMs.

There are several other candidate PFM systems aside form tungsten that could be investigated in the same way as this study. For example, similar principles could be applied to tantalum or vanadium alloy systems to investigate their property evolution under irradiation.

Complementary investigative techniques such as TEM or APT may be completed to provide additional compositional and structural information on both irradiation and thermal ageing induced precipitates for each nuclear material system. It is noted that such techniques were not possible during this work due to the high activation of samples post neutron and x-ray scattering, and the destructive nature of APT which would limit any further investigation on samples in the future.

This work has quantified the irradiation and thermal ageing induced precipitate hardening, to show the embrittlement effect of such damage mechanisms in nuclear material systems. Micro and nano indentation techniques were employed to study such effects due to the limitations sample sizes required for SAS and irradiation volume limited by the proton beam size. In the future, larger samples could be used in precipitation damage studies to allow for additional mechanical property evolution measurements and macroscopic testing such as fracture toughness, Charpy impact testing, and even strength tests. Neutron irradiation could be used on larger samples to combat the proton beam size limitation, although it is noted that this is expensive and time consuming by comparison. Moreover, the precise environmental conditions cannot be controlled without the use of specialised holding cells, loading matrices, and test specifications. This research is typically funded by commercial nuclear organisations, including private ventures that are often outside of the bounds of academia due to the costs of such irradiation programmes.

This thesis has presented several experimental methods for the investigation of radiation damage using advanced scattering. In general, it has shown that SAS can be applied to a variety of nuclear materials for both fission and fusion applications, and that it is a versatile tool for studying irradiation and thermal ageing induced precipitation. The in-situ thermal ageing SANS technique and the use of ASAXS to study the composition of induced precipitates could be applied to different nuclear material systems of interest in the future. For example, ASAXS could be employed to investigate the effect of high energy radiation interactions on transmutation in other candidate plasma facing fusion materials.

LIST OF REFERENCES

[1] US Energy Information Administration. International energy outlook, 2020. https://www.edfenergy.com/energy/nuclear-lifetime-management.

[2] US Energy Information Association. International energy outlook, 2017. https://www.eia.gov/todayinenergy/detail.php?id=32912.

[3] Department for Business Energy and Industrial Strategy. Net zero 2050, 2019. https://www.gov.uk/government/news/uk-becomes-first-major-economy-to-pass-net-zero-emissions-law.

[4] Nuclear Industry Association. Nuclear generation, 2021. https://www.niauk.org/industry-issues/supply-chain/nuclear-generation-supply-chain/.

[5] Department for Business Energy and Industrial Strategy. UK energy in brief 2020. *National Statistics*, 2020. https://www.gov.uk/government/statistics/uk-energy-in-brief-2020.

[6] EUROFusion. History of fusion, 2021. https://www.euro-fusion.org/fusion/history-of-fusion/.

[7] EUROFusion. Road map to fusion, 2018. https://www.euro-fusion.org/eurofusion/roadmap/.

[8] I. Sattari-Far. The significance of cladding material on the integrity of nuclear pressure vessels with cracks, 1989.

[9] Mistubishi Heavy Industries Group. Pressurised water reactor: major systems, 2021. https://www.mhi.com/products/energy/reactor_coolant_pump.html/.

[10] K. L. Murty and I. Charit. Structural materials for gen-iv nuclear reactors: Challenges and opportunities. *Journal of Nuclear Materials*, 383:189–195, 2008.

[11] G. Was. *Fundamentals of Radiation Materials Science*. Springer, 2007.

[12] S.J. Zinkle and G.S. Was. Materials challenges in nuclear energy. *Acta Materialia*, 61:735–758, 02 2013.

[13] F. Bergner, A. Ulbricht, A. Gokhman, and D. Erak. Nature of defect clusters in neutron-irradiated iron-based alloys deduced from small-angle neutron scattering. *Journal of Nuclear Materials*, 373(1):199 – 205, 2008.

[14] E. Meslin, M. Lambrecht, M. Hernández-Mayoral, F. Bergner, L. Malerba, P. Pareige, B. Radiguet, A. Barbu, D. Gómez-Briceño, A. Ulbricht, and A. Almazouzi. Characterization of neutron-irradiated ferritic model alloys and a rpv steel from combined apt, sans, tem and pas analyses. *Journal of Nuclear Materials*, 406(1):73–83, 2010.

[15] Office of Nuclear Reactor Regulation U.S. Nuclear Regulatory Commission. Reactor pressure vessel status report, 1994.

[16] G. Salje and M. Feller-Kneipmeier. The diffusion and solubility of copper in iron. *Journal of Applied Physics*, 48:1833, 1977.

[17] J. Marian, B.D. Wirth, G.R. Odette, and J.M. Perlado. Cu diffusion in α-fe: determination of solute diffusivities using atomic-scale simulations. *Computational Materials Science*, 31(3-4):347–367, 2004.

[18] M. K. Miller, K. F. Russell, P. J. Pareige, M. J. Starink, and R. C. Thomson. Low temperature copper solubilities in fe-cu-ni. *Materials Science and Engineering: A*, 250(1):49–54, 1998.

[19] N. Almirall, P. B. Wells, H. Ke, P. Edmondson, D. Morgan, T. Yamamoto, and G. R. Odette. On the elevated temperature thermal stability of nanoscale mn-ni-si precipitates formed at lower temperature in highly irradiated reactor pressure vessel steels. *Scientific Reports*, 9:9587, 2019.

[20] J. Buswell, C. A. English, M. Hetherington, W. Phythian, G. D. W. Smith, and G. Worrall. An analysis of small clusters formed in thermally aged and irradiated fecu and fecuni model alloys. In *Effects of Radiation on Materials: 14th International Symposium Volume II*. ASTM International, 1990.

[21] J.M. Hyde, G. Sha, E.A. Marquis, A. Morley, K.B. Wilford, and T.J. Williams. A comparison of

the structure of solute clusters formed during thermal ageing and irradiation. *Ultramicroscopy*, 111(6):664 – 671, 2011. Special Issue: 52nd International Field Emission Symposium.

[22] S. Shu, B. D. Wirth, P. B. Wells, D. D. Morgan, and G. R. Odette. Multi-technique characterization of the precipitates in thermally aged and neutron irradiated fe-cu and fe-cu-mn model alloys: Atom probe tomography reconstruction implications. *Acta Materialia*, 146:237–252, 2018.

[23] T. M. Whiting, P. A. Burr, D. J. M. King, and M. R. Wenman. Understanding the importance of the energetics of mn, ni, cu, si and vacancy triplet clusters in bcc fe. *Journal of Applied Physics*, 126(11):115901, 2019.

[24] A.T. Al-Motasem, M. Posselt, and F. Bergner. Nanoclusters in bcc-Fe containing vacancies, copper and nickel: Structure and energetics. *Journal of Nuclear Materials*, 418(1-3):215–222, 2011.

[25] The ITER Organisation. The ITER tokamak, 2021. https://www.iter.org/mach.

[26] R.A. Pitts, S. Bardin, B. Bazylev, M.A. van den Berg, P. Bunting, S. Carpentier-Chouchana, J.W. Coenen, Y. Corre, R. Dejarnac, F. Escourbiac, J. Gaspar, J.P. Gunn, T. Hirai, S-H. Hong, J. Horacek, D. Iglesias, M. Komm, K. Krieger, C. Lasnier, G.F. Matthews, T.W. Morgan, S. Panayotis, S. Pestchanyi, A. Podolnik, R.E. Nygren, D.L. Rudakov, G. De Temmerman, P. Vondracek, and J.G. Watkins. Physics conclusions in support of ITER W divertor monoblock shaping. *Nuclear Materials and Energy*, 12:60–74, 2017.

[27] Akira Hasegawa, Makoto Fukuda, Kiyohiro Yabuuchi, and Shuhei Nogami. Neutron irradiation effects on the microstructural development of tungsten and tungsten alloys. *Journal of Nuclear Materials*, 471:175 – 183, 2016.

[28] G.A. Cottrell. Sigma phase formation in irradiated tungsten, tantalum and molybdenum in a fusion power plant. *Journal of Nuclear Materials*, 334(2):166 – 168, 2004.

[29] G. H. Kinchin and R. S. Pease. The displacement of atoms in solids by radiation. *Reports on Progress in Physics*, 18(1):1–51, 1955.

[30] M. J. Norgett, M. T. Robinson, and I. M. Torrens. A proposed method of calculating displacement dose rates. *Nuclear Engineering Design*, 33(1):50–54, 1975.

[31] E. Young, J. Young, H. Side, B. O'Brien, and K. Samra. Irradiation of reactor pressure vessel steels: A study on irradiation induced damage in the context of precipitation and embrittlement, 2016.

[32] I. Jones. Irradiation materials science lectures, 2017.

[33] M. Novovic. Nuclear reactor life extension lectures, 2017.

[34] J. Linke, J. Du, T. Loewenhoff, G. Pintsuk, B. Spilke, I. Steudel, and M. Wirtz. Challenges for plasma-facing components in nuclear fusion. *Matter and Radiation at Extremes*, 4:056201, 2018.

[35] A. Hasegawa, M. Fukuda, S. Nogami, and K. Yabuuchi. Neutron irradiation effects on tungsten materials. *Fusion Engineering and Design*, 89(7):1568 – 1572, 2014. Proceedings of the 11th International Symposium on Fusion Nuclear Technology-11 (ISFNT-11) Barcelona, Spain, 15-20 September, 2013.

[36] T. Tanno, A. Hasegawa, J.C. He, M. Fujiwara, M. Satou, S. Nogami, K. Abe, and T. Shishido. Effects of transmutation elements on the microstructural evolution and electrical resistivity of neutron-irradiated tungsten. *Journal of Nuclear Materials*, 386-388:218 – 221, 2009.

[37] M. Fukuda, K. Yabuuchi, S. Nogami, A. Hasegawa, and T. Tanaka. Microstructural development of tungsten and tungsten–rhenium alloys due to neutron irradiation in hfir. *Journal of Nuclear Materials*, 455(1):460 – 463, 2014. Proceedings of the 16th International Conference on Fusion Reactor Materials (ICFRM-16).

[38] Y.-W. You, X.-S. Kong, X. Wu, C.S. Liu, Q.F. Fang, J.L. Chen, and G.-N. Luo. Clustering of transmutation elements tantalum, rhenium and osmium in tungsten in a fusion environment. *Nuclear Fusion*, 57(8):086006, 2017.

[39] F. Bergner, F. Gillemot, M. Hernandez-Mayoral, M. Serrano, G. Torok, A. Ulbricht, and E. Altstadt. Contributions of cu-rich clusters, dislocation loops and nanovoids to the irradiation-induced hardening of cu-bearing low-ni reactor pressure vessel steels. *Journal of Nuclear Materials*, 461, 06 2015.

[40] G. R. Odette, C. L. Liu, and B. D. Wirth. On the composition and structure of nanoprecipitates in irradiated pressure vessel steels. *Materials Research Society Proceedings*, 439:457–469, 1997.

[41] B. D Wirth, G. R. Odette, W. A. Pavinich, G. E Lucas, and S. E. Spooner. Small angle neutron scattering study of linde 80 rpv welds. In *Effects of Radiation on Materials: 18th International Symposium*, pages 102–121. ASTM International, 1999.

[42] M.J. Konstantinovic, I. Uytdenhouwen, G. Bonny, N. Castin, L. Malerba, and P. Efsing. Radiation induced solute clustering in high-ni reactor pressure vessel steel. *Acta Materialia*, 179, 08 2019.

[43] A. D. LeClaire and G. Neumann. Landolt-börnstein - group iii condensed matter volume 26: Diffusion in solid metals and alloys, 1990.

[44] H. Mehrer, N. Stolica, and N. A. Stolwijk. Landolt-börnstein - group iii condensed matter volume 26: Diffusion in solid metals and alloys, 1990.

[45] P. J. Othen, M. L. Jenkins, G. D. W. Smith, and W. J. Phythian. Transmission electron microscope investigations of the structure of copper precipitates in thermally-aged fe—cu and fe—cu—ni. *Philosophical Magazine Letters*, 64(6):383–391, 1991.

[46] S. C Glade, B. D Wirth, G. R Odette, P Asoka-Kumar, P. A Sterne, and R. H Howell. Positron annihilation spectroscopy and small-angle neutron scattering characterization of the effect of mn on the nanostructural features formed in irradiated fe-cu-mn alloys. *Philosophical Magazine*, 85(4-7):629–639, 2005.

[47] X. Liu, Y. Li, C. Xu, F. Xue, W. Qian, and P. Huang. Cu precipitation behaviour in long-term thermally aged, high-copper model reactor pressure vessel steels. In *IOP Conference Series: Earth and Environmental Science, Volume 440, Material Application and Chemical Engineering*, volume 440, page 022061, 2020.

[48] Liang Chen, Kenji Nishida, Kenta Murakami, Li Liu, Tomohiro Kobayashi, Zhengcao Li, and Naoto Sekimura. Effects of solute elements on microstructural evolution in fe-based alloys during neutron irradiation following thermal ageing. *Journal of Nuclear Materials*, 498:259–268, January 2018.

[49] A. V. Barashev and A. C. Arokiam. Monte carlo modelling of cu atom diffusion in α-fe via the vacancy mechanism. *Philosophical Magazine Letters*, 86(5):321–332, 2006.

[50] F. Bergner, M. Lambrecht, A. Ulbricht, and A. Almazouzi. Comparative small-angle neutron

scattering study of neutron-irradiated fe, fe-based alloys and a pressure vessel steel. *Journal of Nuclear Materials*, 399(2):129 – 136, 2010.

[51] F. Christien and A. Barbu. Modelling of copper precipitation in iron during thermal aging and irradiation. *Journal of Nuclear Materials*, 324:90–96, 01 2004.

[52] K. Fukuya, K. Ohno, H. Nakata, S. Dumbill, and J. M. Hyde. Microstructural evolution in medium copper low alloy steels irradiated in a pressurized water reactor and a material test reactor. *Journal of Nuclear Materials*, 312(2):163–173, February 2003.

[53] Li Liu, Kenji Nishida, Kenji Dohi, Akiyoshi Nomoto, Naoki Soneda, Kenta Murakami, Zhengcao Li, Dongyue Chen, and Naoto Sekimura. Effects of solute elements on hardening and microstructural evolution in neutron-irradiated and thermally-aged reactor pressure vessel model alloys. *Journal of Nuclear Science and Technology*, 53(10):1546–1553, 2016.

[54] P. Styman, J. Hyde, A. Morley, K. Wilford, N. Riddle, and G.D.W. Smith. The effect of ni on the microstructural evolution of high cu reactor pressure vessel steel welds after thermal ageing for up to 100,000h. *Materials Science and Engineering: A*, 736:111–119, 2018.

[55] G. Solt, F. Frisius, W. B. Waeber, and P. Tipping. Irradiation induced precipitation in model alloys with systematic variation of cu, ni and p content: A small angle neutron scattering study. In *Effects of Radiation on Materials: Sixteenth International Symposium*, pages 444–461. ASTM International, 1994.

[56] F. Bergner, A. Ulbricht, P. Lindner, U. Keiderling, and L. Malerba. Post-irradiation annealing behavior of neutron-irradiated fecu, femnni and femnnicu model alloys investigated by means of small-angle neutron scattering. *Journal of Nuclear Materials*, 454(1):22 – 27, 2014.

[57] M. Hasegawa, Z. Tang, Y. Nagai, T. Chiba, E. Kuramoto, and M. Takenaka. Irradiation-induced vacancy and cu aggregations in fe-cu model alloys of reactor pressure vessel steels: state-of-the-art positron annihilation spectroscopy. *Philosophical Magazine*, 85(4-7):467–478, 2005.

[58] M. Fukuda, A. Hasegawa, T. Tanno, S. Nogami, and H. Kurishita. Property change of advanced tungsten alloys due to neutron irradiation. *Journal of Nuclear Materials*, 442(1, Supplement 1):S273 – S276, 2013.

[59] J.C. He, G.Y. Tang, A. Hasegawa, and K. Abe. Microstructural development and irradiation hardening of w-re alloys after high temperature neutron irradiation to 0.15dpa. *Nuclear Fusion*, 46(11):877, 2006.

[60] P.D. Styman, J.M. Hyde, K. Wilford, A. Morley, and G.D.W. Smith. Precipitation in long term thermally aged high copper, high nickel model rpv steel welds. *Progress in Nuclear Energy*, 57:86 – 92, 2012. Nuclear Materials: Selected articles from the E-MRS 2011 Spring Meeting.

[61] W. J. Phythian, A. J. E. Foreman, C. A. English, J. T. Buswell, M. Hetherington, K. Roberts, and S. Pizzini. The structure and hardening mechanism of copper precipitation in thermally aged or irradiated fe-cu and fe-cu-ni model alloys. In *Effects of Radiation on Materials: 15th International Symposium*, pages 131–150. ASTM International, 1992.

[62] J. Hyde, R.M. Boothby, C. English, P. Styman, H. Thompson, G. Smith, K. Wilford, and T. J. Williams. Microstructural characterisation of nanometre scale irradiation damage in high-ni welds. In *Supplemental Proceedings: Materials Properties, Characterization, and Modeling, Volume 2*, volume 2, pages 487–502, 06 2012.

[63] P Asoka-Kumar, B.D Wirth, P.A Sterne, R.H Howell, and G.R Odette. Composition and magnetic character of nanometre-size cu precipitates in reactor pressure vessel steels: Implications for nuclear power plant lifetime extension. *Philosophical magazine letters*, 82(11):609–615, 2002.

[64] M. Schober, E. Eidenberger, H. Leitner, P. Staron, D. Reith, and R. Podloucky. A critical consideration of magnetism and composition of (bcc) cu precipitates in (bcc) fe. *Applied Physics / A (Series A, Materials Science & Processing)*, pages 697–704, 2010.

[65] International Atomic Energy Agency. *Regulations for the Safe Transport of Radioactive Material.* Number SSR-6 in IAEA Safety Standards Series. International Atomic Energy Agency, Vienna, 2012.

[66] M.K. Miller, M.A. Sokolov, R.K. Nanstad, and K.F. Russell. Apt characterization of high nickel rpv steels. *Journal of Nuclear Materials*, 351(1):187 – 196, 2006. Proceedings of the Symposium on Microstructural Processes in Irradiated Materials.

[67] M.K. Miller, K.A. Powers, R.K. Nanstad, and P. Efsing. Atom probe tomography characterizations

of high nickel, low copper surveillance rpv welds irradiated to high fluences. *Journal of Nuclear Materials*, 437(1):107 – 115, 2013.

[68] S. Shu, P. B. Wells, N. Almirall, G. R. Odette, and D. D. Morgan. Thermodynamics and kinetics of core-shell versus appendage co-precipitation morphologies: An example in the fe-cu-mn-ni-si system. *Acta Materialia*, 157:298–306, 2018.

[69] M.K. Miller and K.F. Russell. Embrittlement of rpv steels: An atom probe tomography perspective. *Journal of Nuclear Materials*, 371(1-3):145–160, 2007.

[70] K. Fujii and K. Fukuya. Irradiation-induced microchemical changes in highly irradiated 316 stainless steel. *Journal of Nuclear Materials*, 469:82 – 88, 2016.

[71] J.M. Hyde, M.G. Burke, G.D.W. Smith, P. Styman, H. Swan, and K. Wilford. Uncertainties and assumptions associated with apt and sans characterisation of irradiation damage in rpv steels. *Journal of Nuclear Materials*, 449(1):308 – 314, 2014.

[72] S. Lozano-Perez, J. M. Titchmarsh, and M. L. Jenkins. Determination of the fe content of embedded cu-rich particles in ferritic alloys using energy-filtered tem. *Ultramicroscopy*, 106(2):75–91, 2006.

[73] R. Pynn. Neutron scattering: A primer, 1990.

[74] T. Chatterji. *Neutron scattering from magnetic materials*. Elsevier, 2006.

[75] A. Jackson. Introduction to small-angle neutron scattering and neutron reflectometry, 2008.

[76] I. Grillo. *Small-Angle Neutron Scattering and Applications in Soft Condensed Matter*, pages 723–782. Springer Netherlands, 2008.

[77] B. Hammouda. Sans toolbox, 2010.

[78] G. L. Squires. *Introduction to the Theory of Thermal Neutron Scattering*. Cambridge University Press, 3 edition, 2012.

[79] V. F. Sears. Neutron scattering lengths and cross sections. *Neutron News*, 3(3):26–37, 1992.

[80] T. Saerbeck. Chapter three - magnetic exchange phenomena probed by neutron scattering. In

Robert E. Camley and Robert L. Stamps, editors, *Solid State Physics*, volume 65, pages 237–352. Academic Press, 2014.

[81] O. Halpern and M. H. Johnson. On the magnetic scattering of neutrons. *Physical Review*, 55:898–923, 1939.

[82] A. Michels. Magnetic small-angle neutron scattering of bulk ferromagnets. *Journal of Physics: Condensed Matter*, 26(38), 2014.

[83] C. Kittel. Introduction to solid state physics, 2005.

[84] H. Danan, A. Herr, and A.J.P Meyer. New determinations of the saturation magnetization of nickel and iron. *Journal of Applied Physics*, 39(2):669–670, 1968.

[85] G. E. Bacon and J. S. Plant. The neutron-scattering amplitude of potassium. *Zeitschrift fur Kristallographie - Crystalline Materials*, 126(1-6):460–461, 1968.

[86] D. T. Cromer and D. Liberman. Relativistic calculation of anomalous scattering factors for x rays. *Journal of Chemical Physics*, 53(5):1981–1898, 1970.

[87] H. B. Stuhrmann. Anomalous small angle scattering. *Quarterly Reviews of Biophysics*, 14(3):433–462, 1981.

[88] Armin Hoell, Dragomir Tatchev, Sylvio Haas, Jörg Haug, and Peter Boesecke. On the determination of partial structure functions in small-angle scattering exemplified by al89ni6la5 alloy. *Journal of applied crystallography*, 42(2):323–325, 2009.

[89] J. Potton, G. Daniell, and B. Rainford. Particle size distributions from sans data using the maximum entropy method. *Journal of Applied Crystallography*, 21(6):663–668, 1988.

[90] J. Potton, G. Daniell, and B. Rainford. A new method for the determination of particle size distributions from sans measurements. *Journal of Applied Crystallography*, 21(6):891–897, 1988.

[91] S. Martelli and P. Emilio Di Nunzio. Particle size distribution of nanospheres by Monte Carlo fitting of SAXS curves. *Particle and Particle Systems Characterization*, 19(6):247–255, 2002.

[92] B. R. Pauw, J. S. Pedersen, S. J. Tardif, M. Takatab, and B. B. Iversena. Improvements and

considerations for size distribution retrieval from small-angle scattering data by Monte Carlo methods. *Journal of Applied Crystallography*, 46:365–371, 2013.

[93] A. F. Thünemann I. Bressler, B. R. Pauw. Mcsas: software for the retrieval of model parameter distributions from scattering patterns. *Journal of Applied Crystallography*, 48:962–969, 2015.

[94] S. R. Kline. Reduction and analysis of sans and usans data using igor pro. *Journal of Applied Crystallography*, 39:895, 2006.

[95] P. R. Jemian J. Ilavsky. Irena: tool suite for modeling and analysis of small-angle scattering. *Journal of Applied Crystallography*, 42:347–353, 2009.

[96] Heinz Maier-Leibnitz Zentrum et al. Sans-1: Small angle neutron scattering. *Journal of large-scale research facilities*, 1:A10, 2015.

[97] Institut Laue-Langevin. D22 - large dynamic range small-angle diffractometer.

[98] N. M. Kirby, S. T. Mudie, A. M. Hawley, D. J. Cookson, H. D. Mertens, N. Cowieson, and V. Samardzic-Boban. A low-background-intensity focusing small-angle x-ray scattering undulator beamline. *Journal of Applied Crystallography*, 46(6):1670–1680, 2013.

[99] Australian Synchrotron ANSTO. Saxs/waxs technical information, 2019.

[100] J. S. Pedersen. Analysis of small-angle scattering data from colloids and polymer solutions: modeling and least-squares fitting. *Advances in Colloid and Interface Science*, 70:171–210, 1997.

[101] Xiaodong Li and Bharat Bhushan. A review of nanoindentation continuous stiffness measurement technique and its applications. *Materials Characterization*, 48(1):11–36, 2002.

[102] G.M. Pharr and W.C. Oliver. Measurement of thin film mechanical properties using nanoindentation. *MRS Bulletin*, 17(7):28–33, 1992.

[103] W.C. Oliver and G.M. Pharr. An improved technique for determining hardness and elastic modulus using load and displacement sensing indentation experiments. *Journal of Materials Research*, 7(6):1564–1583, 1992.

[104] A.C. Fischer-Cripps. *Nanoindentation*. Mechanical Engineering Series. Springer New York, 2011.

[105] MatWeb Material Property Data. Material property data sheet: Tungsten, 2021.

[106] C. A. Schneider, W. S. Rasband, and K. W. Eliceiri. ImageJ: 25 years of image analysis. *Nature Methods*, 9:671–675, 2012.

[107] Paul Scherrer Institute. Magnetic small-angle neutron scattering, 2012.

[108] K. Krycka, A. Jackson, and C. Dennis. Magnetic structure of iron oxide nanoparticles using sans, 2010.

[109] C. Dewhurst. Grasp software package, 2019.

[110] A. J. Allen, F. Zhang, R. J. Kline, W. F. Guthrie, and J. Ilavsky. Nist standard reference material 3600: Absolute intensity calibration standard for small-angle x-ray scattering. *Journal of Applied Crystallography*, 50:462–473, 2017.

[111] D.-G. Park, K. Mb, K.-H. Kim, N.H. Lee, D.H. Lee, S. Kobayashi, and D. Son. The effects of nano-sized defects on the magnetic properties in thermal aged fe–cu alloys. *IEEE Transactions on Magnetics*, 50:1–3, 2014.

[112] P. J. Othen, M. L. Jenkins, and G. D. W. Smith. High-resolution electron microscopy studies of the structure of cu precipitates in α-fe. *Philosophical Magazine A*, 70(1):1–24, 1994.

[113] A. Deschamps, M. Militzer, and W. J. Poole. Precipitation kinetics and strengthening of a fe-0.8wt%cu alloy. *ISIJ International*, 41(2):196–205, 2001.

[114] E. T. Jaynes. Information theory and statistical mechanics i. *Physical Review*, 106:620–630, 1957.

[115] E. T. Jaynes. Information theory and statistical mechanics ii. *Physical Review*, 108:171–190, 1957.

[116] A. Etienne, B. Radiguet, and P. Pareige. Understanding silicon-rich phase precipitation under irradiation in austenitic stainless steels. *Journal of Nuclear Materials*, 406(2):251 – 256, 2010.

[117] R. K. Desu, H. N. Krishnamurthy, A. Balu, A. K. Gupta, and S. K. Singh. Mechanical properties of austenitic stainless steel 304l and 316l at elevated temperatures. *Journal of Materials Research and Technology*, 5(1):13 – 20, 2016.

[118] J. Hyde and K. Wilford. Correlating irradiation-induced solute clustering with changes of hardness in low and high flux reactor pressure vessel steels. *Microscopy and Microanalysis*, 23:632–633, 07 2017.

[119] E.H. Lee, P.J. Maziasz, and A.F. Rowcliffe. Structure and composition of phases occurring in austenitic stainless steels in thermal and irradiation environments, 1 1980.

[120] D.L. Porter. Irradiation-induced microstructural changes in neutron-irradiated cold-worked and aged type 316 stainless steel. *Journal of Nuclear Materials*, 92(1):155 – 159, 1980.

[121] W. Zhong, Z. Tong, G. Ning, C. Zhang, H. Lin, and W. Yang. The fatigue behavior of irradiated reactor pressure vessel steel. *Engineering Failure Analysis*, 82, 08 2017.

[122] T. Takeuchi, J. Kameda, Y. Nagai, T. Toyama, Y. Matsukawa, Y. Nishiyama, and K. Onizawa. Microstructural changes of a thermally aged stainless steel submerged arc weld overlay cladding of nuclear reactor pressure vessels. *Journal of Nuclear Materials*, 425(1):60 – 64, 2012. Microstructure Properties of Irradiated Materials.

[123] J. Young. Radiation damage in reactor pressure vessel (rpv) steels: a study of irradiation induced precipitates, 2017.

[124] S. Samothrakitis. Paper in preparation, 2017.

[125] M. Rabung and K. Pranzas. Characterization of copper precipitates in fe-cu alloys with small-angle neutron scattering, 2004.

[126] T. Chairuangsri and D. V. Edmonds. The precipitation of copper in abnormal ferrite and pearlite in hyper-eutectoid steels. *Acta Materialia*, 48:3931–3949, 2000.

[127] G. Was, Z. Jiao, A. Van der ven, S. Bruemmer, and D. Edwards. Aging and embrittlement of high fluence stainless steels, 12 2012.

[128] G. R. Odette and B. D. Wirth. A computational microscopy study of nanostructural evolution in irradiated pressure vessel steels. *Journal of Nuclear Materials*, 251:157 – 171, 1997.

[129] D. Chen, K. Murakami, K. Dohi, K. Nishida, T. Ohnuma, N. Soneda, Z. Li, L. Liu, and N. Sekimura. First-principles investigation on the composition of ni-si precipitates formed in irradiated stainless steels. *Journal of Nuclear Materials*, 494:354 – 360, 2017.

[130] D.J.M. King, P.A. Burr, S.C. Middleburgh, T.M. Whiting, M.G. Burke, and M.R. Wenman. The

formation and structure of fe-mn-ni-si solute clusters and g-phase precipitates in steels. *Journal of Nuclear Materials*, 505:1 – 6, 2018.

[131] B. Ingham, N. Kirby, C. Wang, M. Brady, and A. Carr. Elemental fingerprinting of mineral species in iron-fortified milk: anomalous small-angle x-ray scattering and resonant soft x-ray scattering studies. *Journal of Synchrotron Radiation*, 25(4):1106–1112, 2018.

[132] G. Yeli, M. A. Auger, K. Wilford, G. D. W. Smith, P. A. J. Bagot, and M. P. Moody. Sequential nucleation of phases in a 17-4ph steel: Microstructural characterisation and mechanical properties. *Acta Materialia*, 125:38 – 49, 2017.

[133] S. Samothrakitis. Neutron and x-ray scattering studies of fe-based materials, 2018.

[134] S. Muhlbauer, D. Honecker, E. A. Perigo, F. Bergner, S. Disch, A. Heinemann, S. Erokhin, D. Berkov, C. Leighton, M. R. Eskildsen, and A. Michels. Magnetic small-angle neutron scattering. *Reviews of Modern Physics*, 91, 2019.

[135] J. Ilavsky. Nika: software for two-dimensional data reduction. *Journal of Applied Crystallography*, 45:324–328, 2012.

[136] M.K. Miller, B.D. Wirth, and G.R. Odette. Precipitation in neutron-irradiated fe–cu and fe–cu–mn model alloys: a comparison of apt and sans data. *Materials Science and Engineering: A*, 353(1):133–139, 2003. 47 th International Field Emission Symposium.

[137] A. K. Seeger. On the theory of radiation damage and radiation hardening. In *Proceedings of the Second UN Conference on Peaceful Uses of Atomic Energy*, volume 6, page 250, 1958.

[138] S.J Zinkle and Y Matsukawa. Observation and analysis of defect cluster production and interactions with dislocations. *Journal of Nuclear Materials*, 329-333:88–96, 2004. Proceedings of the 11th International Conference on Fusion Reactor Materials (ICFRM-11).

[139] G.E. Lucas. An evolution of understanding of reactor pressure vessel steel embrittlement. *Journal of Nuclear Materials*, 407(1):59–69, 2010.

[140] B.M. Jenkins, P.D. Styman, N. Riddle, P.A.J. Bagot, M.P. Moody, G.D.W. Smith, and J.M. Hyde.

Observation of mn-ni-si-rich features in thermally-aged model reactor pressure vessel steels. *Scripta Materialia*, 191:126–130, 2021.

[141] T. Toyama, F. Takahama, A. Kuramoto, H. Takamizawa, Y. Nozawa, N. Ebisawa, M. Shimodaira, Y. Shimizu, K. Inoue, and Y. Nagai. The diffusivity and solubility of copper in ferromagnetic iron at lower temperatures studied by atom probe tomography. *Scripta Materialia*, 83:5–8, 2014.

[142] G. Cacciamani, J. De Keyzer, R. Ferro, U.E. Klotz, J. Lacaze, and P. Wollants. Critical evaluation of the fe–ni, fe–ti and fe–ni–ti alloy systems. *Intermetallics*, 14(10):1312–1325, 2006. EUROMAT 2005 "European Congress on Advanced Materials and Processes".

[143] V. T. Witusiewicz, F. Sommer, and E. J. Mittemeijer. Reevaluation of the fe-mn phase diagram. *Journal of Phase Equilibria and Diffusions*, 25(4):346–354, 2004.

[144] E. D. Eason, G. R. Odette, R. K. Nanstad, and T. Yamamoto. A physically based correlation of irradiation-induced transition temperature shifts for rpv steels, 2006.

[145] E. A Brandes and G. B. Brook. Chapter 11 - equilibrium diagrams. In W.F. Gale and T.C. Totemeier, editors, *Smithells Metals Reference Book (Eighth Edition)*, pages 11–1–11–534. Butterworth-Heinemann, Oxford, eighth edition edition, 2004.

[146] P. Auger, P. Pareige, M. Akamatsu, and D. Blavette. Apfim investigation of clustering in neutron-irradiated fecu alloys and pressure vessel steels. *Journal of Nuclear Materials*, 225:225–230, 1995.

[147] M. K. Miller and P. Pareige. Atomic level characterization of neutron irradiated pressure vessel steels. *Materials Research Society Proceedings*, 650:R6.1, 2000.

[148] Y. Nagai, M. Hasegawa, Z. Tang, A. Hempel, K. Yubuta, T. Shimamura, Y. Kawazoe, A. Kawai, and F. Kano. Positron confinement in ultrafine embedded particles: Quantum-dot-like state in an fe-cu alloy. *Phys. Rev. B*, 61:6574–6578, Mar 2000.

[149] E. Vincent, C.S. Becquart, C. Pareige, P. Pareige, and C. Domain. Precipitation of the fecu system: A critical review of atomic kinetic monte carlo simulations. *Journal of Nuclear Materials*, 373(1):387–401, 2008.

[150] S. R. Goodman, S. S. Brenner, and J. R. Low. An fim-atom probe study of the precipitation of copper from iron-1.4 at.% copper. part i: Field-ion microscopy. *Metallurgical Transactions*, 4:2363–2369, 1973.

[151] K. Osamura, H. Okuda, M. Takashima, K. Asano, and M. Furusaka. Small-angle neutron scattering study of phase decomposition in fe-cu binary alloy. *Materials Transactions, JIM*, 34(4):305–311, 1993.

[152] C.L. Liu, G.R. Odette, B.D. Wirth, and G.E. Lucas. A lattice monte carlo simulation of nanophase compositions and structures in irradiated pressure vessel fe-cu-ni-mn-si steels. *Materials Science and Engineering: A*, 238(1):202–209, 1997. Microstructure Evolution in Bulk Phases F.

[153] G. J. Dienes and A. C. Damask. Radiation enhanced diffusion in solids. *Journal of Applied Physics*, 29(12):1713–1721, 1958.

[154] Y. Nagai, Z. Tang, M. Hassegawa, T. Kanai, and M. Saneyasu. Irradiation-induced cu aggregations in fe: An origin of embrittlement of reactor pressure vessel steels. *Phys. Rev. B*, 63:134110, Mar 2001.

[155] Frédéric Soisson and Chu-Chun Fu. Cu-precipitation kinetics in $\alpha-$Fe from atomistic simulations: Vacancy-trapping effects and cu-cluster mobility. *Phys. Rev. B*, 76:214102, Dec 2007.

[156] Yaroslav I. Shtrombakh, Boris A. Gurovich, Evgenia A. Kuleshova, Dmitry A. Maltsev, Svetlana V. Fedotova, and Anna A. Chernobaeva. Thermal ageing mechanisms of vver-1000 reactor pressure vessel steels. *Journal of Nuclear Materials*, 452(1):348–358, 2014.

[157] M. Charleux, F. Livet, F. Bley, F. Louchet, and Y. Bréchet. Thermal ageing of an fe–cu alloy: Microstructural evolution and precipitation hardening. *Philosophical Magazine A*, 73(4):883–897, 1996.

[158] Yong Dai and Pierre Marmy. Charpy impact tests on martensitic/ferritic steels after irradiation in sinq target-3. *Journal of Nuclear Materials*, 343(1):247–252, 2005. Proceedings of the 6th International Workshop on Spallation Materials Technology.

[159] G.E Lucas. The evolution of mechanical property change in irradiated austenitic stainless steels. *Journal of nuclear materials*, 206(2):287–305, 1993.

[160] O. Chopra, E. E. Gruber, and W. J. Shack. Fracture toughness and crack growth rates of irradiated austenitic stainless steels. In *U.S. Department of Energy Office of Scientific and Technical Information Report*, 2003.

[161] D. J. Bacon, U. F. Kocks, and R. O. Scattergood. The effect of dislocation self-interaction on the orowan stress. *The Philosophical Magazine: A Journal of Theoretical Experimental and Applied Physics*, 28(6):1241–1263, 1973.

[162] Z. Zhang, C. T. Liu, M. K. Miller, X. Wang, Y. Wen, T. Fujita, A. Jirate, M. Chen, G. Chen, and B. A. Chin. A nanoscale co-precipitation approach for property enhancement of fe-base alloys. *Scientific Reports*, 3:1327, 2013.

[163] Jiu Zhou Zhao and Qing Liang Wang. Microstructure evolution during thermal aging of fe-cu alloys. In *Key Engineering Materials II*, volume 488 of *Advanced Materials Research*, pages 164–168. Trans Tech Publications Ltd, 4 2012.

[164] D. G. Park, K. S. Ryu, S. Kobayashi, S. Takahashi, and Y. M. Cheong. Change in magnetic properties of a cold rolled and thermally aged fe–cu alloy. *Journal of Applied Physics*, 107(9):09A330, 2010.

[165] S. R. Kline. Reduction and analysis of SANS and USANS data using IGOR Pro. *Journal of Applied Crystallography*, 39(6):895–900, 2006.

[166] Toshiharu Ohnuma, Naoki Soneda, and Misako Iwasawa. First-principles calculations of vacancy–solute element interactions in body-centered cubic iron. *Acta Materialia*, 57(20):5947–5955, 2009.

[167] A. Barbu, Marie-Hélène Mathon, F. Maury, J. Belliard, B. Beuneu, and C. Novion. A comparison of the effect of electron irradiation and of thermal aging on the hardness of fecu binary alloys. *Journal of Nuclear Materials*, 257:206–211, 11 1998.

[168] AZO Materials. The properties and effects of manganese as an alloying element, 2016.

[169] N. Hashimoto, T. S. Byun, K. Farrell, and S. J. Zinkle. Deformation microstructure of neutron-irradiated pure polycrystalline metals. *Journal of Nuclear Materials*, 329-333:947–952, August 2004.

[170] Yoshitaka Matsukawa. *Crystallography of Precipitates in Metals and Alloys: (2) Impact of Crystallography on Precipitation Hardening*, chapter 3, pages 1–19. Intech Open, 02 2019.

[171] The Nickel Institute. The nickel advantage, 2021.

[172] P.J. Karditsas, G. Lloyd, M. Walters, and A. Peacock. The european fusion material properties database. *Fusion Engineering and Design*, 81(8):1225–1229, 2006. Proceedings of the Seventh International Symposium on Fusion Nuclear Technology.

[173] Michael Gorley, Eberhard Diegele, Ermile Gaganidze, Ferenc Gillemot, Gerald Pintsuk, Frank Schoofs, and Ildiko Szenthe. The eurofusion materials property handbook for demo in-vessel components—status and the challenge to improve confidence level for engineering data. *Fusion Engineering and Design*, 158:111668, 2020.

[174] EUROFusion. The demonstration power plant: DEMO, 2021. https://www.euro-fusion.org/programme/demo/.

[175] M.R. Gilbert, S.L. Dudarev, S. Zheng, L.W. Packer, and J.-Ch. Sublet. An integrated model for materials in a fusion power plant: transmutation, gas production, and helium embrittlement under neutron irradiation. *Nuclear Fusion*, 52(8):083019, 2012.

[176] R. Prokopec, D. X. Fischer, H. W. Weber, and M. Eisterer. Suitability of coated conductors for fusion magnets in view of their radiation response. *Superconductor Science and Technology*, 28(1):014005, dec 2014.

[177] N Long, N Strickland, B Chapman, N Ross, J Xia, X Li, W Zhang, T Kodenkandath, Y Huang, and M Rupich. Enhanced in-field critical currents of YBCO second-generation (2g) wire by dy additions. *Superconductor Science and Technology*, 18(12):S405–S408, nov 2005.

[178] N. M. Strickland. Qualifying high-temperature superconductors for fusion reactors. *Superconductor Science and Technology*, 34(11):110502, oct 2021.

[179] F. Guern, Werner Gulden, Sergio Ciattaglia, Glenn Counsell, A. Bengaouer, Jerome Brinster, Frederic Dabbene, A. Denkevitz, Thomas Jordan, M.T. Porfiri, Reinhard Redlinger, Philippe Roblin, J. Roth, J. Segré, K. Sugiyama, Isabelle Tkatschenko, and Zhanjie Xu. F4e r&d

programme and results on in-vessel dust and tritium. *Fusion Engineering and Design*, 86:2753–2757, 2011.

[180] Sungbo Moon, Soo Lim, and In Cheol Bang. Analysis of hydrogen and dust explosion after vacuum vessel rupture: Preliminary safety analysis of korean fusion demonstration reactor using melcor. *International Journal of Energy Research*, 42, 2017.

[181] T. Yamashina and T. Hino. Characterization of graphite as fusion first wall material and evaluation of stability against plasmas. *Journal of Nuclear Science and Technology*, 27(7):589–600, 1990.

[182] G F Matthews, M Beurskens, S Brezinsek, M Groth, E Joffrin, A Loving, M Kear, M-L Mayoral, R Neu, P Prior, V Riccardo, F Rimini, M Rubel, G Sips, E Villedieu, P de Vries, and M L Watkins and. JET ITER-like wall—overview and experimental programme. *Physica Scripta*, T145:014001, 2011.

[183] Y. Ueda, K. Schmid, M. Balden, J.W. Coenen, Th. Loewenhoff, A. Ito, A. Hasegawa, C. Hardie, M. Porton, and M. Gilbert. Baseline high heat flux and plasma facing materials for fusion. *Nuclear Fusion*, 57(9):092006, 2017.

[184] M.R. Gilbert and J.-Ch. Sublet. Neutron-induced transmutation effects in w and w-alloys in a fusion environment. *Nuclear Fusion*, 51(4):043005, 2011.

[185] R.G. Abernethy. Predicting the performance of tungsten in a fusion environment: a literature review. *Materials Science and Technology*, 33(4):388–399, 2017.

[186] M. Klimenkov, U. Jäntsch, M. Rieth, H.C. Schneider, D.E.J. Armstrong, J. Gibson, and S.G. Roberts. Effect of neutron irradiation on the microstructure of tungsten. *Nuclear Materials and Energy*, 9:480 – 483, 2016.

[187] Alan Xu, David E.J. Armstrong, Christian Beck, Michael P. Moody, George D.W. Smith, Paul A.J. Bagot, and Steve G. Roberts. Ion-irradiation induced clustering in w-re-ta, w-re and w-ta alloys: An atom probe tomography and nanoindentation study. *Acta Materialia*, 124:71 – 78, 2017.

[188] Yoshiyuki Nemoto, Akira Hasegawa, Manabu Satou, and Katsunori Abe. Microstructural development of neutron irradiated w–re alloys. *Journal of Nuclear Materials*, 283-287:1144 – 1147, 2000. 9th Int. Conf. on Fusion Reactor Materials.

[189] Takashi Tanno, Akira Hasegawa, Jian-Chao He, Mitsuhiro Fujiwara, Shuhei Nogami, Manabu Satou, Toetsu Shishido, and Katsunori Abe. Effects of transmutation elements on neutron irradiation hardening of tungsten. *Materials Transactions*, 48(9):2399–2402, 2007.

[190] M. Dürrschnabel, M Klimenkov, U. Jäntsch, M. Rieth, H. C. Schneider, and D. Terentyev. New insights into microstructure of neutron-irradiated tungsten. *Scientific Reports*, 11:7572, 2021.

[191] A. Taylor, B.J. Kagle, and N.J. Doyle. The constitution diagram of the tungsten-osmium binary system. *Journal of the Less Common Metals*, 3(4):333 – 347, 1961.

[192] J. Wharry, M. Swenson, C. Dolph, and K. Yano. Evolution of yield strength of fe-9irradiation. *Transactions of the American Nuclear Society*, 114:1255–1257, 06 2016.

[193] I. Ipatova, R. W. Harrison, S. E. Donnelly, M. J. D. Rushton, S. C. Middleburgh, and E. Jimenez-Melero. Void evolution in tungsten and tungsten-5wt.% tantalum under in-situ proton irradiation at 800 and 1000 °c. *Journal of Nuclear Materials*, 526:151730, 2019.

[194] C.M. Logan, J.D. Anderson, and A.K. Mukherjee. Proton simulation of displacement effects induced in metals by 14 mev neutrons. *Journal of Nuclear Materials*, 48(3):223–232, 1973.

[195] G.S Was, J.T Busby, Todd Allen, E.A Kenik, A Jensson, S.M Bruemmer, J. Gan, A.D Edwards, P.M Scott, and P.L Andreson. Emulation of neutron irradiation effects with protons: Validation of principle. *Journal of Nuclear Materials*, 300:198–216, 02 2002.

[196] Goodfellow. Global material supplier.

[197] ASTM International. Astm e521-16, standard practice for investigating the effects of neutron radiation damage using charged-particle irradiation, 2016.

[198] Birmingham Centre for Nuclear Education and Research. Mc40 cyclotron facility.

[199] R. Rayaprolu, S. Möller, Ch. Linsmeier, and S. Spellerberg. Simulation of neutron irradiation damage in tungsten using higher energy protons. *Nuclear Materials and Energy*, 9:29 – 35, 2016.

[200] J. F. Ziegler. Srim software package, 2013.

[201] R. Stoller, M. Toloczko, G. Was, A. Certain, S. Dwaraknath, and F. Garner. On the use of srim

for computing radiation damage exposure. *Nuclear Instruments and Methods in Physics Research Section B: Beam Interactions with Materials and Atoms*, 310:75 – 80, 2013.

[202] M. Jaser and T. Oda. Evaluation of threshold displacement energy in tungsten. In *Transactions of the Korean Nuclear Society Autumn Meeting*, 10 2016.

[203] K. S. Krane. *Introductory Nuclear Physics.* John Wiley & Sons, 1998.

[204] E. Dupont N. Soppera, M. Bossant. Janis 4: an improved version of the nea java-based nuclear data information system. *Nuclear Data Sheets*, 120:294–296, 2014.

[205] National Nuclear Decay Chart. Nudat2.8: Chart of nuclides.

[206] United Kingdom Atomic Energy Authority. Fispact-ii.

[207] A. J. Koning, D. Rochman, J. Kopecky, J. Ch. Sublet, E. Bauge, S. Hilaire, P. Romain, B. Morillon, H. Duarte, S. van der Marck, S. Pomp, H. Sjostrand, R. Forrest, H. Henriksson, O. Cabellos, S. Goriely, J. Leppanen, H. Leeb, A. Plompen, and R. Mills. Tendl-2015: Talys-based evaluated nuclear data library.

[208] J. E. Jakes. Improved methods for nanoindentation berkovich probe calibrations using fused silica. *Journal of Materials Science*, 53:4814–4827, 2018.

[209] J.G. Swadener, E.P. George, and G.M. Pharr. The correlation of the indentation size effect measured with indenters of various shapes. *Journal of the Mechanics and Physics of Solids*, 50(4):681–694, 2002.

[210] L. M. Brown. Indentation size effect and the hall-petch 'law'. In *Mechanical Behaviour of Materials*, volume 662 of *Materials Science Forum*, pages 13–26. Trans Tech Publications Ltd, 1 2011.

[211] Y. V. Milman, A. A Golubenko, and S. N. Dub. Indentation size effect in nanohardness. *Acta Materialia*, 59(20):7480–7487, 2011.

[212] Takahito Ohmura and Masato Wakeda. Pop-in phenomenon as a fundamental plasticity probed by nanoindentation technique. *Materials*, 14(8), 2021.

[213] F. Pohl. Pop-in behavior and elastic-to-plastic transition of polycrystalline pure iron during sharp nanoindentation. *Scientific Reports*, 9:15350, 2019.

[214] Ling Zhang and Takahito Ohmura. Plasticity initiation and evolution during nanoindentation of an iron–3 *Physical Review Letters*, 112:145504, 2014.

[215] K. Jin, Y. Xia, M. Crespillo, H. Xue, Y. Zhang, Y.F. Gao, and H. Bei. Quantifying early stage irradiation damage from nanoindentation pop-in tests. *Scripta Materialia*, 157:49–53, 2018.

[216] T. Y. Tsui and G. M. Pharr. Substrate effects on nanoindentation mechanical property measurement of soft films on hard substrates. *Journal of Materials Research*, 14(1):292–301, 1999.

[217] Peter Hosemann, Daniel Kiener, Yongqiang Wang, and Stuart A. Maloy. Issues to consider using nano indentation on shallow ion beam irradiated materials. *Journal of Nuclear Materials*, 425(1):136–139, 2012.

[218] Corey K. Dolph, Douglas J. da Silva, Matthew J. Swenson, and Janelle P. Wharry. Plastic zone size for nanoindentation of irradiated fe–9%cr ods. *Journal of Nuclear Materials*, 481:33–45, 2016.

[219] X. Hu, T. Koyanagi, M. Fukuda, N. A. P. Kiran Kumar, L. L. Snead, B. D. Wirth, and Y. Katoh. Irradiation hardening of pure tungsten exposed to neutron irradiation. *Journal of Nuclear Materials*, 480:235–243, 2016.

[220] Takashi Tanno, Makoto Fukuda, Shuhei Nogami, and Akira Hasegawa. Microstructure development in neutron irradiated tungsten alloys. *MATERIALS TRANSACTIONS*, 52(7):1447–1451, 2011.

[221] Yasuhisa Oya, Xiaochun Li, Misaki Sato, Kenta Yuyama, Makoto Oyaidzu, Takumi Hayashi, Toshihiko Yamanishi, and Kenji Okuno. Deuterium permeation behavior for damaged tungsten by ion implantation. *Journal of Nuclear Science and Technology*, 53(3):402–405, 2016.

[222] R.A. Causey, Richard Karnesky, and Chris San Marchi. Tritium barriers and tritium diffusion in fusion reactors. *Comprehensive Nuclear Materials*, 4:511–549, 12 2012.

[223] Alice Ying, Haibo Liu, and Mohamed Abdou. Analysis of tritium/deuterium retention and

permeation in fw/divertor including geometric and temperature operating features. *Fusion science and technology*, 64(2):303–308, 2013.